Reversible addition-fragmentation chain transfer emulsion polymerisation for preparation of biologically compatible nanoparticles

Pratik Gurnani

A thesis submitted in partial fulfilment of the requirements for the degree of

Doctor of Philosophy in Chemistry

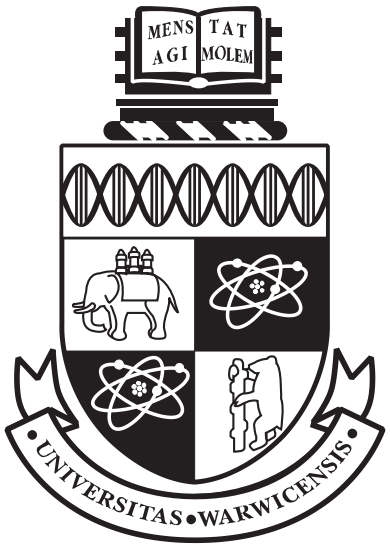

Department of Chemistry

University of Warwick

August 2018

Do, or do not. There is no try.

-Master Yoda

I believe there are no questions that science can't answer about a physical universe

-Prof. Stephen Hawking

Table of contents

List of figures

List of tables

List of schemes

List of publications

The following publications have been produced from the work detailed in this thesis.

Gurnani, P.; Perrier, S., Heterogeneous reversible deactivation radical polymerisation to generate nanoparticles for biological applications. – *To be submitted*

Gurnani, P.; Lunn, A. M.; Perrier, S., Synthesis of mannosylated and PEGylated nanoparticles via RAFT emulsion polymerisation, and investigation of particle-lectin aggregation using turbidimetric and DLS techniques. – *Polymer* **2016,** *106*, 229-237.

Gurnani, P.; Sanchez-Cano, C.; Abraham, K.; Xandri-Monje, H.; Cook, AB.; Hartlieb, M.; Levi, F.; Dallmann, R., Perrier, S., RAFT emulsion polymerisation as a platform to generate well-defined biocompatible latex nanoparticles. – *Macromol. Biosci.*, **2018**, 1800213.

Gurnani, P.; Sanchez-Cano, C.; Xandri-Monje, H.; Zhang, J.; Hartlieb, M.; Yu, K.; Hodges, C.; Harbottle, D.; Cayre, OJ.; Dallmann, R.; Perrier, S., Probing the effect of nanoparticle rigidity on the cellular uptake of core-shell polymer latex nanoparticles. – *To be submitted*

Gurnani, P.; Bray, CP.; Richardson, RAE.; Peltier, R.; Perrier, S., Heparin-mimicking sulfonated polymer nanoparticles via RAFT polymerisation-induced self-assembly. – *Macromol. Rapid Commun.*, **2018**, 1800314.

Abbreviations

^{13}C NMR	Carbon 13 NMR
^{19}F NMR	Fluorine-19 NMR
^{1}H NMR	Proton NMR
AA	Acrylic acid
ACVA	4,4'Azobis(4-cyanovaleic acid)
AGET	Activators generated by electron transfer
AMPS	2-Acrylamido-2-methyl-1-propanesulfonic acid
ASNS	L-Aspariginase
ATRP	Atom transfer radical polymerisation
BDMAT	Butyl dimethyl acid trithiocarbonate
bFGF	Basic fibroblast growth factor
bFGFR	Basic fibroblast growth factor receptor
BMA	Butyl methacrylate
BODIPY	Boron dipyrromethene
BODIPYA	Boron dipyrromethene acrylate
BSA	Bovine serum albumin
CDCl3	Deuterated chloroform
CLSM	Confocal laser scanning microscope
CMP	Cobalt mediated polymerisation
Con A	Concanavalin A
Conv	Monomer conversion
CPT	Camptothecin
Cryo-TEM	Cryogenic transmission electron microscopy
CuAAC	Copper azide-alkyne cycloaddition
Cy7.5	Cyanine7.5
Đ	Dispersity
DAAm	Diacetone acrylamide
DCC	Dicyclohexane carbodiimide
DEGMA	(Diethylene glycol) methyl ether methacrylate
DLS	Dynamic light scattering
DMAEMA	2-(Dimethylamino)ethyl methacrylate
DMAP	4-Dimethylaminopyridine
DMB	Dimethoxybenzidine
DMEM	Dulbecco's modified eagle medium
DMF	Dimethylformamide
DMSO	Dimethylsulfoxide
d*n*/d*c*	Incremental refractive index by concentration
DNA	Deoxyribonucleic acid
DOX	Doxorubicin
DP_n	Number average degree of polymerisation
DTT	Dithiothreitol
EDTA	Ethylenediaminetetracetic acid

EPR	Enhanced permeability and retention
ESI-MS	Electrospray ionisation mass spectrometry
FGF	Fibroblast growth factor
FRP	Free radical polymerisation
Gd-DOTA	Gadolinium tetra-azacyclododecatetraacetic acid
GFP	Green fluorescent protein
GMA	Glycerol methacrylate
Gox	Glucose oxidase
GSH	Glutathione
HEA	Hydroxyethyl acrylate
HPMAm	2-Hydroxypropylmethacrylamide
HRP	Horseradish peroxidase
i.p.	Intraperitoneal
LbL	Layer-by-layer
M_a	Apparent molar mass
macro-RAFT agent	Macromolecular reversible addition-fragmentation chain transfer agent
MEA	2-methoxyethylacrylate
MMA	Methyl methacrylate
M_n	Number average molar mass
$M_{n,th}$	Theoretical number average molar mass
$M_{n,SEC}$	Number average molar mass determined by SEC
MRI	Magnetic resonance imaging
Mw	Weight average molar mass
N_{agg}	Number of aggregation
NAM	*N*-acryloyl morpholine
NAT	*N*-acryloyl thiomorpholine
n-BA	n-butyl acrylate
NBMA	2-nitrobenzyl methacrylate
NIPAM	*N*-isopropylacrylamide
NIR	Nearinfrared
NMM	*N*-methoxymorpholine
NMP	Nitroxide mediated polymerisation
PABTC	Propanoic acid butyl trithiocarbonate
PBS	Phosphate buffer saline
PCC	Pearsons correlation coefficient
PDi	Polydispersity index
PEGA	Poly(ethylene glycol) methyl ether acrylate
PEGMA	Poly(ethylene glycol) methyl ether methacrylate
PEO	Poly(ethylene oxide)
PISA	Polymerisation-induced self-assembly
PS	Polystyrene
PVA	Poly(vinyl alcohol)
PyBOP	(Benzotriazol-1-yloxy)tripyrrolidinophosphonium hexafluorophosphate
QCM-D	Quartz crystal microbalance with dissapation
qDMAEMA	Quaternised DMAEMA
RAFT	Reversible addition-fragmentation chain transfer

RDRP	Reversible deactivation radical polymerisation
RI	Refractive index
RITC-Dx	Rhodamine isothiocyanate dextran
RNA	Ribonucleicacid
RPMI	Roswell Park Memorial Institute
SANS	Small angle neutron scattering
SDS	Sodium dodecyl sulfate
SEC	Size exclusion chromatography
siRNA	Small interfering RNA
SLS	Static light scattering
TBAF	Tetrabutyl ammonium fluoride
t-BMA	*tert*-butylmethacrylate
TEM	Transmission electron microscopy
TERP	Organotellerium-mediated radical polymerisation
TFEA	Trifluoroethyl acrylate
T_g	Glass transition temperature
TLC	Thin layer chromatography
TMS	Trimethylsilane
UV-VIS	Ultraviolet-visible
VA-044	2,2'-Azobis[2-(2-imidazolin-2-yl)propane]dihydrochloride
VA-057	2,2'-Azobis[N-(2-carboxyethyl)-2-methylpropionamidine]tetrahydrate
VA-086	2,2'-Azobis[2-methyl-N-(2-hydroxyethyl)propionamide]
VBA	Vinylbenzylaldehyde
ZP	Zetapotential

Acknowledgements

First I would like to thank my supervisor, Prof. Sébastien Perrier for giving me the amazing opportunity to do my PhD here. I've had a brilliant time and learnt more things than I thought I could handle, and that's mainly down to the opportunities I was able to take advantage of by being in this group. Thanks for being a great support, both in dishing advice out and listening (from time to time) to my point of view and I know I will take a lot from this experience for the future.

Before moving on to the other people I need to thank for my PhD I would like to thank Prof. Peter Scott, my MChem and undergraduate project supervisor. It was definitely with you that I got the research bug, and once I got it, I couldn't get rid of it. The times I had spent in your lab were great, and without that I doubt I would have been here, especially considering the encouragement you gave me to give another research area a go!

Next, I would like to thank my pseudo-second supervisor Dr Robert Dallmann, for the fantastic advice you gave me throughout my PhD both scientifically and career wise. It's not particularly often you meet people who are excellent at what they do, and are also incredibly nice and will go out of their way to help a feeble chemist. While I started my PhD as a chemist, thanks to you I certainly finished it as something else.

Within the group I would like to thanks Dr Carlos Sanchez-Cano for being an excellent mentor and a brilliant friend. Without your guidance, much of this project would have been a disaster but your wisdom led me to brighter pastures and here lies the finished product. Going all the way back to the start, I will thank Dr Guillaume Gody and Dr Ming Liang Koh, now legends of the Perrier group alumni, for teaching me how to do RAFT and how not to saturate a DLS machine. Next, thanks to Dr Johannes Brendel for always being there to ask really dumb questions, but luckily he always had the right answer! Many thanks to Dr Sylvain Catrouillet for the great guidance on scattering techniques, and for letting me come to the ILL in 2016 for my first, and hopefully not last beamline adventure. Thanks to Dr Matthias Hartlieb for being my chemistry sparring buddy, where we would come up with about 10 (probably unfeasible) ideas in about 10 minutes. Raoul, you definitely tipped the office over when it came to weirdness but it wouldn't have been the same without you, even if you did think that protein synthesis happened by magic. Ed, for being just a big a nerd as I am. Even though it was only one year, many thanks to

Dr Jie Yang and Dr Qiao Song, who were always great to talk to about science and thesis writing. Finally, I will thank our most distant member, Dr Joaquin Sanchis (Ximo), I always appreciated the time you took to talk and give project ideas even if the meetings were at a 12 h time difference, which you certainly took the brunt of.

A PhD certainly isn't an individual feat, and would be incredibly arduous if you didn't have company along the way. For that I would like to thank all of the PhD students in the Perrier group, past and present, Liam, Tammie, Sophie, Junliang, Caroline, Guillaume, Joji, Alex (Cookie), Andy K, Majda, Andy L, Agnes, Julia, Sean, Robert, Fannie, Tom and Satu. I really hope I will get to see some of you guys again, and I hope most of the people in my future are just as friendly and welcoming. I also want to thank my Gibbet Hill colleagues/friends, Helena, Swati, Laura, Ewan and Kristin for the company and collaboration!

Next for the work related stuff, I thank Prof. Francis Levi, Prof. Peter Sadler, Dr Annabelle Ballesta and Dr Isolda Romero Canelon, for the useful discussions we had during the chronotherapy aspect of the project.

Of course I want to thank my parents and brother for being incredibly supportive during my PhD, even if you didn't think it was a good idea!

Finally, I'd like to thank the person who has kept me going these last four years, who has seen the best and worst parts of me but still stood by. Sascha, I really couldn't have done this without you and I'm so grateful to have you by my side.

Declaration

Experimental work contained in this thesis is original research carried out by the author, unless otherwise stated, in the Department of Chemistry at the University of Warwick, between October 2014 and July 2018. No material contained has been submitted for any other degree, or at any other institution.

Results from other authors are referenced in the usual manner.

Signed:_____ Date: _____

Pratik Gurnani

Abstract

Reversible deactivation radical polymerisation represents a versatile route to prepare well-defined polymeric materials with complex architecture, controlled molecular weight and tuneable end-groups. RDRP techniques have now been translated to heterogeneous polymerisations (emulsion, dispersion, suspension etc.) allowing large scale preparation of nanoparticles with tuneable cores and shells in an aqueous environment. Such systems show great promise in biomedical applications due to their long circulation time, passive tumour accumulation, and core-shell architecture capable of drug loading and controlled release. The overall aim of this thesis is to assess RAFT emulsion polymerisation as a route to prepare nanoparticles for potential biomedical applications, and to study their physical properties, cytotoxicity, cellular uptake and *in vivo* distribution.

Firstly, the synthesis of nanoparticles from amphiphilic block copolymers *via* RAFT emulsion polymerisation is explored, revealing optimum conditions. Preliminary *in vitro* and *in vivo* cytotoxicity and biodistribution studies indicated high biocompatibility with significant liver accumulation post-injection. Following this, a systematic study identifying the effect of nanoparticle rigidity on cellular uptake is explored using a library of hard, intermediate or soft cores tuned with their glass transition temperature. Intracellular fluorescence studies display an increasing amount of uptake with decreasing nanoparticle rigidity, with mechanistic studies suggesting this could be due to a preference of the harder nanoparticles to be internalised *via* clathrin and caveolae-mediated endocytosis. In the next chapter, alkyne functional RAFT agents are prepared to impart functionality at the nanoparticle surface. It is found that by replacing the initial carboxylate with other functionality significantly reduces colloidal stability. Finally, polysulfonated macro-RAFT agents are used to synthesise heparin-mimicking nanoparticles, *via* RAFT emulsion polymerisation, capable of stabilising growth factors. The nanoparticles outperform linear analogues and heparin itself, suggesting that the high local concentration at the particle surface significantly improves bioactivity.

Overall, this thesis describes how aspects such as particle size, core and shell composition, and corona functionality can be modified individually for specific biological applications.

Chapter 1

Heterogeneous reversible deactivation radical polymerisation to generate nanoparticles for biological applications

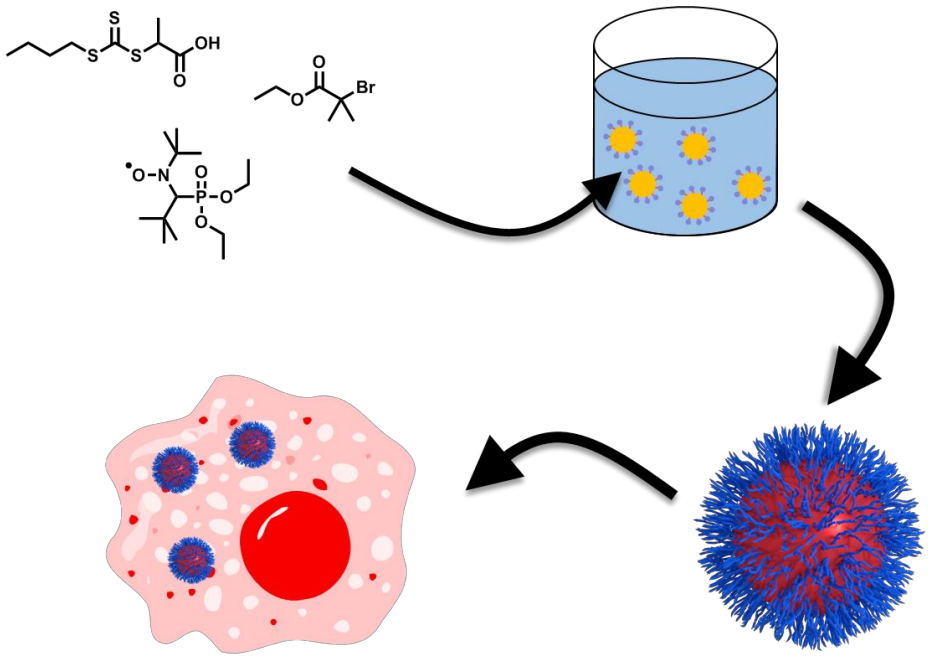

1.1 Introduction

Over the past few decades, nanomaterials, specifically nanoparticles have become ubiquitous in modern biomedical research. There are now many examples of organic (polymeric, liposomal, protein)[1-3] and inorganic (metallic, quantum dots, silica)[4-6] nanoparticles which excel in applications such as cargo (drug/protein/nucleic acid)[7-9] delivery, bio-imaging[10] and diagnostics.[11] While to date their clinical use has been limited,[12, 13] 'nanomedicine' is an active field of research within the academic and industrial world, largely due to the versatility of materials available, and the advantageous properties they display. Their large volumes (relative to molecular drugs) are known to significantly increase circulation time[14] and encapsulate/protect a tremendous amount of pharmaceutic payloads.[15] Whereas their large surface area has been exploited to improve biocompatibility and disease targeting through conjugation of 'stealthy' polymers[16] and bio-active moieties respectively. This property minimises the formation of protein coronas, which is known to enhance clearance via the immune system.[17] In particular, nanoparticles have been studied for their potential use in cancer therapy, mostly driven by their ability to passively accumulate in leaky malignant tumour tissue, known as the enhanced permeability and retention (EPR) effect.[18, 19] Overall these properties can improve therapeutic efficacy and minimise clinical side effects while reducing the maximum dose requirements.

Out of the plethora of reported biomedical targeted nanoparticle systems, polymeric systems have shown great promise due to their chemical versatility.[20] For example, factors such as chemical functionality, charge, stimuli-responsivity and degradability can be easily introduced by tuning the monomer composition. Furthermore, a variety of polymeric nanoparticle architectures (self-assembled micelles,[21] nanoworms,[22] polymersomes,[23] latex particles,[24] branched polymers (hyperbranched[25] and dendrimers[26]) and nanogels[27]) can now be prepared with relative ease.

Perhaps the most prominent advancements in polymer nanoparticle design have arisen from developments surrounding reversible deactivation radical polymerisations (RDRP), either based on reversible deactivation (e.g. atom transfer radical polymerisation (ATRP),[28] nitroxide mediated polymerisations (NMP)[29, 30] and single electron transfer-living radical polymerisation (SET-LRP)[31]) or degenerative chain transfer (e.g. reversible addition fragmentation chain transfer (RAFT)) (Figure 1.1).[32] These methods have

allowed researchers to prepare materials with narrow molecular weight distributions,[33] versatility in terms of block architecture,[34] and functional end-groups.[35] Since RDRP is well suited for preparing block copolymers, self-assembly has been the most popular method to prepare biologically relevant nanoparticles, as the ability to transform intricate polymer design into supramolecular structures is appealing from a design perspective.[36, 37] These processes however suffer from scalability limitations, with suspensions above a few weight percent being difficult to achieve.[38] Furthermore, these nanomaterials may disassemble at low concentrations (such as those found endogenously), thus releasing their cargo prematurely.

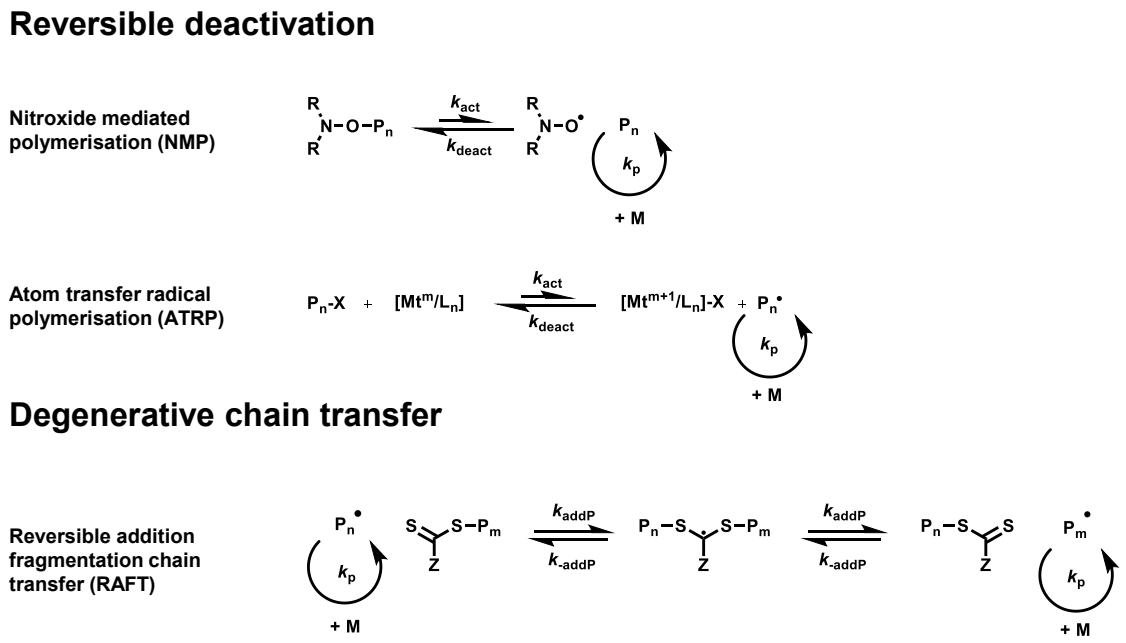

Figure 1.1 Mechanisms of nitroxide mediated polymerisation (NMP), atom transfer radical polymerisation (ATRP) and reversible addition-fragmentation chain transfer (RAFT).

Heterogeneous polymerisations (emulsion,[39] dispersion,[40] suspension,[41] miniemulsion[42] and inverse emulsion)[43] are now heavily exploited to generate polymer colloids reproducibly at large scales and with environmentally friendly conditions. In many, but not all of these systems, compartmentalisation effects (i.e. segregation of propagating radicals) leads to fast propagation rates, full monomer conversion, low termination and therefore high molecular weight materials. However the multicomponent nature of many RDRP techniques mean that these processes cannot be directly translated to heterogeneous systems.[44, 45] Nonetheless, this approach was initially achieved by Bon *et al*. who described the NMP of styrene in emulsion conditions in 1996.[46] However, until 2007, research on RDRP techniques in dispersed states remained fairly fundamental, of

which there are many reviews on this topic.[45-54] Since overcoming many of the obstacles initially presented, much of the present work points to applying these to synthesise nanomaterials geared towards a range of applications.

With the increased use biomedical nanoparticles, and RDRP in dispersed states there are now many examples using these approaches used to generate nanoparticles for these applications. In this chapter, different dispersed state polymerisations will be critically analysed but from the perspective of preparing biologically relevant nanomaterials. In each section a description of the heterogeneous system, examples from the literature, and analysis of the advantages and disadvantages each brings for biological applications will be given. It should be noted that only articles which include biological characterisation have been reviewed, rather than a full assessment of heterogeneous polymerisation.

1.2 Miniemulsion polymerisation

In conventional miniemulsion polymerisations, a water immiscible monomer is emulsified with surfactant in an aqueous continuous phase using external shearing forces such as ultrasonication, resulting in kinetically stable, but thermodynamically unstable droplets (Figure 1.2a).[42] This can also be applied to a water in oil system - inverse miniemulsion polymerisation, in which the polymerisation occurs within aqueous monomer droplets dispersed in an oil continuous phase (Figure 1.2b).[43] In an ideal system, each monomer droplet is converted into a polymeric particle, and as these are effectively a mini-bulk/solution polymerisations, this removes the necessity for monomer diffusion through the aqueous phase (as in normal emulsion polymerisation) and as such many RDRP (RAFT,[55-58] ATRP,[59-61] and NMP[62-65]) miniemulsion polymerisations, either conventional or inverse, have been reported.

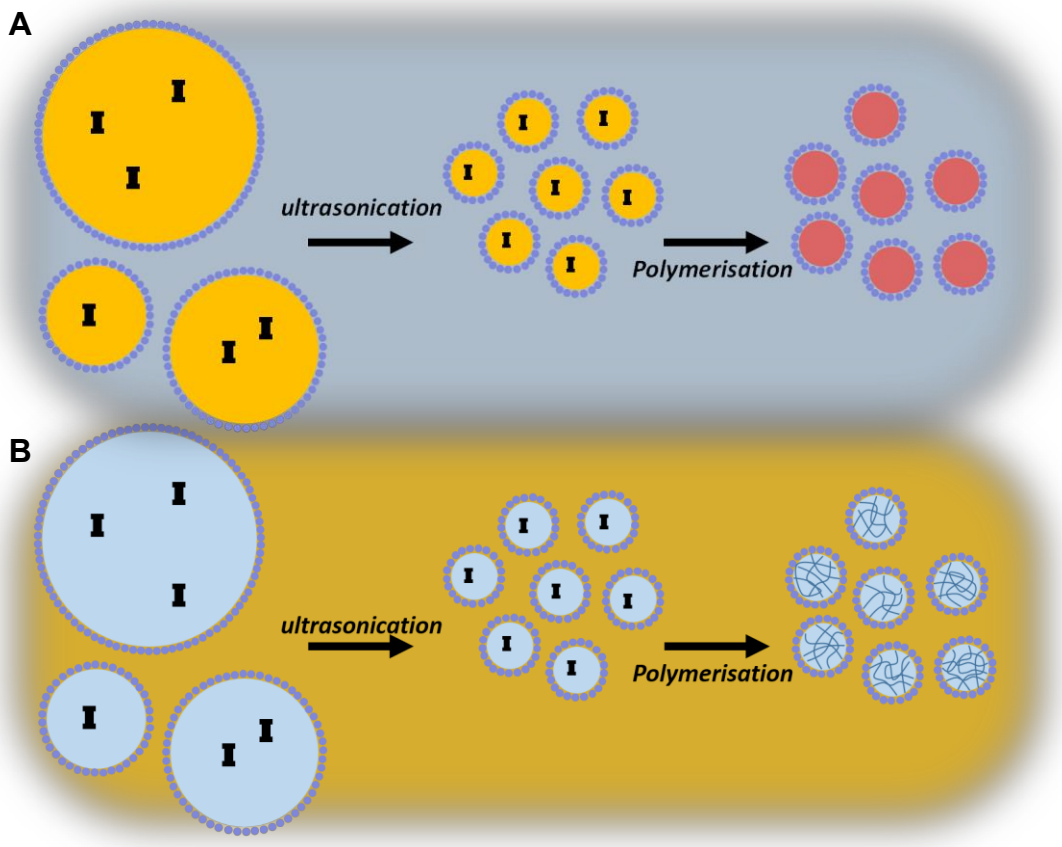

Figure 1.2 Schematic representation of (A) miniemulsion polymerisation and (B) inverse miniemulsion polymerisation. I = initiator species, yellow = oil/monomer phase, blue = aqueous phase, red = polymer phase.

1.2.1 Inverse miniemulsion polymerisation

Inverse miniemulsion polymerisation enables the preparation of fully hydrophilic nanoparticles, in which the polymer chains are cross-linked (covalent or non-covalent) in a network like structure giving them the term 'nanogels'. These are typically swollen when suspended in aqueous solutions, making their chemical structure accessible for potential degradation triggered by endogenous biochemical stimuli (e.g. glutathione,[66] enzymes,[67] pH changes[68]). It should be noted that although these are conventionally called 'inverse emulsion' in reality they are closer to an 'inverse miniemulsion' as the monomer does not diffuse from large droplets to growing particles.

Many examples of nanogels synthesised with free-radical polymerisation exist in the literature, and are used mainly in drug delivery,[69] diagnostics[70] and imaging[71]. However, their network-like structure in particular lends them towards encapsulation of biomacromolecules, such as proteins and nucleic acids by physical entrapment. RDRP techniques even allow for the distribution of cross-linking points thus a more homogenous gel structure directly impacting their biological performance. This has been extensively reported for ATRP and RAFT based nanogels.[72] Notably there are no NMP inverse miniemulsion polymerisations reported, and is likely a consequence of commercially available nitroxides being relatively water insoluble.

1.2.1.1 ATRP nanogels

ATRP relies on an external catalyst (typically a transition metal complex) to reversibly deactivate propagating radicals to a dormant state.[28] This reliance on a secondary species means that for efficient ATRP, the two components must be present in the same phases, without significant partitioning. For these reasons inverse miniemulsion polymerisations, which are simply compartmentalised aqueous polymerisations, are the most commonly used for heterogenous ATRP.

This was first reported by Matyjaszewski and co-workers who prepared 200 nm poly(poly(ethylene glycol) methyl ether methacrylate) (P(PEGMA)) nanogels cross-linked with a redox responsive disulphide functional dimethacrylate monomer, and were synthesised using a cyclohexane continuous phase.[61] They highlight that the sonication process intended for homogenisation also results in oxidation of the active Cu(I) species

back to the Cu(II) complex. For that reason, the authors successfully implemented the activators generated by electron transfer (AGET) ATRP mechanism, using ascorbic acid as a water soluble reducing agent, alongside a PEG macromolecular ATRP (macro-ATRP) initiator to limit partitioning into the oil phase. They found that their ATRP 220 nm nanogels had better colloidal stability, almost doubled swelling ratios, and were degradable into individual polymer chains ($Đ$ < 1.5), when compared to analogous nanogels prepared with free radical polymerisation.

In a follow up study, these nanogels were evaluated as potential anticancer agents with the encapsulation of up to 16.4 wt% doxorubicin, which released steadily after biodegradation with tripeptide glutathione.[73] The drug loaded nanogels gave reduced viability in *in vitro* studies against a cervical cancer cell line (HeLa). Further to this, they exploited the RDRP approach, and chain extended the initial nanogel with 2-hydroxyethyl acrylate (HEA) to introduce hydroxyl functionality to the nanogel surface, and subsequently conjugated with bioactive moiety biotin.

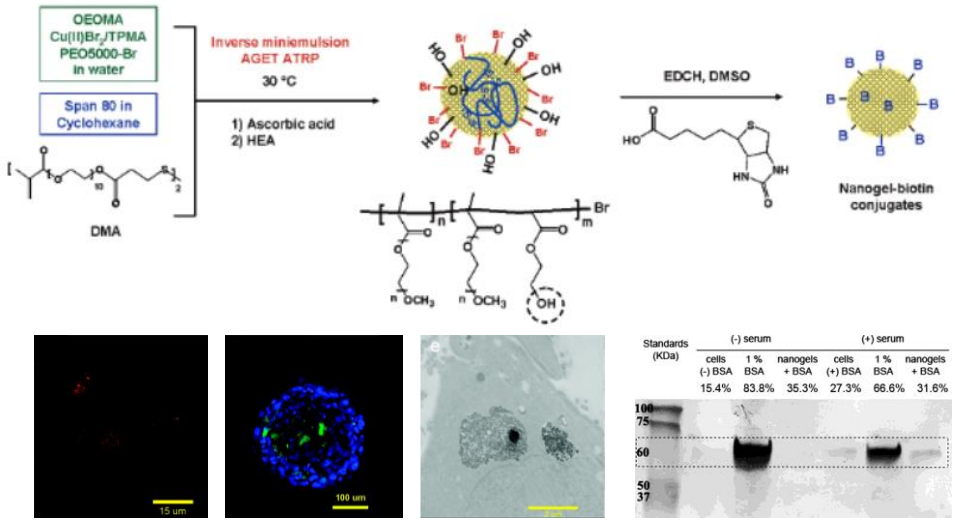

Figure 1.3 Typical ATRP inverse miniemulsion polymerisation to produce disulphide cross-linked nanogels. Adapted from Matyjaszewski *et al*.[61, 73]

As stated above, the ability to entrap hydrophilic objects within a nanogel matrix remains a major advantage. Matyjaszewski and co-workers have thoroughly exploited this property with their ATRP nanogel system. Initially they reported encapsulation of rhodamine modified dextran (RITC-Dx), as a model for carbohydrate therapeutics.[74] These were entrapped with over 80% efficiency, with a maximum loading of 6.4 wt%. Upon degradation with glutathione, the released dextran was able to bind strongly to Concanavalin A (ConA), causing aggregation which was monitored by an increase in

turbidity with UV-Vis spectroscopy. Analogous non-degradable RITC-Dx loaded nanogels were found to accumulate in clathrin coated pits (indicating uptake *via* clathrin mediated endocytosis) in murine osteoblast cells (MC3T3).[75] This was then further confirmed with TEM by encapsulating gold nanoparticles. By copolymerising PEGMA and an RGD (integrin binding peptide) functionalised monomer, an increased cellular internalisation of the nanogels was observed.[75] To evaluate if protein encapsulation was viable during such harsh preparation conditions (sonication, heating high radical flux), bovine serum albumin (BSA) was added into the aqueous polymerisation phase. Western-blot analysis of lysed cells which were treated with BSA-nanogels indicated that a large amount of the protein remained native after nanogel preparation (Figure 1.3).[75]

Instead of physical entrapment, an alternative approach to generate protein-nanogel hybrids was reported, whereby a green fluorescent protein (GFP) was genetically engineered such that a phenyl alanine bearing an ATRP initiator was introduced in a site specific manner.[76] This was used in conjunction with the traditional PEG-ATRP initiator described above to produce nanogels with covalently bound GFP. Confocal microscopy and fluorescence spectroscopy confirmed the incorporation of 2.1 wt% GFP into the nanogels. When compared to physical entrapment, the authors found that no GFP was retained after purification, highlighting the importance of covalent attachment. This is somewhat contradictory to the identical BSA nanogels above which were readily retained after physical entrapment.[75, 76]

More recently this AGET ATRP inverse miniemulsion polymerisation approach was exploited to produce nanogels capable of encapsulating of nucleic acids. Similar systems have been shown to protect these macromolecules from nucleases, potentially enhancing gene delivery applications.[77] PEGMA was copolymerised with quarternised 2-(dimethylamino) ethyl methacrylate (qDMAEMA) as a cationic comonomer following the same inverse miniemulsion approach. The resulting nanogels had a larger hydrodynamic diameter (275 nm) than those without qDMAEMA and a strongly positive zetapotential (+43.7 mV) thus making it capable of complexing plasmid DNA. They found w/w ratios greater than 5:1 nanogel:pDNA was sufficient to bind plasmids, and heparin sulfate could be used to displace it below 10:1. In contrast, siRNA required a ratio of at least 15:1 nanogel:siRNA for full complexation and could be displaced up to 25:1. Nanogel polyplexes with pDNA encoding for firefly luciferase (FLuc), and silencing

siRNA for Renilla luciferase (RLuc) showed comparable transfection and knockdown efficiencies to commercially available FuGENE-HD (Figure 1.4).[77]

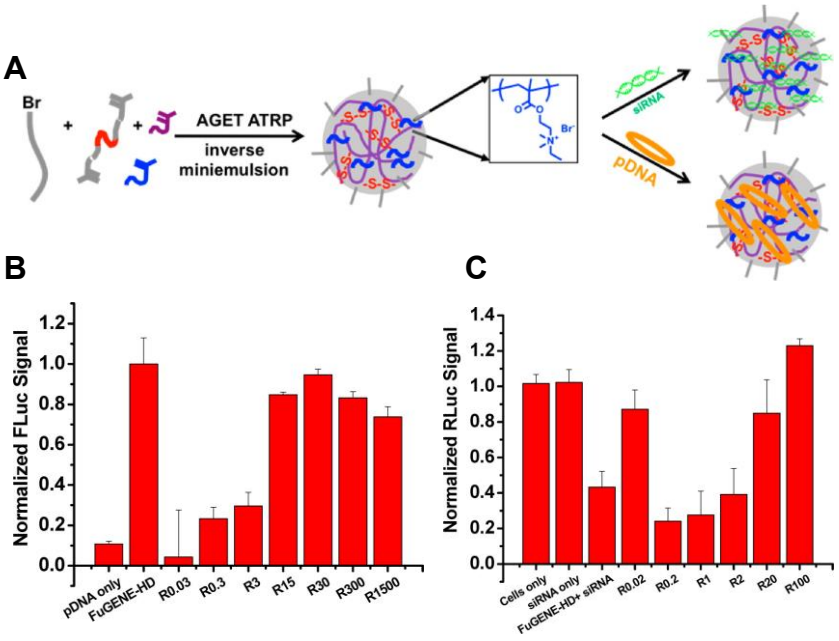

Figure 1.4 (A) ATRP inverse miniemulsion polymerisation of qDMAEMA to produce cationic nanogels capable of complexing both siRNA and plasmid DNA. Relative transfection efficiency of a (B) plasmid containing a firefly luciferase reporter gene and (C) knockdown of Renilla luciferase with siRNA. Adapted from Matyjaszewski *et al*.[77]

Hollinger and co-workers later used these cationic nanogels to complex siRNA which silences *Runx2* and *Osx*, key regulators of osteogenetic differentiation, as a potential treatment of heterotopic ossification (abnormal bone growth).[78] In general, similar silencing capabilities (40-60% reduction in gene expression) were observed between nanogels and commercial transfection agent lipofectamine, however no cytotoxic effects were evident after nanogel treatment whereas lipofectamine yielded 60% cell viability.[78]

1.2.1.2 RAFT nanogels

In contrast to ATRP, RAFT is a degenerative chain transfer process which does not typically require a catalyst, and involves a chain transfer agent (thiocarbonylthio compounds) and an external radical source. From a biological perspective, nanogels synthesised using RAFT may offer significant advantages over ATRP as the synthetic process is simpler, and the presence of excess copper complexes (the most common ATRP catalysts) can be cytotoxic.[79] While most biologically relevant RAFT nanogels are synthesised by precipitation/dispersion polymerisation of thermoresponsive polymers (e.g. P(NIPAM)),[72] or soluble branched structures, there are a few notable examples using inverse miniemulsion procedures for biomedical applications.

As common RAFT agents are fairly hydrophobic, their applicability in fully aqueous polymerisation can be limited. This has been overcome by preparation of hydrophilic macro-RAFT agents to enhance water solubility. For instance, Davis and co-workers report on the synthesis of cationic DMAEMA based nanogels from a hydrophilic P(PEGMA) macro-RAFT agent, previously prepared in acetonitrile, for gene delivery applications.[80] Inverse miniemulsions were performed with and without macro-RAFT agent at 60°C, and cross-linked with a similar disulphide dimethacrylate. Interestingly only the RAFT inverse miniemulsion achieved over 98% monomer conversion in 6 h, whereas the analogous free radical polymerisation was limited to 90% within the same time frame. Narrow dispersity polymers ($Đ < 1.3$), and consistent average molar masses were achieved with the RAFT system, however a small proportion of the macro-RAFT agent remained unconsumed. In contrast, the free radical polymerisation (FRP) nanogels consisted of much higher molecular weight polymers, however the particles had smaller diameters (~100 nm), compared to the RAFT nanogels (~250 nm), both with zetapotentials of +42 mV which is in agreement with the ATRP nanogels described above. This difference in size depending on polymerisation technique may have significant implications on their biological activity. [80]

Klok and co-workers have reported the synthesis of poly(*N*-(2-hydroxypropyl)methacrylamide) P((HPMAm)) nanogels using a similar approach.[81] P(HPMAm) is widely used in polymer therapeutics as it shows high biocompatibility, tuneable functionality, and is included in materials which have entered clinical trials after FDA approval.[82] In contrast to the above study, the authors use a solvent mixture of 9:1

H_2O:Methanol to aid solubility of their RAFT agent. A variety of RAFT P(HPMAm) nanogels were synthesised using different experimental conditions (DP, surfactant, initiator concentration, cross-linker concentration) as well as a free radical analogue cross-linked with a disulphide bridge. With high concentrations of initiator, quantitative monomer conversions were attained, yielding P(HPMAm) RAFT nanogels between 150-200 nm in diameter and dispersities around 1.4 for the component polymers. As a proof of concept protein encapsulation experiment, cytochrome C (5 wt%) was added to the aqueous phase with 73% incorporation. Release studies showed rapid protein release (100% within 1 h) only after disulphide reduction with a phosphine, with none observed without nanogel degradation (Figure 1.5).[81]

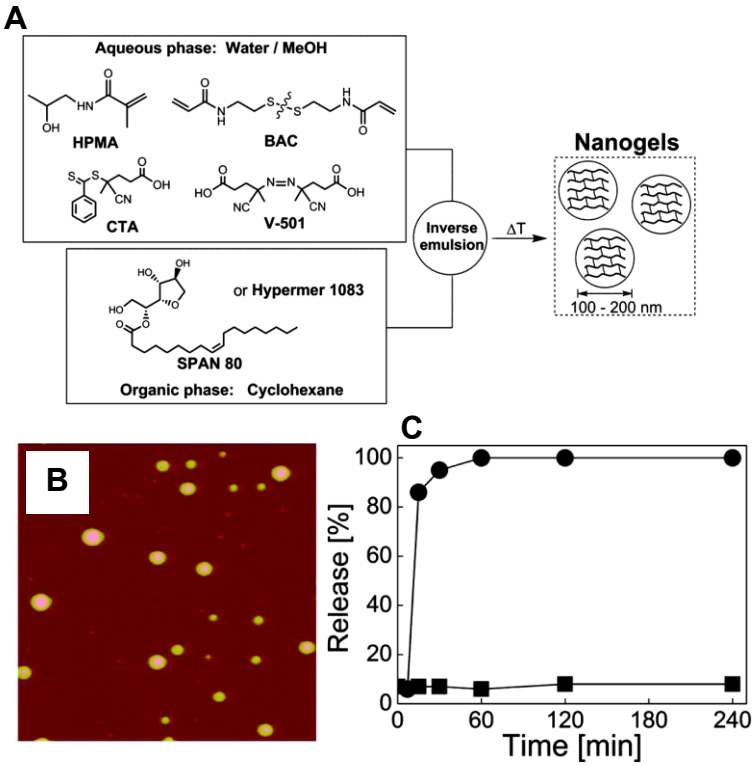

Figure 1.5 (A) Inverse RAFT miniemulsion polymerisation of HPMAm to produce disulphide cross-linked nanogels. (B) Atomic force micrographs of the synthesised nanogels and (C) release of encapsulated cytochrome C with (cirlces) and without (squares) addition of Tris(2-carboxyethyl)phosphine hydrochloride (TCEP) as a reducing agent. Adapted from Klok *et. al.*[81]

1.2.1.3 General remarks on RDRP nanogels

As mentioned previously, inverse emulsion polymerisations are a highly favourable route to design fully hydrophilic nanoparticles for loading and transport of biomacromolecular cargo. However excess surfactant and the continuous phase (typically cyclohexane) must be removed prior to biological use due to inherent cytotoxicity or aqueous incompatibility. Surfactant use can be circumvented by utilising amphiphilic RDRP control agents (inistab),[83, 84] however with this it is impossible to independently tune the colloidal stability and the molecular weight of resulting polymers. The sonication procedures used are unfeasible in large volume reactors and the low monomer concentrations used limit their scale up potential. Nanoparticle size is a key parameter in a variety of biomedical applications, with nanoparticles with diameters below 200 nm reported being most effective.[85] From the above studies, it seems that RDRP inverse miniemulsion procedures are rarely able to produce nanoparticles below this threshold, potentially limiting clinical translation. Additionally, the above RDRP nanogel assemblies use proteins such as BSA and cytochrome C, which are relatively tolerant to extreme conditions such as sonication, heating and solvents during purification. Therapeutic proteins under these conditions could easily denature thus rendering them inactive thus reducing efficacy. In general, RDRP techniques have been shown to improve release rate and targeting potential through chain extension with functional moieties, however as of yet have not improved synthetic issues limiting their biological use.

1.2.2 Conventional Miniemulsion polymerisation

Conventional miniemulsion polymerisation occurs within sub-500 nm monomer droplets, stabilised by surfactant. This results in the formation of solid hydrophobic particles potentially capable of encapsulating hydrophobic drugs for controlled delivery. While some examples of ATRP and NMP miniemulsion polymerisation have been reported,[59, 60, 62-64, 86, 87] none are for biological purposes, with RAFT being the most favoured option for this application due to its compatibility with many monomer families, and is easily translated from traditional free radical systems, simply by addition of a suitable RAFT agent.

Introduction of glycosylated moieties at the particle surface has been shown to significantly improve disease targeting and cellular uptake, especially in immune cells.[88, 89] Yaacoub and co-workers reported the RAFT miniemulsion polymerisation of protected glucose and fructose methacrylates, with a subsequent chain extension with either methyl methacrylate (MMA) or butyl methacrylate (BMA).[90] Polymerisations were attempted with three different RAFT agents, with one yielding significantly narrow dispersities, as low as 1.10 and particle diameters between 150 and 350 nm. Nonetheless no biological characterisation (lectin binding, toxicity etc) were reported, possibly due to the large quantities of surfactant present in the polymerisation mixture.[90]

It is desirable to avoid conventional surfactants during nanoparticle synthesis, and such 'surfactant free' systems, which use amphiphilic macro-RAFT agent stabilisers are prevalent within this field. While not specifically for biological applications, Clavier and co-workers report on the RAFT miniemulsion copolymerisation of styrene and various boron-dipyrromethene (BODIPY) monomer types (styrenic, acrylate, methacrylate) to produce fluorescently labelled nanoparticles.[91, 92] This approach used a poly(ethylene oxide)-*b*-(acrylic acid) (PEO-*b*-PAA) macro-RAFT agent as the stabiliser and therefore avoids the use of conventional surfactants. Depending on the analogue of BODIPY monomer used in the polymerisations, some particles were up to 2000 times brighter than typical quantum dots, and as such could be useful in bioimaging applications.[91] It should be noted however that quantum dots are significantly smaller than the nanoparticles synthesised here (> 60 nm diameters), which would impact their circulation time.

An elegant approach which combines miniemulsion polymerisation with nanogel formation was described by Stenzel and co-workers using a P(PEGMA)-*b*-

P(DMAEMA)-*b*-P(*t*-BMA) macro-RAFT agent stabiliser.[93] This was chain extended with miniemulsion polymerisation using *t*-BMA and crosslinked with different ethylene glycol dimethacrylate (EGDMA) amounts (10, 20 or 30%) resulting in nanoparticles with roughly 200 nm diameters. Hydrolysis of the tert-butyl methacrylate cores with trifluoroacetic acid yielded swollen P(MAA) nanogels with varying cross-linking densities. The anionic core was then used to encapsulate large quantities (50 wt%) of anticancer therapeutic doxorubicin with electrostatic interactions, also enabling almost quantitative drug loading efficiencies. In release studies, they found that addition of acid shrunk the P(MAA) core and swelled the P(DMAEMA) shell resulting in a gated squeezing effect releasing over 90% of the encapsulated drug. This translated into a lower IC_{50} concentration for the drug loaded nanoparticles compared to free doxorubicin, which is exceptionally difficult to achieve (Figure 1.6).[93]

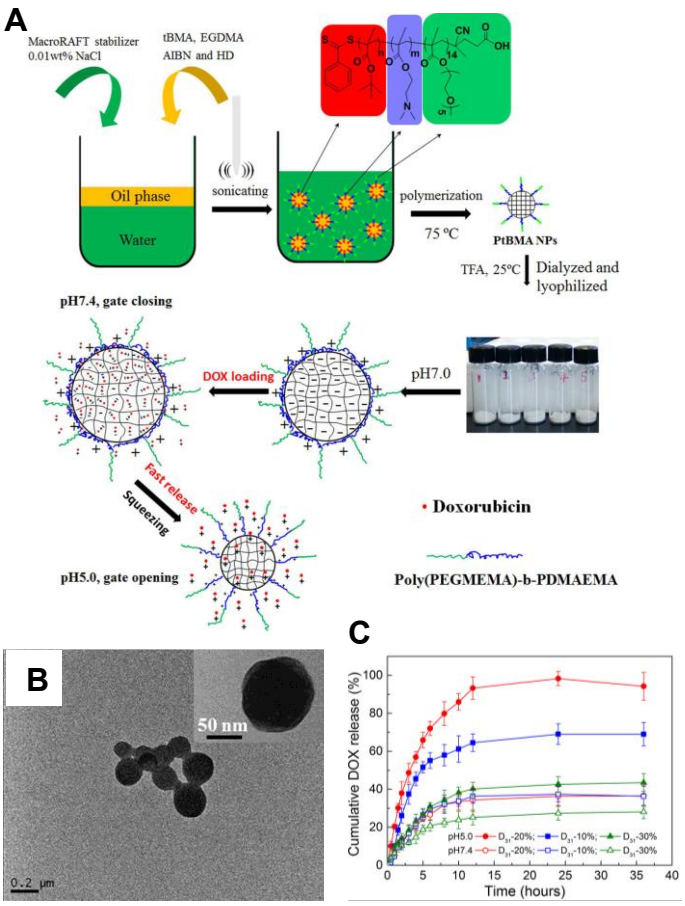

Figure 1.6 (A) Conventional miniemulsion polymerisation of *tert*-butyl methacrylate stabilised by a P(PEGMA)-*b*-P(DMAEMA)-*b*-P(*t*-BMA) macro-RAFT agent and subsequent hydrolysis with trifluoroacetic acid to produce pH gated nanogels. (B) TEM images of P(*t*-BMA) latexes and (C) release of loaded doxorubicin at pH 5.0 and 7.4. Adapted from Stenzel *et al*.[93]

The lack of RDRP miniemulsion polymerisation systems for biologically relevant nanoparticles may arise from rising popularity of other techniques yielding similar core-shell structures without the limitations of miniemulsion polymerisation. For instance, the requirement of high shearing limits the scalability of this process in comparison to polymerisation-induced self-assembly or conventional emulsion procedures (*vide infra*). Furthermore, the effect of molecular weight control may not influence any biological activity, as particle size and surface functionality are controlled by shearing and surfactant composition. This may then render FRP and RDRP latexes identical when using surfactant stabilised miniemulsion polymerisation, and therefore the added complexity of RDRP agents may be redundant. However, a key advantage of RDRP techniques here is the introduction of particular functionality at the particle surface, and the evasion of conventional surfactant use to improve potential biocompatibility.

1.3 Dispersion polymerisation

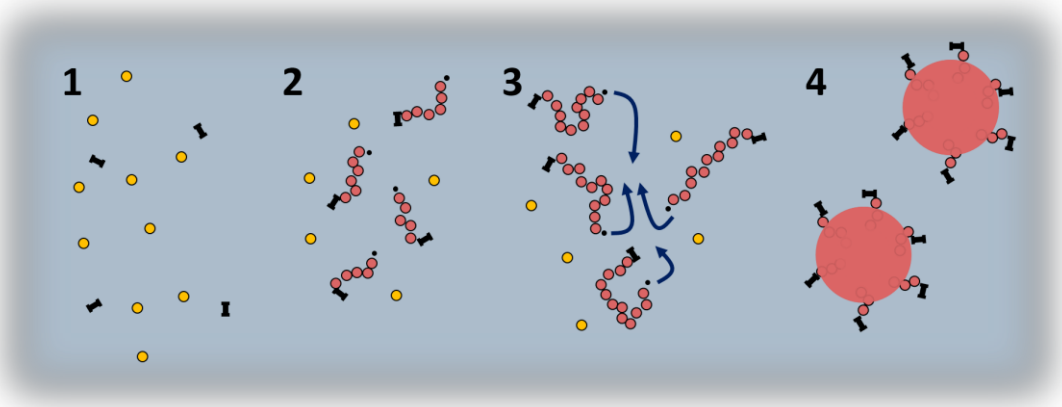

Figure 1.7 Mechanism of aqueous dispersion polymerisation. I = initiator species, yellow = monomer, blue = aqueous phase, red = polymer phase.

In contrast to other heterogeneous systems, in dispersion polymerisations all of the components (monomer, chain transfer agents, initiator) are soluble in the continuous phase at the start of the reaction.[40] The phase separation then occurs during the polymerisation, where the polymer chains reach a critical chain length then become insoluble in the continuous phase and precipitate resulting in particle formation (Figure 1.7). Common RDRP dispersion polymerisations have manifested themselves as a type

of polymerisation-induced self-assembly (PISA), which is where a solvophilic unit is chain extended with a block which selectively precipitates leading to self-assembled nano-objects coated in the initial solvophilic block (Figure 1.8).[94] The resulting morphologies are then dependent on the solvophobic/solvophilic volume ratio, and are often similar to those found using conventional selective solvent self-assembly procedures.[95, 96] Typically PISA is performed by taking a single solvophilic homopolymer and throughout the elongation of the second solvophobic block, the morphology reorganises from spheres, to worms, to vesicles and in some cases to lamellae as the polymerisation ensues. The *in situ* self-assembly allows for a much higher solids contents (up to 40%) in comparison to conventional self-assembly. Unfortunately, very few monomers have been found to display this phenomenon. Many RDRP dispersion polymerisations have been reported including NMP,[97] ATRP,[98] cobalt mediated polymerisation (CMP),[99] and organotellerium-mediated radical polymerisation (TERP),[100] however RAFT remains the most popular approach and is the only method used for biologically relevant particles. Aspects such as particle morphology, particle size and core/shell compositions can be easily tuned using RAFT, and as such, PISA is highly attractive from a biological standpoint either for fundamental studies or specific applications.

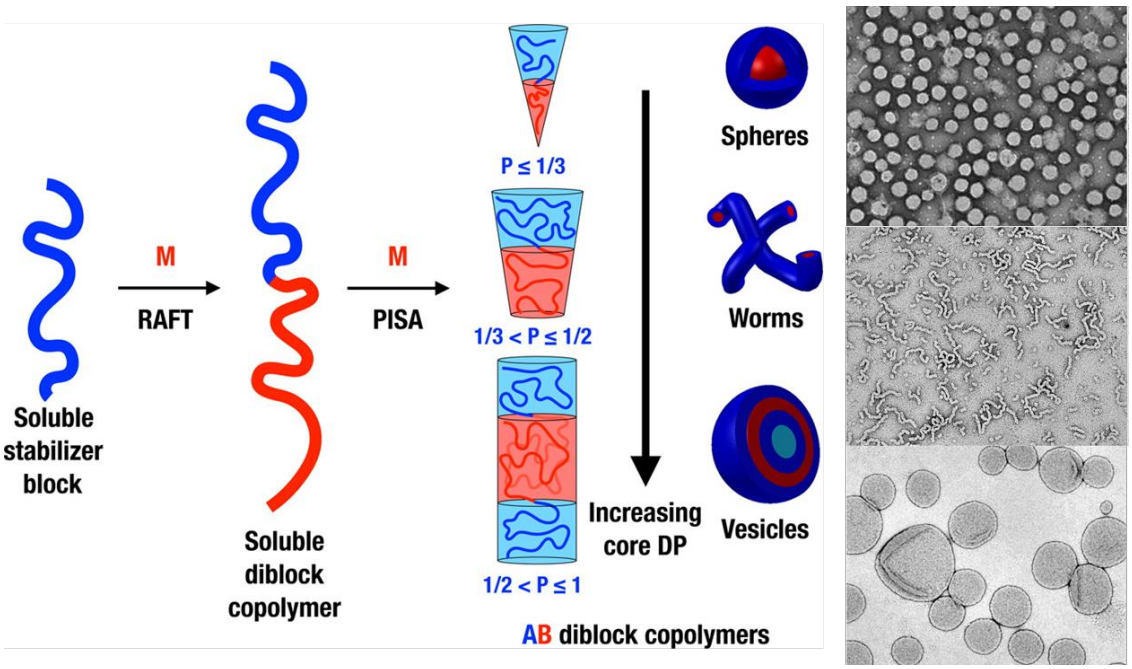

Figure 1.8 Generalised representation of RAFT polymerisation-induced self-assembly from a solvophilic macro-RAFT agent by chain extending with a monomer which upon polymerisation becomes solvophobic inducing self-assembly into spherical, worm and vesicle morphologies. Adapted from Armes *et. al*.[94]

1.3.1 Fundamental biological studies

The design of biomedical nanoparticles is often led by fundamental studies identifying the effect of individual physico-chemical properties (size, shape and surface functionality)[85, 101] on cellular uptake, biodistribution and pharmacokinetics. Non-spherical nanoparticles have attracted significant interest as many reports suggest they have improved cellular uptake and circulation time, and therefore greater therapeutic efficacy compared to spherical counterparts.[22] As such, PISA represents a promising method to probe this feature as morphology can be easily tuned without significantly affecting their surface chemistry which is also known to heavily influence biological performance.

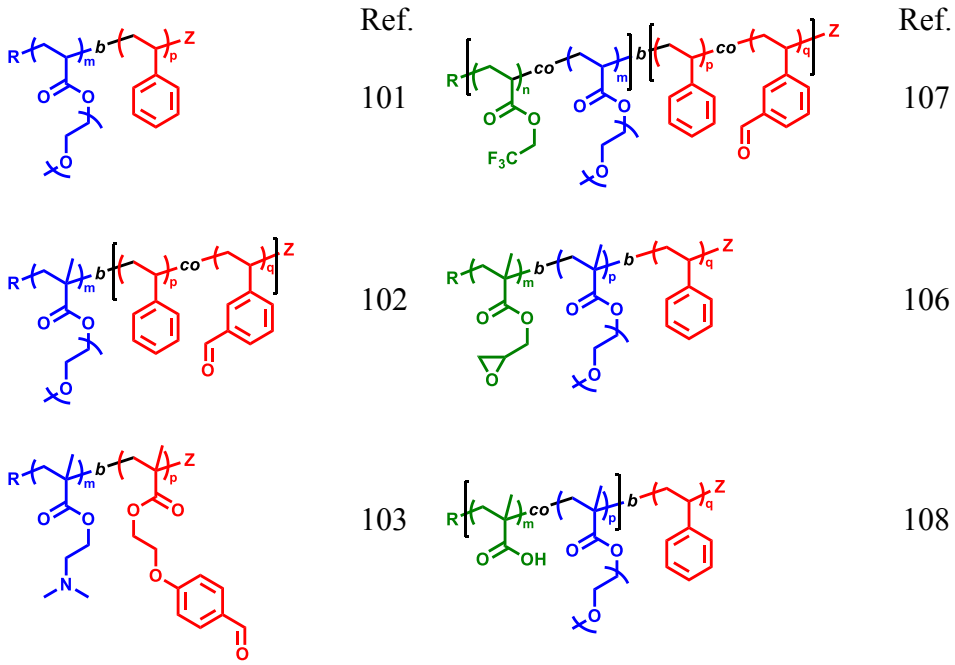

Figure 1.9 Block copolymers produced using polymerisation-induced self-assembly in alcoholic medium for biological applications. Green = functional group used for specific application, blue = solvophilic block, red = solvophobic block.

Boyer and Davis report RAFT PISA of styrene from a P(PEGMA) macro-RAFT in methanol, where styrene is soluble but polystyrene is insoluble.[102] As expected nanoparticle morphology evolved from spheres through to polymersomes with increasing monomer conversion. When relating the DP of styrene to the resulting morphology, it became apparent that isolating individual morphologies, particularly high aspect ratio particles was non-trivial as mixed morphologies could be seen at various chain lengths. To probe the *in situ* encapsulation of a model hydrophobic drug Nile Red was added at the start of the polymerisation. UV-Vis analysis showed higher encapsulation with longer

PS chain length (i.e. higher conversion), and Nile Red concentrations over 10 fold of that found in the methanol highlighting their potential use in drug delivery.[102]

In a subsequent study, styrene was copolymerised with vinyl benzaldehyde (VBA) during the PISA process to produce pH-responsive pro-drug imine containing nanoparticles with doxorubicin to evaluate the effect of morphology on drug delivery efficiency.[103] Narrow particle size distributions and the expected morphologies were produced depending on styrene chain length. Perhaps one of the major disadvantages in this approach is that large DP's e.g. 5000 were targeted, and therefore specific morphologies were formed at very low monomer conversion (< 20%). This meant that extensive purification was necessary to fully remove monomeric styrene and methanol before use in biological studies. Nonetheless, cellular studies with nanoparticles carrying a 5 wt% drug load indicated significantly higher cellular uptake for rod and worm-like micelles, which yielded the lowest IC_{50} values (0.796 and 0.302 μM for rod and worm-like nanoparticles respectively).[103]

In a similar approach, Pan and co-workers performed PISA with an aldehyde functional methacrylate from a P(DMAEMA) macro-RAFT agent in ethanol for post-functionalisation.[104] In contrast to the above studies, the particle morphology was controlled by targeting different solvophobic chain lengths (50, 100, 150, 200 and 250), each reaching full monomer conversions in 18 h. Although this eliminated the need to remove unconsumed monomer, purification was still necessary to remove the ethanol continuous phase. All of the resulting nanoparticles, regardless of morphology, had a smaller total diameter, as measured by dynamic light scattering (DLS), below 200 nm, which is the cited upper limit for endocytosis.[105] Doxorubicin loading was achieved using Schiff base formation, which naturally increased with longer aldehyde chain lengths reaching up to 16.2 wt%. Similar to the studies described above, DOX-loaded nanorods displayed the greatest cytotoxic effects against HeLa cells in comparison to spheres and vesicles, however longer nanowires showed minimal activity. This was rationalised with cellular uptake studies which indicated that nanorods had greater lysosomal (low pH compartment) residence time, thus improving drug release potential.[104]

The study of doxorubicin release was further investigated by Gooding and Gaus using pair correlation microscopy to probe the intracellular trafficking and site of drug release for different shaped nano-objects.[106] In this work, similar nanoparticles to those reported

by Davis and co-workers were prepared instead with a PS-*co*-P(VBA) core. Their findings indicated that worm and rod-like materials passively enter the nucleus in a five-fold higher amount than spherical and vesicular systems. Furthermore, attachment of nuclear localising peptides resulted in much greater doxorubicin release within the nucleus and enhanced cytotoxic effects.[106]

Many of the above studies use relatively simple block copolymer compositions (P(PEGMA)-*b*-PS) for nano-object synthesis (Figure 1.9). As dispersion polymerisations begins in solution, complex functionality can be introduced through the copolymerisation of functional monomers when preparing the solvophilic block which can be further utilised for specific biological applications. Kaminskas and Whittaker reported the first fundamental *in vivo* study on particle morphology using nano-objects decorated with functional groups generated via PISA.[107] In this work, a hydrophilic diblock copolymer of poly(glycidyl methacrylate-*b*-P(PEGMA)) was synthesised to introduce amine reactive functionality to the particle surface. Dispersion polymerisation of styrene in methanol was then used to generate various nanoparticle morphologies with an amine reactive epoxide surface, which were subsequently ring-opened with a tritium labelled (^{3}H) ethanolamine for radiolabelling. Biodistribution studies indicated significantly higher accumulation in reticuloendothelial organs (liver, spleen) for worms and rods, however small 21 nm micelles showed much greater association with tumour tissue.[107]

Drug delivery and cancer therapy are not the only applications in which nanomaterials can excel within biomedicine. The long circulation times and non-specific biodistribution exhibited by these structures makes them ideal imaging agents. In particular there are now a number of reports describing dispersion polymerisation to produce nano-objects for magnetic resonance imaging (MRI) and the effect of morphology on their contrast.

Whittaker and co-workers report the synthesis of block copolymer nano-objects with a fluorine containing monomer as potential ^{19}F MRI contrast agents.[108] The authors describe that fluorine density is a major parameter in MRI performance and therefore different morphologies may yield different contrasts. Initially a range of PEGA and trifluoroethyl acrylate (TFEA) copolymers were synthesised with different feed monomer compositions, with relaxivity studies indicating 2.68 wt% TFEA as optimum to avoid ^{19}F association. Dispersion polymerisations of styrene and VBA were then performed in isopropanol, targeting a total DP of 5000 stopping at 4.4 (spheres), 11.3 (worms), 17.2

(vesicles) and 22.5% (compound vesicles) styrene conversion to isolate individual morphologies. Relaxivity studies of block copolymer nanoassemblies suggested that T_1 and T_2 relaxation was independent of morphology.[108]

In a different approach, Davis and co-workers adapted their epoxide functional macro-RAFT agents to introduce gadolinium chelates into their nano-objects as potential MRI contrast agents.[109] Polystyrene nano-assemblies were prepared in methanol as described above. Prior to gadolinium functionalisation, the epoxide functionality was modified with thiols to generate azide functional particles, highlighting the tuneable functionality possible with RAFT dispersion. Amine functional Gd-tetra-azacyclododecatetraacetic acid (Gd-DOTA) was used to ring open the surface functional epoxides on spherical, worm and vesicle nanoparticles. Similarly to Whittaker and co-workers, little difference in relaxivity was evident between morphologies.[109]

In an earlier study, Davis and Boyer used dispersion polymerisation to generate nanoparticles containing iron-oxide nanoparticles which are well-known MRI contrast agents.[110] In a versatile approach, Fe(II) and Fe(III) salts were fed to aqueous solutions of spheres, worms and vesicles which bound electrostatically to the methacrylic acid moieties introduced into the macro-RAFT agents. Subsequent addition of ammonia resulted in precipitation of iron oxide on the surface of the nanoparticles. Interestingly the size of the resulting iron oxide nanoparticles could be tuned by increasing the MAA content of the solvophilic sections. In contrast to the above studies, micellar morphologies gave the highest transverse relaxivity (r_2 = 582 mM^{-1} s^{-1}), several times higher than commercially available contrast agent Feridex (r_2 = 100 mM^{-1} s^{-1}) .[110]

1.3.2 Aqueous dispersion polymerisation

All of the above studies use RAFT dispersion polymerisation within an alcoholic medium, which requires extensive purification typically through dialysis before biological use. Early developments of aqueous RAFT dispersion polymerisation were reported by Hawker and co-workers who described polymerisation of *N*-isopropylacrylamide to generate block copolymer micelles *in situ*.[111] Following this study, a number of different monomers, such as diethyl acrylamide (DEAm),[112] 2-methoxyethyl acrylate (MEA)[113, 114] and di(ethylene glycol) methyl ether methacrylate (DEGMA)[115] were also shown to be capable of dispersion polymerisations, usually

utilising the thermoresponsive behaviour of their respective polymers (Figure 1.10). The above systems were only capable of producing spherical systems, however over the past eight years it has been established that morphological controlled assemblies can easily be achieved using other core forming monomers such as 2-hydroxy propyl methacrylate (HPMA),[96, 116] diacetone acrylamide (DAAm)[117-119] and NIPAM (Figure 1.10).[120] This is potentially useful for biomedical applications, as the formed nano-objects could be injected directly for therapy, bolstered by compartmentalisation effects resulting in a rapid increase in polymerisation rate and high monomer conversions. Furthermore, the cost, abundance and high boiling point of water make this an attractive solvent from an industrial perspective potentially enabling scale up of aqueous dispersion polymerisations. Given this, a number of aqueous PISA formulations have been employed to generate biologically relevant nanoparticles.

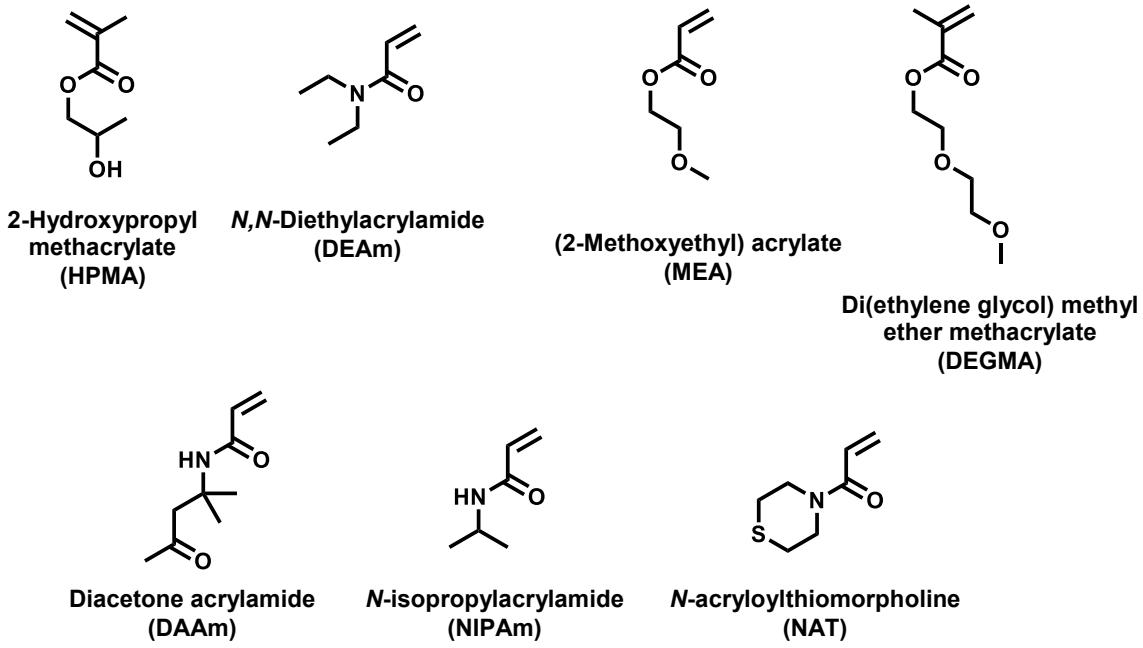

Figure 1.10 Monomers used for the core-forming block of aqueous dispersion polymerisation-induced self-assembly.

Aqueous dispersions of HPMA have been widely used due to its robust control over individual morphologies.[96, 116, 121-126] Chain extension of a poly(glycerol methacrylate) (P(GMA) macro-RAFT agent with HPMA of three different chain lengths (90, 140 and 220) yielded the conventional sphere, worm, vesicle morphologies.[121] Importantly, quantitative monomer conversions were observed within 2 h. Upon cooling to room temperature, the $P(GMA)_{54}$-$P(HPMA)_{140}$ worm-like assemblies formed a soft malleable gel at 10 wt% due to worm-worm entanglements. Interestingly further cooling to 4°C

resulted in a free flowing solution, which was later found be due to a worm to sphere transformation. The authors postulated that such a system could be used as a thermoresponsive biological storage medium, which can be sterilised by degelation and passing through a typical 0.45 μm filter upon degelation. To probe this the free flowing dispersion was contaminated with fluorescently labelled *S. aureus* and after sterilisation negligible contamination was observed. Furthermore the worm-gels were found to be fully biocompatible in cell viability assays.[121]

In two follow-up publications, this system was shown to be versatile in a number of biological applications as a potential replacement for cryopreservation. In one study, the authors used the worm-gels as mucin mimics which are known to induce stasis of mammalian embryos consisting of pluripotent stem cells *in utero*.[122] Storage of human embryos within these worm gels showed significantly greater stability than those in a commercially available alternative (Matrigel). Remarkably a high degree of a nuclear envelope statin was observed through immunostaining experiments, suggesting cell stasis within these conditions. When repeated with only pluripotent stem cell colonies, the majority of cells continued to express pluripotency markers rather than those for differentiation. The promising results observed are clearly related to the close mucin-mimicry available (worm-like and hydroxyl rich) through PISA and RAFT dispersion polymerisation.[122]

Gibson and co-workers have previously shown that polyalcohols are capable of mimicking anti-freeze glycoproteins in solvent-free cryopreservation of biologics.[127] This was recently expanded to use the above HPMA worm-gel system.[124] Ice recrystallization inhibition studies with worm-gels indicated limited activity, and neither ice growth nor nucleation was promoted in these conditions. Interestingly, the worm-gels alone only resulted in 20% red blood cell recovery, however a cooperative effect between the worms and poly(vinyl alcohol) (PVA) was apparent resulting in over 60% erythrocyte recovery with no indication of haemaglutination or abnormal cell shape.

In the above cases, control over the surface monomer composition was critical to their performance in the desired applications. This approach has been employed to introduce biologically active moieties. Armes and co-workers described simultaneous co-PISA from the previous P(GMA) macro-RAFT agent, and a novel glycosylated poly(galactose methacrylate) macro-RAFT agent using HPMA as the core-forming block forming

assemblies containing different degrees of galactose at the surface.[123] Similar to other studies, the dispersions display reversible thermoresponsive gelation between worm and spherical assemblies, albeit with less rheological hysteresis than the previous example. Lectin binding studies indicated a much faster and greater response from worms and vesicles than the respective spherical nanoparticles, which likely contributed to the strong cellular uptake observed in live HDF cells.[123]

In an inspiring strategy, Huang and co-workers describe protein coated block copolymer assemblies *via* PISA by modifying BSA with an *N*-hydroxysuccinimide functionalised RAFT agent capable of reacting with lysine residues.[128] This was then used as the solvophilic block and chain extended with HPMA using a mild low temperature light activated RAFT to avoid denaturation of the protein during polymerisation. In this case however only spherical nanoparticles, albeit with increasing size, were obtained as the P(HPMA) chain length increased. Importantly by monitoring the hydrolysis of 4-nitrophenyl acetate, it was observed that the esterase activity of BSA was retained, and the hydrophobic nature of the core was used for encapsulation of a hydrophobic drug model, pyrene.[128]

1.3.3 Stimuli responsive nano-assemblies

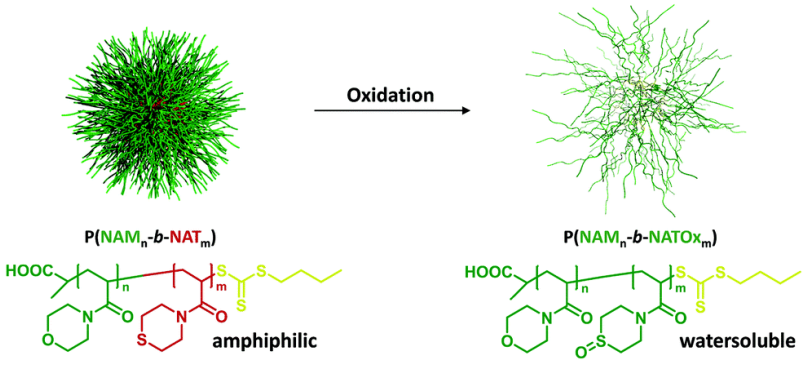

Figure 1.11 Oxidation responsive micelles synthesised by polymerisation-induced self-assembly of *N*-acryloylthiomorpholine from a poly(*N*-acryloylmorpholine) macro-RAFT agent. Adapted from Brendel *et al*.[129]

One of the major problems in nanoparticle drug delivery is that most therapeutics can be cytotoxic in any area of the body, causing adverse side effects once released from its carrier. This has typically been overcome through introduction of functionalities which have either a chemical or physical transition after treatment with a particular stimulus.[130] This can either be an external stimulus, such as temperature or light, which can give

spatial control over the site of drug release, or using endogenous biochemical stimuli such as the low pH and high glutathione content found in cancer tissue. Such a stimuli-responsive nature has been incorporated into dispersion polymerisations through copolymerisation of functional monomers.

With this in mind, Pan and co-workers report a redox-responsive system using PISA for delivery of a topoisomerase inhibitor camptothecin (CPT).[131] A disulphide functional prodrug containing solvophilic block copolymer was chain extended with benzyl methacrylate and a disulphide cross linker as the core-forming block to form 35 nm spherical micelles. All of the polymerisations reached full monomer conversion negating the need for extensive purification. The covalent drug-monomer approach allowed for high (12.8 wt%) drug content, and when incubated with 10 mM GSH (cytosolic concentration), 40% drug release occurred over 48 h. Although high loading was obtained, IC_{50} values of the micelles against HeLa cells were found to be between 6-7 μg mL^{-1} which is significantly higher than values reported for free CPT (0.08 μg mL^{-1}).[131, 132]

In a second study, a photo-sensitive system using 2-nitrobenzyl methacrylate (NBMA) and a coumarin methacrylate was developed.[133] In this work the above monomers were chain extended from a P(HPMA) macro-RAFT agent to form spherical, worm-like and vesicle nano-objects in methanol as previously described. Upon photoirradiation (UV 365 nm) it was expected that the nitrobenzyl unit of NBMA would cleave and become a carboxylate group, and subsequently cause disassembly of the nano-objects. However, inclusion of the coumarin groups resulted in their dimerization as subsequent chain-chain cross-linking producing anionic nanogels. This strong transition from hydrophobic to hydrophilic was exploited for fast and efficient release of doxorubicin from each of the morphologies generated. The vesicle assemblies had the greatest cytotoxicity in comparison to worm-like and spherical morphologies.[133]

Brendel and co-workers, report an oxidation responsive system as a possible vector to inflammatory disorders which exhibit increased levels of reactive oxygen species.[129, 134] By chain extending an *N*-acryloylmorpholine (NAM) macro-RAFT agent with *N*-acryloylthiomorpholine (NAT), a PISA process ensued resulting in 25-75 nm spherical micelles depending on the comonomer composition. After incubation with 10 mM hydrogen peroxide the thiomorpholine solvophobic block oxidised into a hydrophilic

polysulfoxide, resulting in particle disassembly. This was further probed by the reduction of fluorescence intensity of a model hydrophobic drug, Nile Red, which was released after treatment with hydrogen peroxide, highlighting this systems potential use for drug delivery (Figure 1.11).[129]

1.3.4 Biomacromolecule encapsulation

As discussed in the previous section, delivery and transportation of biomacromolecules, such as therapeutic proteins are a potential alternative to small molecule drug delivery. Polymeric vesicles (polymersomes) have been shown as promising carriers for enzymes, proteins and antibodies due to their large hydrophilic compartment.[135] Typically polymersomes are prepared at low polymer concentrations and with organic solvents, using traditional self-assembly methods[95] or thin-film rehydration[136] of block copolymers which becomes problematic at large scales. In the above sections, we have highlighted how PISA can be used to produce a variety of morphologies including polymersomal vesicles, which may be able to encapsulate cargo in high quantities. Traditional PISA protocols are an adaptation of conventional RAFT polymerisations, and as such are performed at high temperatures (e.g. 70°C), which could lead to denaturation of biological materials. This has been overcome by low temperature PISA protocols, such as redox initiation,[113] however many of these examples only resulted in spherical morphology. Boyer and co-workers reported on the photoinduced PISA of HPMA from a PEGylated macro-RAFT agent able to produce spheres worms and vesicles. This approach has been extended in three separate studies for protein encapsulation and subsequent biological applications.[125]

Zhang and co-workers describe an adaptation of Boyer and co-workers HPMA photo-PISA, where at HPMA concentrations > 15 wt%, higher order morphologies, including vesicles could be prepared.[137] Using this system full monomer conversions were achieved in under 30 mins irradiation. As a proof of concept for encapsulation, fluorescein labelled BSA was added into the PISA formulations, which remained 90% active as determined by the hydrolysis of 4-nitrophenyl acetate. Interestingly the BSA encapsulated within the polymersomes was 65% more active than BSA heated to 70°C, similar to that if the polymerisation was conducted with thermally initiation.[137]

Such polymersome-protein hybrids can also be used as enzymatic nanoreactors assuming that the membrane is permeable to small molecule substrates. This approach was studied by Gibson and co-workers who utilised the above HPMA photo-PISA technique to generate separate glucose oxidase (GOx) and horseradish peroxidase (HRP) loaded vesicles with encapsulation efficiencies of around 25%.[138] First proof of concept experiments, showed that HRP vesicles could catalyse the oxidation of 3,3'-dimethoxybenzidine (DMB) despite the substrates residence in the external medium, indicating the vesicle membranes were permeable to small molecules. Furthermore, using the GOx and HRP loaded vesicles, D-glucose was metabolised into d-glucono-1,5'-lactone, producing hydrogen peroxide as a by-product which facilitated the catalytic oxidation of DMB by HRP within a separate vesicle (Figure 1.12), highlighting how multiple enzymes can be used in a cascade even though they are physically seperated.[138]

The above strategy was further utilised by Gibson and O'Reilly in which L-asparaginase (ASNS) was encapsulated into the permeable vesicles as a possible treatment for lymphoblastic leukaemia. Importantly, the ASNS loaded vesicles showed excellent stability towards proteolysis from α-chymotrypsin, whereas free ASNS and PEGylated ASNS had no activity after the same treatment. To test this effect *in vitro*, human lung cancer fibroblasts were silenced to inhibit ASNS activity, thus rendering the cells reliant on the treated ASNS loaded vesicles for proliferation. *In vivo* biodistribution studies of the ASNS loaded vesicles showed accumulation within the typical organs for nanoparticle systems (spleen, liver, kidneys) and slower clearance in comparison to the free enzyme.[139]

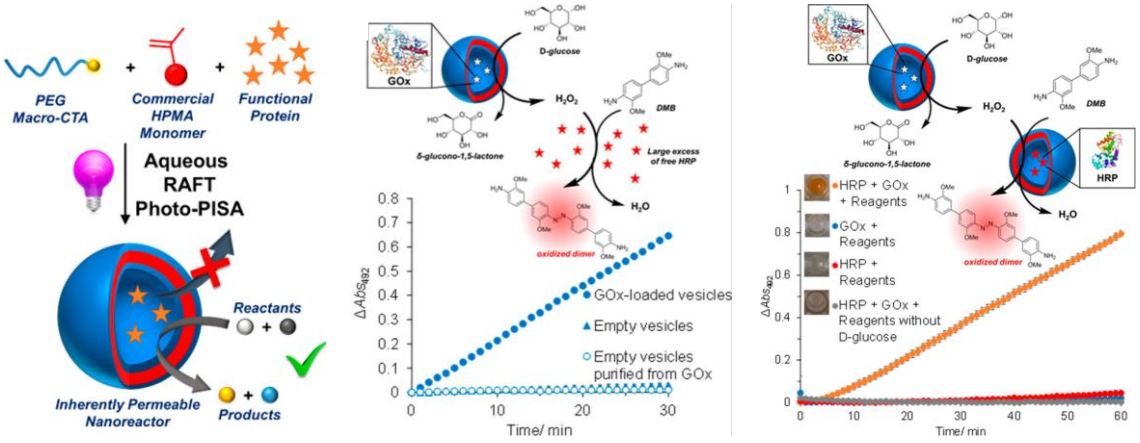

Figure 1.12 Encapsulation of proteins and enzymes using photo-PISA of HPMA to produce permeable catalytic polymersomes. Adapted from O'Reilly *et al.*[138]

Over the last 5-7 years RAFT dispersion polymerisations in the form of PISA has made nanoparticle formation more accessible than ever before. The ability to modulate surface and core chemistries, as well as particle morphology in one-step has made this particularly attractive for fundamental or application driven research at the biological interface. Recent synthetic advances now mean that these systems can easily be generated in aqueous conditions with no by-products (100% monomer conversion), in low temperature and oxygenated conditions.[140, 141] Nonetheless, the limited number of core-forming monomers capable of aqueous PISA mean that introduction of stimuli-responsivity is a challenging prospect, unlike in traditional self-assembly processes. Furthermore, what is clear from PISA oriented literature is that the resulting spherical particles are relatively small (< 30 nm diameter)[94] and unlike in emulsion systems (*vide infra*), altering the molecular weight of the core forming block typically does not modify particle size without a morphological transformation, which is not suitable for all applications. Even still, if worm-like or polymersomal morphologies are required from novel/unreported block copolymer compositions, one must perform the arduous task of producing a pseudo-phase diagram by mapping the morphologies of the resulting nano-objects by solvophobe chain length and total solids content.

1.4 Suspension polymerisation

Suspension polymerisations take place within micron sized monomer droplets, using a monomer soluble initiator stabilised by conventional surfactants.[41] They are similar to miniemulsion polymerisations in the sense that they are essentially compartmentalised bulk polymerisations, however are dispersed with agitation only and not with sonication (Figure 1.13). This typically results in the formation of microparticles (> 1 μm diameter) decorated with the surfactants present during the polymerisation. While this chapter is focussed on the synthesis of biologically relevant nanoparticles (not micron sized) using RDRP, an interesting approach to generate non-spherical nanoparticles has arisen using a post-polymerisation strategy pioneered by Monteiro and co-workers using RAFT suspension polymerisation.[142] As mentioned in the previous section, the formation of non-spherical, elongated nanoparticles is becoming increasingly important due to their longer circulation time and thus greater therapeutic efficacy compared to spherical analogues. This approach operates on the use of a thermoresponsive macro-RAFT agents which

collapse and become hydrophobic during the high temperatures (70°C) of suspension polymerisations. Upon cooling the macro-RAFT agent swells within the aqueous phase, and after addition of a small amount of plasticiser, the 1-2 µm spheres transform into long worm-like fibrils stabilised by the thermoresponsive shell. Notably in many of the works which use this technique, it is mistakenly called a dispersion or emulsion polymerisation whereas it is actually a suspension polymerisation.

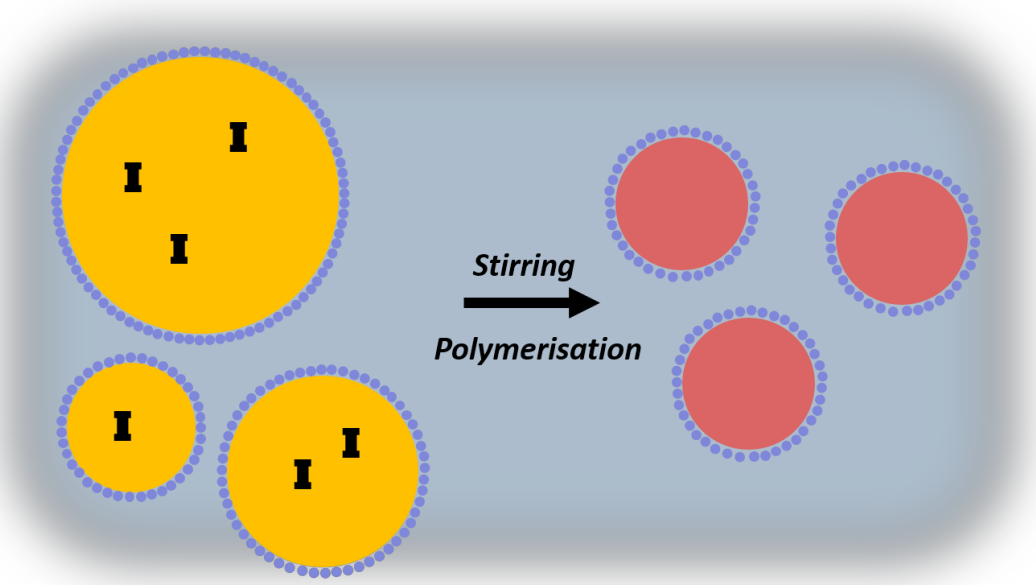

Figure 1.13 Mechanism of suspension polymerisation. I = initiator species, yellow = oil/monomer phase, blue = aqueous phase, red = polymer phase.

Davis and co-workers have expanded on this approach using poly((diethyleneglycol) methyl ether methacrylate)-*co*-(HPMA) (P(DEGMA)-*co*-(HPMA)) macro-RAFT agents with P(DEGMA) being the thermoresponsive component.[143] Following suspension polymerisation of styrene droplets stabilised by sodium dodecyl sulfate (SDS), 1 µm polystyrene block copolymer spheres were generated, and after cooling and addition of different volumes of toluene (20-160 µL mL^{-1}) polymeric nanowires, vesicles and lamellae were produced (Figure 1.14). Interestingly, as seen in other supramolecular systems, sonication could be used to cut the nanowires into much shorter rod-like structures. To expand the scope of this approach Davis and co-workers have now shown it is possible to achieve these nano-objects with a variety of polymer cores in multigram quantities, and showing high biocompatibility in human endothelial (HUVEC) and fibrosarcoma (HT1080) cells regardless of morphology.[143, 144]

Although this technique allows for control over nanoparticle morphology, the specific thermoresponsive shell composition required to achieve this phenomenon severely limits surface functionality available for further modification. Furthermore, the requirement of external cytotoxic surfactants and organic solvents mean that lengthy purification procedures must be performed before biological studies, also limiting potential scale-up. Relatively little biological work (only cell viability) has been reported using nanoparticles prepared with this particular technique thus far. However, it is easy to see that molecular drug delivery, bioimaging and other applications not requiring biologics (which may denature in the presence of surfactant and organic solvent), could be achieved using this approach. Aqueous dispersion polymerisations (as discussed above) can achieve many of the same properties (morphology control, tuneable surface and core composition), but can be performed in the absence of surfactant and at low temperatures, possibly making this suspension polymerisation method less useful.

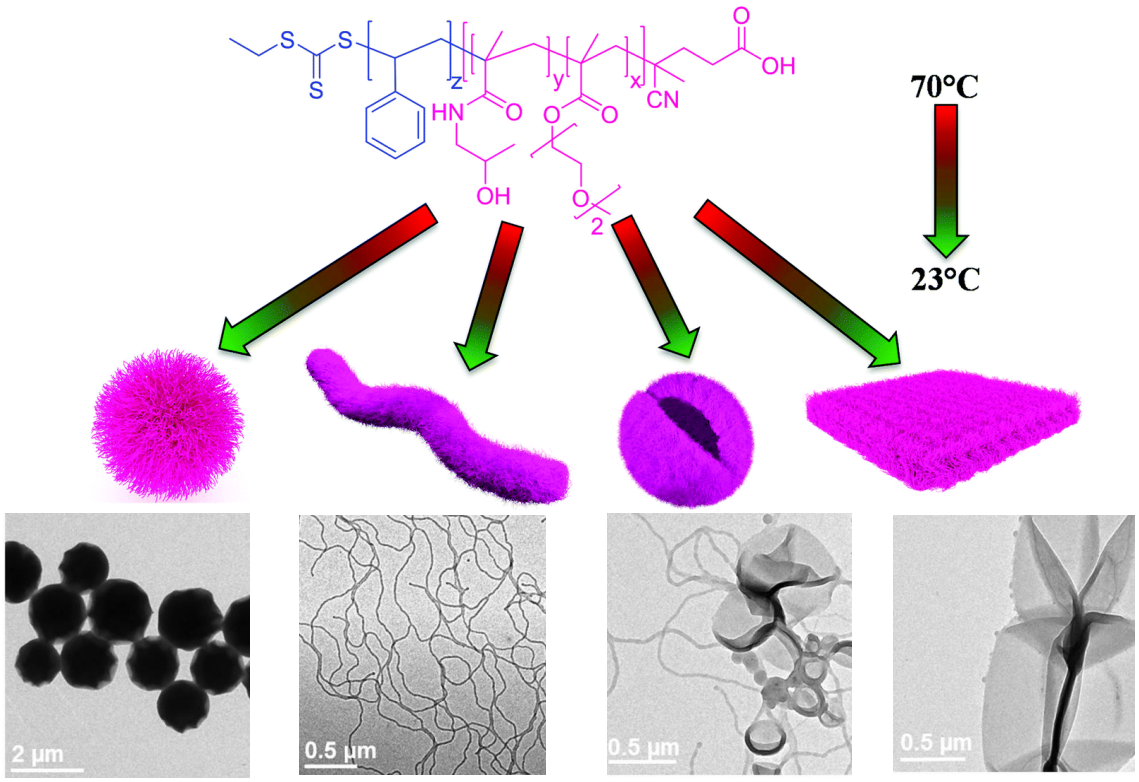

Figure 1.14 Suspension polymerisation of styrene from a hydrophilic thermoresponsive macro-RAFT agent. Upon addition of different volumes of toluene (0, 20, 40, 80 and 160 µL mL^{-1}) and cooling to room temperature various morphologies were formed. Adapted from Davis *et. al.*[143]

1.5 Emulsion polymerisation

In a typical emulsion polymerisation, the initial reaction mixture is comprised of micrometre sized monomer droplets which are immiscible in the aqueous continuous phase, surfactant micelles and a water soluble initiator.[39] Particles are generated first through monomer propagation in the aqueous phase, forming hydrophobic Z_{mers} which subsequently nucleate micelles (or self-nucleate in surfactant free emulsion polymerisations). Particle growth ensues during polymerisation of monomer which is continuously diffusing from monomer droplets into the surfactant micelles, which when complete, results in surfactant coated solid latex nanoparticles. This process has been implemented using free-radical polymerisation for decades to generate vinyl polymers at large scales and in environmentally friendly conditions. The compartmentalisation effect enables fast propagation rates, high monomer conversions and importantly low termination rates resulting in high molecular products.[39] Due to these key advantages, especially for industrial applications, much work has gone into translating RDRP techniques to emulsion polymerisation. However, the complex monomer and radical transfer mechanisms mean that RDRP methods cannot be implemented in *ab initio* emulsion polymerisations by simply adding in a control agent.

In general, early studies to implement RDRP methods in emulsion processes resulted in one or more of the following drawbacks: (1) poor colloidal stability of the resulting latex; (2) lack of control over the molar mass, and (3) high M_w/M_n values.[44] This was overcome by implementing stabilising amphiphilic macroinitiators, which were chain extended in the emulsion polymerisation and avoids the use of external surfactant. This was first pioneered by Hawkett and co-workers who used poly(acrylic acid)-*b*-poly(*n*-butyl acrylate) macro-RAFT agent micelles to seed a RAFT emulsion polymerisation of *n*-butyl acrylate (*n*-BA) leading to colloidally stable uniform block copolymer nanoparticles (D_h = 60 nm, PDi < 0.01) which are coated with P(AA) at their surface (Figure 1.16).[145, 146] After dissolution in organic solvent, the block copolymers displayed narrow molecular weight distributions ($Đ$ < 1.3) and excellent molecular weight control. This tactic was further implemented using NMP (poly(acrylic acid) based macroalkoxyamines) however little progress has been made on this topic since 2008, possibly due to its incompatibility with methacrylates.[147-150] One successful approach, prior to the first reports of RAFT, was using methacrylate end-group addition fragmentation chain transfer agents, which have a

very low chain transfer constant in solution. However, in the confined space and low monomer concentrations of emulsion polymerisation, they become excellent chain transfer agents.[151] In contrast, ATRP emulsion procedures have mainly focussed on inistabs (amphiphilic surfactant-like ATRP initiators) and water soluble initiators using either conventional ATRP or ARGET ATRP.[152-155] Many examples utilising these approaches unfortunately led to broad particle size distributions and unsatisfactory molecular weight control likely due to phase separation of the transition metal catalyst from the ATRP initiator.[53] As such the degenerative chain transfer mechanism of RAFT, and its compatibility with most monomer families, have led to this technique being the most popular RDRP emulsion polymerisation method and has now been expanded to a large range of monomers and stabilisers (cationic, anionic and neutral).[156] Many of these studies focus on synthetic aspects (kinetics and morphology control)[157-159], however some features could be useful in designing nanoparticles for biological applications.

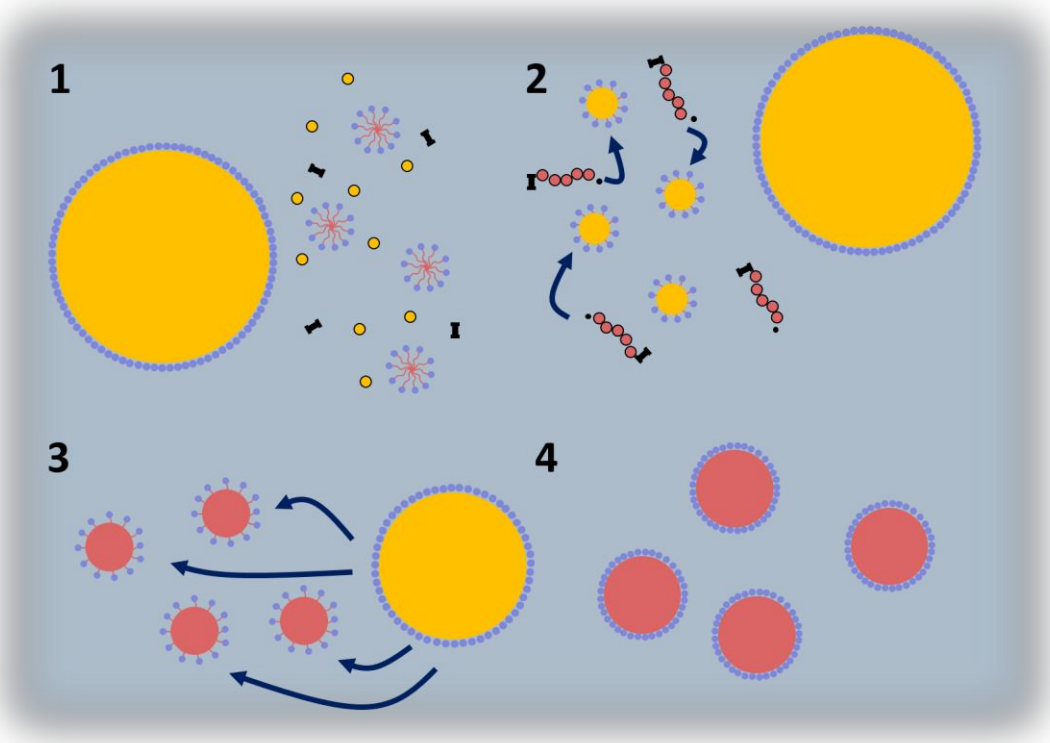

Figure 1.15 Mechanism of emulsion polymerisation (1) reaction mixture, (2) initiation phase, (3) propagation and diffusion of monomer from monomer droplets to growing particles, (4) final latex particles. I = initiator species, yellow = oil/monomer phase, blue = aqueous phase, red = polymer phase.

1.5.1 RAFT emulsion polymerisation

Particle size has been shown to drastically influence biological performance, affecting nanoparticle cellular uptake, biodistribution and thus potential therapeutic efficacy.[85] Even though most reports on RAFT emulsion polymerisations yields only spherical morphologies the resulting nanoparticles are highly uniform over different size ranges (30-200 nm diameters).[85] Davis and co-workers have previously shown that particle volume has a linear relationship with the molecular weight of the polymeric core and as such can be tuned during the core-forming step.[160] The particle sizes produced by RAFT emulsion polymerisation are significantly larger than those produced by dispersion polymerisations (<30 nm diameters), which may make the former more useful *in vivo* by reducing their susceptibility to renal clearance.[161]

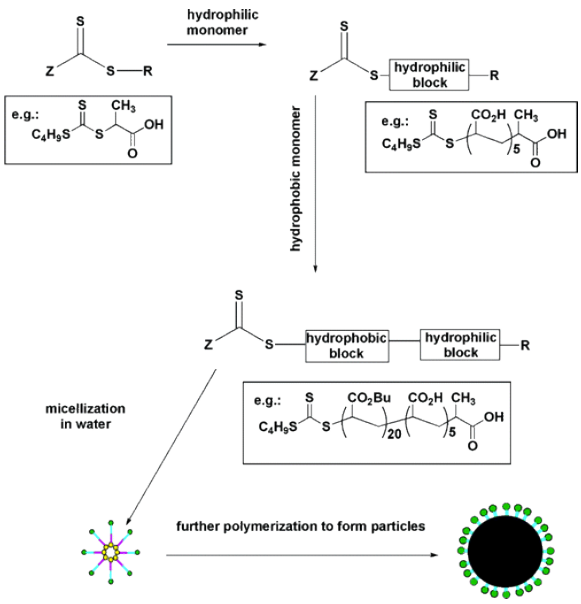

Figure 1.16 Schematic representation of RAFT emulsion polymerisation using an amphiphilic macro-RAFT agent stabiliser. Adapted from Hawkett *et. al*.[146]

As with the dispersion PISA formulations previously described, the stabilising macro-RAFT agents in RAFT emulsion processes are imparted at the particle surface. Stenzel and co-workers were the first to exploit this approach for biological applications, through the introduction of glycosylated moieties, which are known to improve disease targeting and bacterial interactions *in vivo*, when present at the particle surface.[162] To achieve this, poly(glucose methacrylamide)-*b*-PS was used to stabilise the emulsion cross-linking copolymerisation of styrene and a redox responsive disulphide diacrylate monomer. The resulting nanoparticles were produced within 6 h, were fairly uniform (*PDi* < 0.2) and

within a biologically relevant size range (50-80 nm diameters). While the particles did disassemble after dithiothreitol addition (DTT), this did not occur in an aqueous environment but had to be pre-swollen in organic media making this response unsuitable for redox responsivity *in vivo*. Nonetheless, turbidimetric binding assays revealed a strong binding event to lectin Con A, with similar performances evident in bacterial adhesion studies. Importantly the RAFT emulsion polymerisation approach yields a particle whereby the polymeric corona is covalently attached to the nanoparticle core, thus cannot desorb *in vivo* potentially inducing toxicity or other negative side effects.[162]

More recently, Lansalot and co-workers reported RAFT emulsion polymerisation using glycopolymer stabilisers. In this work, alginate derived polysaccharide macromonomers were copolymerised with NAM and further chain extended with styrene emulsion polymerisation to generate polysaccharide coated nanoparticles.[163] Surprisingly, when emulsion polymerisations were performed with polysaccharide macromonomers, severely decreased particle uniformity ($D_w/D_n > 1.07$) and broadened molecular weight distributions ($Đ > 1.50$) were seen in comparison to pure P(NAM) stabilisers ($D_w/D_n < 1.05$; $Đ < 1.3$).[163]

Wang and co-workers report the synthesis of shell cross-linked pH responsive nanoparticles using RAFT emulsion polymerisation.[164] Emulsion polymerisation of styrene was initiated from a poly(2-(dimethylamino)ethyl methacrylate) (P(DMAEMA)) and cross-linked during the early phase of the polymerisation with a disulphide diacrylate monomer yielding 95 nm particles. Similarly, degradation studies were performed in DMF, with particles completely disassembling after addition of DTT. In proof of concept drug release studies, indomethacin was encapsulated within the nanoparticles, and due to the pH responsive P(DMAEMA) shell, a fast release (70% with 24 h) was evident at pH 5.4 with the addition of DTT. Finally, although high cell viability was reported against human cervical cancer (HeLa) cells, this was only measured with concentrations up to 50 μg mL^{-1} yielding 70% viability, which is relatively cytotoxic for such a low concentration.[164]

One of the major advantages of RDRP methods is the possibility of introducing functional groups at both ends of the polymer chain typically imparted by the respective control agent(s). These can then be used to introduce biologically relevant functional molecules (e.g. nucleic acids, proteins, targeting peptides etc.). This approach was applied to RAFT

emulsion polymerisation by Poon *et al*. who described the post-modification of carboxylated particles with microRNA.[165] First a poly(acrylamide)-*b*-PS stabiliser was synthesised with a RAFT agent exhibiting a functional carboxylic acid on the reinitiating group. This was then chain extended in an *ab initio* RAFT emulsion polymerisation of styrene yielding very small 11 nm nanoparticles. The carboxylic functionality was first modified with an amino functional pyridyldisulfide as a redox-responsive linker for the microRNA, which was further conjugated at the particle surface in a typical thiol exchange reaction. Addition of 10 mM GSH resulted in 60% microRNA release from the particle surface over 72 h. They explain that the particular microRNA used (miR-200b) can suppress the epithelial-mesenchymal cell transition (Figure 1.17).[165]

The high functional group density that RAFT emulsion polymerisation imparts on the particle corona was further used for attachment of a rhodamine dye to produce nanoparticles capable in *in vitro* and *in vivo* imaging applications.[166] In this case, Poon *et al* synthesised both 11 and 22 nm polystyrene particles which were subsequently conjugated with rhodamine amine at 10 and 12% efficiencies respectively. After incubation with HK2 cells, the punctuated structure in fluorescence microscopy images indicated endosomal or lysosomal colocalisation, consistent with many other studies. Finally, the 22 nm rhodamine labelled nanoparticles were injected intravenously into healthy mice, with the highest accumulation occurring in the liver and kidneys. While this was the first *in vivo* study of latex nanoparticles synthesised *via* RAFT emulsion, as of yet there is no published information on the short- or long-term toxicity of this type of nanoparticle *in vivo*.[166]

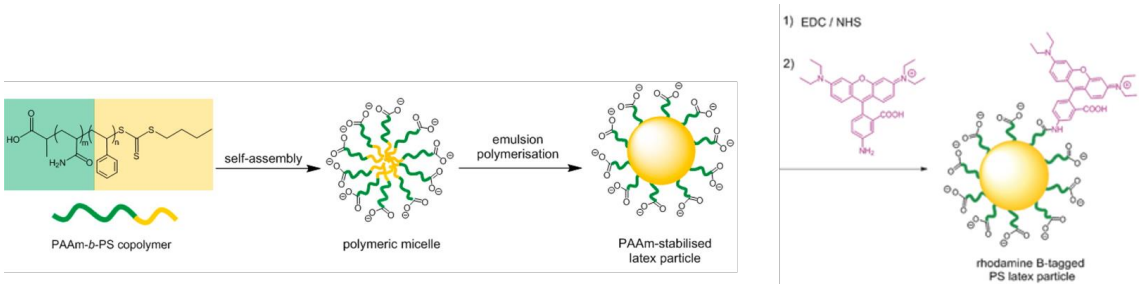

Figure 1.17 Synthesis and post-modification of carboxylic functional polystyrene nanoparticles synthesised using RAFT emulsion polymerisation, with amine function rhodamine or microRNA. Adapted from Poon *et. al*.[166]

Not all biological applications are needed to be biomedical. For instance, Carlmark and co-workers have recently reported the preparation of both low and high T_g latexes with RAFT emulsion polymerisation for cellulose modification. Emulsion polymerisations of BMA and MMA were initiated from a P[(DMAEMA)-*co*-(MAA)] macro-RAFT agent, resulting in uniform nanoparticles (PDi < 0.1). The aqueous system allowed for direct adsorption onto cellulose fibres monitored using a quartz crystal microbalance. Contact angle measurements indicated that P(BMA) latexes induced hydrophobicity before and after annealing, whereas with high T_g P(MMA) latexes this only occurred after annealing. It was found that these latexes significantly improved the mechanical strength of these biocomposites after annealing.[167]

From a biological perspective, RAFT emulsion polymerisation is a relatively simple method to produce uniform nanoparticles with tuneable (monomer composition) cores and corona, specific surface functionality (reinitiating group on RAFT agent) with a variable size range (target molar mass), in an aqueous environment without external surfactants. Many of the advantages seen here are also comparable with RAFT aqueous dispersion polymerisations, which can also produce non-spherical species (except for the very few emulsion systems with this property)[168] using similar conditions. However, there are very few monomers capable of the soluble monomer to insoluble polymer transition required for aqueous dispersion polymerisation (*vide supra*).[94] In contrast, the number of monomers capable of emulsion polymerisation (i.e. water immiscible molecules such as MMA, styrene, BA) is far greater, which may be useful when tailoring core properties. Furthermore, the most common use of core-shell nanoparticles is controlled drug delivery, powered by the high loading efficiencies of insoluble therapeutics.[169] The components used in aqueous dispersion polymerisations are typically much more hydrophilic components than analogous emulsion polymerisations, potentially limiting this application.

Nonetheless similar core-shell structures with higher order morphologies can also be prepared using popular self-assembly procedures such as solvent-switch protocols.[95] To date, these are the most heavily used methods and have been used to prepare nanoparticles far more complex (stimuli-responsiveness,[170] degradability[171] and specific disease targeting[172]) than any heterogenous RDRP technique. However, as stated above, these efforts can only be realised at low concentrations and require organic solvents, thus must

be purified before biological use. Moreover, the resulting particles are generally dynamic and may disassemble at low concentrations, possibly leading to premature clearance *in vivo*.

There have been some efforts to avoid the use of surfactants without using RDRP methods (i.e. surfactant free emulsion polymerisations using conventional free radical polymerisation), which can be achieved in one step from monomer directly to nanoparticle.[173-175] However, these typically lead to a large proportion of high molar mass hydrophilic polymers contaminating the continuous phase, which must be removed through dialysis or centrifugation. Furthermore, unless specific monomer combinations are used with this approach, it is non-trivial to produce sub 200 nm particles which are the most efficacious in biological studies.[176] As such, RAFT emulsion procedures remain perhaps the only route to produce core-shell frozen particles in an organic solvent free environment without a high proportion of residual monomer, but with full tuneabiliy of surface and core compositions.

1.6 Conclusions and motivation for this work

Overall, the field of RDRP in dispersed states is undergoing a clear revolution from primarily synthetic work towards understanding how it can be implemented in modern applications, including biomedicine. It is now well understood how to translate popular RDRP techniques with many heterogeneous polymerisations types. Furthermore, the biomedical advantages of this have now been exploited to prepare systems applicable for delivery (gene and drug), and study fundamental bio-nano interactions *in vitro* and *in vivo*. The degenerative chain transfer mechanism of RAFT, and its synthetic versatility (monomer compatibility, aqueous and low temperature polymerisations) have resulted in this approach being applied in all heterogeneous polymerisations discussed above, with NMP and ATRP being largely forgotten. An important factor in this, has been the development of RAFT aqueous dispersion polymerisations to produce non-spherical nanoparticles, such as rods and vesicles in low temperature environments which show enhanced cellular uptake and can be used to entrap hydrophilic cargo. Nonetheless, the limited number of core-forming monomers severely reduces the flexibility of this system. In contrast, RAFT emulsion procedures can be performed with practically any water immiscible monomer, and by modifying the monomer and stabilising macro-RAFT

agents involved, the polymer shell, core, particle size and surface functionality can easily be tuned. With this in mind, the present examples utilising this approach remain fairly fundamental, with few reports of particles specifically designed for improved biocompatibility and targeting specific biological applications (i.e. biocompatible coronas, orthogonal chemistry for ligand binding and bioactive surface functionality). The overall aim of this thesis is to expand RAFT emulsion polymerisation procedures to exploit the advantages described above and to purposely design nanoparticle systems applicable in biomedicine. This will be achieved by meeting the following objectives:

- Optimise the synthesis of nanoparticles using RAFT emulsion polymerisation stabilised by a biocompatible amphiphilic macro-RAFT agent.

- Evaluate their toxicological effects both *in vitro* and *in vivo*, as well as their organ distribution post injection in mouse models.

- Use RAFT emulsion polymerisation to produce polymeric nanoparticles with different core glass transition temperatures to study the effect of nanoparticle rigidity on cellular uptake.

- Generate nanoparticles with specific surface functionality for potential post-modification using RAFT emulsion polymerisation.

- Tune the polymeric shell of nanoparticles synthesised *via* RAFT emulsion polymerisation and use this for a specific targeted biological application.

References

1. M. Elsabahy and K. L. Wooley, *Chem. Soc. Rev*, 2012, **41**, 2545-2561.
2. A. Samad, Y. Sultana and M. Aqil, *Curr. Drug Delivery*, 2007, **4**, 297-305.
3. W. Lohcharoenkal, L. Wang, Y. C. Chen and Y. Rojanasakul, *BioMed Research International*, 2014, **2014**, 12.
4. H. Liao, C. L. Nehl and J. H. Hafner, *Nanomedicine*, 2006, **1**, 201-208.
5. X. Michalet, F. F. Pinaud, L. A. Bentolila, J. M. Tsay, S. Doose, J. J. Li, G. Sundaresan, A. M. Wu, S. S. Gambhir and S. Weiss, *Science*, 2005, **307**, 538-544.
6. I. I. Slowing, J. L. Vivero-Escoto, C.-W. Wu and V. S. Y. Lin, *Adv. Drug Delivery Rev.*, 2008, **60**, 1278-1288.
7. W. H. De Jong and P. J. A. Borm, *Int. J. Nanomed.*, 2008, **3**, 133-149.
8. Z. Gu, A. Biswas, M. Zhao and Y. Tang, *Chem. Soc. Rev*, 2011, **40**, 3638-3655.
9. J. Panyam and V. Labhasetwar, *Adv. Drug Delivery Rev.*, 2003, **55**, 329-347.
10. S. K. Nune, P. Gunda, P. K. Thallapally, Y.-Y. Lin, M. L. Forrest and C. J. Berkland, *Expert Opin. Drug Delivery*, 2009, **6**, 1175-1194.
11. G. Chen, I. Roy, C. Yang and P. N. Prasad, *Chem. Rev.*, 2016, **116**, 2826-2885.
12. S. Wilhelm, A. J. Tavares, Q. Dai, S. Ohta, J. Audet, H. F. Dvorak and W. C. W. Chan, *Nat. Rev. Mater*, 2016, **1**, 16014.
13. D. Bobo, K. J. Robinson, J. Islam, K. J. Thurecht and S. R. Corrie, *Pharm. Res.*, 2016, **33**, 2373-2387.
14. Y. Jin-Wook, C. Elizabeth and M. Samir, *Curr. Pharm. Des.*, 2010, **16**, 2298-2307.
15. C. Pinto Reis, R. J. Neufeld, A. J. Ribeiro and F. Veiga, *Nanomedicine.*, 2006, **2**, 8-21.
16. J. S. Suk, Q. Xu, N. Kim, J. Hanes and L. M. Ensign, *Adv. Drug Delivery Rev.*, 2016, **99**, 28-51.
17. S. D. Steichen, M. Caldorera-Moore and N. A. Peppas, *Eur. J. Pharm. Sci.*, 2013, **48**, 416-427.
18. J. Fang, H. Nakamura and H. Maeda, *Adv. Drug Delivery Rev.*, 2011, **63**, 136-151.
19. H. Maeda, J. Wu, T. Sawa, Y. Matsumura and K. Hori, *J. Controlled Release*, 2000, **65**, 271-284.
20. J. P. Rao and K. E. Geckeler, *Prog. Polym. Sci.*, 2011, **36**, 887-913.
21. S. R. Croy and G. S. Kwon, *Curr. Pharm. Des.*, 2006, **12**, 4669-4684.
22. N. P. Truong, J. F. Quinn, M. R. Whittaker and T. P. Davis, *Polym. Chem.*, 2016, **7**, 4295-4312.

23. R. P. Brinkhuis, F. P. J. T. Rutjes and J. C. M. van Hest, *Polym. Chem.*, 2011, **2**, 1449-1462.

24. N. Anton, J.-P. Benoit and P. Saulnier, *J. Controlled Release*, 2008, **128**, 185-199.

25. Y. Zheng, S. Li, Z. Weng and C. Gao, *Chem. Soc. Rev*, 2015, **44**, 4091-4130.

26. E. Abbasi, S. F. Aval, A. Akbarzadeh, M. Milani, H. T. Nasrabadi, S. W. Joo, Y. Hanifehpour, K. Nejati-Koshki and R. Pashaei-Asl, *Nanoscale Res. Lett.*, 2014, **9**, 247-247.

27. K. Raemdonck, J. Demeester and S. De Smedt, *Soft Matter*, 2009, **5**, 707-715.

28. K. Matyjaszewski and J. Xia, *Chem. Rev.*, 2001, **101**, 2921-2990.

29. C. J. Hawker, A. W. Bosman and E. Harth, *Chem. Rev.*, 2001, **101**, 3661-3688.

30. J. Nicolas, Y. Guillaneuf, C. Lefay, D. Bertin, D. Gigmes and B. Charleux, *Prog. Polym. Sci.*, 2013, **38**, 63-235.

31. A. Anastasaki, V. Nikolaou and D. M. Haddleton, *Polym. Chem.*, 2016, **7**, 1002-1026.

32. S. Perrier, *Macromolecules*, 2017, **50**, 7433-7447.

33. K. Matyjaszewski and J. Spanswick, *Mater. Today*, 2005, **8**, 26-33.

34. Y. K. Chong, T. P. T. Le, G. Moad, E. Rizzardo and S. H. Thang, *Macromolecules*, 1999, **32**, 2071-2074.

35. U. Mansfeld, C. Pietsch, R. Hoogenboom, C. R. Becer and U. S. Schubert, *Polym. Chem.*, 2010, **1**, 1560-1598.

36. H. A. Klok and S. Lecommandoux, *Adv. Mater.*, 2001, **13**, 1217-1229.

37. A. Rösler, G. W. M. Vandermeulen and H.-A. Klok, *Adv. Drug Delivery Rev.*, 2001, **53**, 95-108.

38. R. Paliwal, R. J. Babu and S. Palakurthi, *AAPS PharmSciTech*, 2014, **15**, 1527-1534.

39. S. C. Thickett and R. G. Gilbert, *Polymer*, 2007, **48**, 6965-6991.

40. S. Kawaguchi and K. Ito, in *Polymer Particles*, ed. M. Okubo, Springer Berlin Heidelberg, Berlin, Heidelberg, 2005, DOI: 10.1007/b100118, pp. 299-328.

41. H. G. Yuan, G. Kalfas and W. H. Ray, *J. Macromol. Sci., Part C*, 1991, **31**, 215-299.

42. J. M. Asua, *Prog. Polym. Sci.*, 2002, **27**, 1283-1346.

43. J. W. Vanderhoff, E. B. Bradford, H. L. Tarkowski, J. B. Shaffer and R. M. Wiley, in *Polymerisation and Polycondensation Processes*, American Chemical Society, 1962, vol. 34, ch. 2, pp. 32-51.

44. S. W. Prescott, M. J. Ballard, E. Rizzardo and R. G. Gilbert, *Aust. J. Chem.*, 2002, **55**, 415-424.

45. P. B. Zetterlund, Y. Kagawa and M. Okubo, *Chem. Rev.*, 2008, **108**, 3747-3794.

46. S. A. F. Bon, M. Bosveld, B. Klumperman and A. L. German, *Macromolecules*, 1997, **30**, 324-326.

47. M. F. Cunningham, *Prog. Polym. Sci.*, 2008, **33**, 365-398.

48. M. Save, Y. Guillaneuf and R. G. Gilbert, *Aust. J. Chem.*, 2006, **59**, 693-711.

49. J. B. McLeary and B. Klumperman, *Soft Matter*, 2006, **2**, 45-53.

50. M. F. Cunningham, *C. R. Chim.*, 2003, **6**, 1351-1374.

51. M. F. Cunningham, *Prog. Polym. Sci.*, 2002, **27**, 1039-1067.

52. J. Qiu, B. Charleux and K. Matyjaszewski, *Prog. Polym. Sci.*, 2001, **26**, 2083-2134.

53. K. Min and K. Matyjaszewski, *Open Chem.*, 2009, **7**, 657.

54. O. J. Kwon, *J. Polym. Sci., Part A: Polym. Chem.*, 2008, **46**, 6983-7001.

55. T. Boursier, I. Chaduc, J. Rieger, F. D'Agosto, M. Lansalot and B. Charleux, *Polym. Chem.*, 2011, **2**, 355-362.

56. Y. Yitao, Z. Qinghua, Z. Xiaoli and C. Fengqiu, *J. Appl. Polym. Sci.*, 2013, **127**, 2557-2565.

57. Y. Wang, G. Jiang, X. Sun, M. Ding, H. Hu and W. Chen, *Polym. Chem.*, 2010, **1**, 1638-1643.

58. B. T. T. Pham, D. Nguyen, C. J. Ferguson, B. S. Hawkett, A. K. Serelis and C. H. Such, *Macromolecules*, 2003, **36**, 8907-8909.

59. H. Dong and K. Matyjaszewski, *Macromolecules*, 2010, **43**, 4623-4628.

60. K. Min, H. Gao and K. Matyjaszewski, *J. Am. Chem. Soc.*, 2005, **127**, 3825-3830.

61. J. Oh, C. Tang, H. Gao, N. V. Tsarevsky and K. Matyjaszewski, *J. Am. Chem. Soc.*, 2006, **128**, 5578-5584.

62. Z. P. B., A. M. Nur, M. Hideto and O. Masayoshi, *Macromol. Rapid Commun.*, 2005, **26**, 955-960.

63. Z. P. B. and O. Masayoshi, *Macromol. Theory Simul.*, 2005, **14**, 415-420.

64. E. T. E., C. M. F. and K. Barkev, *Macromol. React. Eng.*, 2010, **4**, 186-196.

65. C. Farcet, B. Charleux and R. Pirri, *Macromol. Symp.*, 2002, **182**, 249-260.

66. Y.-J. Pan, Y.-Y. Chen, D.-R. Wang, C. Wei, J. Guo, D.-R. Lu, C.-C. Chu and C.-C. Wang, *Biomaterials*, 2012, **33**, 6570-6579.

67. Y. Wang, Y. Luo, Q. Zhao, Z. Wang, Z. Xu and X. Jia, *ACS Appl. Mater. Interfaces*, 2016, **8**, 19899-19906.

68. S.-i. Yusa, M. Sugahara, T. Endo and Y. Morishima, *Langmuir*, 2009, **25**, 5258-5265.

69. J. K. Oh, R. Drumright, D. J. Siegwart and K. Matyjaszewski, *Prog. Polym. Sci.*, 2008, **33**, 448-477.

70. M. Oishi and Y. Nagasaki, *Nanomedicine*, 2010, **5**, 451-468.

71. U. Hasegawa, S.-i. M. Nomura, S. C. Kaul, T. Hirano and K. Akiyoshi, *Biochem. Biophys. Res. Commun.*, 2005, **331**, 917-921.

72. N. Sanson and J. Rieger, *Polym. Chem.*, 2010, **1**, 965-977.

73. J. Oh, D. J. Siegwart, H.-i. Lee, G. Sherwood, L. Peteanu, J. O. Hollinger, K. Kataoka and K. Matyjaszewski, *J. Am. Chem. Soc.*, 2007, **129**, 5939-5945.

74. J. K. Oh, D. J. Siegwart and K. Matyjaszewski, *Biomacromolecules*, 2007, **8**, 3326-3331.

75. D. J. Siegwart, A. Srinivasan, S. A. Bencherif, A. Karunanidhi, J. Oh, S. Vaidya, R. Jin, J. O. Hollinger and K. Matyjaszewski, *Biomacromolecules*, 2009, **10**, 2300-2309.

76. S. E. Averick, A. J. D. Magenau, A. Simakova, B. F. Woodman, A. Seong, R. A. Mehl and K. Matyjaszewski, *Polym. Chem.*, 2011, **2**, 1476-1478.

77. S. E. Averick, E. Paredes, A. Irastorza, A. R. Shrivats, A. Srinivasan, D. J. Siegwart, A. J. Magenau, H. Y. Cho, E. Hsu, A. A. Averick, J. Kim, S. Liu, J. O. Hollinger, S. R. Das and K. Matyjaszewski, *Biomacromolecules*, 2012, **13**, 3445-3449.

78. A. R. Shrivats, E. Hsu, S. Averick, M. Klimak, A. C. S. Watt, M. DeMaio, K. Matyjaszewski and J. O. Hollinger, *Clin. Orthop. Relat. Res.*, 2015, **473**, 2139-2149.

79. B. Cao, Y. Zheng, T. Xi, C. Zhang, W. Song, K. Burugapalli, H. Yang and Y. Ma, *Biomed. Microdevices*, 2012, **14**, 709-720.

80. M. M. Oliveira, C. Boyer, M. Nele, J. Pinto, P. B. Zetterlund and T. P. Davis, *Macromolecules*, 2011, **44**, 7167-7175.

81. H. Wutzel, F. H. Richter, Y. Li, S. S. Sheiko and H.-A. Klok, *Polym. Chem.*, 2013, **5**, 1711-1719.

82. P. A. Vasey, S. B. Kaye, R. Morrison, C. Twelves, P. Wilson, R. Duncan, A. H. Thomson, L. S. Murray, T. E. Hilditch, T. Murray, S. Burtles, D. Fraier, E. Frigerio and J. Cassidy, *Clin. Cancer Res.*, 1999, **5**, 83-94.

83. W. Li, K. Matyjaszewski, K. Albrecht and M. Möller, *Macromolecules*, 2009, **42**, 8228-8233.

84. J. Ryan, F. Aldabbagh, P. B. Zetterlund and M. Okubo, *Polymer*, 2005, **46**, 9769-9777.

85. A. Albanese, P. S. Tang and W. C. W. Chan, *Annu. Rev. Biomed. Eng.*, 2012, **14**, 1-16.

86. J. Nicolas, B. Charleux, O. Guerret and S. Magnet, *Macromolecules*, 2004, **37**, 4453-4463.

87. C. Farcet, J. Nicolas and B. Charleux, *J. Polym. Sci., Part A: Polym. Chem.*, 2002, **40**, 4410-4420.

88. J. M. de la Fuente and S. Penadés, *Biochim. Biophys. Acta*, 2006, **1760**, 636-651.

89. V. Ladmiral, E. Melia and D. M. Haddleton, *Eur. Polym. J.*, 2004, **40**, 431-449.

90. M. Al-Bagoury, K. Buchholz and E. J. Yaacoub, *Polym. Adv. Technol.*, 2007, **18**, 313-322.

91. C. Grazon, J. Rieger, R. Méallet-Renault, B. Charleux and G. Clavier, *Macromolecules*, 2013, **46**, 5167-5176.

92. C. Grazon, J. Rieger, R. Méallet-Renault, G. Clavier and B. Charleux, *Macromol. Rapid Commun.*, 2011, **32**, 699-705.

93. J.-B. Qu, R. Chapman, F. Chen, H. Lu and M. H. Stenzel, *ACS Appl. Mater. Interfaces*, 2017, **9**, 13865-13874.

94. N. J. Warren and S. P. Armes, *J. Am. Chem. Soc.*, 2014, **136**, 10174-10185.

95. Y. Mai and A. Eisenberg, *Chem. Soc. Rev*, 2012, **41**, 5969-5985.

96. A. Blanazs, A. J. Ryan and S. P. Armes, *Macromolecules*, 2012, **45**, 5099-5107.

97. X. G. Qiao, M. Lansalot, E. Bourgeat-Lami and B. Charleux, *Macromolecules*, 2013, **46**, 4285-4295.

98. G. Wang, M. Schmitt, Z. Wang, B. Lee, X. Pan, L. Fu, J. Yan, S. Li, G. Xie, M. R. Bockstaller and K. Matyjaszewski, *Macromolecules*, 2016, **49**, 8605-8615.

99. D. Cordella, F. Ouhib, A. Aqil, T. Defize, C. Jérôme, A. Serghei, E. Drockenmuller, K. Aissou, D. Taton and C. Detrembleur, *ACS Macro Lett.*, 2017, **6**, 121-126.

100. K. Yukiya, K. Kazuya, M. Hideto and O. Masayoshi, *J. Polym. Sci., Part A: Polym. Chem.*, 2012, **50**, 1991-1996.

101. C. He, Y. Hu, L. Yin, C. Tang and C. Yin, *Biomaterials*, 2010, **31**, 3657-3666.

102. B. Karagoz, C. Boyer and T. P. Davis, *Macromol. Rapid Commun.*, 2014, **35**, 417-421.

103. B. Karagoz, L. Esser, H. T. Duong, J. S. Basuki, C. Boyer and T. P. Davis, *Polym. Chem.*, 2013, **5**, 350-355.

104. L. Qiu, C.-R. Xu, F. Zhong, C.-Y. Hong and C.-Y. Pan, *ACS Appl. Mater. Interfaces*, 2016, **8**, 18347-18359.

105. S. Zhang, J. Li, G. Lykotrafitis, G. Bao and S. Suresh, *Adv. Mater.*, 2009, **21**, 419-424.

106. E. Hinde, K. Thammasiraphop, H. T. T. Duong, J. Yeow, B. Karagoz, C. Boyer, J. J. Gooding and K. Gaus, *Nat. Nanotechnol.*, 2016, **12**, nnano.2016.2160.

107. S. Kaga, N. P. Truong, L. Esser, D. Senyschyn, A. Sanyal, R. Sanyal, J. F. Quinn, T. P. Davis, L. M. Kaminskas and M. R. Whittaker, *Biomacromolecules*, 2017, **18**, 3963-3970.

108. W. Zhao, H. T. Ta, C. Zhang and A. K. Whittaker, *Biomacromolecules*, 2017, **18**, 1145-1156.

109. L. Esser, N. P. Truong, B. Karagoz, B. A. Moffat, C. Boyer, J. F. Quinn, M. R. Whittaker and T. P. Davis, *Polym. Chem.*, 2016, **7**, 7325-7337.

110. B. Karagoz, J. Yeow, L. Esser, S. M. Prakash, R. P. Kuchel, T. P. Davis and C. Boyer, *Langmuir*, 2014, **30**, 10493-10502.

111. Z. An, Q. Shi, W. Tang, C.-K. Tsung, C. J. Hawker and G. D. Stucky, *J. Am. Chem. Soc.*, 2007, **129**, 14493-14499.

112. C. Grazon, J. Rieger, N. Sanson and B. Charleux, *Soft Matter*, 2011, **7**, 3482-3490.

113. G. Liu, Q. Qiu, W. Shen and Z. An, *Macromolecules*, 2011, **44**, 5237-5245.

114. G. Liu, Q. Qiu and Z. An, *Polym. Chem.*, 2012, **3**, 504-513.

115. W. Shen, Y. Chang, G. Liu, H. Wang, A. Cao and Z. An, *Macromolecules*, 2011, **44**, 2524-2530.

116. A. Blanazs, J. Madsen, G. Battaglia, A. J. Ryan and S. P. Armes, *J. Am. Chem. Soc.*, 2011, **133**, 16581-16587.

117. S. J. Byard, M. Williams, B. E. McKenzie, A. Blanazs and S. P. Armes, *Macromolecules*, 2017, **50**, 1482-1493.

118. X. Wang, J. Zhou, X. Lv, B. Zhang and Z. An, *Macromolecules*, 2017, **50**, 7222-7232.

119. W. Zhou, Q. Qu, Y. Xu and Z. An, *ACS Macro Lett.*, 2015, **4**, 495-499.

120. C. A. Figg, A. Simula, K. A. Gebre, B. S. Tucker, D. M. Haddleton and B. S. Sumerlin, *Chem. Sci.*, 2015, **6**, 1230-1236.

121. A. Blanazs, R. Verber, O. O. Mykhaylyk, A. J. Ryan, J. Z. Heath, C. W. I. Douglas and S. P. Armes, *J. Am. Chem. Soc.*, 2012, **134**, 9741-9748.

122. I. Canton, N. J. Warren, A. Chahal, K. Amps, A. Wood, R. Weightman, E. Wang, H. Moore and S. P. Armes, *ACS Cent. Sci.*, 2016, **2**, 65-74.

123. V. Ladmiral, M. Semsarilar, I. Canton and S. P. Armes, *J. Am. Chem. Soc.*, 2013, **135**, 13574-13581.

124. D. E. Mitchell, J. R. Lovett, S. P. Armes and M. I. Gibson, *Angew. Chem., Int. Ed.*, 2016, **55**, 2801-2804.

125. Y. Jonathan and B. Cyrille, *Adv. Sci.*, 2017, **4**, 1700137.

126. L. D. Blackman, K. E. B. Doncom, M. I. Gibson and R. K. O'Reilly, *Polym. Chem.*, 2017, **8**, 2860-2871.

127. C. I. Biggs, T. L. Bailey, G. Ben, C. Stubbs, A. Fayter and M. I. Gibson, *Nat. Commun.*, 2017, **8**, 1546.

128. C. Ma, X. Liu, G. Wu, P. Zhou, Y. Zhou, L. Wang and X. Huang, *ACS Macro Lett.*, 2017, **6**, 689-694.

129. F. H. Sobotta, F. Hausig, D. O. Harz, S. Hoeppener, U. S. Schubert and J. C. Brendel, *Polym. Chem.*, 2018, **9**, 1593-1602.

130. C. d. l. H. Alarcon, S. Pennadam and C. Alexander, *Chem. Soc. Rev*, 2005, **34**, 276-285.

131. W.-J. Zhang, C.-Y. Hong and C.-Y. Pan, *Biomacromolecules*, 2016, **17**, 2992-2999.

132. A. Zare-Mirakabadi, A. Sarzaeem, S. Moradhaseli, A. Sayad and M. Negahdary, *Iran, J, Cancer Prev.*, 2012, **5**, 109-116.

133. W.-J. Zhang, C.-Y. Hong and C.-Y. Pan, *Biomacromolecules*, 2017, **18**, 1210-1217.

134. M. Mittal, M. R. Siddiqui, K. Tran, S. P. Reddy and A. B. Malik, *Antioxid. Redox Signaling*, 2014, **20**, 1126-1167.

135. J. S. Lee and J. Feijen, *J. Controlled Release*, 2012, **161**, 473-483.

136. C. P. O'Neil, T. Suzuki, D. Demurtas, A. Finka and J. A. Hubbell, *Langmuir*, 2009, **25**, 9025-9029.

137. J. Tan, H. Sun, M. Yu, B. S. Sumerlin and L. Zhang, *ACS Macro Lett.*, 2015, **4**, 1249-1253.

138. L. D. Blackman, S. Varlas, M. C. Arno, A. Fayter, M. I. Gibson and R. K. O'Reilly, *ACS Macro Lett.*, 2017, **6**, 1263-1267.

139. L. D. Blackman, S. Varlas, M. C. Arno, Z. H. Houston, N. L. Fletcher, K. J. Thurecht, M. Hasan, M. I. Gibson and R. K. O'Reilly, *ACS Cent. Sci.*, 2018, **4**, 718-723.

140. G. Ng, J. Yeow, J. Xu and C. Boyer, *Polym. Chem.*, 2017, **8**, 2841-2851.

141. J. Tan, D. Liu, Y. Bai, C. Huang, X. Li, J. He, Q. Xu and L. Zhang, *Macromolecules*, 2017, **50**, 5798-5806.

142. C. I. Holdsworth, Z. Jia and M. J. Monteiro, *Polymer*, 2016, **106**, 200-207.

143. N. P. Truong, M. R. Whittaker, A. Anastasaki, D. M. Haddleton, J. F. Quinn and T. P. Davis, *Polym. Chem.*, 2015, **7**, 430-440.

144. N. P. Truong, J. F. Quinn, A. Anastasaki, M. Rolland, M. N. Vu, D. M. Haddleton, M. R. Whittaker and T. P. Davis, *Polym. Chem.*, 2017, **8**, 1353-1363.

145. C. J. Ferguson, R. J. Hughes, B. T. Pham, B. S. Hawkett, R. G. Gilbert, A. K. Serelis and C. H. Such, *Macromolecules*, 2002, **35**, 9243-9245.

146. C. J. Ferguson, R. J. Hughes, D. Nguyen, B. T. Pham, R. G. Gilbert, A. K. Serelis, C. H. Such and B. S. Hawkett, *Macromolecules*, 2005, **38**, 2191-2204.

147. B. Charleux and J. Nicolas, *Polymer*, 2007, **48**, 5813-5833.

148. G. Delaittre, J. Nicolas, C. Lefay, M. Save and B. Charleux, *Soft Matter*, 2006, **2**, 223-231.

149. J. Nicolas, B. Charleux, O. Guerret and S. Magnet, *Macromolecules*, 2005, **38**, 9963-9973.

150. G. Delaittre, J. Nicolas, C. Lefay, M. Save and B. Charleux, *Chem. Commun.*, 2005, **0**, 614-616.

151. C. L. Moad, G. Moad, E. Rizzardo and S. H. Thang, *Macromolecules*, 1996, **29**, 7717-7726.

152. Z. S., X. B. and X. Y., *Pigm. Resin Technol.*, 2012, **41**, 95-99.

153. C. Cheng, S. Gong, Q. Fu, L. Shen, Z. Liu, Y. Qiao and C. Fu, *Polymer Bulletin*, 2011, **66**, 735-746.

154. J. Shu, C. Cheng, Y. Zheng, L. Shen, Y. Qiao and C. Fu, *Polymer Bulletin*, 2011, **67**, 1185-1200.

155. C. Cheng, J. Shu, S. Gong, L. Shen, Y. Qiao and C. Fu, *New J. Chem*, 2010, **34**, 163-170.

156. J. Zhou, H. Yao and J. Ma, *Polym. Chem.*, 2018, **9**, 2532-2561.

157. W. Zhang, F. D'Agosto, O. Boyron, J. Rieger and B. Charleux, *Macromolecules*, 2012, **45**, 4075-4084.

158. J. Rieger, W. Zhang, F. o. Stoffelbach and B. Charleux, *Macromolecules*, 2010, **43**, 6302-6310.

159. M. Manguian, M. Save and B. Charleux, *Macromol. Rapid Commun.*, 2006, **27**, 399-404.

160. T. P. Davis, N. Truong Phuoc, M. Dussert, M. R. Whittaker and J. F. Quinn, *Polym. Chem.*, 2015, **6**, 3865-3874.

161. F. Alexis, E. Pridgen, L. K. Molnar and O. C. Farokhzad, *Mol. Pharm.*, 2008, **5**, 505-515.

162. S. S. R. Ting, E. Min, P. B. Zetterlund and M. H. Stenzel, *Macromolecules*, 2010, **43**, 5211-5221.

163. I. Chaduc, E. Reynaud, L. Dumas, L. Albertin, F. D'Agosto and M. Lansalot, *Polymer*, 2016, **106**, 218-228.

164. G. Jiang, Y. Wang, R. Zhang, R. Wang, X. Wang, M. Zhang, X. Sun, S. Bao, T. Wang and S. Wang, *ACS Macro Lett.*, 2012, **1**, 489-493.

165. C. Poon, O. Tang, X.-M. Chen, B. T. T. Pham, G. Gody, C. A. Pollock, B. S. Hawkett and S. Perrier, *Biomacromolecules*, 2016, **17**, 965-973.

166. C. Poon, O. Tang, X. M. Chen, B. Kim, M. Hartlieb, C. A. Pollock, B. S. Hawkett and S. Perrier, *Macromol. Biosci.*, 2017, **17**, 1600366.

167. J. Engström, F. L. Hatton, L. Wågberg, F. D'Agosto, M. Lansalot, E. Malmström and A. Carlmark, *Polym. Chem.*, 2017, **8**, 1061-1073.

168. J. Lesage de la Haye, X. Zhang, I. Chaduc, F. Brunel, M. Lansalot and F. D'Agosto, *Angew. Chem.*, 2016, **128**, 3803-3807.

169. J. D. Rocca, D. Liu and W. Lin, *Nanomedicine*, 2012, **7**, 303-305.

170. S. Mura, J. Nicolas and P. Couvreur, *Nat. Mater.*, 2013, **12**, 991.

171. M. L. Hans and A. M. Lowman, *Curr. Opin. Solid State Mater. Sci.*, 2002, **6**, 319-327.

172. M. Wang and M. Thanou, *Pharmacol. Res.*, 2010, **62**, 90-99.

173. S. T. Camli, F. Buyukserin, O. Balci and G. G. Budak, *J. Colloid Interface Sci.*, 2010, **344**, 528-532.

174. E. Marc and Z. Rudolf, *Macromol. Chem. Phys.*, 2004, **205**, 1479-1488.

175. K. Tauer, R. Deckwer, I. Kühn and C. Schellenberg, *Colloid Polym. Sci.*, 1999, **277**, 607-626.

176. L. A. M. and P. Sébastien, *Macromol. Rapid Commun.*,1800122.

Chapter 2

RAFT emulsion polymerisation as a platform to generate well-defined biocompatible nanoparticles.

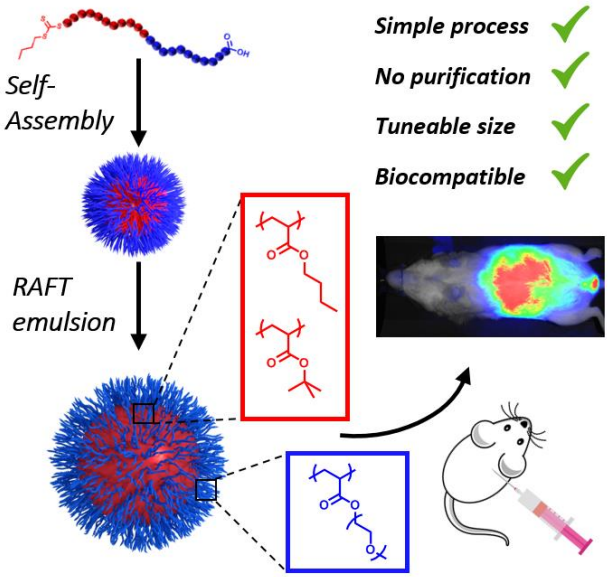

Current approaches to generate core-shell nanoparticles for biomedical applications, are limited by factors such as synthetic scalability and circulatory desorption of cytotoxic surfactant. Developments in controlled radical polymerisation, particularly in dispersed states, represent a promising method of overcoming many of these challenges. In this work, well-defined PEGylated nanoparticles were synthesised using RAFT emulsion polymerisation to control the particle size and surface composition, and further characterised with light scattering, electron microscopy and size exclusion chromatography. Notably, the nanoparticles were found to be non-toxic in vitro and indeed in vivo even at very high dosages without any purification after particle synthesis. Pharmacokinetic and biodistribution studies in mice, following intraperitoneal injection of the nanoparticles, revealed a long circulation time and accumulation in reticuloendothelial organs.

2.1 Introduction

Polymeric nanoparticles are well established as platforms for drug delivery and bio-imaging applications.[1, 2] Their large size promotes extended circulation times through evasion of renal filtration[3] as well as passive tumour accumulation through the enhanced permeability and retention (EPR) effect[4, 5]. Conjugation of 'stealthy' polymers reduces the impact of protein corona formation, reducing trafficking towards other excretion pathways.[6] Encapsulation/conjugation of chemotherapeutic agents inside these vectors protects them from physiological degradation, while also facilitating their transport across the cellular membrane. Additionally, their high surface functionality can be exploited by attaching specific targeting moieties (antibodies,[7] peptides,[8] or glycosylated functionality[9]). These properties culminate in higher therapeutic efficacy, tumour selectivity and reduced side effects for nanoparticle drug delivery vectors, in comparison to their molecular drug counterparts.[10]

In nanomedicine, and particularly for cancer therapy, polymeric nanoparticles are typically engineered to have diameters of 20 - 200 nm (to exploit the EPR effect),[4, 11] a hydrophobic core for high drug loading efficiency,[12] and a cyto-compatible corona for reduced toxicity.[13] These criteria can be fulfilled through a multitude of methods, including self-assembly of amphiphilic block-copolymers,[14, 15] or traditional emulsion polymerisation.[16] Problematically, these architectures have intrinsic disadvantages which limit their clinical use. Self-assembly of block copolymers is typically performed at low concentrations, small scales (2-5 mg mL^{-1}) and in the presence of cytotoxic organic solvents (DMF, THF, Methanol), affecting safety and synthetic reproducibility. In contrast emulsion polymerisation is highly scalable and is conventionally performed in aqueous media. Unfortunately, the low circulatory concentration of both of these systems induced their release/disassembly of/into potentially cytotoxic surfactants, reducing their biocompatibility, while also increasing their clearance rate which can impact therapeutic efficacy.[17] This can be overcome with meticulous design of covalently bound branched/brush-like polymers (unimolecular micelle), however achieving the large sizes (20-200 nm) and scales required for these applications through this method is non-trivial.[18, 19]

Reversible addition fragmentation chain transfer (RAFT) emulsion polymerisation provides a potentially elegant solution to overcome many of these challenges by

combining the advantages of traditional emulsion polymerisation (fast polymerisation rates, green/aqueous conditions and high scalability) with the hallmarks of controlled radical polymerisation (narrow and tuneable molecular weight distributions, block copolymer synthesis and functional end group fidelity).[20, 21] During this process, amphiphilic di-block macromolecular RAFT (macro-RAFT) agent stabilisers are self-assembled into micelles, with the thiocarbonylthio group within the core. These are then chain extended during the emulsion polymerisation with hydrophobic monomer (oil phase), resulting in 'frozen' uniform core-shell latex nanoparticles where the shell is comprised of the hydrophilic section of the stabilising agent. Nanoparticles prepared using this approach are beneficial for biomedical applications, as the shell is covalently attached and cannot desorb from the particle during circulation. Advantageously, this process is performed in the absence of organic solvents (aqueous conditions), is highly scalable, and the stabiliser can be designed to impart biocompatibility.

Nevertheless, most of the studies on RAFT emulsion polymerisation focus on their synthesis (kinetics and morphology),[20, 22-25] with only a few notable studies exploiting this technique to generate nanoparticles aimed at biomedical applications. For example, Stenzel and co-workers used an amphiphilic poly(glucose methacrylamide)-b-polystyrene macro-RAFT agent to generate glycosylated nanoparticles, which displayed high affinity for E. coli.[26] Whereas, Wang and co-workers used RAFT emulsion polymerisation to control the monomer composition of the nanoparticle shell, yielding a system whereby the release rate of a model hydrophobic drug (indomethacin) could be tuned with pH.[27] Furthermore, Poon *et al* have illustrated the potential for surface modification of polyacrylamide stabilised polystyrene nanoparticles synthesised from RAFT emulsion, initially as micro-RNA carriers, and also fluorescent labelling for studies *in vitro* and *in vivo*.[28, 29] Nonetheless, these nanoparticle systems required extensive dialysis purifications, which reduced their scalability potential. Moreover, their suitability in complex biological organisms still remains elusive, with little information reported about these nanoparticles in cellular assays or live animal models.

The aim in this chapter was to showcase how RAFT emulsion polymerisation can be used to easily generate biocompatible nanoparticles, whilst also probing their toxicity *in vitro* and *in vivo*. A series of core-shell polymeric nanoparticles with cores of poly(*tert*-butyl acrylate) (P(*t*-BA)) and poly (*n*-butyl acrylate) (P(*n*-BA)), and a cyto-compatible

poly(poly(ethylene glycol methyl ether acrylate)) (P(PEGA)) corona were synthesised *via* RAFT emulsion polymerisation. The nanoparticles were characterised with light scattering, electron microscopy and size exclusion chromatography. Their toxicity was then evaluated *in vitro* on a colorectal carcinoma cell line (Caco-2), and *in vivo* on mouse models. Finally, a near-infrared (NIR) probe, Cyanine-7.5, was encapsulated into the nanoparticles, and preliminary pharmacokinetics and biodistribution were studied using an *in vivo* fluorescence imager.

2.2 Results and Discussion

2.2.1 Strategy

It has previously been shown that oligomeric amphiphilic diblock macromolecular RAFT agents (macro-RAFT) are suitable stabilisers for RAFT emulsion polymerisation.[20, 25, 30] As the aim of this project was to employ this technique to generate biocompatible nanoparticles, polyethylene glycol (PEG) was selected as the hydrophilic block of the macro-RAFT agents. PEG is well established as the gold standard for imparting biocompatibility, 'stealth' from the immune system, and colloidal stability, to nanomaterials owed to its superior anti-fouling properties, hydrophilicity and steric effects.[31-33] In general, the hydrophobic block of the macro-RAFT agent stabiliser is usually comprised of the same monomer to be used during the emulsion step, and therefore are required to be immiscible in water. Based on the above criteria, P[(PEGA)$_8$-*b*-(*n*-BA)$_8$] and P[(PEGA)$_8$-*b*-(*t*-BA)]$_8$ were conceived as the initial designs for the macro-RAFT agents.

2.2.2 Synthesis of macromolecular RAFT agent stabilisers

Macro-RAFT agents, P[(PEGA)$_8$-*b*-(*n*-BA)]$_8$ (**MRA-*n*BA**) and P[(PEGA)$_8$-*b*-(*t*-BA)]$_8$ (**MRA-*t*BA**), were synthesised in two steps (Scheme 2.1). For the first block, polymerisation of poly(ethylene glycol methyl ether acrylate) (PEGA) was performed at 70°C mediated with RAFT agent (propanoic acid)yl butyl trithiocarbonate (PABTC) in 1,4-dioxane using ACVA as the thermal initiator. PABTC has previously been shown to be an excellent chain transfer agent (CTA) for acrylates[34] and acrylamides[35], and importantly the carboxylic acid R-group will be imparted onto the particle surface, improving the electrostatic stabilisation of the final nanoparticles. Additionally, it has previously been reported that trithiocarbonate end groups cause less toxicity than dithiobenzoate.[36] The polymerisation was stopped at 91% conversion to maintain high chain end fidelity and yielded P(PEGA)$_8$ (**MRA-PEGA**), which was purified *via* precipitation in diethyl ether to remove residual monomer. **MRA-PEGA** was subsequently chain extended with either *tert*-butyl acrylate (*t*-BA) or *n*-butyl acrylate (*n*-BA) to yield **MRA-*t*BA** and **MRA-*n*BA**, reaching 96% and 94% monomer conversion respectively and both purified *via* precipitation in hexane. Full details for polymerisation conditions can be found in Table 2.5.

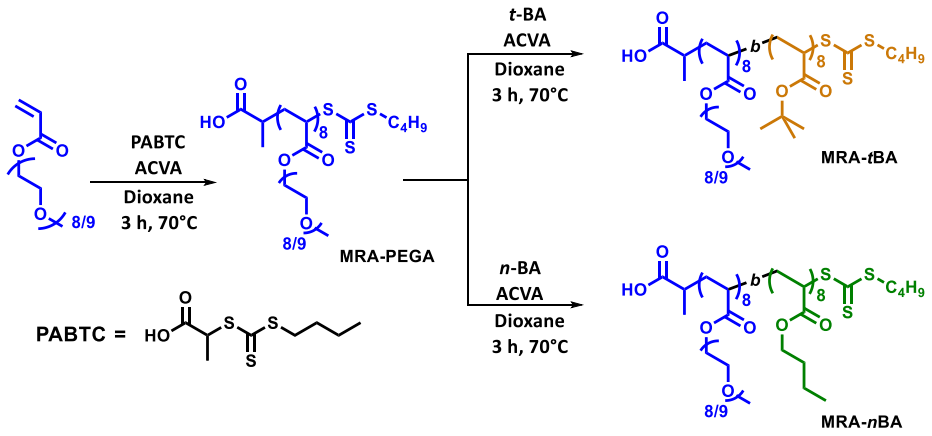

Scheme 2.1. Preparation of **MRA-PEGA**, **MRA-*n*BA and MRA-*t*BA** *via* RAFT polymerisation**.**

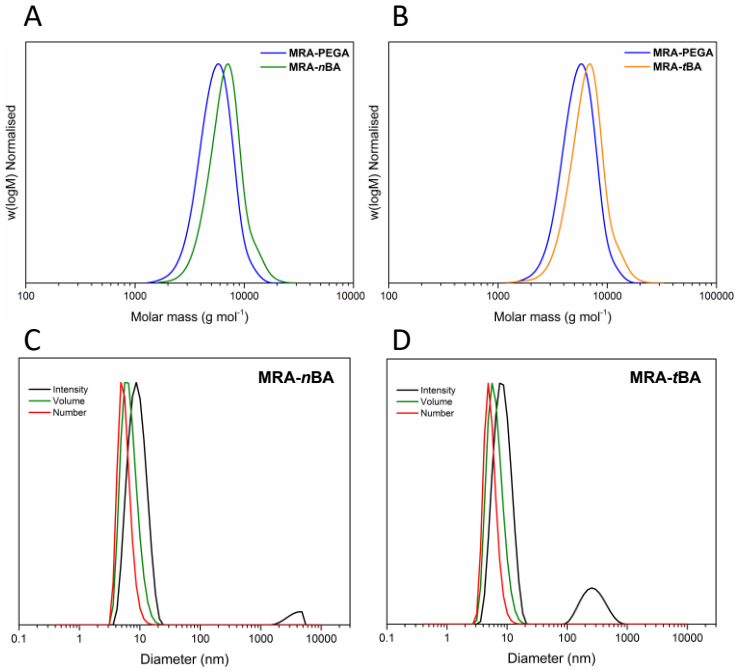

Figure 2.1. $CHCl_3$-SEC traces of **MRA-PEGA** (blue), (A) **MRA-*n*BA** (green) and (B) **MRA-*t*BA** (orange). DLS traces of (C) MRA-*t*BA and (D) MRA-*n*BA micelles at 15 mg mL^{-1} in pure water at 25°C.

Size exclusion chromatography (SEC) of all three polymers indicated narrow molar mass distributions, and clear shifts towards higher molecular weight suggesting successful chain extensions (Đ < 1.2; Figure 2.1). ^{1}H NMR spectra confirmed excellent agreement between theoretical and observed molar masses (Figure 2.2; Table 2.1). Chromatograms of **MRA-*n*BA** and **MRA-*t*BA** revealed a small high molecular weight shoulder which has been attributed to mid- or side- chain branching, expected for acrylate monomers (Figure 2.1a and Figure 2.1b). Dynamic light scattering (DLS) indicated the formation of uniform micelles (PDi < 0.07) with diameters of 6.4 and 6.2 nm for **MRA-*n*BA** and

MRA-*t*BA respectively (Figure 2.1c and Figure 2.1d; Table 2.1). The observed radii (~ 3-4 nm) are consistent with theoretical values for fully stretched out polymer chains (16 x 0.25 nm per monomer unit = 4 nm), suggesting that the micelles were spherical in shape. Both block copolymer micelles exhibited negative ζ-potentials (ZP), due to the deprotonated carboxylic functionality at the corona. Overall, these measurements show that **MRA-*n*BA** and **MRA-*t*BA** should be suitable stabilising agents during RAFT emulsion polymerisation, due to the steric and electrostatic stability from the carboxylated P(PEGA) corona.

Table 2.1. Characterisation data for macro-RAFT agents MRA-PEGA, MRA-*n*BA and MRA-*t*BA

	% conv[a]	$M_{n,th}$ (g mol^{-1})[b]	$M_{n,SEC}$ (g mol^{-1})[c]	$M_{w,SEC}$ (g mol^{-1})[c]	$Đ$[c]	D_h[d]	PDi[e]	ζ-Potential (mV)[f]
MRA-PEGA	91	4100	5100	5800	1.14	-	-	-
MRA-*n*BA	96	5100	6300	7200	1.14	6.6	0.069	-10
MRA-*t*BA	94	5100	6000	6950	1.15	6.2	0.069	-11

[a]Determined by ^{1}H NMR spectroscopy. [b]Theoretical molar masses calculated with Equation 2.12. [c]Determined by $CHCl_3$-SEC and analysed against PMMA standards. [d]Determined using DLS. [e]Calculated using Equation 2.13. [f]Measured using a Zetasizer.

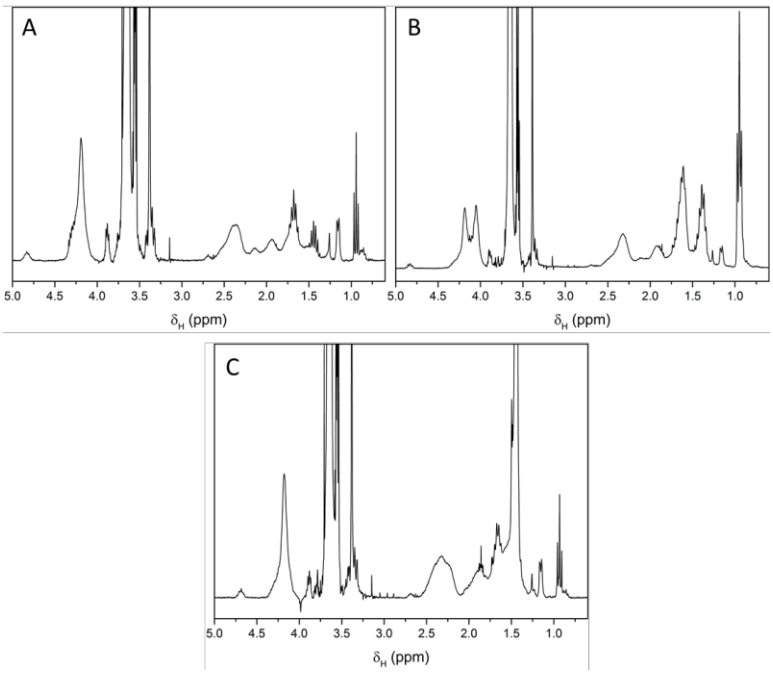

Figure 2.2. ^{1}H NMR spectra of (a) MRA-PEGA (b) MRA-*n*BA and (c) MRA-*t*BA in $CDCl_3$ at 300 MHz.

2.2.3 Nanoparticle synthesis *via* RAFT emulsion polymerisation

Although RAFT emulsion polymerisation was first introduced over a decade ago, there are no universal conditions to achieve low polydispersity nanoparticles and narrow molecular weight distributions. Conditions typically vary depending on macro-RAFT agent composition, monomer choice and reagent concentrations.[24, 37] The RAFT emulsion polymerisation process was optimised with a systematic study on initiator type starting from conditions adapted from previous work.[28, 29]

2.2.3.1 Optimisation of initiator

Prior to optimisation of initiator type, parameters such as initiator and macro-RAFT agent concentrations were established from literature procedures. For the study, *n*-BA was chosen as the monomer as its use has been far more prevalent in the literature as compared to *t*-BA.[23, 38, 39] In the first report of RAFT emulsion polymerisation, Hawkett and co-workers used a macro-RAFT agent concentration of between 1.28 and 5.06 mM for successful polymerisations of *n*-butyl acrylate.[40] While Poon *et al*. used azo-initiator 4,4'-Azobis(4-cyanovaleric acid) (ACVA, V-501) at high concentrations ($[\text{macro-RAFT}]_0/[I]_0$ = 1.1), to generate a high radical flux enabling fast nucleation of seed micelles and uniform particle growth, resulting in low polydispersity particles.[28] Using reaction parameters from these systems, initiators 2,2'-Azobis[2-(2-imidazolin-2-yl)propane]dihydrochloride (VA-044) and ACVA were investigated as positive and negatively charged initiators for RAFT emulsion polymerisation of *n*-butyl acrylate mediated by **MRA-*n*BA** at 70°C. These initiators however have vastly different 10 h decomposition half-life temperatures (44°C for VA-044, and 69°C for ACVA), therefore at the same initial concentration, a larger amount of VA-044 would be consumed at 70°C compared to ACVA, per unit time.

$$k_d = \frac{\left(\frac{\ln 2}{36000s}\right)}{e^{\frac{E_A}{RT_{t1/2}}}} \cdot e^{\frac{E_A}{RT_X}}$$

Equation 2.1. Calculation of the decomposition rate constant (s^{-1}). EA = activation energy of homolytic fission of initiator (J mol^{-1}), R = molar gas constant 8.314 (J K^{-1} mol^{-1}), $T_{t1/2}$ = 10 h half-life temperature of initiator, T_x = temperature of reaction.

$$[I]_{t(y)} = [I]_{t(0)} - [I]_0 e^{-k_d t(y)}$$

Equation 2.2. Calculation of initiator consumed at time y. $[I]_{t(y)}$ = concentration of initiator at time y (mol dm^{-3}), $[I]_{t=0}$ = initiator concentration at the start of the reaction (mol dm-3).

From Equation 2.1 and Equation 2.2, it was determined a 5 fold decrease in initial initiator concentration ($[I]_0$) was necessary for VA-044, in comparison to ACVA, to ensure the same radical flux. For polymerisations using ACVA the same initiator ratios as Poon *et al* were chosen. ($[Macro\text{-}RAFT]_0/[I]_0 = 1.1$), and therefore $[Macro\text{-}RAFT]_0/[I]_0 = 5.5$ for polymerisations initiated with VA-044. Meanwhile $[Macro\text{-}RAFT]_0$ was set to 2.85 mM as a compromise of the upper and lower values used by Hawkett and co-workers.[20]

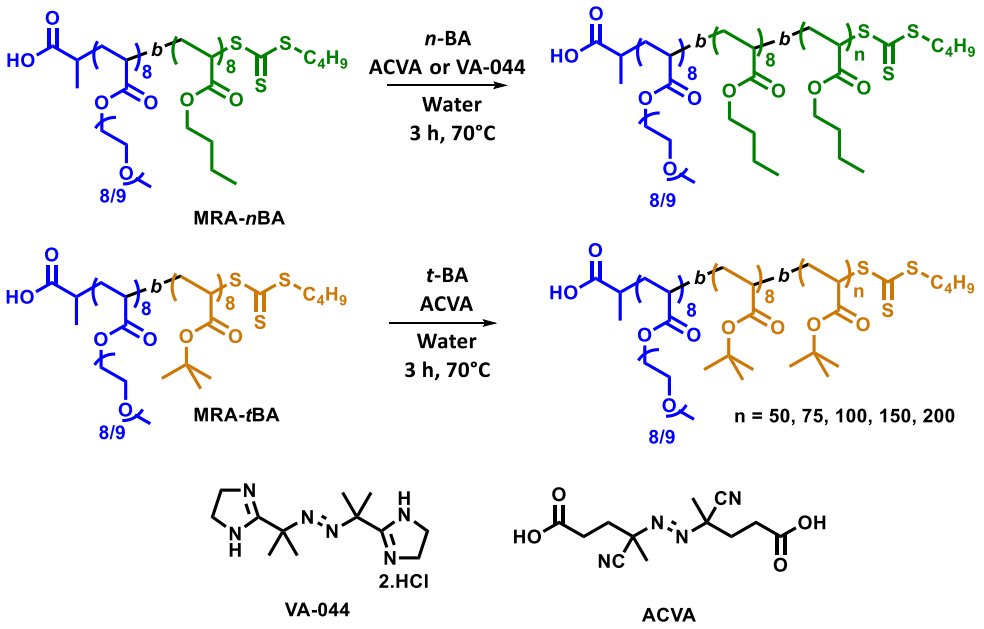

Scheme 2.2. RAFT emulsion polymerisation of *n*-BA and *t*-BA mediated by MRA-*n*BA and MRA-*t*BA respectively using thermal initiators ACVA and VA-044.

Table 2.2. Characterisation data of P(*n*-BA) and P(*t*-BA) nanoparticles synthesised using azo-initiators VA-044 and ACVA.

	Initiator	Monomer	Macro-RAFT	DP_{target} [a]	D_h (nm) [b]	PDi [b]	ZP (mV) [b]	$M_{n,th}$ (g mol^{-1}) [c]	$M_{n,SEC}$ (g mol^{-1}) [d]	$M_{w,SEC}$ (g mol^{-1}) [d]	$Đ$ [d]
1	VA-044	*n*-BA	**MRA-*n*BA**	200	282	0.12	-31.6	30700	31000	59500	1.92
2				150	257	0.11	-32.3	24300	25800	75600	2.93
3				100	139	0.09	-29.5	17900	17800	24500	1.60
4				75	104	0.10	-30.9	14700	14800	25200	1.70
5				50	55	0.09	-29.1	11500	11400	15400	1.35
6	ACVA	*n*-BA	**MRA-*n*BA**	200	130	0.05	-47.3	30700	25700	48600	1.86
7				150	92	0.06	-37.8	24300	22500	34000	1.60
8				100	75	0.06	-35.4	17900	18400	24400	1.39
9				75	50	0.06	-37.1	14700	14200	18500	1.35
10				50	28	0.06	-34.2	11500	11500	13300	1.22
11	ACVA	*t*-BA	**MRA-*t*BA**	200	119	0.05	-48.5	30700	30700	47000	1.54
12				150	86	0.05	-45.1	24300	22000	34900	1.58
13				100	66	0.06	-39.2	17900	16500	24400	1.47
14				75	49	0.06	-42.6	14700	13300	17600	1.32
15				50	31	0.07	-37.4	11500	10200	12600	1.23

[a]Refers to the target DP of RAFT emulsion polymerisations performed to obtain the third (core forming) block. [b]Determined by DLS. [c]Determined using Equation 2.12. [d]Determined by $CHCl_3$-SEC (values are obtained by integrating the whole region, including all three peaks), calibrated with PMMA standards. All polymerisations reached >99% monomer conversion, determined by gravimetry.

For RAFT emulsion polymerisations, **MRA-*n*BA,** thermal initiator (ACVA or VA-044), *n*-BA and water were homogenised and subsequently heated to 70°C for 3 h under vigorous stirring. Over the course of the reaction, the emulsions turned milky white as the polymerisations proceeded. Syntheses were performed with both ACVA and VA-044 with five different $[M]_0/[\text{Macro-RAFT}]_0$ ratios (50, 75, 100, 150 and 200) in order to alter the chain length of the third (core-forming) block (Scheme 2.2). ACVA emulsion polymerisations were conducted with two equivalents NaOH relative to the initiator to ensure complete deprotonation and water solubility. All polymerisations rapidly reached full conversion within 3 h, due to the compartmentalisation effects typically found in emulsion polymerisations. This is particularly useful in a biomedical context, as residual monomers are known to be highly cytotoxic.[41] SEC analysis of the dissolved nanoparticles exhibited significant shifts toward higher molecular weight from **MRA-*n*BA** traces for both VA-044 and ACVA emulsion polymerisations, suggesting chain extension within the core was successful. Interestingly, chromatograms for VA-044 polymerisations displayed broad dispersities ($Đ$ = 1.35-2.93), unsymmetrical molar mass distributions, and in some cases multimodal distributions (Table 2.2, Entry 1-5; Figure

2.3a). In comparison, size exclusion chromatograms for ACVA polymerisations, revealed smoother molecular weight distributions and an increasing trend of $M_{n,SEC}$ with DP_{target} (11,500 to 30,700 g mol^{-1}) (Table 2.2, Entry 6-10; Figure 2.3b). Nonetheless, these polymerisations were not completely controlled as chromatograms exhibited three distinct populations: a small high molecular weight shoulder due branching or bimolecular termination; a second low molecular population of unconsumed macro-RAFT agent; and a main narrow population of the targeted polymer. The non-quantitative macro-RAFT agent consumption is most likely due to a low chain transfer constant when assembled into micelles, and has been observed in other reports of RAFT emulsion polymerisations of acrylate monomers.[23] The observed molar masses ($M_{n,SEC}$) showed close agreement with theoretical values ($M_{n,th}$), however the discrepancy between $M_{n,th}$ and $M_{n,SEC}$ is attributed to differences in hydrodynamic volume of PMMA standards with the analysed polymers during size exclusion chromatography.

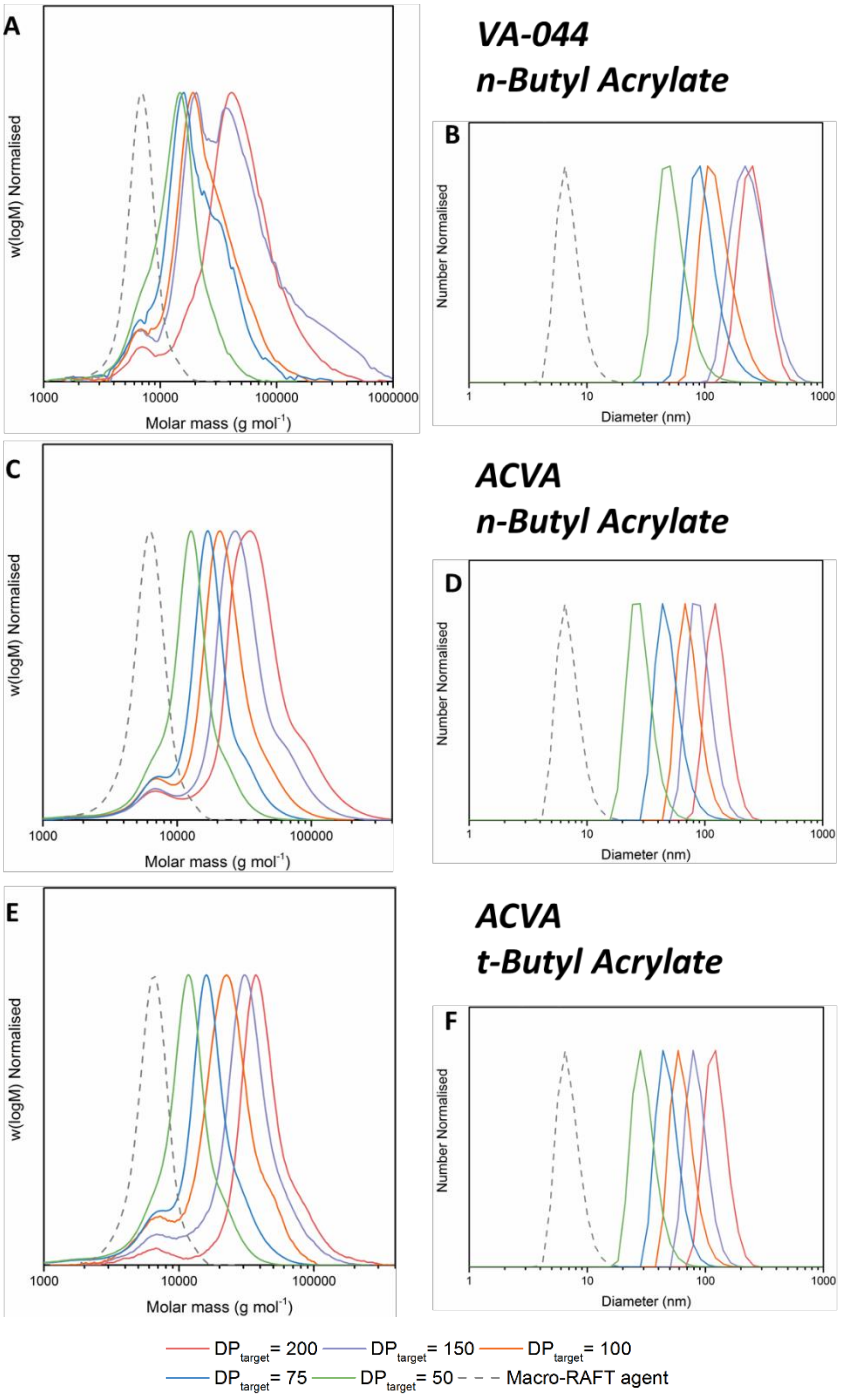

Figure 2.3. $CHCl_3$-SEC chromatograms depicting the increasing DP_{target} chain extensions (A) MRA-*n*BA with *n*-butyl acrylate using VA-044 as initiator, (C) MRA-*n*BA with *n*-butyl acrylate using ACVA as initiator and (E) MRA-*t*BA with *t*-butyl acrylate using ACVA as initiator. Chromatograms were obtained by dissolving dried nanoparticles in SEC eluent. DLS traces (number distribution) of P(*n*-BA) nanoparticles prepared with (B) VA-044 or (D) ACVA, and P(*t*-BA) nanoparticles (F) prepared with ACVA as well as their respective macro-RAFT agents (dashed grey lines). Measurements were taken at 25°C with nanoparticles dilute 1/1000 in pure water.

Particle size distributions in solution were analysed using DLS. Nanoparticles synthesised using VA-044 generally showed larger particle diameters (D_h = 55 – 282 nm; Table 2.2, Entry 1-5; Figure 2.3b), and broader distributions (PDi = 0.09 – 0.12) compared to their ACVA counterparts (D_h = 28 – 130 nm; PDi = 0.05 – 0.06; Table 2.2, Entry 6-10; Figure 2.3d). Intriguingly, both sets of nanoparticles (VA-044 and ACVA) displayed increasing particle size with larger DP_{target}, suggesting there was a tuneable relationship between DP_{target}/M_n and particle size.

The poorer performance of VA-044 polymerisations is likely due to the net positive charge formed from initiator derived Z_{mer}'s. These will be electrostatically attracted to the carboxylated seed particles increasing the number of radicals present in each growing particle.[42] This culminates in greater termination events, and also a more neutral surface charge, from positive Z_{mers} neutralising the negatively charged carboxylates. This leads to reduced electrostatic stability, broader molecular weight distributions and larger particle sizes, evident from the SEC, DLS and ZP analysis (Table 2.2). Conversely the negative Z_{mer}'s from ACVA will enhance stabilisation and reduce the number of radicals per particle.

It is advantageous for nanoparticles designed for biomedical applications to be between 20-200 nm such that they can be transported through fine capillary networks, and in particular for cancer therapy, exploit the EPR effect.[43] Nanomedicine systems larger than 200 nm therefore can have a reduced therapeutic benefit due to these limitations. The ACVA system represents an ideal method to generate particles for these applications by simply modifying the DP_{target}, narrow dispersity particles with precisely controlled sizes can be prepared. To show the versatility of this approach, the ACVA conditions were applied to a second monomer, *tert*-butyl acrylate (*t*-BA). SEC and DLS analysis of the P(*t*-BA) nanoparticles revealed similar characteristics to P(*n*-BA) nanoparticles, with narrow dispersity particle size distributions and an increasing trend between M_n and particle diameter (Table 2.2, Entry 11-15; Figure 2.3e and f). In general P(*t*-BA) nanoparticles displayed comparable $Đ$ and diameters to their P(*n*-BA) counterparts. Overall, it is clear that using ACVA as the initiator for RAFT emulsion polymerisation yields superior nanoparticles, which has been evaluated using two analogous monomers.

2.2.3.2 Optimisation of pH

In the previous section, a variety of nanoparticle sizes were synthesised by modifying the [M]:[macro-RAFT] ratio. As the surface of the macro-RAFT agent micelles contained a carboxylate moiety, it was important to determine how pH would affect the RAFT emulsion polymerisations, as this would alter the surface ionisation and therefore the macro-RAFT agent stabilisation.

Five RAFT emulsion polymerisations of *n*-BA were performed with DP_{target} = 100 and different [NaOH]:[macro-RAFT] ratios (0, 0.1, 0.25, 0.75, 1.0). As ACVA contains two acid groups, which are required to be deprotonated for full aqueous solubility, changing the [NaOH] may induce different solubility properties, therefore inadvertently altering $[I]_0$. To circumvent this, azo-initiator 2,2'-Azobis[*N*-(2-carboxyethyl)-2-methylpropionamidine]tetrahydrate (VA-057) was employed as this has complete water solubility, regardless of pH owed to its zwitterionic structure. These polymerisations however, were performed at the 10 h decomposition half-life temperature of 57°, therefore the difference in initiator cannot be extracted from this information. The pH of each polymerisation mixture was measured prior to heating (Table 2.3; Scheme 2.3).

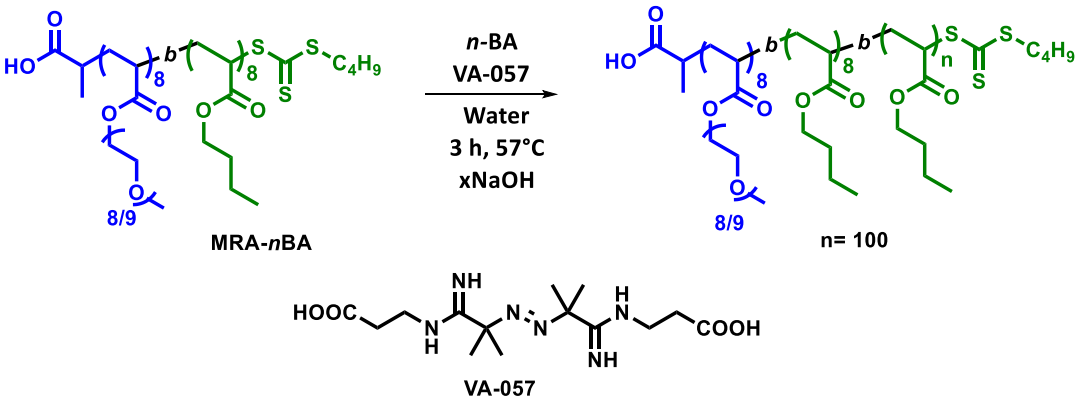

Scheme 2.3. Preparation of P(*n*-BA) nanoparticles at various pH. x = 0, 0.1, 0.25, 0.75, 1 eq relative to MRA-*n*BA using VA-057 as thermal initiator.

Table 2.3. Effect of pH on RAFT emulsion polymerisations of *n*-BA mediated with MRA-*n*BA.

			Number distribution		Intensity distribution				
	[NaOH]/ [MRA-*n*BA]	pH	D_h [a] (nm)	PDi[a]	D_h [a] (nm)	PDi[a]	$M_{n,SEC}$ (g mol^{-1}) [b]	$M_{w,SEC}$ (g mol^{-1}) [b]	$Đ$[b]
1	0	4.67	38	0.07	66	0.12	18200	30800	1.69
2	0.1	4.87	42	0.07	65	0.10	22600	34800	1.54
3	0.25	5.20	32	0.06	50	0.14	20500	34900	1.70
4	0.75	6.38	21	0.05	251	0.58	20000	39200	1.96
5	1.0	7.09	19	0.05	332	0.60	16400	44000	2.68

$M_{n,th}$ for all entries is 17900 g mol^{-1}. [a]Determined by DLS. [b]Determined by $CHCl_3$-SEC (values are obtained by integrating the whole region, including all three peaks), calibrated with PMMA standards. All polymerisations reached >99% monomer conversion, determined by gravimetry.

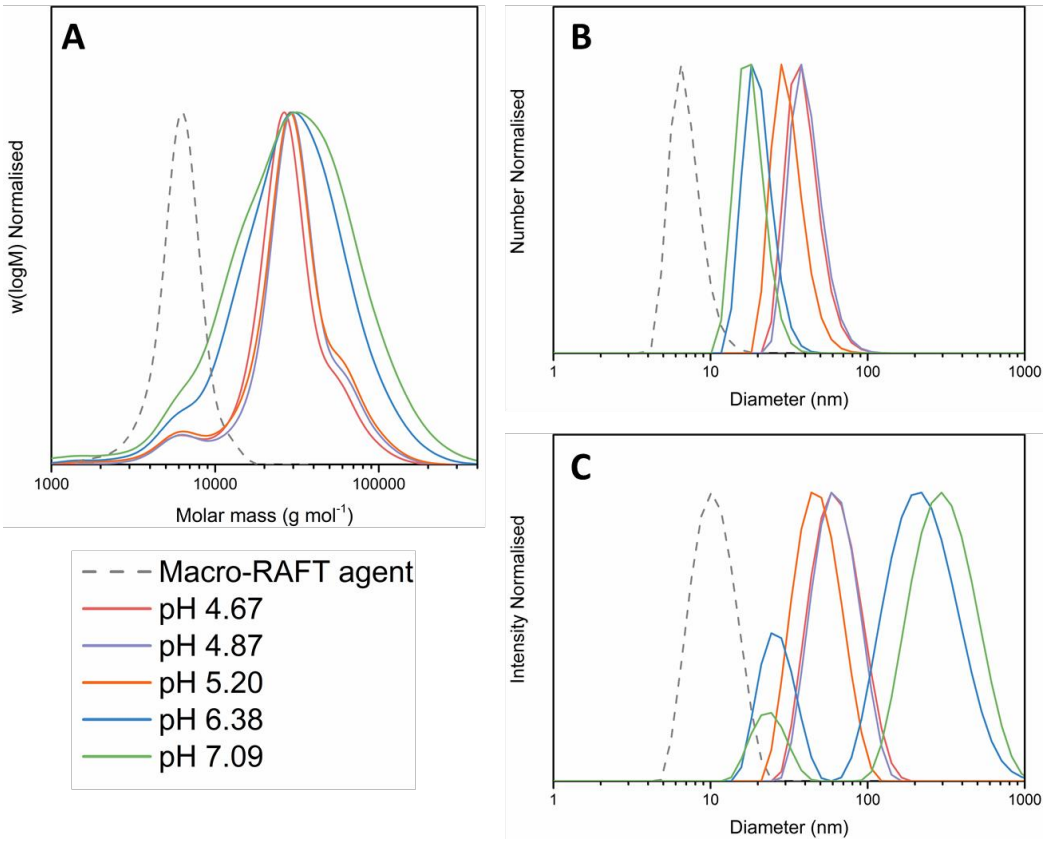

Figure 2.4. Effect of pH (pH = 4.67, 4.87, 5.20, 6.38, 7.09) on RAFT emulsion polymerisations of *n*-BA mediated with MRA-*n*BA using initiator VA-057. (A) THF-SEC chromatograms of dried latexes, and DLS distributions (B) number and (C) intensity of particles diluted 1/1000 in pure water, measured at 25°C.

Polymerisation mixture pH's ranged from 4.67 (native pH/ no NaOH addition), to 7.09 for equimolar NaOH addition relative to **MRA-*n*BA**. SEC analysis of the resulting nanoparticles revealed similar $M_{n,SEC}$ to theoretical values, however, above pH 5.20 ([NaOH]/[Macro-RAFT] > 0.25) broad molar mass distributions were observed ($Đ \geq$ 1.96). Below this value, SEC chromatograms remained comparable to data obtained in Section 2.2.3.1 (Figure 2.4a). Particle diameters reduced from 42 nm to 19 nm (number distribution) with increasing pH, likely due to the increased electrostatic stabilisation from greater charge on the particle surface (Figure 2.4b). Similar to SEC data, DLS traces of RAFT emulsion polymerisations performed above pH 5.20 displayed wide and multimodal particle size distributions by intensity values (Figure 2.4c). A similar study conducted by Lansalot and co-workers revealed a comparable trend for RAFT emulsion polymerisation of styrene at different pH's. They rationalised that the increased ionisation of the surface provided an unsuitably hydrophilic environment for chain extension to occur uniformly.[44] Overall, it is clear that polymerisations performed at acidic pH's yielded uniform particles, with narrower polymer molar mass distributions, compared to those at higher pH's. It is interesting to note that at the native pH, conditions with VA-057 yielded smaller nanoparticles (38 nm) compared to ACVA (75 nm) at the same DP_{target}/ M_n (~ 18,000 g mol^{-1}), however, as they were not conducted at the same temperature, this could be due to either initiator or temperature effects and cannot be compared directly.

2.2.4 Nanoparticle characterisation

Only nanoparticles synthesised with ACVA (section 2.2.3.1) were taken forward for in-depth characterisation, due to the extensive library generated with this system (Table 2.2, Entry 6-15). As the RAFT emulsion polymerisations were performed in aqueous conditions and reached full monomer conversions, any future biological studies could be conducted without removal of cyto-toxic solvents or monomers. Nanoparticle characterisation was therefore conducted without post-synthesis purification.

2.2.4.1 PEG-tannin aggregation assay

To elicit if the P(PEGA) block remained at the particle surface, a PEG selective aggregation assay was employed based on the well-known property of PEG as a tannin binding agent.[45-47]. This operates on a similar basis to lectin-glycopolymer assays where addition of multivalent lectin induces an increase in turbidity/absorbance, caused by accumulation of particles. A selection of nanoparticles (*t*-BA and *n*-BA) were treated with tannic acid and the absorbance was monitored at 500 nm in a UV-VIS spectrometer (Figure 2.5). Interestingly, a rapid increase in absorbance (at 500 nm) was observed when nanoparticles (both P(*t*-BA) and P(*n*-BA)) were treated with tannic acid suggesting high availability of PEG in their surface. These results are consistent with other PEG-tannin systems, however it is believed this is the first time it has been used to study PEGylation of nanoparticles.[48] This technique gives a good understanding of the surface properties, but cannot quantify how many chains are available at the particle corona.

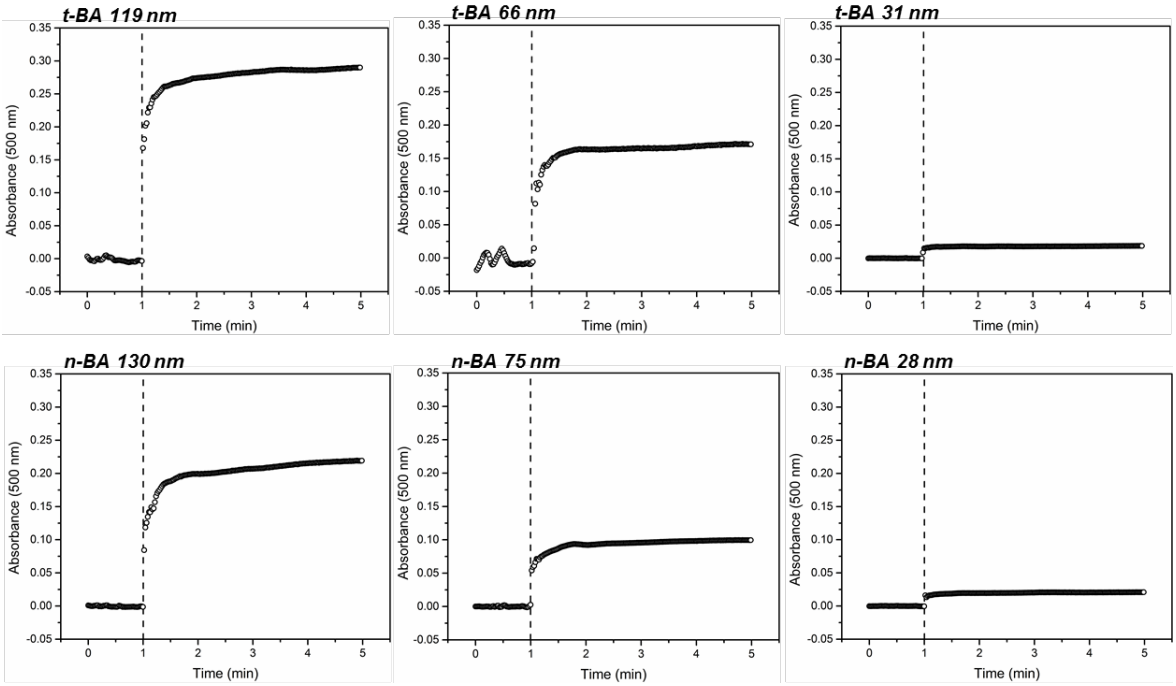

Figure 2.5. Absorbance-time curves of tannic acid-PEG binding assay measured on a UV-VIS spectrometer at 500 nm over 6 minutes with 119, 66 and 31 nm P(*t*-BA) and 130, 75 and 28 nm P(*n*-BA) nanoparticles. Dashed lines indicate time of tannic acid (10 μg mL^{-1}) addition to nanoparticle solutions (10 μg mL^{-1}).

2.2.4.2 Determination of the number of aggregation

Nanoparticle-cell interactions are generally governed by many parameters, such as size, shape and charge. The surface grafting density or the number of aggregation (N_{agg}), has also been shown to heavily influence interactions with biological material.[49-51] Typically for latexes synthesised by RAFT emulsion polymerisation, this is calculated by determining the number of macro-RAFT per unit volume and dividing it by the number of particles (Equation 2.3 and Equation 2.4). The N_{agg} was calculated, revealing an increasing trend with particle diameter for both *n*-BA (600 to 22500) and *t*-BA (800 to 17300) nanoparticles. The observed values displayed a comparable trend to those reported by Hawkett and co-workers and similar N_{agg} values, increasing from 2665 and 15800 for increasing nanoparticle diameter.[20]

$$N_p = \frac{6\tau}{\pi (D_h)^3 d_p}$$

Equation 2.3. Determination of the number of particles per volume. N_p = number of particles per mL τ = solids content (g mL^{-1}), D_h = average hydrodynamic particle diameter, d_p = density of polymeric core.

$$N_{agg} = \frac{[macro - RAFT] \cdot N_A}{N_p}$$

Equation 2.4. Number of macro-RAFT agents per particle (N_{agg}).

These equations however are derived with the assumptions that the nanoparticles are spherical, are entirely comprised of the core polymer and 100% of the macro-RAFT agent is chain extended during the polymerisation, which from our data we know is incorrect (Section 2.2.3). This information however can be experimentally measured using scattering techniques, overcoming some of these assumptions.

Static light scattering (SLS) is a powerful technique to study materials in solution and allows the direct determination of N_{agg}. It relies on the intensity of scattered light at defined angle θ from an irradiated particle with an incident beam of wavelength λ_0. From these values, the wave vector (q) can be determined (Equation 2.5).

$$q = \frac{4\pi n}{\lambda_0} \sin\frac{\theta}{2}$$

Equation 2.5. Determination of wave-vector (q) using the wavelength of the incident (λ_0) and the refractive index of the solvent (n) and the angle of measurement (θ)

The wave vector (q) is inversely proportional to the size of the window of observation, hence by varying θ and λ_0, information can be garnered about different aspects of the measured objects. In the case of light scattering (long wavelength), measurements are therefore at low q where entire particles are observed. However, if further information was required on the structural properties of the surface (polymer chains), measurements would typically be performed at high q with short wavelength irradiation, using small angle X-ray (SAXS) or small angle neutron scattering (SANS) (Figure 2.6).

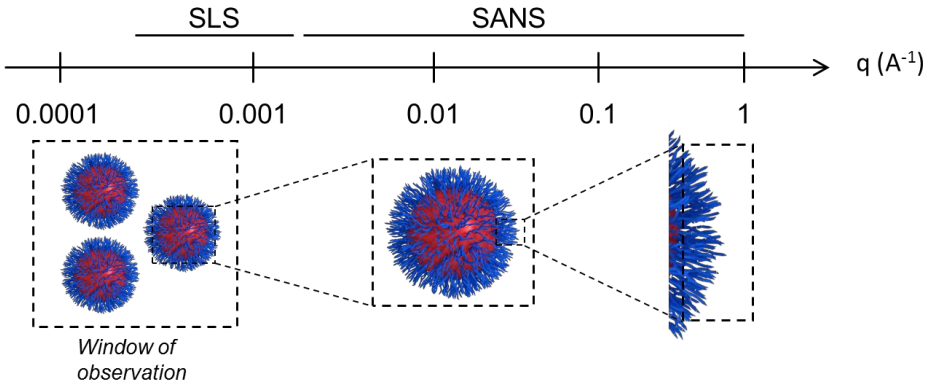

Figure 2.6. Relationship between the wave vector (q) and the domain size of the window of observation.

All ten nanoparticle suspensions were measured at four concentrations each across 8 angles (Figure 2.7) and the Rayleigh ratio (R_θ) was determined (Equation 2.6).

$$R_\theta = \frac{I_{solution}(\theta) - I_{solvent}(\theta)}{I_{toluene}(\theta)} \cdot \left(\frac{n_{solvent}}{n_{toluene}}\right)^2 \cdot R_{toluene}$$

Equation 2.6. Determination of Rayleigh ratio. $I_{solution}$, $I_{solvent}$ and $I_{toluene}$ are the scattering intensities of the solution solvent and reference (toluene) respectively. n is the refractive index ($n_{water} = 1.333$, $n_{toluene} = 1.496$) and $R_{toluene}$ is the Rayleigh ratio of toluene ($R_{toluene} = 1.36 \times 10^{-5}$ cm^{-1} for $\lambda = 633$ nm).

Subsequently the relationship between refractive index and concentration (dn/dC) was determined by measuring multiple nanoparticle concentrations with differential refractometry, and the optical constant (K) was evaluated (Equation 2.7).

$$K = \frac{4\pi^2 n_{solvent}^2}{\lambda^4 N_A} \cdot \left(\frac{dn}{dC}\right)^2$$

Equation 2.7. Determination of the optical constant. N_A is Avogadro's constant and dN/dC is the constant relating to how the refractive index changes with sample concentration, calculated using Equation 2.8.

$$\frac{dN}{dC} = \frac{RI_{water} \times Z}{RI_{constant}}$$

Equation 2.8. Determination of the change in refractive index with concentration (dN/dC). Z = gradient of RI vs concentration, $RI_{constant}$ = 1,194,000.

The apparent molar masses (M_a) per particle, were then determined at multiple concentrations (Equation 2.9) and values extrapolated to infinite dilution, where particle-particle interactions are minimal, simplifying the relationship (Equation 2.10; Figure 2.7).

$$\frac{KC}{R_\theta} = \frac{1}{M_a} \cdot (1 + \frac{q^2 \cdot R_g^2}{3})$$

Equation 2.9. Relationship between the Rayleigh ratio and apparent molar mass (M_a).

$$\frac{KC}{R_\theta} = \frac{1}{M_a}$$

Equation 2.10. Simplified relationship between the Rayleigh ratio and apparent molar mass (M_a).

The N_{agg} was further calculated by dividing this by unimer M_w estimated from SEC chromatograms (Equation 2.11) in Section 2.2.3.

$$N_{agg} = \frac{M_{a,particle}}{M_{w,unimer}}$$

Equation 2.11. Calculation of number of aggregation (N_{agg}). $M_{a,particle}$ = apparent particle molar mass determined by SLS. $M_{w,\,unimer}$ = weight average molar mass of particle unimers approximated with SEC.

Table 2.4. Determination of whole particle molar masses (M_a) and number of unimer aggregates per particle (N_{agg}) for both P(*n*-BA) and P(*t*-BA) nanoparticles.

					Experimental		Theoretical
Nanoparticle core	**DP_{target}**	**D_h [a] (nm)**	***dn/dC*[b]**	**$M_{w,SEC}$ (g mol^{-1})[c]**	**M_a (Mg mol^{-1})[d]**	**N_{agg}[d]**	**N_{agg}[e]**
P(*n*-BA)	200	130	0.105	48600	1060	21800	22500
	150	92	0.147	34000	350	10300	10100
	100	75	0.107	24400	157	6600	7400
	75	50	0.149	18500	21	1200	2700
	50	28	0.107	13300	6.9	520	600
P(*t*-BA)	200	119	0.088	47000	777	16500	17300
	150	86	0.08	34900	283	8100	8300
	100	66	0.082	24400	127	5200	5100
	75	49	0.106	17600	37	2100	2700
	50	31	0.77	12600	13	1000	800

[a]Determined by DLS. [b]Determined using differential refractometry and Equation 2.8 [c]Determined using SEC against PMMA standard. [d]Determined by SLS. [e]Determined using Equation 2.11.

Surprisingly, for both sets of nanoparticles, the experimental N_{agg} showed excellent agreement with theoretical values calculated above. Consistent findings were observed where N_{agg} increased with particle size, ranging from $N_{agg} < 1000$ for the smallest nanoparticles, up to > 15,000 for the largest (Table 2.4). This finding suggests that there must be some rearrangement in macro-RAFT agents, and therefore does not maintain the same N_{agg} during the polymerisation process. This trend also can be rationalised as larger nanoparticles have a larger surface area, hence require greater stabilisation than smaller nanoparticles.

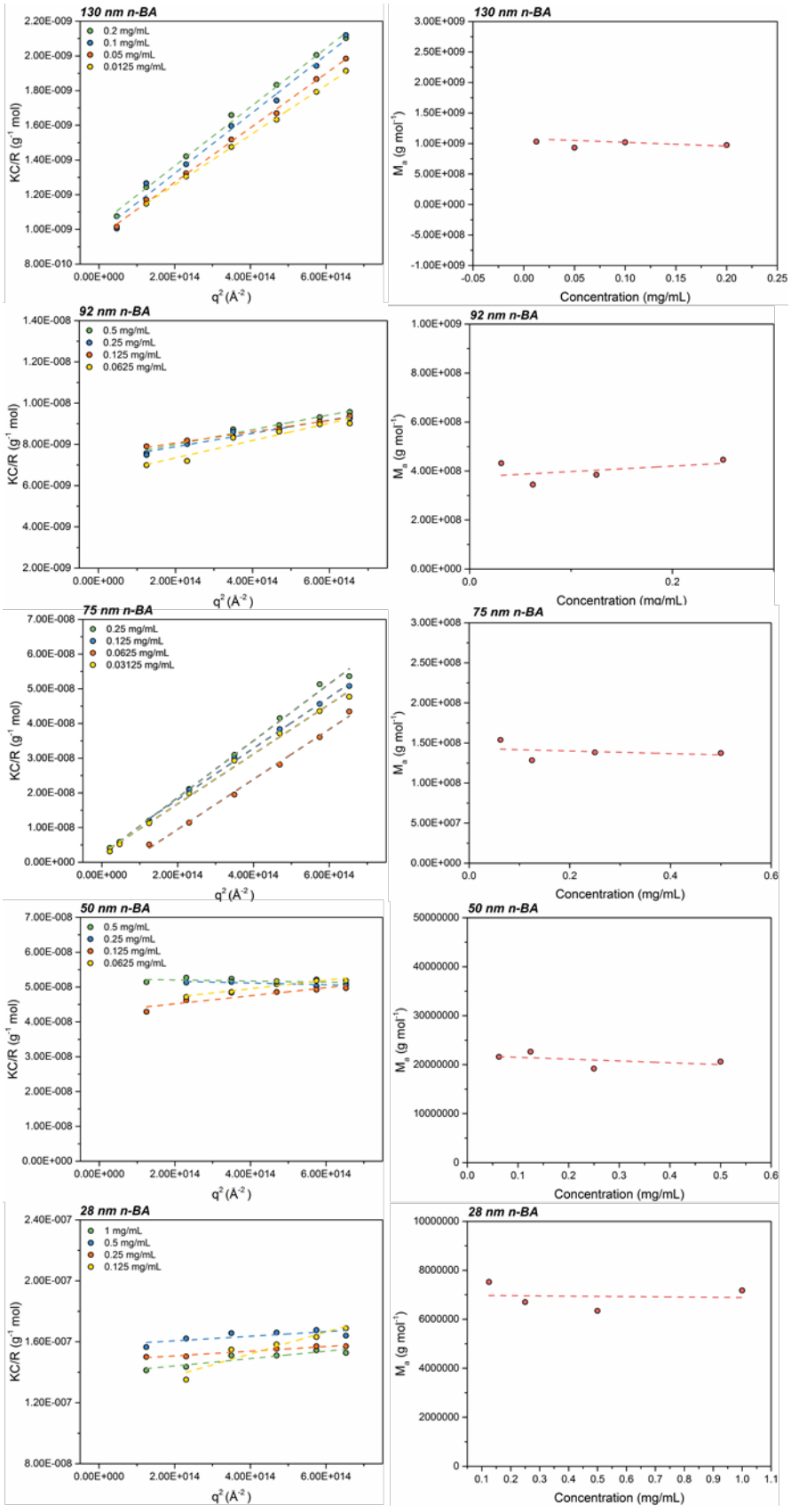
130 nm n-BA
0.2 mg/mL
0.1 mg/mL
0.05 mg/mL
0.0125 mg/mL
KC/R (g⁻¹ mol)
q² (Å⁻²)
130 nm n-BA
Mₐ (g mol⁻¹)
Concentration (mg/mL)
92 nm n-BA
0.5 mg/mL
0.25 mg/mL
0.125 mg/mL
0.0625 mg/mL
KC/R (g⁻¹ mol)
q² (Å⁻²)
92 nm n-BA
Mₐ (g mol⁻¹)
Concentration (mg/mL)
75 nm n-BA
0.25 mg/mL
0.125 mg/mL
0.0625 mg/mL
0.03125 mg/mL
KC/R (g⁻¹ mol)
q² (Å⁻²)
75 nm n-BA
Mₐ (g mol⁻¹)
Concentration (mg/mL)
50 nm n-BA
0.5 mg/mL
0.25 mg/mL
0.125 mg/mL
0.0625 mg/mL
KC/R (g⁻¹ mol)
q² (Å⁻²)
50 nm n-BA
Mₐ (g mol⁻¹)
Concentration (mg/mL)
28 nm n-BA
1 mg/mL
0.5 mg/mL
0.25 mg/mL
0.125 mg/mL
KC/R (g⁻¹ mol)
q² (Å⁻²)
28 nm n-BA
Mₐ (g mol⁻¹)
Concentration (mg/mL)

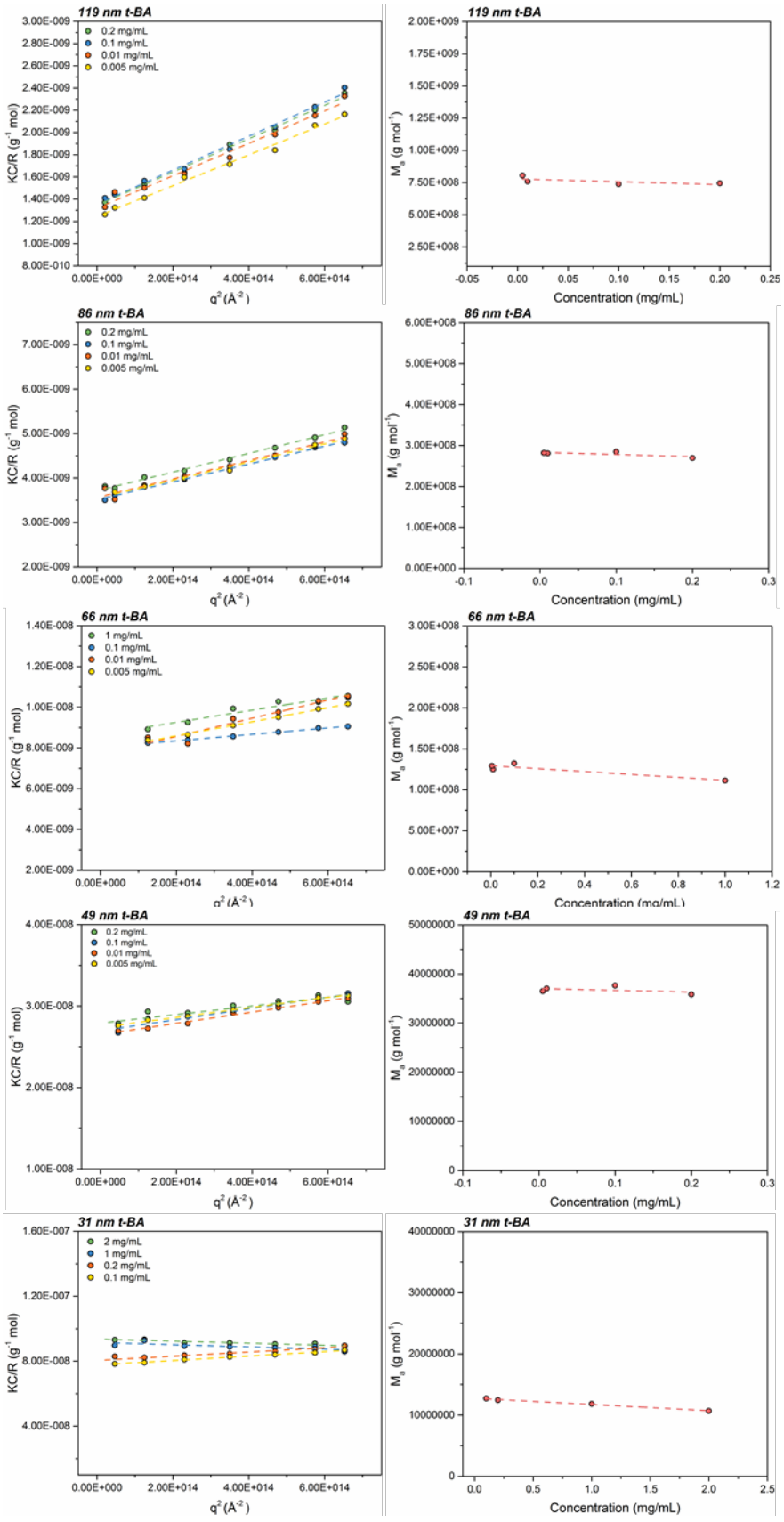

Figure 2.7. KC/Rθ vs q^2 and concentration vs apparent molar mass (M_a) plots for P(*n*-BA) and P(*t*-BA) nanoparticles across 4 concentrations, measured using static light scattering.

2.2.4.3 Cryogenic transmission electron microscopy

From the previous characterisation methods, the particle size, zetapotential and N_{agg} have been determined. To confirm the shape, nanoparticles were imaged with cryogenic transmission electron microscopy (Cryo-TEM). Electron micrographs revealed spherical nanoparticles with sizes that correlated well with diameters determined by DLS, and the absence of any aggregate formation. Although the images showed relatively uniform nanoparticle distributions, any discrepancy between particle sizes could be due to the thickness of the formed ice layer, where particles towards the bottom may appear smaller in relation to those at the top.

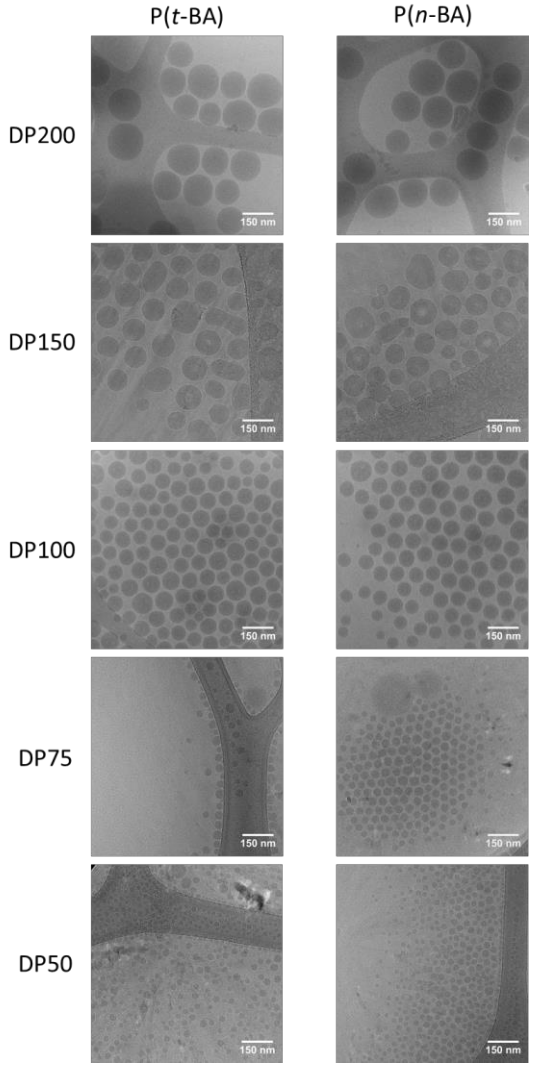

Figure 2.8. Cryo-TEM images of undiluted P(*t*-BA) (left column) and P(*n*-BA) (right column) nanoparticles deposited on lacey carbon coated grids.

2.2.5 Toxicity studies

Having extensively characterised the synthesised nanoparticles, their biocompatibility was evaluated *in vitro* and *in vivo*.

2.2.5.1 *In vitro* cell viability

All ten nanoparticles, without prior purification, were exposed to colorectal carcinoma (Caco-2) cells for 72 h across six concentrations (2 mg mL^{-1} – 100 ng mL^{-1}), and the *in vitro* cell viability measured using the SRB assay. None of the nanoparticles inhibited cell growth up to 0.5 mg mL^{-1}. Nonetheless, the 75 nm P(*n*-BA), and all P(*t*-BA) nanoparticles with D_h > 31 nm showed reduction in cell proliferation at 2 mg mL^{-1} (Figure 2.9), but this concentration is far greater than any envisaged clinical dosage for these, or other similar systems.

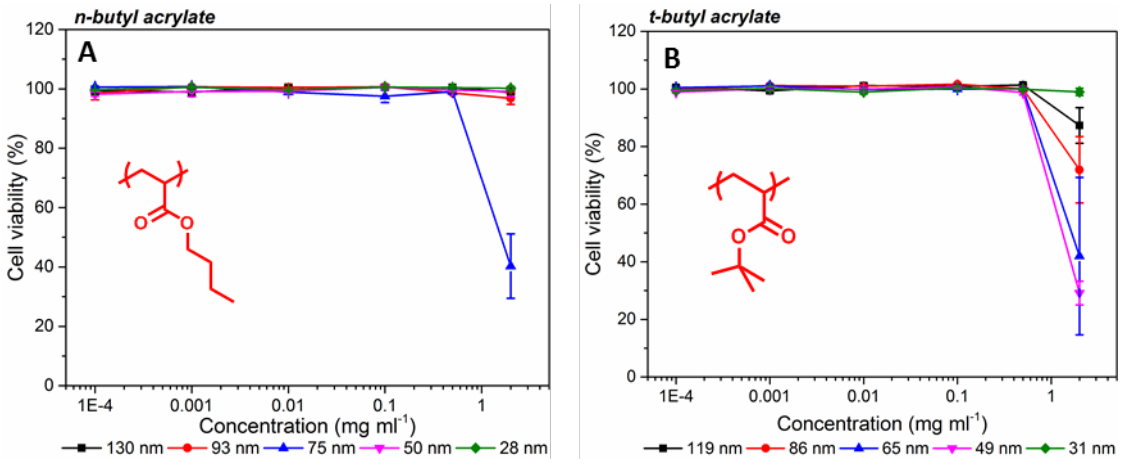

Figure 2.9. Antiproliferative activity of P(*n*-BA) (28 – 130 nm) and P(*t*-BA) (31 – 119 nm) on Caco-2 cells (seeded 10,000 per well) over 72 h at 2, 0.5, 0.2, 0.01, 0.001 and 0.0001 mg mL^{-1} monitored as a function of cell biomass with the sulforhodamine B assay. Data are expressed as the arithmetic mean ± standard deviation of two independent experiments performed in triplicate (*N*=6).

2.2.5.2 *In vivo* toxicity

Satisfied that the synthesised particles were non-toxic *in vitro*, the 49 and 86 nm *t*-BA, and the 50 and 93 nm *n*-BA nanoparticles were chosen for the *in vivo* toxicity studies as these were the most comparable between the two core varieties. To assess the *in vivo* toxicity, two experiments were performed by Dr Robert Dallmann, Kristin Abraham and Helena Xandri-Monje at the Warwick Medical School, University of Warwick, UK. Firstly, an acute toxicity study, where mice were treated with one intraperitoneal (i.p.) dose of nanoparticles at two concentrations (1.2 mg kg^{-1} and 12 mg kg^{-1}), and secondly,

sub-acute toxicity, whereby mice were treated with multiple doses, once per day, however only at the higher concentration. In both experiments, body weight and well-being parameters such as fur, appetite and activity were monitored for a period of 7 days after i.p. administration. Control experiments (mice administered with PBS and not injected) were performed in parallel (Figure 2.10).

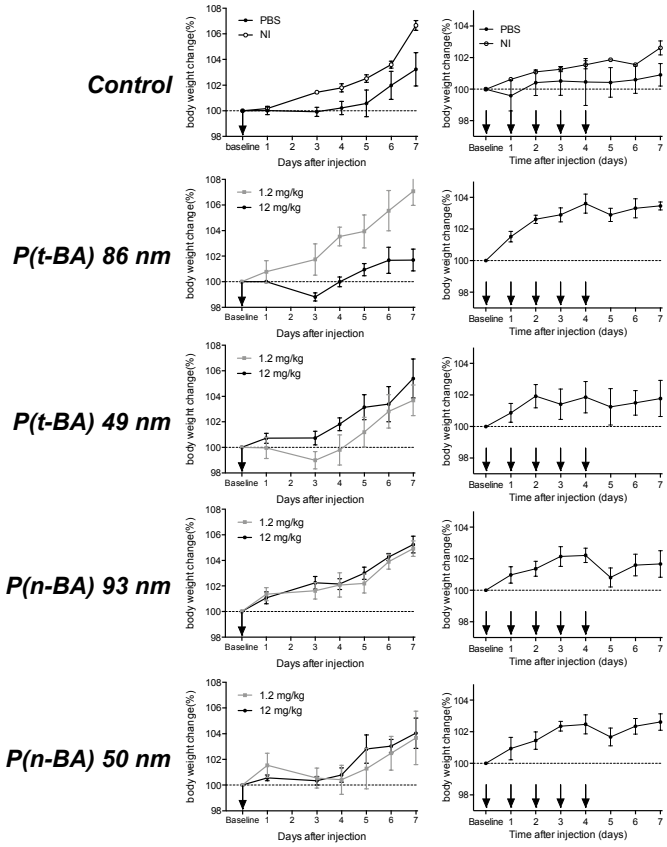

Figure 2.10. Acute (left column) and 7 day repeated (right column) toxicity in mice for the 50 and 93 nm *n*-BA, and 49 and 86 nm *t*-BA nanoparticles at both 1.2 mg kg^{-1} (grey lines) and 12 mg kg^{-1} (black lines), measured as a function of animal body weight monitored over 7 days ($N = 3$ for acute toxicity, $N = 6$ for 7 day repeated dosing). Controls of PBS injection ($N = 3$ for both acute toxicity and 7 day dosing) and noninjected ($N = 2$ for both acute toxicity and 7 day dosing) mice are also displayed. Data is reported as mean ± SEM. Arrows indicate administration points.

Encouragingly, in both acute and sub-acute experiments, minimal toxicity effects were observed for all nanoparticles tested. All mice administered with nanoparticle suspensions had similar weight changes to control treatments or, in some cases higher body weight. Importantly, none of the mice showed any reduction in body weight over the seven day period, nor any loss of fur, appetite or reduction in activity even for very high doses (12 mg kg^{-1}). This observed biocompatibility *in vitro* and *in vivo* is likely due to the dense P(PEGA) shell on all of the nanoparticles, known to reduce immune response through low adsorption of serum proteins.[52] This is in accordance with a report from

Tamanoi and co-workers, showing limited toxicity for intraperitoneally administered mesoporous silica nanoparticles through full serological, haematological and histopathological investigations.[53]

2.2.6 Preliminary biodistribution studies

NIR fluorescence is a highly sensitive and non-invasive method to study pharmacokinetics, biodistribution and organ accumulation.[54] Having established a low toxicity profile *in vivo* and *in vitro*, NIR probe, Cyanine 7.5 amine (Cy7.5), was therefore encapsulated into intermediate sized 50 nm P(*n*-BA) nanoparticles following an adapted procedure from Resch-Genger and co-workers.[55] This approach works by swelling the particles with *ca.* 10% organic solvent, in the presence of the hydrophobic dye, partitioning it into the core of the nanoparticles. The particles were purified by extensive dialysis, and analysed with fluorescence spectroscopy (Figure 2.11)

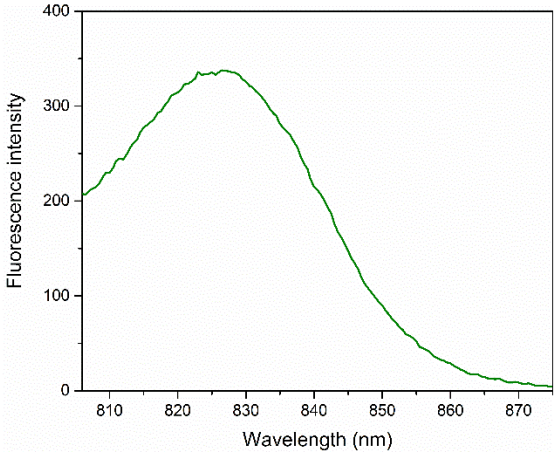

Figure 2.11. Fluorescence emission spectrum of Cy7.5 loaded 50 nm P(*n*-BA) nanoparticles diluted 1/100 in pure water excited at 780 nm and emission profiles monitored from 785 to 900 nm.

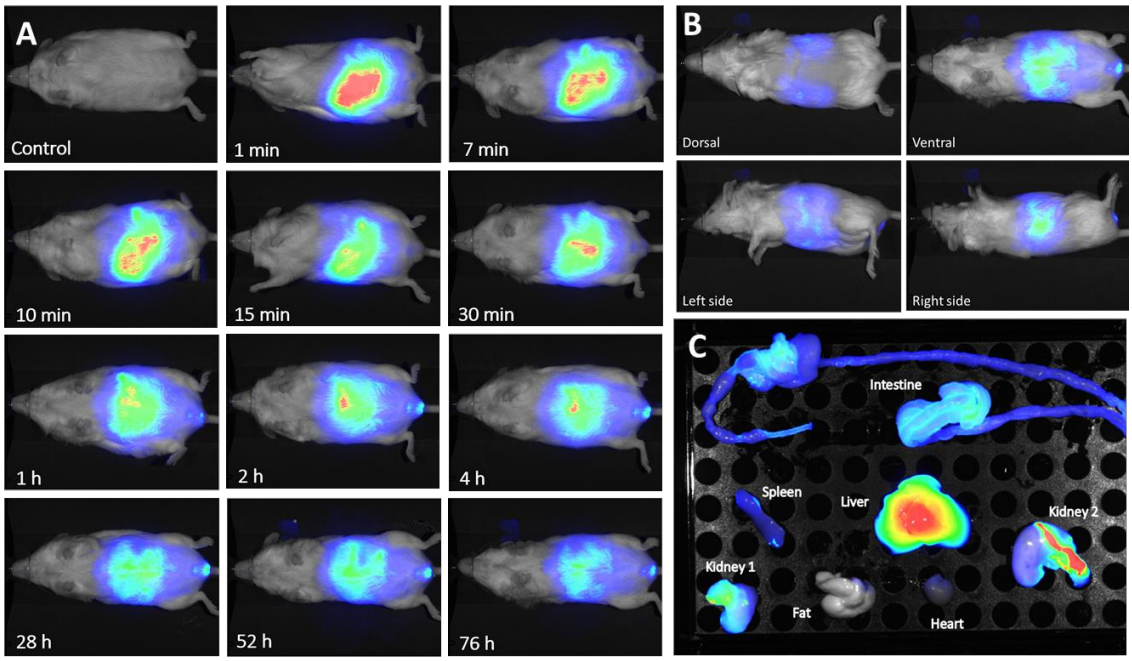

Figure 2.12. Biodistribution studies after a single i.p. injection of Cy7.5 loaded 50 nm P(*n*-BA) nanoparticles (1.2 mg kg^{-1}) in mice. Distribution was monitored using the 800 nm fluorescence channel with a LICOR Pearl® Trilogy. (A) Pharmacokinetic study over 76 h (B) 360° view of 76 h time point (C) *Ex vivo* images of organs samples 76 h after injection.

A dilute suspension of NIR-particles (1.2 mg kg^{-1}) was administered to male mice *via* i.p. injection, and the nanoparticle distribution was followed periodically over 76 h using a LICOR NIR *in vivo* imager. Prior to injection, no fluorescence signal was observed from any part of the animal (control). A bright signal from the abdominal cavity was immediately detected after administration, which decreased rapidly during the first 2 h of exposure, likely due to adsorption into systemic circulation (Figure 2.12a and Figure 2.13). This was followed by slow clearance, over the next 74 h (Figure 2.12a and Figure 2.13), with 36% of the injected dose being retained at the end of the experiment. *Ex vivo* imaging of the excised organs (76 h) revealed high nanoparticle accumulation in the liver, with significant quantities also found in the intestine and spleen, and only small amounts in the heart or fat of the animal (Figure 2.12 and Figure 2.14). Some of the intestinal signal may be attributed to NIR chlorophyll fluorescence.[56] This was examined by imaging the faeces of non-injected mice, which showed a small but detectable fluorescence in the 800 nm region (Figure A2.1). However, it is unlikely that a large proportion of the fluorescence detected from the intestine is only due to diet, as no signal is observable around the anus area of untreated mice. Furthermore, anal fluorescence starts to be detected in treated mice 1 h post injection. This suggests that the majority of the NIR emission is indeed associated with the nanoparticles. Interestingly, a large

fluorescence signal was also observed in both kidneys. However, this accumulation appears outside the cortex region, most probably being trapped in surrounding connective tissue. Therefore, the particles are likely being excreted via the gastrointestinal/ hepatobiliary system. This excretion route is well known for nanoparticles, as their size is above the renal filtration limit (4.5 -5 nm)[57], and will typically accumulate in the liver, spleen and intestine.[58]

There are relatively few reports on the biodistribution and pharmacokinetics of intraperitoneally administered polymeric nanoparticles.[59, 60] Nonetheless, this system can still be compared to similar studies using non-polymeric nanomaterials. For example, in contrast to 100 nm mesoporous silica nanoparticles (MSN), this system shows far quicker clearance from the peritoneal cavity, (64% after 76 h compared to 0-5% after 160 h), but greater accumulation in the abdominal organs (liver, spleen, intestine).[53] Meanwhile, a similar study on gold nanoparticles revealed almost complete clearance within 24 h, with similar accumulation in the liver and spleen.[61] Overall, these results indicate that P(*n*-BA) nanoparticles may prove effective against liver and intestinal cancers as they are deposited and retained in these organs. Importantly, the observed intestinal accumulation (probably due to hepatobiliary clearance) may enhance their drug delivery potential, (compared to other systems which are mainly retained in the peritoneal cavity) as it is possible for secondary re-adsorption to occur.[58]

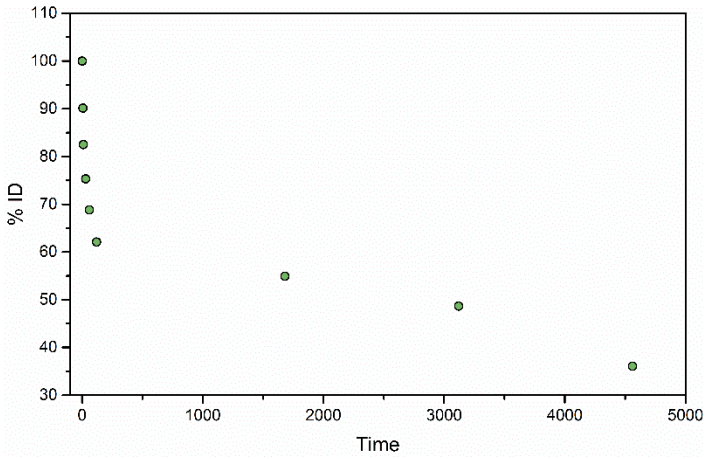

Figure 2.13. Total fluorescence, measured with the 800 nm channel of a LICOR Pearl®trilogy observed from entire mouse over 76 h after a single intraperitoneal injection (1.2 mg kg^{-1}) of Cy7.5 loaded 50 nm P(*n*-BA) nanoparticles.

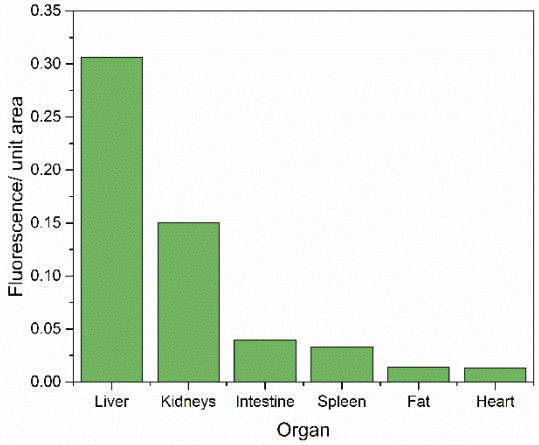

Figure 2.14. Total fluorescence per unit area of excised organs, measured with the 800 nm channel of a LICOR Pearl®trilogy, 76 h after a single intraperitoneal injection (1.2 mg kg^{-1}) of Cy7.5 loaded 50 nm P(*n*-BA) nanoparticles.

2.3 Conclusion

By generating a library of P(PEGA) shell and P(*n*-BA) and P(*t*-BA) core nanoparticles, we have shown that RAFT emulsion polymerisation is a highly versatile method to synthesise biocompatible nanomaterials. Furthermore, this approach is particularly interesting for its industrial scale up potential as reactions are performed in environmentally friendly aqueous environments, and reach full consumption of cytotoxic monomer within a matter of hours. These advantages allow use of the nanoparticles for biological purposes without prior purification. The particles displayed no toxicity in *in vitro* and *in vivo* experiments, and relatively long retention in mice post administration with high accumulation in the liver. Overall, this synthetic approach has the potential to influence future nanoparticle design aimed at biomedical applications.

2.4 Experimental

2.4.1 Materials

Poly(ethylene glycol) methyl ether acrylate (PEGA, average M_n = 480 g mol^{-1}), *n*-butyl acrylate (*n*-BA, >99%) and *t*-butyl acrylate (*t*-BA 98%), bromo-propionic acid (>99%), 1-butanethiol (99%), carbon disulphide (>99%) and tannic acid (ACS reagent) were obtained from Sigma-Aldrich. All monomers above were passed through basic aluminium oxide to remove inhibitor before use. Dimethyl sulfoxide-d_6 (99.9% D atom), chloroform-d_3 (99.8% D atom), were obtained from Sigma Aldrich and used for ^{1}H NMR spectroscopy. Thermal initiators 4,4′-azobis(4-cyanovaleric acid) (ACVA, >98%, Aldrich), 2,2'-Azobis[2-(2-imidazolin-2-yl)propane]dihydrochloride (VA-044) and 2,2'-Azobis[*N*-(2-carboxyethyl)-2-methylpropionamidine]tetrahydrate (VA-057) (Wako) were used as received. Cyanine 7.5 amine was purchased from Lumiprobe. TEM grids were purchased from EM Resolutions Ltd (Sheffield, UK). RAFT agent, 2-(((butylthio)carbonothioyl)thio)propanoic acid (PABTC) was synthesised as previously described.[20] Materials for cell culture were purchased from Greiner Bio-one (Germany), and culture medium prepared in-house.

2.4.2 Instrumentation and Analysis

2.4.2.1 NMR spectroscopy

^{1}H and ^{13}C NMR spectra were recorded on a Bruker DPX-250, DPX-300, DPX-400 or DPX-500 spectrometer using deuterated solvent (materials section). The residual protonated solvent was used as an internal reference

2.4.2.2 Size exclusion chromatography

SEC was performed using an Agilent 390-LC MDS instrument equipped with differential refractive index (DRI), viscometry (VS), dual angle light scatter (LS) and two wavelength UV detectors. The system was equipped with 2 x PLgel Mixed C columns (300 x 7.5 mm) and a PLgel 5 μm guard column. The eluent was $CHCl_3$ with 2% TEA (triethylamine) additive. Samples were run at 1 mL min^{-1} at 30°C. Poly(methyl methacrylate), and polystyrene standards (Agilent EasyVials) were used for calibration. Ethanol was added as a flow rate marker. Analyte samples were filtered through a GVHP membrane with

0.22 μm pore size before injection. Respectively, experimental molar mass ($Mn_{,SEC}$) and dispersity ($Đ$) values of synthesized polymers were determined by conventional calibration using Agilent GPC/SEC software.

2.4.2.3 Theoretical molar mass calculation

$$M_{n,th} = \frac{[M]_0 \, pM_M}{[CTA]_0} + M_{CTA}$$

Equation 2.12. Calculation of theoretical number average molar mass ($M_{n,th}$) where $[M]_0$ and $[CTA]_0$ are the initial concentrations (in mol dm-3) of monomer and chain transfer agent respectively. p is the monomer conversion as determined by ^{1}H NMR spectroscopy. M_M and M_{CTA} are the molar masses (g mol^{-1}) of the monomer and chain transfer agent respectively.

2.4.2.4 Dynamic light scattering, size and zeta-potential

Size and ζ-potential measurements were carried out using a Malvern Zetasizer Nano-ZS at 25°C with a 4 mW He-Ne 633 nm laser at a scattering angle of 173° (back scattering). Measurements were taken assuming the refractive index of: polyethylene glycol for macro-RAFT agents, and the refractive index of the core material (e.g. *n*-butyl acrylate, *t*-butyl acrylate) for latex particles. DLS samples of latex particles were prepared by diluting by 1000 with 1 mL of water and measured unfiltered in 1.5 mL polystyrene cuvettes for measuring size and a Malvern DTS-1070 zeta cuvette for ζ-potential. Diblock copolymer macro-RAFT agent samples were measured at the concentration of a typical RAFT emulsion polymerisation (15 mg mL^{-1}). Samples were incubated for 60 seconds at 25°C prior to measurement. Measurements were repeated three times with automatic attenuation selection and measurement position. Results were analysed using Malvern DTS 6.20 software. PDi values were calculated using the following equation. Measurements of ζ-potential were modelled with the Smoluchowski theory.

$$PDi = \frac{\sigma^2}{d_h^2}$$

Equation 2.13. Calculation of nanoparticle polydispersity (PDi) from standard deviation (σ), and diameter (d).

2.4.2.5 Static light scattering

Static light scattering measurements were conducted using an ALV-CGS3 system (ALV-Langen) operating with a vertically polarized laser with wavelength λ = 632.8 nm and conducted on the non-fluorescent nanoparticle derivatives. The measurements were performed at 20°C over a range of angles (20, 30, 50, 70, 90, 110, 130 and 150 degrees) with water as the solvent. Samples were measured unfiltered. The intercepts for each concentration of plots for q vs KC/R were then plotted against concentration, and the intercept of the latter graph was taken as the apparent molar mass.

2.4.2.6 Different Refractometry

Measurements were performed with an RI-101 from Shodex (λ_0=632 nm). The refractive index increment was measured in water using 5 concentrations of nanoparticles and the dn/dC was calculated using Equation 2.8.

2.4.2.7 Cryogenic-transmission electron microscopy

8 μL of the sample was applied to a glow-discharged lacey carbon grid (EM Resolutions), blotted for 4 seconds and frozen in liquid propane/ethane (30% 70% v/v) using a custom-made plunge-freezing device. Grids were imaged in the JEOL 2200FS with a Gatan K2 camera and a Gatan 914 cryo-holder cooled to -180 ˚C.

2.4.2.8 Fluorescence spectroscopy

Fluorescence emission spectra were measured using an Agilent Cary Eclipse fluorescence spectrometer. Studies were performed by exciting at the absorption maxima of Cy7.5 (800 nm) and measured from 805 nm to 875 nm. The photomultiplier voltage was set such that the maxima was below 1000 arbitrary units. Samples were diluted 1:100 fold in pure water for measurement.

2.4.3 Synthetic Procedures

2.4.3.1 Synthesis of (propanoic acid)yl butyl trithiocarbonate (PABTC)[20]

A 50% w/w sodium hydroxide solution (9.68 g NaOH, 0.242 mol, 1.1 eq) in water was added to a mixture of butanethiol (20 g, 0.22 mol, 1 eq) dissolved in acetone (11 mL). Water (40 mL) was added and the solution was stirred for 30 min at room temperature. Carbon disulphide (17.32 g, 0.228 mol, 1.025 eq) was added and the orange solution was stirred for 30 minutes at room temperature, then cooled in ice below 10°C. 2-Bromopropionic acid (34.9 g, 0.228 mol, 1.025 eq) was added slowly, monitoring the temperature, and subsequently a further 19.36 g of 50% w/w sodium hydroxide solution was added. The reaction mixture was left to stir for 18 h at ambient temperature. 200 mL of water was added to the reaction mixture, cooled in ice, and a 10 M solution of HCl was added dropwise until the pH reached between 2-3. The resulting precipitate was filtered, washed with water, and recrystallised in hot hexane to afford 36.53 g of 2-(((butylthio)carbonothioyl)thio)propanoic acid. Yield = 70%. ^{1}H NMR (400 MHz, $CDCl_3$) δ_H 6.06 (br, 1H, CO_2**H**), 4.86 (q, *J* = 7.4 Hz, 1H, SC**H**), 3.37 (t, *J* = 7.4 Hz, 2H, C**H**$_2$S), 1.69 (quint, *J* = 7.5 Hz, 2H, C**H**$_2$CH$_2$S), 1.63 (d, *J* = 7.4 Hz, 3H, SCHC**H**$_3$), 1.43 (sext, *J* = 7.5 Hz, 2H, CH$_3$C**H**$_2$CH$_2$), 0.94 (t, *J* = 7.3 Hz, 3H, C**H**$_3$CH$_2$). ^{13}C NMR (100 MHz, 298 K $CDCl_3$) δ_c 175.4 (**C**OOH), 47.2 (S**C**H), 37.1(**C**H$_2$S), 29.88 (**C**H$_2$CH$_2$S), 22.1(CH$_3$**C**H$_2$CH$_2$), 16.4 (**C**H$_3$CH), 13.6 (**C**H$_3$CH$_2$CH$_2$). FTIR (cm^{-1}): 3093, 2958, 2929, 2871, 2362, 2340, 1454, 1412, 1285, 1230, 1200, 1089, 1059, 912, 861. MS (ESI) m/z 237.0 [M-H], 238 [M-]

2.4.3.2 P(PEGA)$_8$ (MRA-PEGA) synthesis

PABTC (0.31 g, 1.30 x 10^{-3} mol), PEGA (5 g, 10.4 x 10^{-3} mol) and ACVA (from a pre-made stock solution in 1,4-dioxane) (18 mg, 6.51 x 10^{-5} mol) were dissolved in 4.9 mL 1,4-dioxane in a 25 mL round bottom flask equipped with a magnetic stirrer bar. The solution was fitted with an appropriately sized rubber septum, and purged with nitrogen for 20 minutes. The round bottom flask was subsequently immersed in an oil bath preheated to 70°C and stirred for 3 h. The reaction vessel was cooled to ambient temperature and opened to oxygen to quench further polymerisation. The polymer was purified by precipitation into a mixture of 20% hexane and 80% diethyl ether (v/v), collected, and the precipitation repeated once more. Finally, the precipitated polymer was

dissolved in DCM, transferred to a 20 mL vial, the DCM evaporated and dried in a vacuum oven overnight at 40°C to yield $P(PEGA)_8$ as a yellow viscous liquid (4.5 g).

2.4.3.3 Macro-RAFT agent synthesis

Both **MRA-*n*BA** and **MRA-*t*BA** macro-RAFT agents were synthesized with the following general procedure, as an example $P(PEGA)_8$-P(*n*-BA)$_8$ (**MRA-nBA**) is described. *n*-Butyl acrylate (0.25 g, 1.95 x 10^{-3} mol) and 0.68 mL of a 5 mg ml^{-1} ACVA stock solution in 1,4-dioxane (3.4 mg, 1.21 x 10^{-5} mol) were added to **MRA-PEGA** (0.94 g, 2.43 x 10^{-4}). The polymerisation mixture was purged with nitrogen for 20 minutes and heated to 70°C for 3 h. The resulting polymer solution was cooled to room temperature and subsequently purified by precipitation in hexane. The yellow viscous liquid was re-dissolved in dichloromethane and the precipitation was repeated once more. Finally, the solvent was evaporated under reduced pressure to yield the di-block macro-RAFT agent as a yellow viscous liquid (0.95 g). ^{1}H NMR spectra and SEC chromatograms can be found above (Figure 2.2 and Figure 2.1) respectively.

Table 2.5. Summary of polymerisation conditions for Macro-RAFT agents. All reactions were performed at [M] = 1M, T = 3 h at 70°C using ACVA as thermal initiator and 1,4-dioxane as the solvent.

	Monomer	RAFT agent	$[M]_0/[RAFT]_0$	$[CTA]_0/[I]_0$	Conversion (%)
MRA-PEGA	PEGA	PABTC	9	20	91
MRA-*n*BA	*n*-BA	**MRA-PEGA**	8	20	96
MRA-*t*BA	*t*-BA	**MRA-PEGA**	8	20	94

2.4.3.4 RAFT emulsion polymerisation procedure

Nanoparticles of different sizes and core compositions were prepared by altering various conditions, full details can be found in Table 2.6. As an example, P[$(PEGA)_8$-*b*-(*t*-$BA)_8$-*b*-(*t*-$BA)_{200}$] was prepared as follows. 1.43 mL of a 10 mg mL^{-1} sodium hydroxide stock solution (14.3 mg, 3.6 x 10^{-4} mol) was added to a suspension of ACVA (50 mg, 1.8 x 10^{-4} mol) in water (8.57 mL) and stirred for 30 min to ensure full solubility. P[$(PEGA)_8$-*b*-(*t*-$BA)_8$] (**MRA-*t*BA)** (0.145 g, 2.85 x 10^{-5} mol) was dissolved in 7.71 mL of water, in a 25 mL round bottomed flask and equipped with a magnetic stirrer. 1.45 mL of the above ACVA stock solution was added, the vial fitted with a rubber septum, and the solution was deoxygenated with dinitrogen gas for 20 minutes. Deoxygenated *t*-BA (0.83 mL, 2.14 x10^{-3} mol) was added *via* syringe and the polymerisation mixture was immersed in

a 70°C oil bath and stirred for 3 h at 400 RPM. Monomer conversion was determined *via* gravimetric techniques.

Table 2.6. Synthetic conditions used to generate P[(PEGA)$_8$-*b*-(*n*-BA)$_8$-*b*-(*n*-BA)$_n$] and P[(PEGA)$_8$-*b*-(*t*-BA)$_8$-*b*-(*t*-BA)$_n$] nanoparticles (where n = 200, 150, 100, 75 and 50) using RAFT emulsion polymerisation.

Product	Macro-RAFT agent	Monomer	$[M]_0$/ $[CTA]_0$	$[CTA]_0$/ $[I]_0$	[M] (mol L^{-1})
P[(PEGA)$_8$-*b*-(*n*-BA)$_8$-(*n*-BA)$_{200}$]	**MRA-*n*BA**	*n*-BA	200	1.1	0.57
P[(PEGA)$_8$-*b*-(*n*-BA)$_8$-(*n*-BA)$_{150}$]	**MRA-*n*BA**	*n*-BA	150	1.1	0.428
P[(PEGA)$_8$-*b*-(*n*-BA)$_8$-(*n*-BA)$_{100}$]	**MRA-*n*BA**	*n*-BA	100	1.1	0.285
P[(PEGA)$_8$-*b*-(*n*-BA)$_8$-(*n*-BA)$_{75}$]	**MRA-*n*BA**	*n*-BA	75	1.1	0.214
P[(PEGA)$_8$-*b*-(*n*-BA)$_8$-(*n*-BA)$_{50}$]	**MRA-*n*BA**	*n*-BA	50	1.1	0.143
P[(PEGA)$_8$-*b*-(*t*-BA)$_8$-(*n*-BA)$_{200}$]	**MRA-*t*BA**	*t*-BA	200	1.1	0.57
P[(PEGA)$_8$-*b*-(*t*-BA)$_8$-(*n*-BA)$_{150}$]	**MRA-*t*BA**	*t*-BA	150	1.1	0.428
P[(PEGA)$_8$-*b*-(*t*-BA)$_8$-(*n*-BA)$_{100}$]	**MRA-*t*BA**	*t*-BA	100	1.1	0.285
P[(PEGA)$_8$-*b*-(*t*-BA)$_8$-(*n*-BA)$_{75}$]	**MRA-*t*BA**	*t*-BA	75	1.1	0.214
P[(PEGA)$_8$-*b*-(*t*-BA)$_8$-(*n*-BA)$_{50}$]	**MRA-*t*BA**	*t*-BA	950	1.1	0.143

All polymerisations were performed in aqueous conditions, with $[\text{macro-RAFT}]_0$ = 2.85 mM and reached full (>99%) monomer conversion.

2.4.3.5 PEG binding assay

Tannic acid was diluted to a concentration of 10 μg mL^{-1} in deionised water. Nanoparticle suspensions were diluted with deionised water to a concentration of 10 μg mL^{-1}. 1 mL of the nanoparticle suspensions were transferred to a polystyrene cuvette and placed in the UV-VIS spectrometer. Absorbance measurements were recorded once every 1 s. After 1 min, 250 μL of the tannic acid solution was added via micropipette and mixed briefly without allowing the pipette tip into the detection window. The absorption was monitored for a further 4 minutes.

2.4.3.6 Encapsulation of Cyanine 7.5

Cy7.5 (1 mg) was added to 1 mL of 10% DMF in THF and sonicated until the powder had fully dissolved. 100 μL of the Cy7.5 solution was added to 900 μL of nanoparticle suspension and shaken for 1 h. The suspension was then dialysed (3500-5000 Da MWCO) against pure water for 48 h to remove residual DMF and THF. Loaded particles were used immediately after encapsulation for *in vivo* fluorescence studies.

2.4.4 *In vitro* studies

2.4.4.1 Cell culture

Caco-2 cells were purchased from ECACC (European Collection of Animal Cell Culture, Salisbury, UK) and cultured as single monolayers at 37°C in a humidified atmosphere containing 5% CO_2. Cells were cultured in a 50:50 mixture of Dulbecco's Modified Eagle Medium (DMEM) and HAMS F12 supplemented with 10% of foetal calf serum, 1% of L-glutamine and 1% penicillin/streptomycin sub-cultured at regular intervals, and passages made by trypsinising cells when at 80-90% confluence.

2.4.4.2 Cell viability assay

Caco-2 cells were seeded at a density of 10,000 cells per well in a flat bottomed clear 96 well plate and incubated for 24 h. Nanoparticles were diluted with cell culture medium into a 2 mg mL^{1} suspension. The stock solution was then serially diluted to make solutions of 100 ng mL^{1}, 1 µg mL^{-1}, 10 µg mL^{-1}, 100 µg mL^{-1}, 500 µg mL^{-1} and 2 mg mL^{-1}. The cells were incubated in the presence of the nanoparticle suspensions for 72 h. To determine the cell viability the sulforhodamine B colourimetric assay was used. 50 µL of cold 50% trifluoroacetic acid were added to each well of the plate and left to incubate for 1 h at 4°C. The plate was subsequently washed 10 times with slow running tap water to remove excess trifluoroacetic acid and the plate was heated gently with warm air to remove moisture. 50 µL of 0.4% sulforhodamine B (prepared in 1% acetic acid) were added to each well of the plate and the plate was allowed to stand for 30 min at ambient temperature. Excess dye was removed by washing the plate 5 times with 1% acetic acid. 200 µL of 10 mM Tris base solution (pH 10.5) was added to each well of the plate and left to stand at ambient temperature for 1 h. The absorbance of each well was measured at 570 nm on a BioRad iMark 96-well microplate reader. The experiments were carried out as duplicates of triplicates in two independent experiments.

2.4.5 *In vivo* studies

2.4.5.1 Animal handling

All *in vivo* studies were conducted on male CD1 mice purchased from Charles River (UK). Upon arrival, mice were allowed to adjust to the new environmental condition for at least two weeks. Humidity and temperature were kept between 45 to 60% and between 20 to 24°C, respectively, and animals had 12 hours of light per day with light onset at 07:00. Mice had *ad libitum* access to food and water. All *in vivo* experiments were carried out in accordance with the Animal Scientific Procedure Act 1986 under the Procedure Project Licence (PPL) number 70/3685.

2.4.6 *In vivo* toxicity

For acute, single dose toxicity evaluation, 29 six to seven week old male mice were randomised into eight groups and intraperitoneally (i.p.) injected with the different nanoparticles (N=3/group), vehicle (PBS, N=3) or nothing (N=2). Nanoparticle groups were injected with 49 and 86 nm P(*t*-BA), and 50 and 93 nm P(*n*-BA) nanoparticles at either 1.2 mg kg^{-1} (0.2 mg ml^{-1} in 200 µl PBS) or 12 mg kg^{-1} (2 mg ml^{-1} in 200 µl PBS). Of note, nanoparticle dilutions were prepared in sterile PBS under aseptic conditions and stored at 2 to 8°C until treatment. After injection, mice were monitored daily for the following 7 days, and body weight as well as signs of pain or distress were recorded.

For the repeat dosing study, 35 six-week old male mice were selected. Mice were randomised into four nanoparticle treatment groups (N=6/groups) and 2 control groups (PBS N=3; no-injection N=2) as described above. Each mouse was i.p. injected daily with 12 mg kg^{-1} (200 µl of 2 mg ml^{-1}) 49 and 86 nm P(*t*-BA), and 50 and 93 nm P(*n*-BA) nanoparticles or PBS for five consecutive days. The second control group was not injected and left untreated. After the first injection, mice were monitored daily for the following 8 days, and body weight as well as signs of pain or distress were recorded.

2.4.7 *In vivo* biodistribution

For biodistribution studies, CD1 mice were injected intraperitoneally with a single dose of Cy 7.5 labelled P(*n*-BA) 50 nm nanoparticles (1.2 mg kg^{-1}). *In vivo* fluorescence was followed periodically up to 76 h post injection using a LICOR Pearl® Trilogy *in vivo* imager on the 800 nm channel. Pharmacokinetic curves were obtained by quantifying the total fluorescence coming from the animal using open access software Image Studio Lite™. Organs were excised and imaged immediately. Organ fluorescence/ unit area was established by drawing around each organ and dividing this value by the area reported in the software.

References

1. M. Elsabahy and K. L. Wooley, *Chem. Soc. Rev*, 2012, **41**, 2545-2561.
2. M. Beija, R. Salvayre, N. Lauth-de Viguerie and J.-D. Marty, *Trends Biotechnol.*, 2012, **30**, 485-496.
3. F. Alexis, E. Pridgen, L. K. Molnar and O. C. Farokhzad, *Mol. Pharm.*, 2008, **5**, 505-515.
4. H. Maeda, H. Nakamura and J. Fang, *Adv. Drug Delivery Rev.*, 2013, **65**, 71-79.
5. H. Maeda, *J. Controlled Release.*, 2012, **164**, 138-144.
6. P. C. Ke, S. Lin, W. J. Parak, T. P. Davis and F. Caruso, *ACS Nano*, 2017, **11**, 11773-11776.
7. D. A. Richards, A. Maruani and V. Chudasama, *Chem. Sci.*, 2016, **8**, 63-77.
8. M. Roveri, M. Bernasconi, J.-C. Leroux and P. Luciani, *J. Mater. Chem. B*, 2017, **5**, 4348-4364.
9. B. Kang, T. Opatz, K. Landfester and F. R. Wurm, *Chem. Soc. Rev*, 2015, **44**, 8301-8325.
10. L. Zhang, F. X. Gu, J. M. Chan, A. Z. Wang, R. S. Langer and O. C. Farokhzad, *Clin. Pharmacol. Ther. (St. Louis)*, 2008, **83**, 761-769.
11. A. Albanese, P. S. Tang and W. Chan, *Annu. Rev. Biomed. Eng.*, 2012, **14**, 1-16.
12. X. Tao, S. Jin, D. Wu, K. Ling, L. Yuan, P. Lin, Y. Xie and X. Yang, *Nanomaterials*, 2015, **6**, 2.
13. A. Verma and F. Stellacci, *Small*, 2010, **6**, 12-21.
14. A. Rösler, G. Vandermeulen and H.-A. Klok, *Adv. Drug Delivery Rev.*, 2001, **53**, 95-108.
15. J. Zhang, J. Tanaka, P. Gurnani, P. Wilson, M. Hartlieb and S. Perrier, *Polym. Chem.*, 2017, **8**, 4079-4087.
16. J. Ugelstad and F. Hansen, *Rubber Chem. Technol.*, 1976, **49**, 536-609.
17. T. Sun, Y. S. Zhang, B. Pang, D. C. Hyun, M. Yang and Y. Xia, *Angew. Chem., Int. Ed.*, 2014, **53**, 12320-12364.
18. G. Cheng, A. Böker, M. Zhang, G. Krausch and A. H. E. Müller, *Macromolecules*, 2001, **34**, 6883-6888.
19. M. Hartlieb, T. Floyd, A. B. Cook, C. Sanchez-Cano, S. Catrouillet, J. A. Burns and S. Perrier, *Polym. Chem.*, 2017, **8**, 2041-2054.
20. C. J. Ferguson, R. J. Hughes, D. Nguyen, B. T. Pham, R. G. Gilbert, A. K. Serelis, C. H. Such and B. S. Hawkett, *Macromolecules*, 2005, **38**, 2191-2204.
21. P. B. Zetterlund, S. C. Thickett, S. Perrier, E. Bourgeat-Lami and M. Lansalot, *Chem. Rev.*, 2015, **115**, 9745-9800.

22. T. P. Davis, N. Truong Phuoc, M. Dussert, M. R. Whittaker and J. F. Quinn, *Polym. Chem.*, 2015, **6**, 3865-3874.

23. M. Chenal, L. Bouteiller and J. Rieger, *Polym. Chem.*, 2013, **4**, 752-762.

24. W. Zhang, F. D'Agosto, O. Boyron, J. Rieger and B. Charleux, *Macromolecules*, 2012, **45**, 4075-4084.

25. D. E. Ganeva, E. Sprong, H. de Bruyn, G. G. Warr, C. H. Such and B. S. Hawkett, *Macromolecules*, 2007, **40**, 6181-6189.

26. S. R. S. Ting, E. H. Min, P. B. Zetterlund and M. H. Stenzel, *Macromolecules*, 2010, **43**, 5211-5221.

27. G. Jiang, Y. Wang, R. Zhang, R. Wang, X. Wang, M. Zhang, X. Sun, S. Bao, T. Wang and S. Wang, *ACS Macro Lett.*, 2012, **1**, 489-493.

28. C. K. Poon, O. Tang, X.-M. Chen, B. T. T. Pham, G. Gody, C. A. Pollock, B. S. Hawkett and S. Perrier, *Biomacromolecules*, 2016, **17**, 965-973.

29. C. K. Poon, O. Tang, X.-M. M. Chen, B. Kim, M. Hartlieb, C. A. Pollock, B. S. Hawkett and S. Perrier, *Macromol. Biosci.*, 2016, **17**.

30. M. Siauw, B. S. Hawkett and S. Perrier, *J. Polym. Sci., Part A: Polym. Chem.*, 2012, **50**, 187-198.

31. F. M. Veronese and G. Pasut, *Drug Discov. Today*, 2005, **10**, 1451-1458.

32. J. M. Harris and R. B. Chess, *Nat. Rev. Drug Discovery*, 2003, **2**, 214-221.

33. K. Knop, R. Hoogenboom, D. Fischer and U. S. Schubert, *Angew. Chem., Int. Ed.*, 2010, **49**, 6288-6308.

34. L. Martin, G. Gody and S. Perrier, *Polym. Chem.*, 2015, **6**, 4875-4886.

35. G. Gody, T. Maschmeyer, P. B. Zetterlund and S. Perrier, *Macromolecules*, 2014, **47**, 3451-3460.

36. D. Pissuwan, C. Boyer, K. Gunasekaran, T. P. Davis and V. Bulmus, *Biomacromolecules*, 2010, **11**, 412-420.

37. J. Rieger, W. Zhang, F. o. Stoffelbach and B. Charleux, *Macromolecules*, 2010, **43**, 6302-6310.

38. F. Wang, Y. Luo, B.-G. Li and S. Zhu, *Macromolecules*, 2015, **48**, 1313-1319.

39. Y. Guo, X. Gao and Y. Luo, *J. Polym. Sci., Part A: Polym. Chem.*, 2015, **53**, 1464-1473.

40. C. J. Ferguson, R. J. Hughes, B. T. Pham, B. S. Hawkett, R. G. Gilbert, A. K. Serelis and C. H. Such, *Macromolecules*, 2002, **35**, 9243-9245.

41. S. S. Gosavi, S. Y. Gosavi and R. K. Alla, *Dent. Res. J.*, 2010, **7**, 82-87.

42. K. Y. van Berkel, G. T. Russell and R. G. Gilbert, *Macromolecules*, 2003, **36**, 3921-3931.

43. M. Gaumet, A. Vargas, R. Gurny and F. Delie, *Eur. J. Pharm. Biopharm.*, 2008, **69**, 1-9.

44. I. Chaduc, A. Crepet, O. Boyron, B. Charleux, F. D'Agosto and M. Lansalot, *Macromolecules*, 2013, **46**, 6013-6023.

45. H. P. S. Makkar, M. Blümmel and K. Becker, *Br. J. Nutr.*, 1995, **73**, 897-913.

46. J. Niu, D. J. Lunn, A. Pusuluri, J. I. Yoo, M. A. O'Malley, S. Mitragotri, T. H. Soh and C. J. Hawker, *Nat. Chem.*, 2017, **9**.

47. N. Silanikove, N. Gilboa, I. Nir, A. Perevolotsky and Z. Nitsan, *J. Agric. Food Chem.*, 1996, **44**, 199-205.

48. M. Shin, K. Kim, W. Shim, J. Yang and H. Lee, *ACS Biomater. Sci. Eng.*, 2016, **2**, 687-696.

49. R. Gref, M. Lück, P. Quellec, M. Marchand, E. Dellacherie, S. Harnisch, T. Blunk and R. H. Müller, *Colloids Surf., B*, 2000, **18**, 301-313.

50. X.-J. Du, J.-L. Wang, W.-W. Liu, J.-X. Yang, C.-Y. Sun, R. Sun, H.-J. Li, S. Shen, Y.-L. Luo, X.-D. Ye, Y.-H. Zhu, X.-Z. Yang and J. Wang, *Biomaterials*, 2015, **69**, 1-11.

51. M. Pröhl, S. Seupel, P. Sungur, S. Höppener, M. Gottschaldt, J. C. Brendel and U. S. Schubert, *Polymer*, 2017, **133**.

52. J. V. Jokerst, T. Lobovkina, R. N. Zare and S. S. Gambhir, *Nanomedicine*, 2011, **6**, 715-728.

53. J. Lu, M. Liong, Z. Li, J. I. Zink and F. Tamanoi, *Small*, 2010, **6**, 1794-1805.

54. J. Eichler, J. Knof and H. Lenz, *Radiat. Environ. Biophys.*, 1977, **14**, 239-242.

55. T. Behnke, C. Würth, K. Hoffmann, M. Hübner, U. Panne and U. Resch-Genger, *J. Fluoresc.*, 2011, **21**, 937-944.

56. L. Fan, Q. Wu and M. Chu, *Int. J. Nanomed.*, 2012, **7**, 3071-3080.

57. W. B. Liechty and N. A. Peppas, *Eur. J. Pharm. Biopharm.*, 2012, **80**, 241-246.

58. M. Longmire, P. L. Choyke and H. Kobayashi, *Nanomedicine (London, England)*, 2008, **3**, 703-717.

59. H. L. Reddy and R. S. Murthy, *Biomed. Pap.*, 2004, **148**, 161-166.

60. P. Maincent, P. Thouvenot and C. Amicabile, *Pharm. Res.*, 1992, **9**, 1534-1539.

61. R. R. Arvizo, O. R. Miranda, D. F. Moyano, C. A. Walden, K. Giri, R. Bhattacharya, D. J. Robertson, V. M. Rotello, J. M. Reid and P. Mukherjee, *PloS one*, 2011, **6**.

Chapter 3

Probing the effect of nanoparticle rigidity on cellular uptake

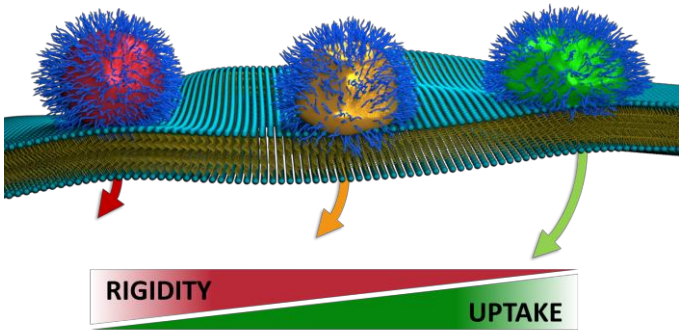

Nanoparticles are well established as vectors for the delivery of a wide range of biologically relevant cargo. The design of these materials has been led by numerous fundamental studies investigating size, shape, charge and functionality on mammalian cellular uptake. Nanoparticle rigidity however has been studied to a far lesser extent. This parameter can easily be controlled using the intrinsic glass transition temperature (T_g) of polymers. Here, we explore this property with a systematic study using a library of core-shell spherical PEGylated nanoparticles with three different polymeric core rigidities: hard, medium and soft, controlled with T_g, synthesised by RAFT emulsion polymerisation. The cellular internalisation, and uptake pathway was investigated, with results indicating that softer particles are taken up faster and in higher amounts, with a 3 fold increase over harder analogues. In addition, this study indicates major differences in the cellular uptake pathway, with harder particles being internalised through clathrin- and caveolae- mediated endocytosis as well as macropinocytosis, while softer particles were taken up with mainly caveolae- and clathrin/caveolae-independent endocytosis. We have also studied if size and rigidity have any complimentary effect, however our smaller (50 nm) derivatives did not show any appreciable differences in uptake efficiency suggesting that rigidity as a parameter in the biological regime may indeed be size dependent.

3.1 Introduction

Over the last two decades, a multitude of studies have been dedicated to understand how individual nanoparticle properties (size[1, 2], shape[3, 4], charge[5, 6], functionality[7, 8] etc) influences their biological interactions *in vitro* and *in vivo*. In particular, understanding how these affect the degree and mechanism of cellular uptake is vital for improving their pharmacological efficacy. It is well established that the mechanical properties of biomaterials are important for maintaining specific biological functions[9,10,11], however the effect of nanoparticle rigidity/elasticity on biological systems remains loosely explored. The current literature surrounding stiffness mediated cellular uptake has no general consensus on whether harder[12, 13] or softer particles[13-15] are preferentially taken up. Based on simulation data, it is however clear that the ability for soft nanoparticles to deform when interacting with the cell surface has a dramatic influence on their mechanism of uptake.[16] This therefore can either increase the adhesion energies required to complete internalisation if single particles are taken up (making hard easier to internalise than soft). This deformation can also increase the chance for cooperative uptake i.e. 2 or more particles at once (making soft preferentially internalised than hard). Nonetheless, simulation data cannot paint the entire picture for nanoparticle interactions with complex biological systems, especially when considering uptake mechanisms such as receptor-mediated endocytosis. So far, the effect of rigidity on cellular uptake has mainly been studied with large particles (~ 1 μm),[17, 18] but again have yielded conflicting results, with either rigid or flexible particles preferentially internalised.[17] Furthermore, although drug delivery vectors using smaller nanoparticles (10 – 200 nm) have shown greater therapeutic efficacy,[19] few studies have focused on rigidity at this scale.

This lack of consensus on the degree of cellular uptake of particles may arise from the range of methods used to control nanoparticle rigidity. For example, the rigidity of colloidal hydrogels[20] were previously modified by adjusting the crosslinking density,[21] regulating the water content of the particle core directly impacting the flexibility of the nanoparticle. Rigidity of layer-by-layer(LbL)/templated nanocapsules[22] was adapted by tuning the charge density and/or number of layers of oppositely charged polyelectrolytes present around the nanocapsules.[14] Unfortunately, these approaches may also impact other physicochemical properties (particle size, shape, surface ionisation and

hydrophobicity)[1, 6, 7] which are known to heavily influence cellular uptake, making the effect of rigidity difficult to characterise in itself.[12]

A traditional method of controlling flexibility in bulk polymeric materials is to vary the monomer composition and thus the glass transition temperature (T_g).[23] T_g is defined as the midpoint of the temperature range at which a material transforms from a hard state to a soft state. This change in properties arises due to a distinct change in mobility of chains within the polymeric matrix upon reaching the T_g. As T_g is an intrinsic material property, this method poses significant advantages over other techniques as one simply has to choose the correct monomer composition to tune nanoparticle rigidity. It can therefore be postulated that if a polymer nanoparticle possesses a $T_g >> 37°C$ this would result in a hard state in physiological conditions, however, if the $T_g << 37°C$ it would exist in a soft state. T_g has been used to modify the rigidity of nanoparticles (synthesised via miniemulsion polymerisation) by increasing the alkyl side chain lengths of polyalkylmethacrylates (from one to 16 carbon; poly(methylmethacrylate) to poly(stearylmethacrylate)),[24]. These results showed that a decrease in T_g triggered an increase in cellular uptake of nanoparticles over a wide range of cell lines. However, the use of longer side chains led to both lower T_g and increased surface hydrophobicity, which is known to drastically impact cellular uptake.[7] To achieve a real understanding of the importance of rigidity in cellular uptake, nanoparticles with different T_g should be generated with identical surface chemistry, such that changes in hydrophobicity and other physical properties do not interfere with the study.

In chapter 2, RAFT emulsion polymerisation was used to generate well-defined core-shell nanoparticles, whereby the surface and core chemistry could be easily tuned, as well as particle size. Nanoparticles synthesised with this approach lend themselves towards fundamental studies, as they maintain their structural integrity at low concentration, and a variety of core monomers can be used to adapt the desired particle rigidity. In this chapter, a series of inert uniform PEGylated core-shell nanoparticles (with diameters of 50 and 100 nm) were synthesised *via* RAFT emulsion polymerisation with three differing core rigidities/T_g and identical surface chemistry. Using these, we have evaluated various aspects of their cellular internalisation, including degree of uptake, uptake pathway, and intracellular trafficking.

3.2 Results and discussion

The aim of this chapter was to utilise RAFT emulsion polymerisation to generate nanoparticles of different rigidity, and investigate the degree and mechanism of their cellular uptake. We hypothesised that polystyrene (PS) ($T_{g,lit}$ = 100°C) , poly(*t*-butyl acrylate) (P(*t*-BA)) ($T_{g,lit}$ = 43°C), and poly(*n*-butyl acrylate) (P(*n*-BA)) ($T_{g,lit}$ = -54°C)[25] had appropriate T_g as the polymeric materials to obtain 'hard' 'medium' and 'soft' core nanoparticles respectively. In addition, we wanted to examine if rigidity effects were size dependent, therefore both 100 and 50 nm diameter nanoparticles of hard, medium and soft varieties were targeted for this study. In chapter 2, we showed how RAFT emulsion polymerisation could be used to prepare PEGylated P(*n*-BA) ('soft') and P(*t*-BA) ('medium') nanoparticles, with diameters ranging from ~30 nm to ~130 nm. Hence prior to conducting this study, similar PEGylated PS based nanoparticles were synthesised as a 'hard' rigidity derivative.

3.2.1 Optimising styrene RAFT emulsion polymerisations

3.2.1.1 Synthesis of styrene based macro-RAFT agent

Initially, an analogous macro-RAFT agent P(PEGA)$_8$-*b*-Sty$_8$] (**MRA-PS**) was prepared by chain extending **MRA-PEGA** (synthesised in Section 2.2.2) using adapted literature conditions and purified as mentioned above (Section 2.2.2; Scheme 3.1).[26]

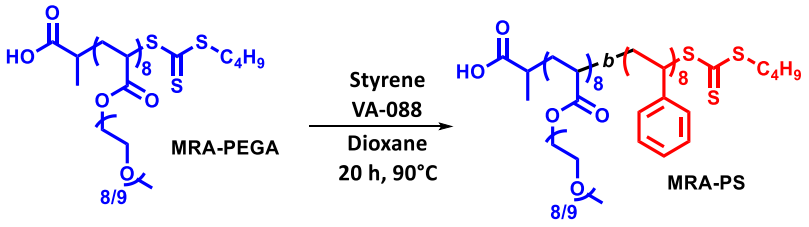

Scheme 3.1 Preparation of MRA-PS *via* chain extension of MRA-PEGA in dioxane at 90°C.

Similarly to **MRA-*n*BA** and **MRA-*t*BA**, size exclusion chromatograms of **MRA-PS** revealed narrow molecular weight distributions, comparable experimental M_n to theoretical values obtained from ^{1}H NMR spectra, and a shift toward higher molar mass suggesting successful chain extension (Figure 3.1a and Figure 3.1b). As with the P(*t*-BA) and P(*n*-BA) analogues, dynamic light scattering of **MRA-PS** in aqueous conditions revealed the formation of uniform 6.5 nm micelles (PDi = 0.07; Figure 3.1c), suggesting it would be able to stabilise RAFT emulsion polymerisations.

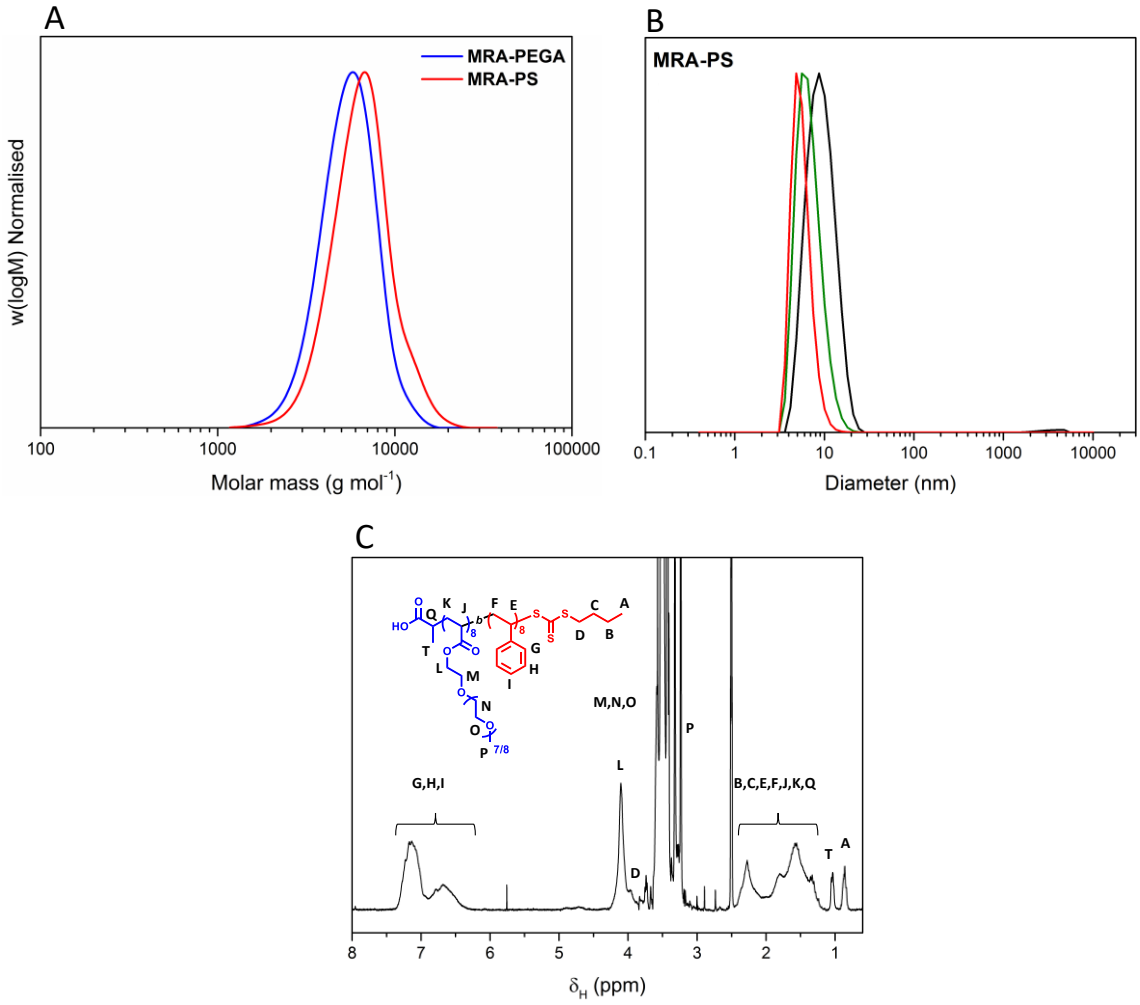

Figure 3.1. Characterisation data for MRA-PS (A) $CHCl_3$-SEC chromatograms of MRA-PEGA (blue) and MRA-PS (red and (B) dynamic light scattering (intensity distribution = black line, volume distribution = green line, number distribution = red line) of self-assembled micelles at 7.5 mg mL^{-1} in pure water measured at 25°C (C) ^{1}H NMR spectrum in d_6-DMSO at 300 MHz

Table 3.1. Summary of characterisation data for MRA-PS.

	% conv[a]	$M_{n,th}$ (g mol^{-1})[b]	$M_{n,SEC}$ (g mol^{-1})[c]	$M_{w,SEC}$ (g mol^{-1})[c]	$Đ$[c]	D_h[d]	PDi[e]
MRA-PEGA	91	4100	5100	5800	1.14	-	-
MRA-PS	92	4900	6000	7000	1.17	6.5	0.070

[a]Determined by ^{1}H NMR spectroscopy, [b]Theoretical molar masses calculated with Equation 2.12, [c]Determined by $CHCl_3$-SEC and analysed against PMMA standards, [d]Determined using DLS, [e]Calculated using Equation 2.13. Data for MRA-PEGA (synthesised in Section 2.2.2) is repeated here for clarity.

3.2.1.2 Styrene RAFT emulsion polymerisation

For RAFT emulsion polymerisations of styrene, the conditions used in section 2.2.3 were initially employed to chain extend **MRA-PS** by 200 monomer units (Scheme 3.2). Surprisingly, the resulting latex appeared colloidally unstable, with significant separation between the aqueous and polymer phases (Figure 3.2a). DLS revealed broad particle size distributions with *PDi* between 0.11 and 0.21 and average hydrodynamic diameters between 36 and 84 nm depending on distribution type, confirming the poor performance and stability of these latexes (Figure 3.2a; Table 3.2, Entry 1). It should be noted that any sediment/coagulum would not be easily detected by DLS, as these could be well above the optimum size range for this technique (1-1000 nm), potentially accounting for the low average particle diameter.

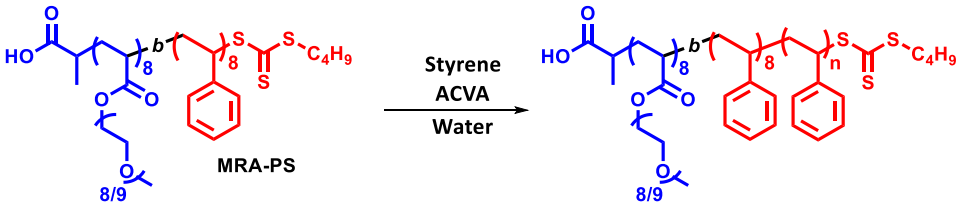

Scheme 3.2. RAFT emulsion polymerisation of styrene mediated with **MRA-PS**

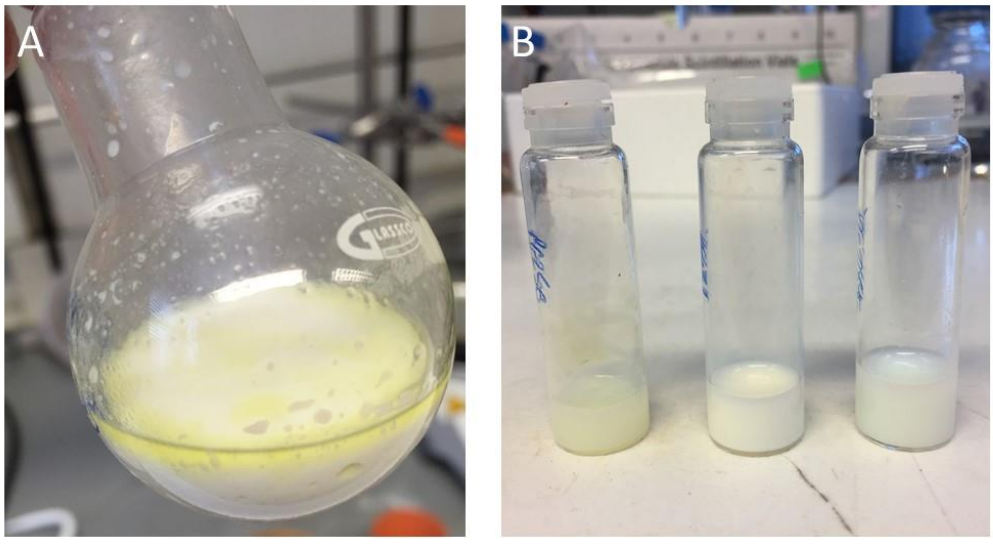

Figure 3.2 Photograph of polystyrene latexes synthesised with (A) [MRA-PS] = 2.85 mM + [M] = 570 mM and (B) [MRA-PS] = 5.70 mM + [M] = 570 mM, [MRA-PS] = 1.425 mM + [M] = 570 mM and [MRA-PS] = 1.425 mM and [M] = 427 mM.

To test alternative conditions, analogous reactions were performed with **MRA-PS** at both 200% (5.70 mM) and 50% (1.425 mM) of its original concentration (2.85 mM), while keeping [M] (570 mM) constant (Table 3.2, Entry 2 and 3). This modification in [**MRA-PS**] causes variation in DP_{target} with the 200% and 50% concentrations yielding chain lengths of 100 and 400 respectively. Both concentrations yielded similar nanoparticle diameters (~100 nm). At the higher concentration (5.70 mM), the resulting latex, although colloidally stable, was more viscous and had a broad *PDi* (0.162). In comparison, at a lower concentration (1.425 mM) the nanoparticle suspension remained colloidally stable, had narrow *PDi* (0.058) and was completely fluid (not viscous). Finally, a fourth polymerisation was conducted whereby the monomer concentration was reduced to 427 mM (75% the original value), [**MRA-PS**] at 1.425 mM (optimum) and therefore a DP_{target} of 300 (Table 3.2, Entry 4; Figure 3.2b). As in section 2.2.3, when [M] was reduced, the resulting particle diameter reduced from 107 nm for DP_{target} = 400, to 64 nm DP_{target} = 300 and retained a narrow *PDi* (Figure 3.3).

Although not all latexes had narrow particle size distributions, size exclusion chromatograms displayed relatively low $Đ$ values ($\leq$ 1.42), compared to the P(*n*-BA) and P(*t*-BA) nanoparticles synthesised above (section 2.2.3). This is largely due to a reduced amount of the side-chain branching and unconsumed macro-RAFT agent, unlike the P(*t*-BA) and P(*n*-BA) nanoparticles synthesised in chapter 2. This could be explained by the low propagation rate constant (k_p) of styrene in the early phase of the polymerisations, artificially increasing the chain transfer constant ($C_{tr} = k_{tr}/k_p$), and therefore improving the chain extension efficiency of **MRA-PS** compared to **MRA-*n*BA** and **MRA-*t*BA.** This could also explain why high **MRA-PS** concentrations result in colloidal instability, as the number of growing particles increases as a function of [**MRA-PS**] when all macro-RAFT agents are consumed, which may promote collisions in solution and therefore induce aggregation/sedimentation (Figure 3.3). Furthermore, this could also be an effect of superswelling, which is where the high proportion of oligomeric diblock stabilisers swell with a large quantity of monomer, causing destabilisation.[27, 28]

Table 3.2 Characterisation data for styrene RAFT emulsion polymerisations with different [MRA-PS] and [M].

	[MRA-PS] (mM)	[M](mM)	DP_{target} [a]	D_h (nm) [b]	PDi [c]	$M_{n,th}$ (g mol^{-1}) [d]	$M_{n,SEC}$ (g mol^{-1}) [e]	$M_{w,SEC}$ (g mol^{-1}) [e]	$Đ$ [e]
1	2.85	570	200	36	0.113	25600	28000	36500	1.30
2	5.70	570	100	101	0.162	15300	8000	9800	1.23
3	1.425	570	400	107	0.058	46500	33900	48100	1.42
4	1.425	427	300	64	0.048	36100	26200	32800	1.25

[a]Refers to the target DP of RAFT emulsion polymerisations performed to obtain the third (core forming) block. [b]Determined by DLS. [c]Determined using Equation 2.13. [d]Determined using Equation 2.12. [e]Determined by THF-SEC (values were obtained by integrating the whole polymer region), calibrated with PS standards. All polymerisations reached >99% monomer conversion, determined by gravimetry, and were performed at 70°C.

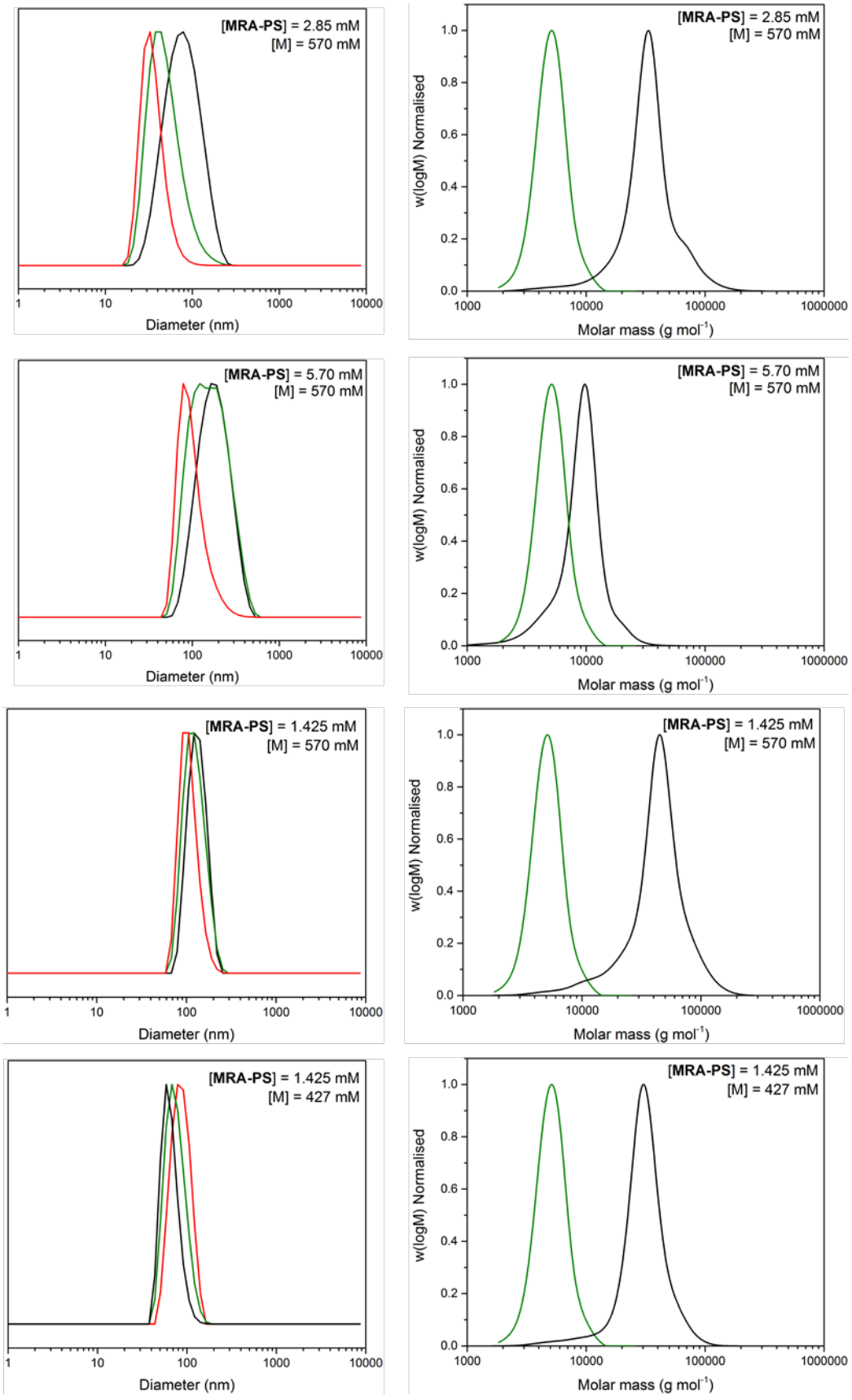

Figure 3.3 (left column) DLS intensity (black), volume (green line) and number (red line) traces and THF-SEC chromatograms (right column) for styrene RAFT emulsion latexes (black line) chain extended from **MRA-PS** (green line) with different [MRA-PS] and [M].

3.2.2 Development of a fluorescent labelling strategy

Having successfully optimised RAFT emulsion polymerisation of styrene (above), *n*-BA and *t*-BA (chapter 2), our next objective was to establish a method of quantifying the cellular uptake of these nanoparticles. Fluorescent labelling is a popular and versatile method of visualising, and quantifying biomaterial distribution, both *in vitro* and *in vivo*. The wide range of commercially available functional fluorophores, and organelle specific fluorescent probes, allows for highly specific measurements of uptake rate and intracellular location for a wide range of materials, including nanoparticles. Labelling typically involves the partial modification of nanoparticle surfaces with water soluble derivatives of common fluorophores (fluorescein, rhodamine, cyanine, etc.). However, small differences in nanoparticle surface hydrophobicity has been shown to heavily influence uptake degree and rate,[7] therefore modification of the particle core is the preferred method to introduce fluorescent moieties without significantly changing other physicochemical properties. Charleux and co-workers recently reported the use of borondipyrromethene (BODIPY) monomer fluorophores to label nanoparticles using a phase inversion RAFT emulsion polymerisation of styrene.[29] These hydrophobic BODIPY monomers were copolymerised in the nanoparticle core during the polymerisation. The resulting nanoparticles were shown to be 200-2000x brighter than quantum dots, with high quantum yields ($0.20 < \Phi\ 0.35$). These monomers therefore represent a facile method to fluorescently label nanoparticles, with minimal modification of the procedures developed above.

3.2.2.1 BODIPY acrylate synthesis

From the library of BODIPY monomers generated by Charleux and co-workers, polymeric nanoparticle cores copolymerised with a phenolic acrylate derivative (BODIPY acrylate) had the highest brightness and quantum yield, in comparison to the other monomers.[29] Additionally, as some of the targeted nanoparticles are polyacrylates (*t*-BA and *n*-BA), using an acrylate fluorescent monomer should yield a random distribution of fluorophore along the polymeric chain, limiting any aggregation induced fluorescence quenching.[30]

BODIPY acrylate (BODIPYA) was therefore synthesised via a two pot, four step approach, using literature procedures.[29] BODIPY phenol was first prepared via a three step, one pot approach, typically used to create the BODIPY centre. Firstly, an acid

catalysed condensation of kryptopyrrole and 4-hydroxybenzaldehyde was performed to afford the dipyrromethane **1**. This was oxidised to dipyrromethene **2** using DDQ, which was subjected to a mild base, and boron trifluoride diethyl etherate yielding BODIPY phenol with 30% yield.

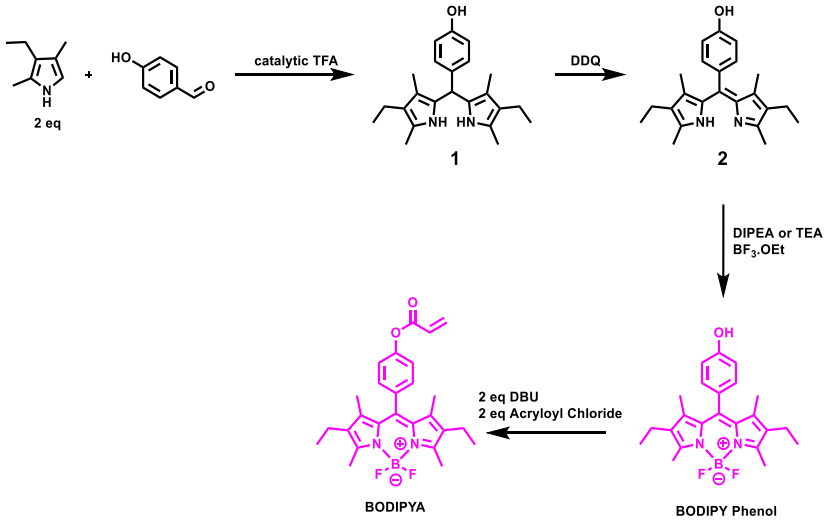

Scheme 3.3. Synthetic approach to generate BODIPYA.

BODIPY acrylate was prepared by esterification of BODIPY phenol with acryloyl chloride, in the presence of a mild base to afford BODIPYA with 70% yield. Both structure and purity of compounds were confirmed with ^{1}H NMR, ^{13}C NMR, ^{19}F NMR, IR, mass spectroscopy and HPLC. The spectroscopic properties of BODIPYA were assessed with fluorescence and absorbance spectroscopy, revealing an excitation maxima of 528 nm and an emission maxima of 542 nm (Figure 3.4) in chloroform.

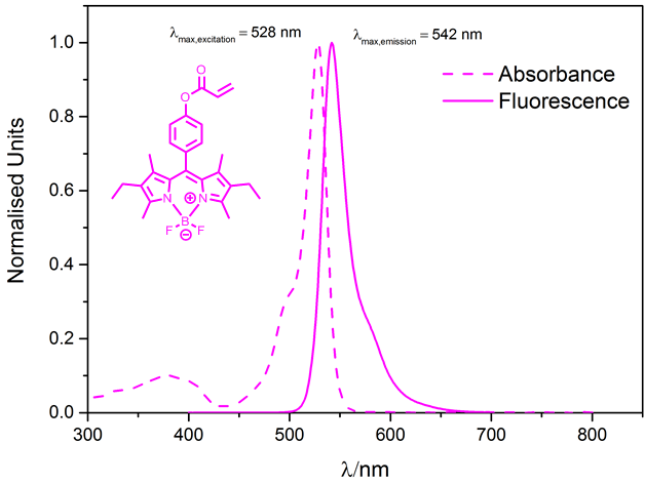

Figure 3.4. Normalised absorbance and fluorescence spectra (λ_{ex} = 528 nm) of BODIPYA (10 µg mL^{-1}) in chloroform.

3.2.2.2 Solution copolymerisation of BODIPYA

For the polymerisation of BODIPYA, 1 mol% fluorescent monomer (relative to PEGA) was copolymerised with PEGA, using solution RAFT polymerisation, targeting a total DP of 10 using conditions established in section 2.2.2. The resulting polymer was analysed with SEC using RI detection and UV detection set to 520 nm to assess the incorporation of BODIPYA within the polymer chain.

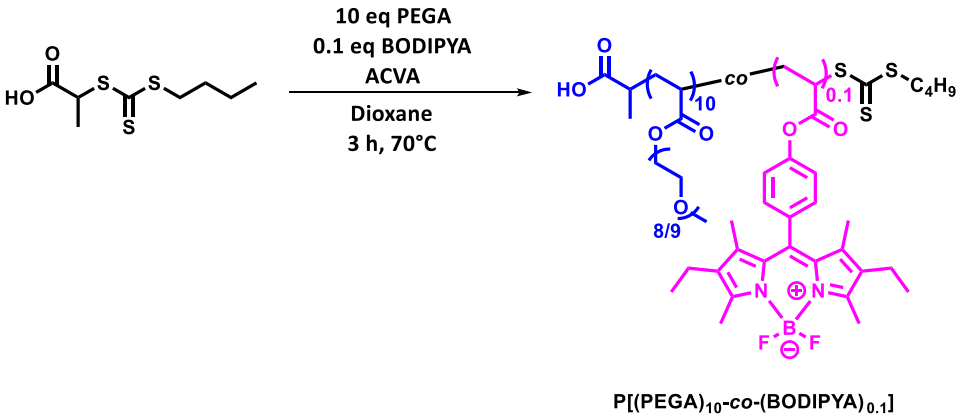

Scheme 3.4. Copolymerisation of PEGA with BODIPYA (1 mol%) mediated with RAFT agent PABTC.

Chromatograms revealed close agreement between $UV_{520\ nm}$ and RI traces suggesting successful incorporation of the fluorescent monomer. However, the presence of a low molecular weight species in the $UV_{520\ nm}$ traces indicated that BODIPYA had not been fully consumed during the polymerisation using these conditions (Figure 3.5). Having shown that BODIPYA is a facile method to fluorescently label polymers in homogenous systems, we proceeded by testing this in a heterogeneous RAFT emulsion polymerisation.

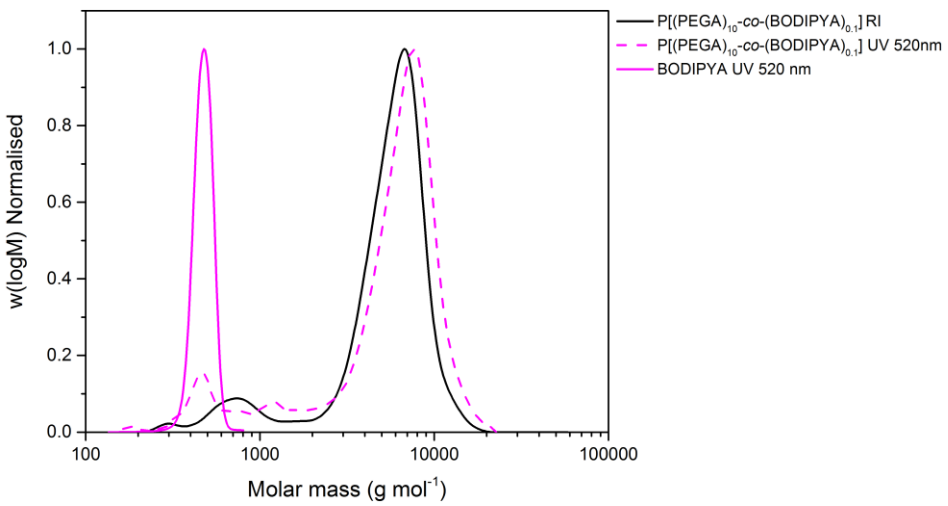

Figure 3.5. THF-SEC chromatograms of crude P[(PEGA)$_{10}$-*co*-(BODIPYA)$_{0.1}$] using both RI detection (black full line) and UV detection at 520 nm to assess BODIPYA incorporation (pink dashed line), and of pure BODIPYA (pink full line).

3.2.2.3 RAFT emulsion copolymerisation of BODIPYA with *n*-BA

RAFT emulsion copolymerisations of BODIPYA and *n*-BA were performed with a DP$_{target}$ of 170 using conditions from chapter 2, but with the addition of 0.1 wt% (relative to [M]) BODIPYA pre-dissolved in the monomer phase.

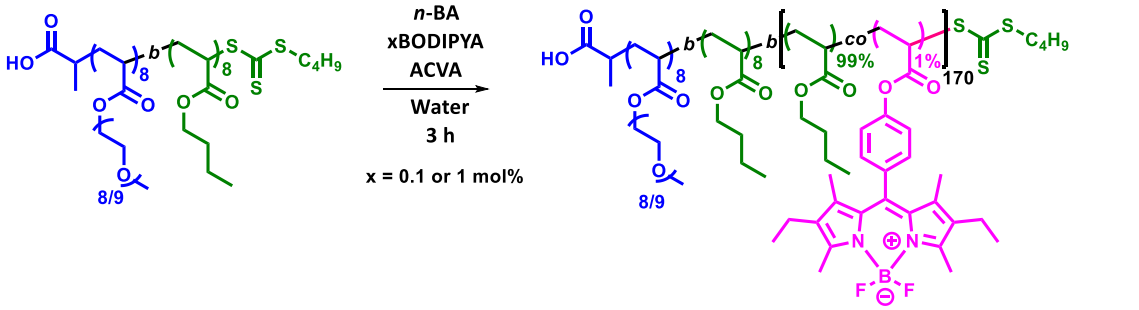

P{[(PEGA)$_8$-*b*-(*n*-BA)$_8$]-*b*-[(*n*-BA)$_{99.9\%}$-*co*-(BODIPYA)$_{0.1\%}$]$_{170}$}

.

Scheme 3.5 RAFT emulsion copolymerisation of *n*-BA with BODIPYA mediated with MRA-*n*BA.

DLS analysis of the resulting latex revealed uniform nanoparticles (*PDi* < 0.05) with a diameter of 108 nm, suggesting addition of BODIPYA (at this concentration) did not perturb the RAFT emulsion process. Similarly to the solution polymerisations above, size exclusion chromatograms revealed successful incorporation of BODIPYA into the polymer chains within the core of the nanoparticle, as observed by the overlap between RI and UV$_{520\ nm}$ traces. Unfortunately, as in the solution state polymerisation, a small amount of fluorescent monomer remained unconsumed, potentially due to the slow diffusion of BODIPYA into the growing nanoparticles, a feature which was also observed

by Charleux and co-workers.[29] Any non-covalently bound BODIPYA has potential to leak out of the nanoparticles during storage leading to non-specific uptake of free dye, and inconclusive results from cellular uptake experiments. To negate these issues, the free BODIPYA must be purified from the nanoparticles.

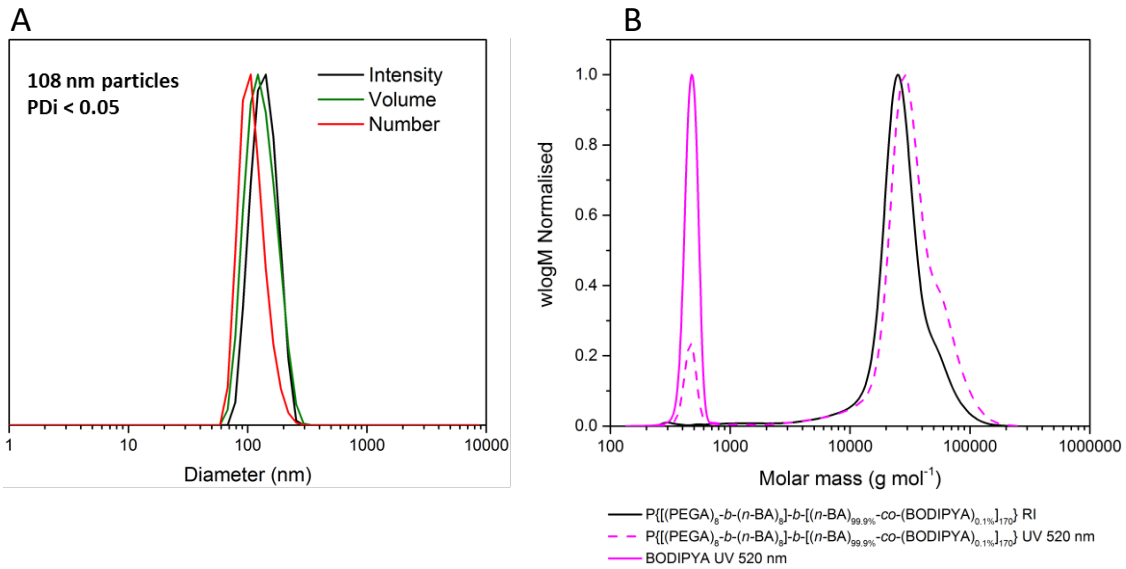

Figure 3.6 (A) DLS distributions (intensity (black), volume (green) and number (red)) of P{[(PEGA)$_8$-*b*-(*n*-BA)$_8$]-*b*-[(*n*-BA)$_{99.9\%}$-*co*-(BODIPYA)$_{0.1\%}$]$_{170}$ nanoparticles diluted 1/1000 in pure water, measured at 25°C. (B) THF-SEC of dried P[(PEGA)$_8$-*b*-(*n*-BA)$_8$]-*b*-[(*n*-BA)$_{99.9\%}$-*co*-(BODIPYA)$_{0.1\%}$]$_{170}$ nanoparticles dissolved in eluent using RI detection (black full line) and UV detection at 520 nm detection (pink dashed line), and of BODIPYA (pink full line).

As BODIPYA was highly hydrophobic, dialysis against pure water would not be sufficient to remove any free fluorophore. Procedures were henceforth conceived where the dialysis media contained a high percentage of organic solvent to solubilise BODIPYA. We found that a 60/40 1,4-dioxane/water (v/v) mixture fully solubilised BODIPYA without any precipitation for 24 h (data not shown). It was possible however, that in these conditions the nanoparticles may dissolve, as the core polymers (P(*t*-BA), P(*n*-BA), PS) and P(PEGA) shell were soluble in organic solvents, resulting in particle collapse. To examine this effect, ~100 nm non-fluorescently labelled nanoparticles with all three polymeric cores were diluted with a solvent mixture of 60/40 1,4-dioxane/water mixture (v/v), shaken for 24 h at 25°C and the particle size distribution monitored with DLS. All three nanoparticles displayed high colloidal stability with no disassembly, or aggregation caused by the presence of organic solvent (Figure 3.7). Surprisingly the nanoparticles showed an increase in diameter from ~100 nm to ~140 nm, which can be attributed to either solvent induced core swelling, or a discrepancy between viscosity of

the chosen dispersant during measurements (water) and the actual solvent mixture. As 1,4-dioxane has a higher viscosity (1.37 cP) than water (1.0 cP) in any binary mixture of these solvents, the nanoparticles will have a slower diffusion rate than in pure water. As DLS estimates particle sizes by their diffusion rate, this artificially enlarges the nanoparticle size reported.

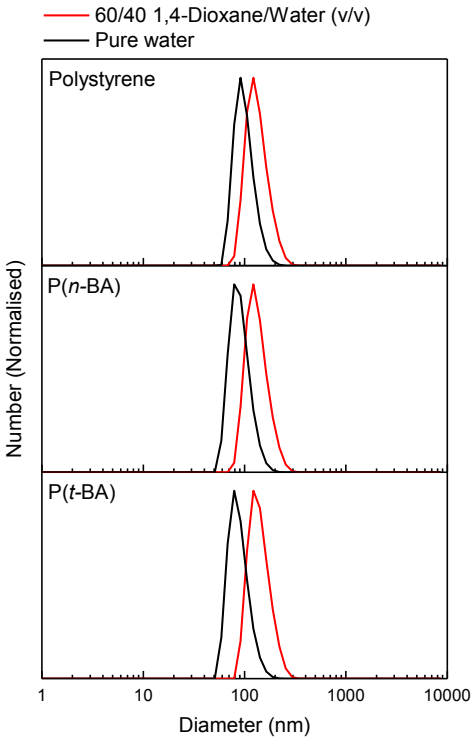

Figure 3.7. Particle size distributions in 60/40 dioxane/water (v/v) solvent mixture (red line) and in pure water (black line) for 100 nm non-fluorescent PS, P(*n*-BA), and P(*t*-BA) nanoparticles, both at 25°C measured with DLS.

To investigate the above conditions for dialysis purification, an analogous RAFT emulsion polymerisation was performed where a 10-fold increase in BODIPYA (1 mol%) was introduced into the reaction mixture. This led to 50% unconsumed BODIPYA, in comparison to 7% at 0.1 mol%, which therefore allows us to visualise the purification process with greater sensitivity. The increased proportion of unconsumed BODIPYA also suggests there may be a maximum amount that can be incorporated. The nanoparticles were then dialysed against a 60/40 1,4-dioxane/water (v/v) mixture and the relative amount of free BODIPYA in the latex was monitored by comparing the BODIPYA integrals and polymer integrals from $UV_{520\ nm}$ SEC traces after each media change (4 h, 16 h and 96 h). Starting at 50% free BODIPYA (relative to polymer peak) before dialysis, a steady decrease was observed over time, with only 5%, 2% and 0.07% detected after 4 h (1st change), 16 h (2nd change) and 96 h (3rd change) respectively (Figure 3.8a), without

a decrease in the polymer peak intensity. The particles were then extensively dialysed against pure water to remove 1,4-dioxane from the latex. Once complete, the resulting particle size distribution remained narrow, with similar average diameters as before purification and no observable aggregate formation (Figure 3.8b and Figure 3.8c).

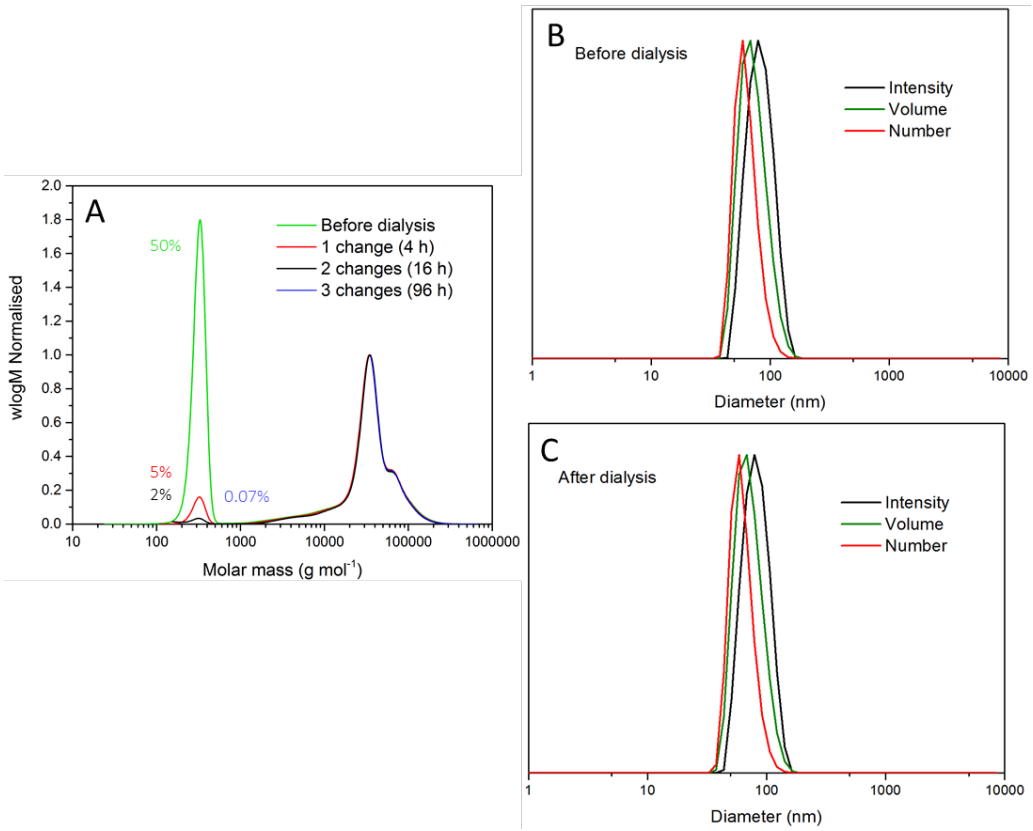

Figure 3.8. Purification of free BODIPYA from P(PEGA)$_8$-*b*-P(*n*-BA)$_8$-[P(*n*-BA)$_{99\%}$-*co*-P(BODIPYA)$_{1\%}$]$_{170}$ nanoparticles *via* dialysis with a 100k MWCO membrane against a 60/40 1,4-dioxane/water (v/v) mixture, monitored over 96 h with (A) SEC (UV detection at 520 nm). DLS distributions (intensity (black), volume (green) and number (red)) (B) before and (C) after dialysis purification.

Overall, these results indicate that BODIPYA can be successfully copolymerised into the nanoparticle polymeric chains during RAFT emulsion. Dialysis against a water/dioxane mixture enables removal of unconsumed fluorescent monomer, without disturbing the colloidal stability of the latex, all which can be monitored simply using UV$_{520\,nm}$ detection with SEC.

3.3 Synthesis and characterisation of Hard, Medium and Soft nanoparticles

Having successfully optimised styrene RAFT emulsion polymerisations (Section 3.2.1), and implemented a fluorescent labelling strategy (Section 3.2.2), the nanoparticle rigidity study was initiated by synthesising a series of six fluorescently-labelled 100 nm and 50 nm nanoparticles. As discussed in Section 3.2, both of these particle sizes would be generated with either PS, P(*t*-BA) or P(*n*-BA) cores and for clarity will be referred to as 100H, 100M, 100S, 50H, 50M, and 50S for 100 nm and 50 nm hard, medium and soft nanoparticles.

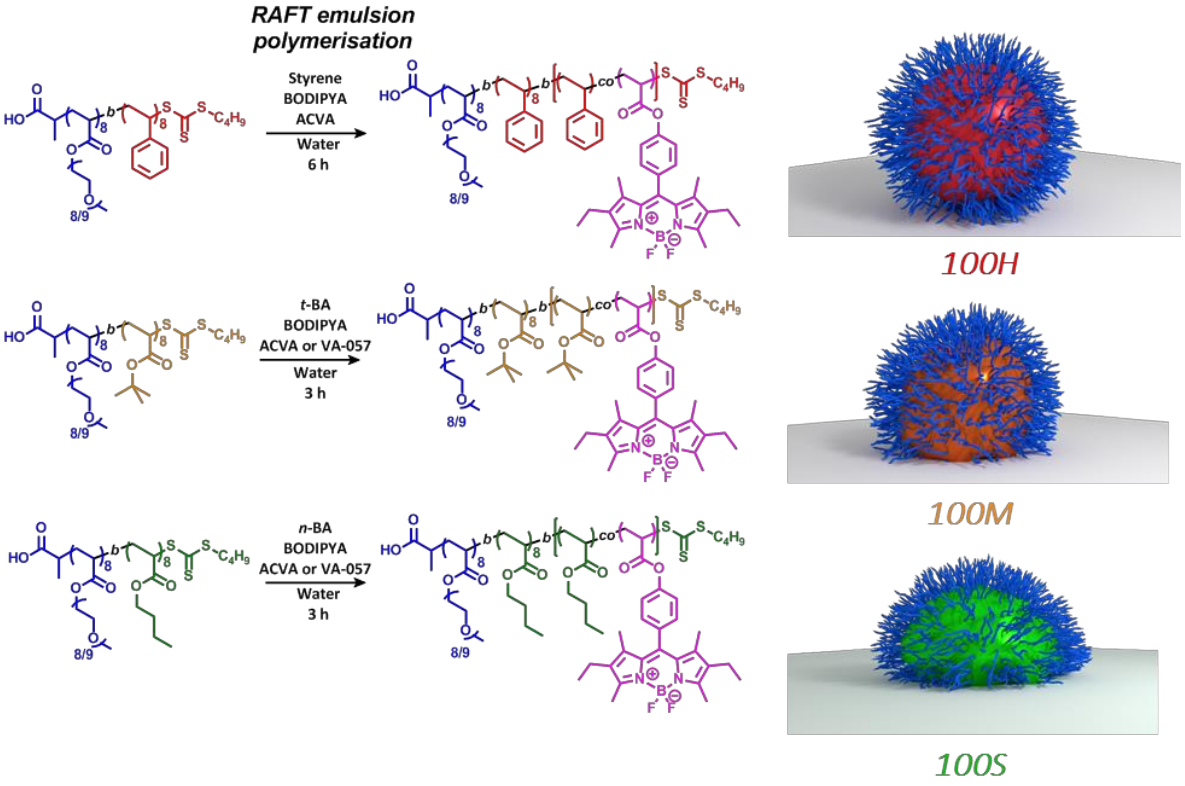

Figure 3.9 (A) Preparation of core-shell nanoparticles via RAFT emulsion polymerisation. (B) Graphical representation of hard, medium and soft nanoparticles.

A library of BODIPYA-labelled PS, P(*t*-BA) and P(*n*-BA) with different rigidities were prepared using adapted procedures from section 3.2.2.3 (Figure 3.9). Particle size was tuned by controlling either the DP_{target} or the initiator type (ACVA or VA-057), as shown in section 2.2.3.1 (full conditions can be found in Table 3.7), with all polymerisations achieving high monomer conversions (> 98%) within 3 h. Additionally, as some characterisation techniques, such as static light scattering (λ_0 = 533 nm), can be perturbed

by coloured samples, an analogous series of non-labelled nanoparticles were prepared using the same conditions but omitting the addition of BODIPYA.

DLS and ζ-potential analysis revealed negatively charged (-30 mV), uniform nanoparticles (*PDi* ~0.05), with diameters close to targeted values for both fluorescent and non-fluorescent analogues (Figure A3.1 and Figure A3.2). Negligible differences in particle diameter or *PDi* were observed in culture medium Dulbecco's Modified Eagle Medium (DMEM) suggesting the suspensions would be colloidally stable during cell uptake experiments (Table 3.3).

Table 3.3. Characterisation data of synthesised nanoparticles.

			Hydrodynamic diameter and ζ-potential					
			Water			DMEM		
Full title	**Core**	**Abb.**	D_h (nm)[a]	*PDi*[b]	ZP (mV)[c]	D_h (nm)[a]	*PDi*[b]	T_g/°C[d]
Fluorescent								
100 nm Hard	PS	100H	107.6	0.054	-31	112.4	0.051	90.0
100 nm Medium	P(*t*-BA)	100M	102.7	0.056	-25	102.8	0.082	37.8
100 nm Soft	P(*n*-BA)	100S	101.5	0.058	-28	104.7	0.062	-57.5
50 nm Hard	PS	50H	53.6	0.062	-24	52.7	0.058	90.0
50 nm Medium	P(*t*-BA)	50M	57.9	0.056	-35	49.1	0.065	31.4
50 nm Soft	P(*n*-BA)	50S	54.2	0.047	-30	55.4	0.050	-58.3
Non-fluorescent								
100 nm Hard	PS	$100H_{NF}$	100.1	0.054	-29	109.0	0.056	91.0
100 nm Medium	P(*t*-BA)	$100M_{NF}$	102.3	0.058	-27	108.4	0.064	37.5
100 nm Soft	P(*n*-BA)	$100S_{NF}$	105.3	0.058	-31	107.1	0.051	-56.5
50 nm Hard	PS	$50H_{NF}$	58.5	0.056	-27	61.5	0.052	82.5
50 nm Medium	P(*t*-BA)	$50M_{NF}$	52.5	0.040	-31	50.4	0.052	32.9
50 nm Soft	P(*n*-BA)	$50S_{NF}$	54.0	0.049	-25	58.3	0.058	-57.8

[a]Mean of three measurements using dynamic light scattering (number distribution). [b]Calculated using Equation 2.13. [c]Mean of three measurements. [d]Measured using differential scanning calorimetry. Subscripts with 'NF' refer to non-fluorescent nanoparticles. All data reported is for nanoparticles after dialysis purification against a 60/40 1,4-dioxane/water (v/v) mixture.

SEC chromatograms of both fluorescent (RI and $UV_{520\,nm}$ detection) and non-fluorescent (RI detection only) nanoparticles indicated successful chain extension from their respective macro-RAFT agents. From $UV_{520\,nm}$ traces, fluorescent derivatives displayed a large proportion of unconsumed BODIPYA. All fluorescently labelled nanoparticles were therefore subjected to the two-step dialysis procedure established in section 3.2.2.3. The complete removal of unconsumed BODIPYA from the polymer latexes was evident from SEC ($UV_{520\,nm}$ detection), while RI detection showed a large reduction in the amount of residual macro-RAFT from the latexes. Retention of the bright orange coloured latex

(Figure 3.10a), and the polymer signal in the $UV_{520\ nm}$ SEC detection (Figure A3.3), suggested a high amount of fluorescent monomer remained incorporated, with dialysis procedures completely removing any free BODIPYA. Importantly, the particle size distributions showed negligible differences after purification (Figure A3.1). Furthermore, the unconsumed macro-RAFT agent in non-fluorescent analogues ($100H_{NF}$, $100M_{NF}$, $100S_{NF}$, $50H_{NF}$, $50M_{NF}$ and $50S_{NF}$) was removed by dialysis against pure water, as confirmed by SEC (RI detection; Figure A3.4). Notable differences in $M_{n,SEC}$ between fluorescent and non-fluorescent nanoparticles were observed, which may be ascribed to differences in chain extension efficiency (amount of residual macro-RAFT agent), leading to either smaller or larger chain length, due to the presence of BODIPYA.

Table 3.4. SEC data for dissolved nanoparticles**.**

		Non-fluorescent			Fluorescent		
	$M_{n,th}$ (g mol^{-1})^a	$M_{n,SEC}$ (g mol^{-1})^b	$M_{w,SEC}$ (g mol^{-1})^b	$Đ^b$	$M_{n,SEC}$ (g mol^{-1})^b	$M_{w,SEC}$ (g mol^{-1})^b	$Đ^b$
100H	46,500	42,000	47,900	1.14	52,000	64,900	1.23
50H	25,800	28,500	33,000	1.18	40,800	50,600	1.24
100S	26,800	32,800	42,600	1.27	35,300	53,450	1.51
50S	20,400	21,900	26,000	1.19	27,200	37,000	1.36
100M	26,800	31,500	41,500	1.32	24,400	31,300	1.28
50M	21,600	25,900	33,200	1.28	23,100	29,600	1.28

^{a}Calculated using Equation 2.12 and ^{1}H NMR spectroscopy. ^{b}Determined with THF-SEC calibrated with PMMA standards.

Fluorescence measurements of the fluorescent nanoparticles showed similar emission and excitation profiles to free BODIPYA (Figure 3.4), suggesting that differences in core chemistry did not affect their spectroscopic properties (Figure A3.5). When placed under a UV lamp (λ=365 nm), bright green fluorescence could be observed from the nanoparticles (Figure 3.10b).

Differential scanning calorimetry was used to evaluate the T_g of all twelve nanoparticles. Thermograms revealed T_g values of approximately 90°C, 37°C and -55°C for soft, medium, and hard varieties, which are in close agreement to literature values for PS, P(*t*-BA) and P(*n*-BA) respectively (Figure A3.6 and Figure A3.7). Interestingly, traces for all soft nanoparticles displayed a small melting transition at approximately 0°C, which could be attributed to trace water.

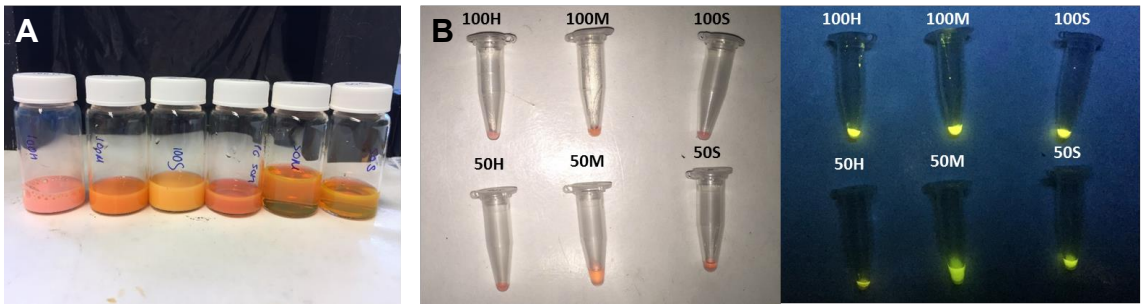

Figure 3.10. Digital photographs of the BODIPY labelled nanoparticles 100H, 100M, 100S, 50H, 50M and 50S under natural and UV light (λ = 365 nm).

Transmission electron micrographs of the fluorescent nanoparticles displayed similar particle sizes to those obtained with DLS, and confirmed their spherical morphology. Unsurprisingly, the low T_g (P(*n*-BA)) analogues were not visible under room temperature dry microscopy, likely due to these nanoparticles flattening as a consequence of flexibility. Cryo-TEM (performed by Dr Saskia Bakker, University of Warwick) was therefore employed to image the P(*n*-BA) (soft) nanoparticles, clearly showing spherical nanoparticles with similar sizes to those found with DLS.

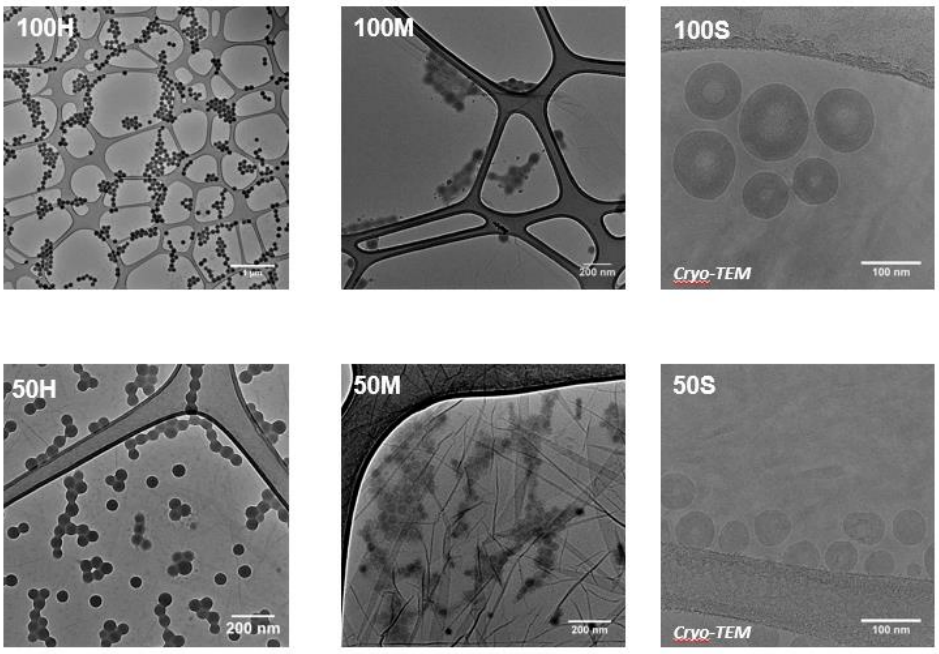

Figure 3.11. Dry state transmission electron micrographs of 100H, 100M, 50H, 50M (deposited on graphene oxide coated lacey carbon grids) and cryogenic transmission electron micrographs of 100S and 50S (deposited on lacey carbon grids). Cryo-TEM images were obtained by Dr Saskia Bakker, University of Warwick.

Solution phase particle size and morphology were further elucidated with a combination of small angle neutron scattering (SANS) and static light scattering (SLS). As described in section 2.2.4, these techniques are complimentary and can give information on different size domains of nanomaterials. For these experiments, only the non-fluorescent 100 nm analogues were investigated as the incident beam wavelength (λ_0= 533) in SLS is exceptionally similar to the excitation maxima for the fluorescent nanoparticles, and as SLS relies on the intensity of scattered light at various angles, any absorption will artificially reduce this value leading to erroneous results. Additionally, due to beam-line limitations only the 100 nm particles were assessed. By combining SLS and SANS data, a wider q range could be observed. The scattering profiles of all three nanoparticles showed similar features, such as a plateau at low q ($q < 0.002$; Figure 3.12b). With the combined SLS measurements, data fits using hard sphere models with particle radii of 550Å and dispersities between 0.05 and 0.15 showed good agreement with acquired data. Overall, the characterisation data confirmed the synthesised particles were highly similar to those targeted, with negligible structural differences between the different particles (except rigidity), making them suitable for this study.

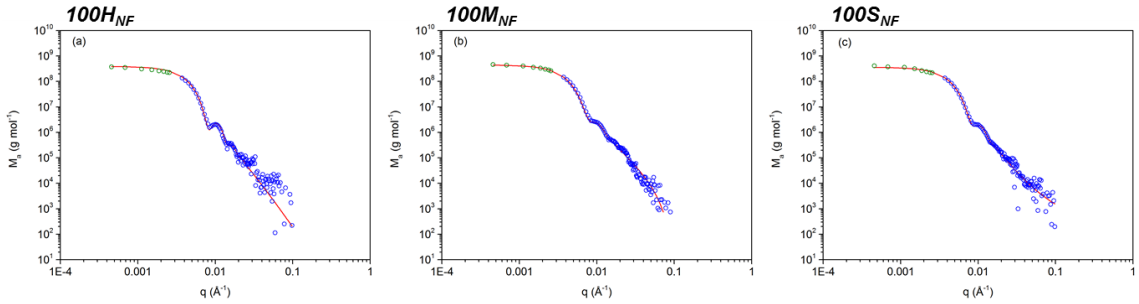

Figure 3.12. Small angle neutron scattering (blue circles), static light scattering profiles (green circles) and fits (red line) of $100H_{NF}$, $100M_{NF}$ and $100S_{NF}$ diluted in deuterium oxide.

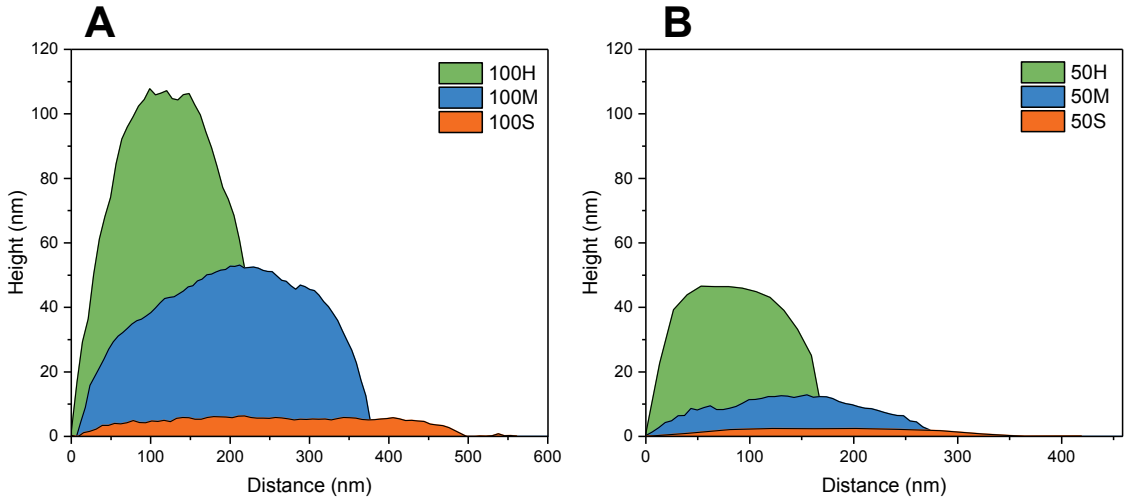

Figure 3.13 Height profiles of a single (A) 100 nm and (B) 50 nm particles with hard (green), medium (blue) and soft (orange) rigidities respectively determined by AFM. Data obtained by Dr Kai Yu and Dr Christopher Hodges at the University of Leeds.

To elucidate rigidity differences, the height profiles of the six fluorescently labelled nanoparticles were studied using AFM after deposition on silanised glass slides. These studies were performed by Dr Kai Yu and Dr Christopher Hodges at the University of Leeds, UK. The heights of both hard derivatives (100H and 50H) matched theoretical values, however the lower T_g (~-59°C) of the soft derivatives (100S and 50S) caused particle flattening, spreading them by almost two-fold compared to the hard analogues. Interestingly, the medium (T_g = 37°C) nanoparticles for both sizes displayed an intermediate maximum height suggesting these analogues did indeed have intermediate rigidity (Figure 3.13). AFM images of the nanoparticles can be found in the appendix (Figure A3.8).

3.4 Biological studies

In the above section, a library of 50 and 100 nm, fluorescent and non-fluorescent nanoparticles were synthesised and extensively characterised using a multitude of techniques. Both sets of nanoparticle sizes show almost identical physicochemical characteristics (particle size, shape and surface charge), except for rigidity; and fluorescent derivatives were completely free of unattached fluorophore. Prior to an in-depth cellular uptake study, comprehensive cytotoxicity and membrane activity experiments were performed.

3.4.1 Cytotoxicity

In the previous chapter, anti-proliferative activity studies of similar nanoparticles (P(*n*-BA) and P(*t*-BA) cores) in human colorectal adenocarcinoma cells (Caco-2), revealed negligible cytotoxicity. As we were introducing an additional nanoparticle system (PS cores), and fluorescently labelled species which had been exposed to high concentrations of 1,4-dioxane, the anti-proliferative activity of the six fluorescently labelled nanoparticles was studied with a range of cell lines using the SRB assay. Experiments were performed with murine embryonic fibroblasts (NIH 3T3), human ovarian adenocarcinoma (A2780), human colorectal adenocarcinoma (Caco-2) and human prostate cancer (PC3) with 72 h exposure with a range of concentrations (0.5 mg mL^{-1} – 10 ng mL^{-1}) (Figure 3.14). All six nanoparticles displayed around 100% cell viability at all concentrations in all cell lines, suggesting that the introduction of BODIPYA, or presence of residual 1,4-dioxane had a negligible effect on cytotoxicity on both healthy and cancer cells of various types.

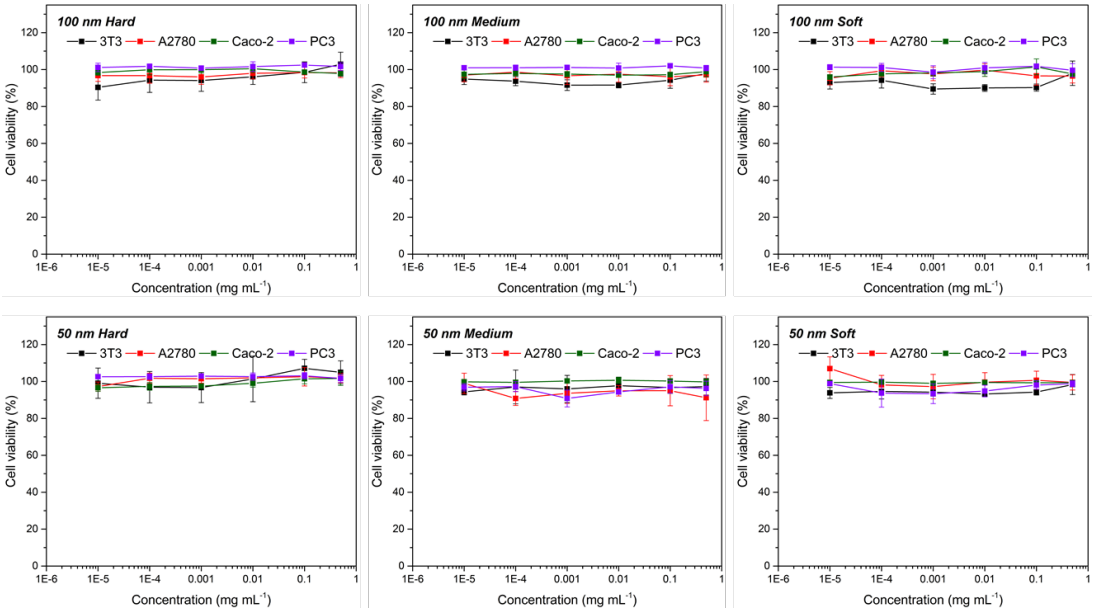

Figure 3.14 Antiproliferative activity of 100H, 100M, 100S, 50H, 50M, 50S fluorescently-labelled nanoparticles, each incubated with NIH 3T3, A2780, Caco-2 and PC3 cells for 72 h, as measured using typical protocol for the SRB assay.

3.4.2 Membrane activity

The membrane activity of the nanoparticles was established using a haemolysis assay using sheep blood. This assay requires absorbance measurements between 400-600 nm wavelengths, which is around the absorption maxima of BODIPYA, hence experiments were performed using the non-fluorescent nanoparticles. Three concentrations (0.1, 0.05 and 0.01 mg mL^{-1}) of each nanoparticle diluted in phosphate buffer saline (PBS) were incubated for 1 h with a dilute erythrocyte suspension and the absorbance recorded at 415 nm to monitor haemoglobin release. Control experiments with pure water and PBS (negative controls) and, 1 wt% Triton-X (positive control, 100% haemolytic activity) were performed in parallel. All of the nanoparticles displayed less than 8% haemolytic activity (in comparison to Triton-X), with either similar or less haemoglobin released in comparison to water (8%) or PBS (7.5%) (Figure 3.15). Overall, this suggests that the particles have low membrane interactions, likely due to the negative surface charge and P(PEGA) surface (steric repulsion), which disfavours interaction with the negatively charged lipid membrane. No notable differences in membrane activity were observed between nanoparticle rigidities.[5]

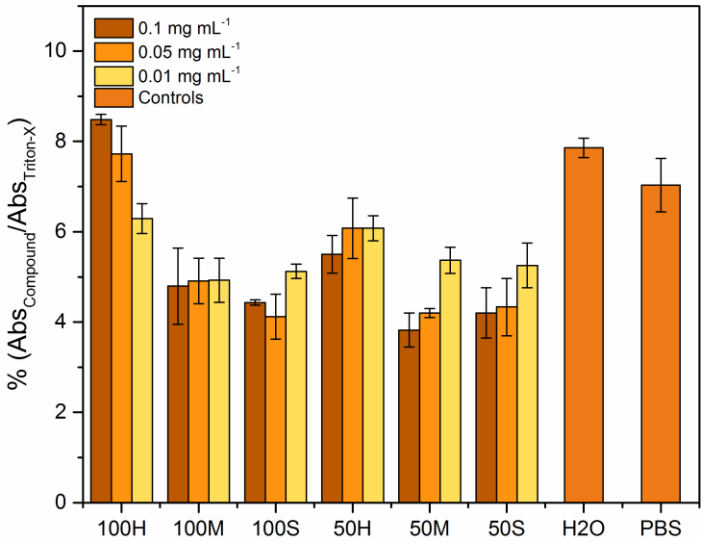

Figure 3.15. Haemolytic activity of the non-fluorescent nanoparticles $100H_{NF}$, $100M_{NF}$, $100S_{NF}$, $50H_{NF}$, $50M_{NF}$ and $50S_{NF}$ measured with % release of haemoglobin as compared to positive control triton-x (1 wt%), and negative controls (H_2O and PBS).

3.4.3 Fluorescence correction factor calculation

Prior to any cellular uptake studies, fluorescence correction factors were established to enable direct quantitation between compounds. This was imperative as the $UV_{520\ nm}$ SEC showed that a different amount of BODIPYA was incorporated into the nanoparticles, which would result in a different fluorescence intensity. In the following cellular uptake studies (*vide infra*), uptake was monitored using a Cytation3^{TM} imaging plate reader with an RFP filter cube (λ_{ex} = 531 ± 20 nm, λ_{em} = 593 ± 20 nm). Fluorescence intensities were therefore determined across a range of concentrations for all six fluorescently labelled nanoparticles using the above wavelengths (Figure 3.16). A linear fit was applied to the acquired intensities, and the slope used to calculate the correction factors. Correction factors were normalised for 100 and 50 nm particles separately, with both soft varieties (50S and 100S) set to 1.00 (Table 3.5).

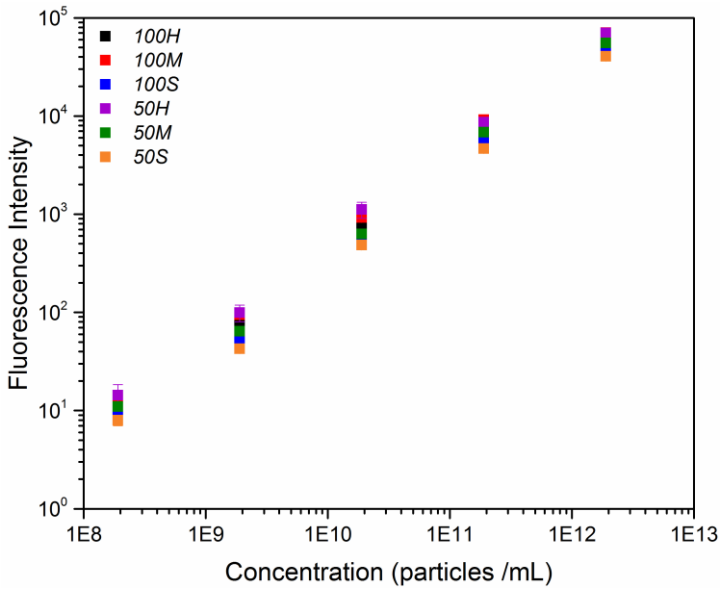

Figure 3.16. Fluorescence normalisation/calibration curves for different particles to account for differences in fluorescence intensity. λ_{ex} = 531 nm λ_{em} = 593 nm (Settings for RFP imaging cube in Cytation 3 imaging system)

Table 3.5. Fluorescence correction factors normalised to 100S for 100 nm particles and 50S for 50 nm particles.

	Slope	R^2 [a]	Correction factor
100H	70602	0.9997	1.38
100M	70810	0.9999	1.39
100S	51125	0.9994	1.00
50H	70568	0.9995	1.74
50M	55731	0.9995	1.38
50S	40529	0.9991	1.00

[a] R^2 values determined using a linear fit on Origin Pro 2016.

3.4.4 Cellular uptake studies

As experiments were performed with two different particle sizes (50 nm and 100 nm), at the same mass concentration (e.g. 100 µg mL^{-1}) the 100H and 50H, for example, would have vastly different particle concentrations (e.g. particle mL^{-1}), calculated using Equation 2.11. For instance, in a typical uptake experiment the mass concentration (100 µg mL^{-1}) would equate to 1.9 x 10^{11} mL^{-1} for 100 nm particles but 1.5 x 10^{12} for 50 nm particles, almost an order of magnitude difference. For clarity, uptake will therefore only be compared within particle sizes, and not between them.

3.4.4.1 Effect of particle concentration

Initially a cellular uptake study was performed with all six fluorescently labelled nanoparticles at three different concentrations (200 µg mL^{-1}, 100 µg mL^{-1} and 50 µg mL^{-1}), to establish at what concentration the particles were detectable. The different concentrations of nanoparticles were incubated with colorectal carcinoma cells (Caco-2) for 2 h, at 37°C, and the cellular uptake efficiency was quantified by fluorescence imaging (Cytation3 imaging system), and normalised to the 'soft' nanoparticles for both sizes at 200 µg mL^{-1} as in section 3.4.3 (Figure 3.17).

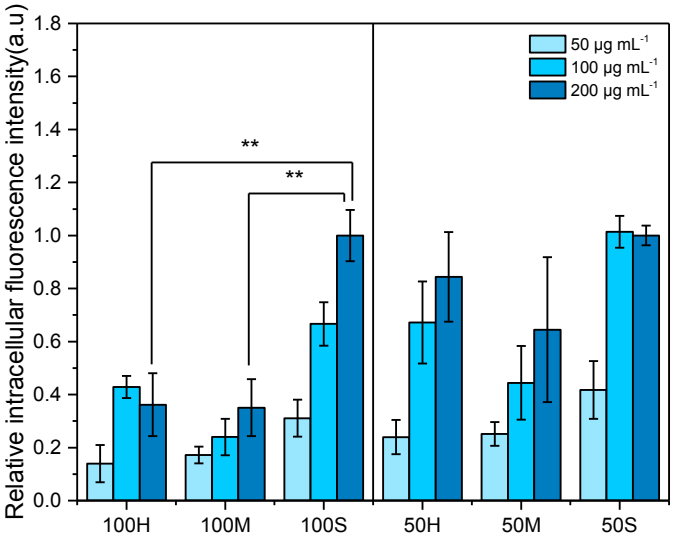

Figure 3.17. Relative intracellular fluorescence intensity after 2 h incubation with 100H, 100M, 100S, 50H, 50M and 50S nanoparticles with Caco-2 cells across three concentrations (200 µg mL^{-1}, 100 µg mL^{-1} and 50 µg mL^{-1}). The reported data represent the mean ± standard deviation for two independent experiments with each treatment performed in triplicate. Asterisks indicate relevant statistically significant results as determined by an analysis of variance (ANOVA) statistical test and a Tukey-Kramer post hoc test (*$p \leq 0.05$, **$p \leq 0.01$), with a 95% confidence interval.

As a general trend, an increase in intracellular fluorescence was observed with higher treatment concentration. At 50 µg mL^{-1} relatively little difference in uptake was observed between particles, suggesting that not enough nanoparticles were internalised to accurately detect any fluctuations between rigidity. However, for both 100 µg mL^{-1} and 200 µg mL^{-1} the variation was much higher and in general had lower variation between replicates. For these reasons, future experiments were performed at 100 µg mL^{-1}. This preliminary experiment shows a greater cellular uptake of the 100S nanoparticles compared to 100H and 100M, with a less pronounced trend for the 50 nm derivatives (Figure 3.17).

3.4.4.2 Time dependent cellular uptake

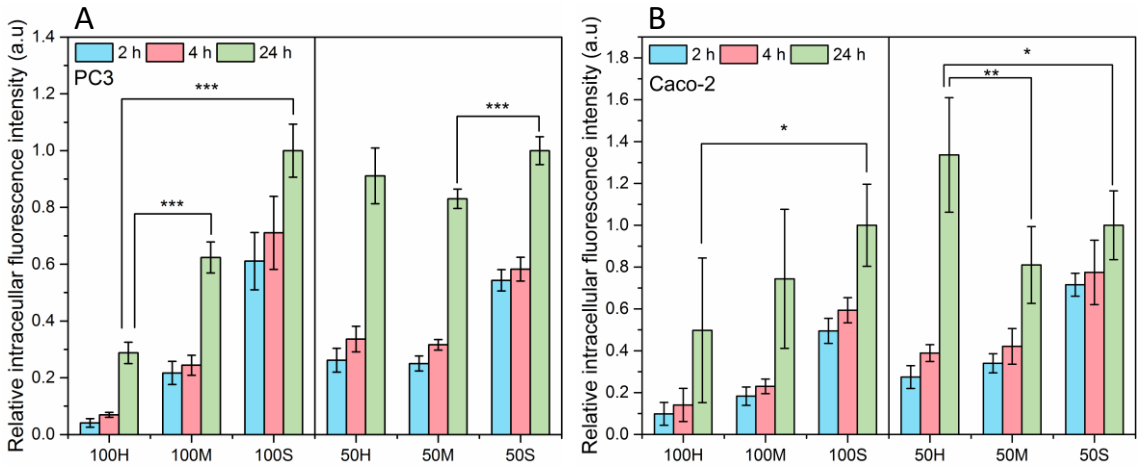

Figure 3.18. Relative intracellular fluorescence intensity after 2 h (blue), 4 h (red), and 24 h (green) incubation with 100H, 100M, 100S, 50H, 50M and 50S nanoparticles with (A) PC3 cells and (B) Caco-2 cells at 100 µg mL^{-1} for 50 nm particles. The reported data represent the mean ± standard deviation for two independent experiments with each treatment performed in triplicate. Asterisks indicate relevant statistically significant results as determined by an analysis of variance (ANOVA) statistical test and a Tukey-Kramer post hoc test (*$p \leq 0.05$, **$p \leq 0.01$, ***$p \leq 0.001$) with a 95% confidence interval.

To better elucidate the differences between nanoparticle rigidities, a time-dependent uptake experiment was performed. All six labelled nanoparticles were incubated for 2 h, 4 h and 24 h at 37°C with both PC3 and Caco-2 cells and intracellular fluorescence normalised as above (section 3.4.3). For 100 nm particles, a clear correlation was observed between uptake efficiency/uptake rate with decreasing rigidity. 100S nanoparticles displayed greater internalisation than the medium and hard counterpart ((2.9 x for 100S-100H) and (1.5 x for 100S-100M) after 24 h), following the trend 100S > 100M > 100H. This difference was best observed in PC3 cells, where cells treated for only 2h with 100S nanoparticles displayed almost double the uptake than 100H

nanoparticles treated for 24 h. In contrast, the 50 nm nanoparticles all displayed similar internalisation after 24 h (Figure 3.18a). Similar values were observed in Caco-2 cells supporting the observed trends (Figure 3.18b). It should be noted that the larger errors observed in Caco-2 data arise from inconsistent cell morphology leading to poorer analysis of images from the Cytation3 imaging systems. Overall, these results suggest that differences in rigidity may be size dependent with smaller sizes less affected than larger sizes. Vogt and co-workers reported that for thin films with >100 nm film thickness, the elastic moduli matched those of bulk materials. However, if the thickness of the film was <50 nm, the onset of confinement effects reduced the difference in elastic moduli for materials with differing T_g, making them more similar to each other.[31] Interestingly, this could explain the differences that we observe for the internalisation of our particles. Rigidity should influence both degree and rate of cellular uptake if particles behaved as bulk materials (100 nm diameter systems; soft nanoparticles are preferred over medium and hard nanoparticles). However, it is possible that at smaller sizes (50 nm diameter), the differences in rigidity are negligible thus reducing the effect on cellular uptake.

Notably, in both cell lines and for all nanoparticles, an increasing trend was observed with incubation time, with much higher internalisation after 24 h than 2 h and 4 h. This is indicative of nanoparticle accumulation, likely due to the a higher rate of endocytosis over exocytosis, well known for nanomaterials.[8]

As mentioned in section 3.1, there is little consensus in the literature on how particle rigidity affects cellular uptake, with either material variation (shape, size and surface hydrophobicity), cell line effects (cancer vs immune cells), and different experimental conditions (incubation time, particle concentration and measurement techniques) cited for the diverse results reported. [12-16, 32-36] Nonetheless, our nanoparticles showed a similar trend than that reported by Lorenz *et al*. They showed increased cellular uptake, in both malignant and primary cells, with reducing particle rigidity using uncoated 140 nm latex nanoparticles, prepared by altering the poly(*n*-alkyl methacrylate) cores. However, it should be noted that by increasing the side chain length of their polymers (methyl methacrylate to stearyl methacrylate), they also heavily influence the surface hydrophobicity of these nanoparticles, making rigidity effects indiscernible. In contrast, the P(PEGA) shell on our nanoparticles is expected to eliminate this entirely.

3.4.4.3 Energy dependency

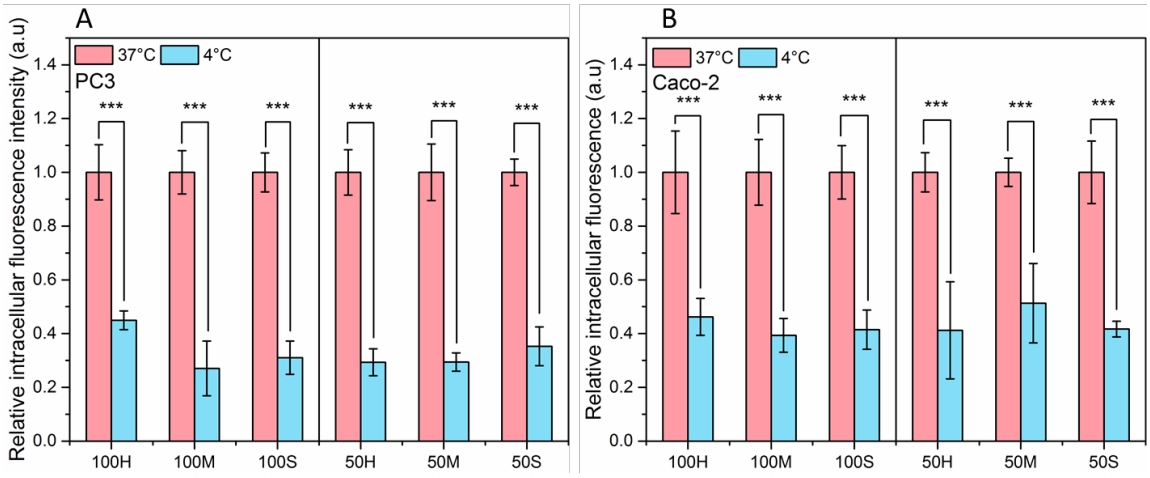

Figure 3.19. Relative intracellular fluorescence intensity after 2 h incubation at 37°C (red) and 4°C (blue; inhibition of energy-dependent pathways) with 100H, 100M, 100S, 50H, 50M and 50S nanoparticles with (A) PC3 cells and (B) Caco-2 cells at 100 μg mL^{-1}. The reported data was normalised to 37°C data and represent the mean ± standard deviation for two independent experiments with each treatment performed in triplicate. Asterisks indicate relevant statistically significant results as determined by an ANOVA and post-hoc Tukey-Kramer test (*$p \leq 0.05$, **$p \leq 0.01$, ***$p \leq 0.001$).

In order to probe the energy dependency of nanoparticle internalisation, the above uptake experiment was performed at 4°C, but with a 2 h incubation. This reduction in temperature inactivates the production of adenosine triphosphate (ATP) and therefore energy dependent pathways. In both cell lines, all nanoparticles displayed a large reduction in cellular uptake (~60-70%; $p < 0.001$), suggesting that the uptake mostly relies on energy dependent pathways, such as endocytosis. This is in accordance with much of the previous literature on nanoparticle uptake pathways.[37-39] It should be noted that a complete reduction (100%) in intracellular fluorescence was not observed. It is likely that this is due to an imperfect inactivation of energy dependent pathways, and not a small amount of passive uptake, with similar observations made in other studies.[7, 40]

3.4.4.4 Endocytosis mechanism

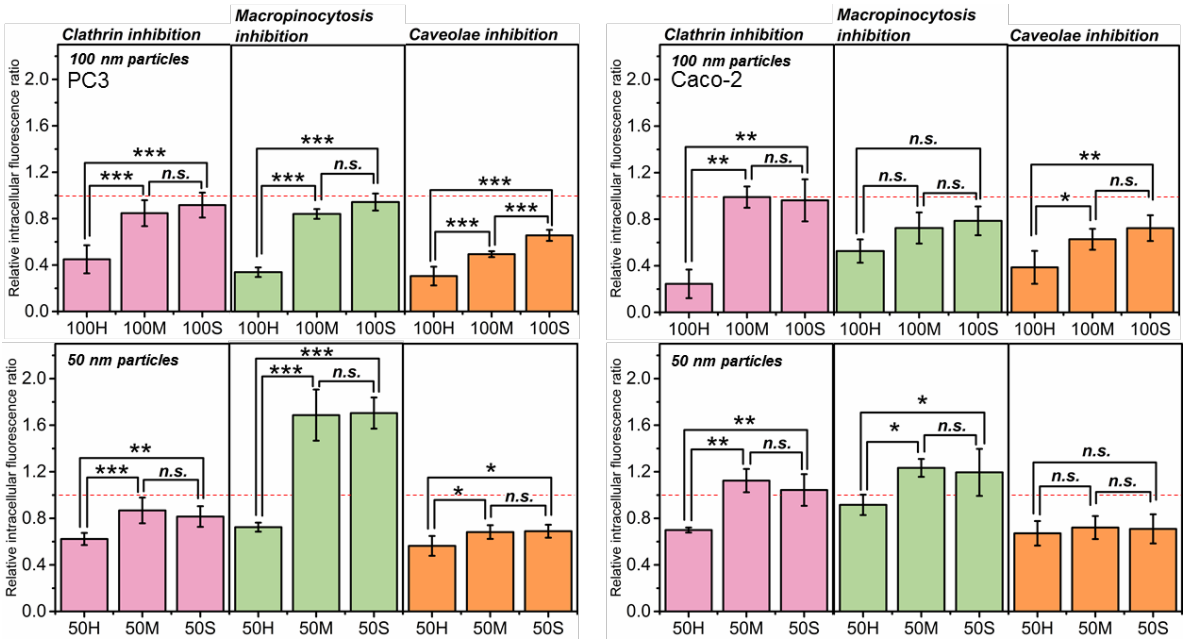

Figure 3.20. Relative intracellular fluorescence intensity after 3 h pre-treatment with endocytosis inhibitors for clathrin- (chloropromazine) and caveolae-(genistein) mediated endocytosis and macropinocytosis (amiloride), and subsequent 2 h incubation with 100H, 100M, 100S, 50H, 50M and 50S nanoparticles with (A) PC3 cells and (B) Caco-2 cells at 100 µg mL^{-1} compared. The reported data represent the mean ± standard deviation for two independent experiments with each treatment performed in triplicate. Asterisks indicate relevant statistically significant results as determined by an ANOVA and post-hoc Tukey-Kramer test (*$p \leq 0.05$, **$p \leq 0.01$, ***$p \leq 0.001$).

There are many possible endocytic uptake mechanisms for uptake of nanoparticles, including: clathrin-mediated endocytosis, micropinocytosis, caveolae-mediated endocytosis, and other independent endocytosis pathways. These pathways can be selectively blocked by addition of specific endocytosis inhibitors: chlorpromazine for clathrin mediated endocytosis; amiloride for macropinocytosis; and genistein for caveloae mediated endocytosis into the culture medium. By conducting cellular uptake experiments with these inhibitors, differences in uptake mechanism between different nanoparticle rigidities can be elucidated. Both Caco-2 and PC3 cells were pre-treated with each of the above endocytosis inhibitors for 3 h and then exposed to each of the labelled nanoparticles. Intracellular fluorescence was then monitored relative to an untreated (no endocytosis inhibitor) control. After treatment with chlorpromazine, which inhibits the assembly of clathrin on endosomal membranes, a larger reduction in uptake was observed for 100H (60-80% decrease) than for 100M and 100S, which showed similar 10-20% reductions. In contrast, the 50 nm particles had a smaller difference in uptake between 50H (50% reduction) and 50M/50S (0-20% reduction) nanoparticles. This suggests that

for both sizes, the harder nanoparticles were preferentially taken up via clathrin-mediated endocytosis over the medium and soft analogues. Treatment with amiloride, a compound which inhibits macropinocytosis by targeting the Na^+/H^+ exchange at the cell surface, showed similar results to chlorpromazine addition, with the exception of 50M and 50S. These nanoparticles showed a surprising increase in intracellular fluorescence (60% increase) compared to the untreated controls. This is typically attributed to a decrease in exocytosis caused by the inhibitor.[41] Finally, caveolae inhibition with genistein, a tyrosine-kinase inhibitor which reduces the recruitment of dynamin II, a key protein in caveolae mediated endocytosis, displayed vastly different results between particle sizes and rigidities. Interestingly, for the 100 nm derivatives a clear trend was observed in PC3 cells, where the lower reduction in uptake (i.e. less uptake via caveolae mediated endocytosis) correlated with increasing flexibility (70% > 55% > 30% reduction for 100H > 100M > 100S respectively). For 50 nm nanoparticles a 40-50% decrease was observed, however this was similar regardless of rigidity (Figure 3.20).

Our results indicate that nanoparticle rigidity significantly impacts their uptake mechanism. Soft and medium rigidity nanoparticles mostly go through caveolae-mediated endocytosis or other independent endocytosis pathways, while hard nanoparticles are taken up through a combination of the three pathways tested, with a clear preference for clathrin and caveolae mediated endocytosis. This effect on caveolae mediated endocytosis has been previously reported for larger 1 μm hydrogel particles, with no prior knowledge on nanoscale particles.[15] It is well known that caveolae can act as mechanosensors on the cell surface, capable of responding to mechanical stress by acting as membrane reservoirs.[42, 43] It is therefore possible that particles with higher rigidity may induce a greater caveolae response after interaction with the cellular membrane. This could account for the clear trend observed in the 100 nm particles, and also explain why relative internalisation between the 50 nm derivatives *via* caveolae-mediated endocytosis was similar, supporting our previous hypothesis that differences in rigidity are less pronounced with smaller size nanoparticles.

3.4.5 Intracellular trafficking

Confocal laser scanning microscopy (CLSM) was used to further study the intracellular trafficking and location of the nanoparticles after internalisation. Initially, PC3 cells were incubated with each of the labelled nanoparticles for 2 h, 4 h and 24 h at 37°C and for 2 h at 4°C, similarly to the uptake experiments in section 3.4.4.2 and section 3.4.4.3. Lysosomes and nuclei were selectively stained with LysoTracker™ Deep Red and Hoechst 33258 respectively.

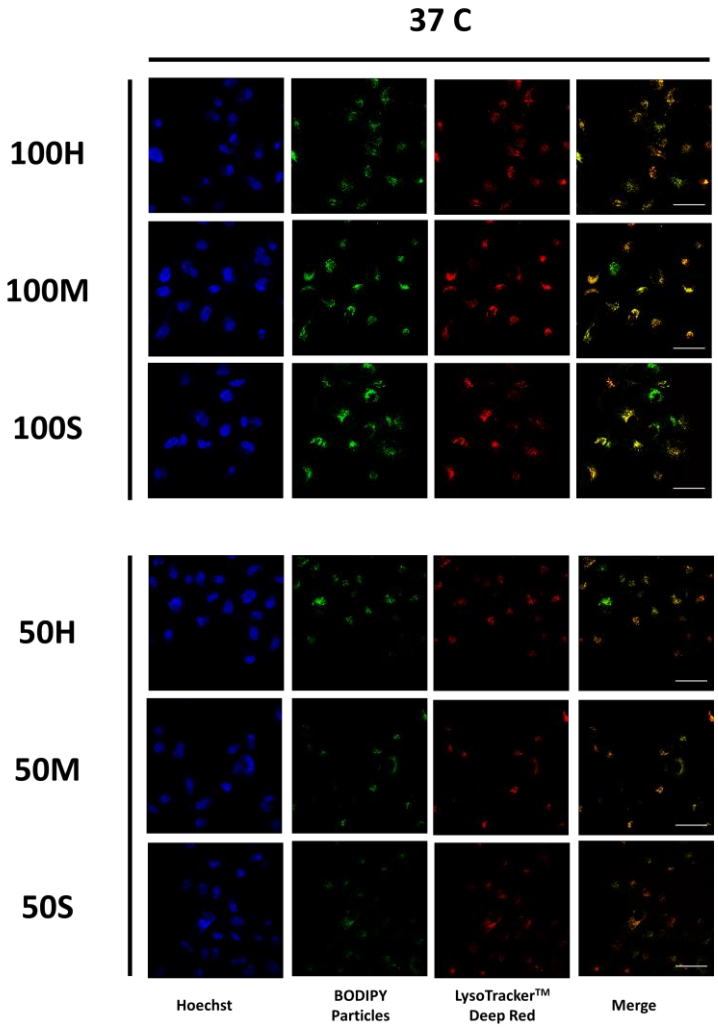

Figure 3.21. CLSM images of PC3 cells incubated with fluorescently-labelled nanoparticles (green; 100H, 100M, 100S, 50H, 50M and 50S) at 100 μg mL^{-1}, incubated for 2 h at 37°C. Lysosomes and nuclei were stained with Lysotracker™ Deep Red (final concentration 50 nM) and Hoechst 33258 (final concentration 5 μg mL^{-1}) respectively. Merged images are a combination of green and red channels. Scale bars are 50 μm in length.

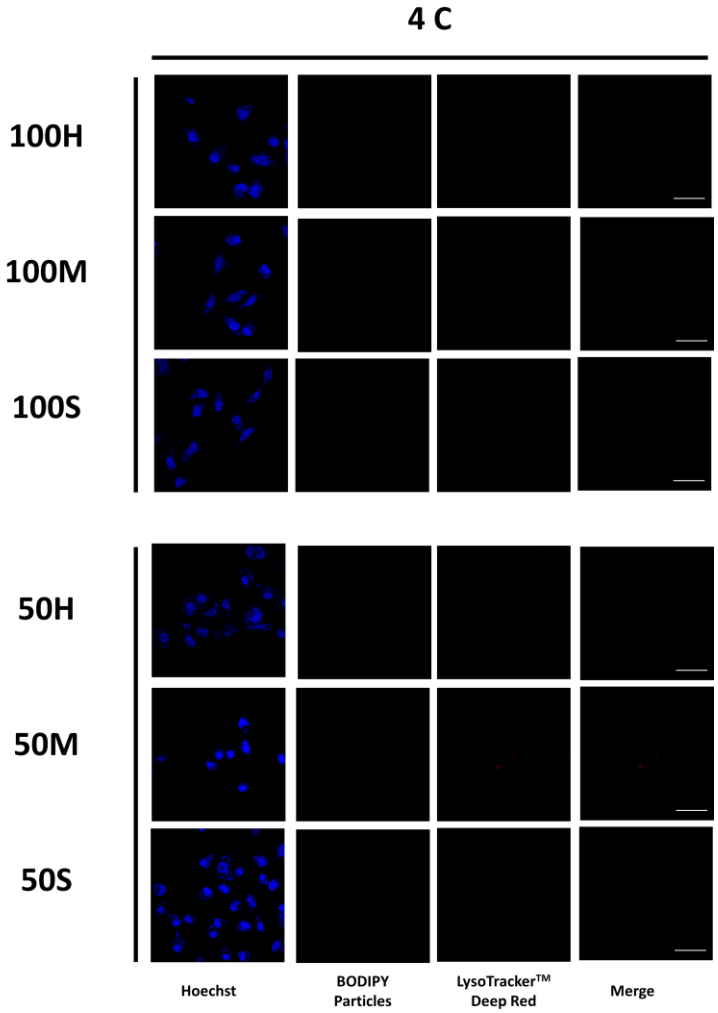

Figure 3.22. CLSM images of PC3 cells incubated with fluorescently-labelled nanoparticles (green; 100H, 100M, 100S, 50H, 50M and 50S) at 100 μg mL^{-1}, incubated for 2 h at 4°C. Lysosomes and nuclei were stained with Lysotracker™ Deep Red (final concentration 50 nM) and Hoechst 33258 (final concentration 5 μg mL^{-1}) respectively. Merged images are a combination of green and red channels. Scale bars are 50 μm in length.

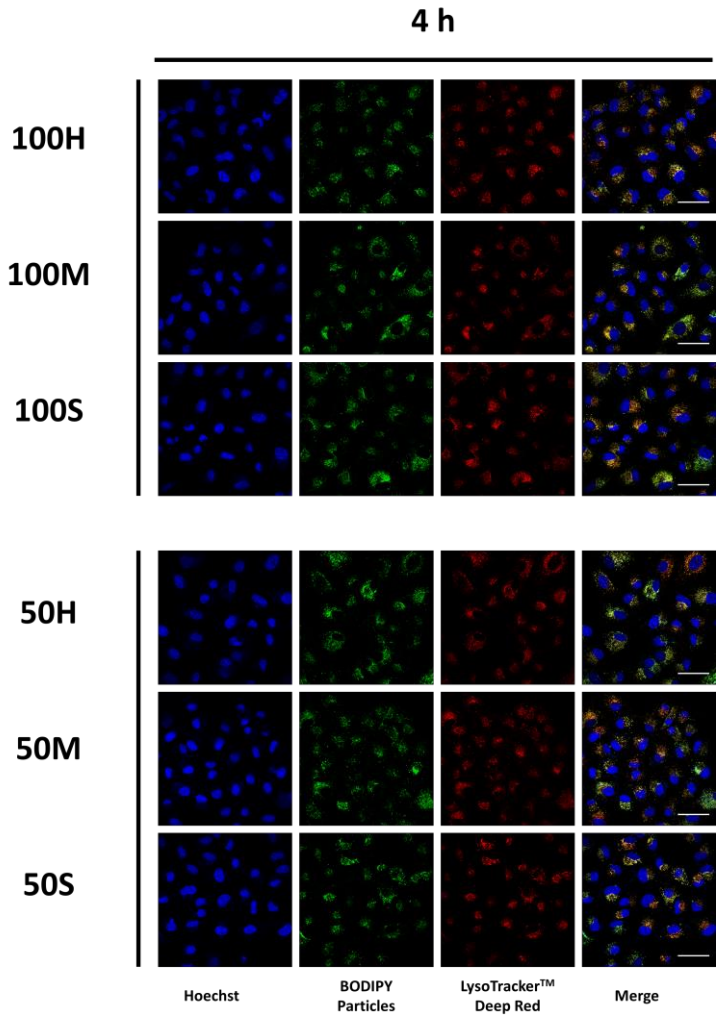

Figure 3.23. CLSM images of PC3 cells incubated with fluorescently labelled nanoparticles (green; 100H, 100M, 100S, 50H, 50M and 50S) at 100 μg mL^{-1}, incubated for 4 h at 37°C. Lysosomes and nuclei were stained with Lysotracker™ Deep Red (final concentration 50 nM) and Hoechst 33258 (final concentration 5 μg mL^{-1}) respectively. Merged images are a combination of green, red and blue channels. Scale bars are 50 μm in length.

After incubation at 4°C, no fluorescence was observed from any of the labelled nanoparticles, nor from the Lysotracker™ Deep Red channel (Figure 3.21). This is in accordance with the previous cellular uptake experiment (Section 3.4.4.3), confirming that uptake of the nanoparticles was indeed energy dependent.

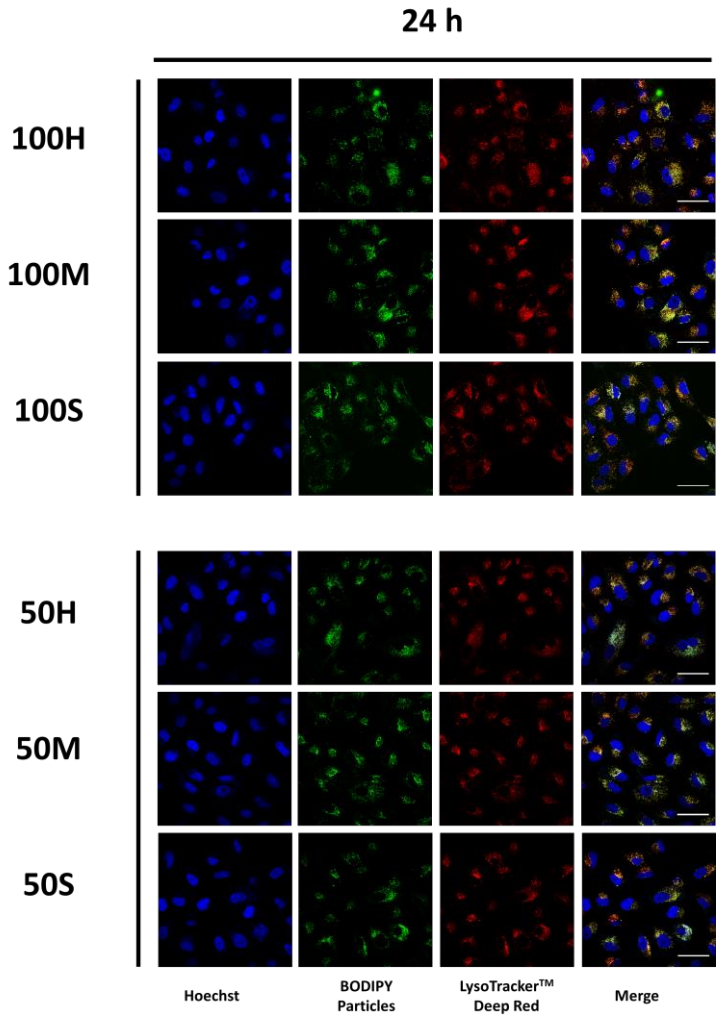

Figure 3.24. CLSM images of PC3 cells incubated with fluorescently labelled nanoparticles (green; 100H, 100M, 100S, 50H, 50M and 50S) at 100 μg mL^{-1}, incubated for 4 h (left) or 24 h (right) at 37°C. Lysosomes and nuclei were stained with Lysotracker™ Deep Red (final concentration 50 nM) and Hoechst 33258 (final concentration 5 μg mL^{-1}) respectively. Merged images are a combination of green, red and blue channels. Scale bars are 50 μm in length.

Imaging of cells treated for 2 h (Figure 3.21), 4 h (Figure 3.23) and 24 h (Figure 3.24) at 37°C showed a high degree of colocalisation between fluorescent nanoparticles and LysoTracker™ (Pearsons correlation coefficient (PCC) = >0.65) was observed, with all particles reaching the lysosome within 2 h of incubation. Interestingly, it has been previously shown that soft microcapsules (4-5 μm diameter) display faster accumulation in the lysosome as compared to stiff ones.[14] However, there were no obvious differences in the intracellular distribution between our soft and hard nanoparticles (for incubations 2 h or longer). Overall, this verified our previous uptake experiments, and confirmed the conventional endosomal-lysosomal trafficking route as the main internalisation mechanism for the nanoparticles.

3.5 Conclusions

In conclusion, using a library of core-shell nanoparticles with three different core T_g and the same surface properties we have investigated the effect of nanoparticle rigidity on the degree, rate and mechanism of uptake by mammalian cells (PC3 and Caco-2). Our study has demonstrated that this parameter does indeed have a significant effect, with softer nanoparticles being internalised faster and to a higher degree than their harder counterparts. This effect however was more prominent for the larger 100 nm particles, with 50 nm particles only displaying minor favourability towards softer particles after 2 and 4 h, and almost none after 24 h. We anticipate that at smaller diameters, confinement effects reduce the difference in rigidity between nanoparticles of different core T_g, thus reducing the impact on cellular uptake. All of the core-shell particles were internalised through energy dependent mechanisms, however particles of different rigidity follow different internalisation pathways: harder nanoparticles go through a combination of clathrin- and caveolae- mediated endocytosis, as well as non-specific macropinocytosis, while softer and medium rigidity nanoparticles are preferentially taken up by caveolae- and other independent endocytosis mechanisms. Interestingly with 100 nm particles, we saw an increasing trend in uptake *via* caveolae-mediated endocytosis of hard > medium > soft nanoparticles, possibly due to their known mechanosensing behaviour at the cell surface, however further investigation is required to fully explain this. Finally, no differences were observed in the intracellular localisation of these nanoparticles, with all following the expected endo-lysosomal route. Overall, our results demonstrate rigidity is a fundamental physicochemical factor in nanoparticle cell uptake, paying particular attention to how this interacts with other important parameters such as nanoparticle size. This study also highlights the usefulness of RAFT emulsion polymerisation, allowing the generation of precisely designed nanoparticles for a fundamental biological study.

3.6 Materials and Methods

3.6.1 Materials

Styrene (>99%), kryptopyrrole (>99%), DDQ (>99%), 4-hydroxybenzaldehyde (>99%), acryloyl chloride (>99%) was obtained from Sigma-Aldrich and all monomers above were passed through basic aluminium oxide to remove inhibitor before polymerisation. Dimethyl sulfoxide-d_6 (99.9% D atom) and chloroform-d_3 (99.8% D atom), were obtained from Sigma Aldrich and used for ^{1}H NMR spectroscopy. Thermal initiators 4,4′-azobis(4-cyanovaleric acid) (ACVA, >98%, Aldrich), 2,2'-Azobis(cyclohexanecarbonitrile) (VA-088, 98%, Aldrich) and 2,2'-Azobis[N-(2-carboxyethyl)-2-methylpropionamidine]tetrahydrate (VA-057, 98%, Wako) were used as received. RAFT agent, 2-(((butylthio)carbonothioyl)thio)propanoic acid (PABTC) was synthesised as previously described.[44] Macro-RAFT agents **MRA-*n*BA** (P[(PEGA)$_8$-*b*-(*n*-BA)$_8$] and **MRA-*t*BA** (P[(PEGA)$_8$-*b*-P(*t*-BA)$_8$] were synthesised in chapter 2. BODIPY acrylate was synthesised as previously described (data below).[29] PABTC was synthesised using previously described conditions as in chapter 2 (Section 2.4.3.1).[44] Solvents were acquired from commercial sources. Materials for cell culture were purchased from Greiner Bio-one, and culture medium prepared in-house.

3.6.2 Instrumentation and Analysis

3.6.2.1 NMR spectroscopy

^{1}H NMR and ^{13}C NMR spectra were recorded as described in section 2.4.2.1

3.6.2.2 Size exclusion chromatography

$CHCl_3$-SEC was performed using conditions described in section 2.4.2.2

THF-SEC was performed using conditions described below: Agilent 390-LC MDS instrument equipped with differential refractive index (DRI) and dual wavelength UV detectors. The system was equipped with 2 x PLgel Mixed D columns (300 x 7.5 mm) and a PLgel 5 μm guard column. The eluent was THF with 2% TEA (triethylamine) and

0.01% BHT (butylated hydroxytoluene) additives. Samples were run at 1 mL min^{-1} at 30°C. Poly(methyl methacrylate) and polystyrene standards (Agilent EasyVials) were used for calibration. Analyte samples were filtered through a GVHP membrane with 0.22 μm pore size before injection. Respectively, experimental molar mass ($M_{n,SEC}$) and dispersity (Đ) values of synthesised polymers were determined by conventional calibration using Agilent SEC software. BODIPY functionalised polymers were analysed with the UV detector set to 520 nm.

3.6.2.3 Theoretical molar mass calculation

Theoretical molar masses were calculated as described in section 2.4.2.3

3.6.2.4 High performance liquid chromatography (HPLC)

HPLC was performed using an Agilent 1260 infinity series stack equipped with an Agilent 1260 binary pump and degasser. The flow rate was set to 1.0 $mLmin^{-1}$ and samples were injected using Agilent 1260 autosampler with a 100 μL injection volume. The temperature of the column was set at 25 °C. The HPLC was fitted with a phenomenex Lunar C18 column (250 x 4.6 mm) with 5 micron packing (100Å). Detection was achieved using an Agilent 1260 variable wavelength detector. UV detection was monitored at λ = 520 nm. Methods were edited and run using Agilent OpenLAB online software and data was analysed using Agilent OpenLAB offline software. Mobile phases solvents used were HPLC grade and consisted of mobile phase A: 100% water, 0.04% TFA; mobile phase B: 100% methanol, 0.04% TFA using a gradient of 50 - 100% methanol over 30 minutes.

3.6.2.5 Dynamic light scattering and ζ-potential

DLS and ζ-potential measurements were carried out as described in 2.4.2.4. DLS measurements in DMEM (phenol red free) were performed at 37°C, and the optical constants set the same as water. *PDi* values were calculated as in Equation 2.13.

3.6.2.6 Small angle neutron scattering

Experiments were performed at the instrument D11 at the Institut Laue-Langevin (ILL) in Grenoble, France. A wavelength of $\lambda = 6$ Å with a polydispersity of $\Delta\lambda/\lambda = 10\%$ was used. The scattering intensity was detected on a ^{3}He gas detector (CERCA) with a detection area of 96×96 cm^2 and a pixel size of 3.75×3.75 mm^2. Narrow Hellma quartz glass cells (type 110-QS) with 1 mm sample thickness were used. Samples were measured at three sample-detector distances of 1.2 m, 10 m and 20 m to cover a wide range of scattering vector, *q,* with a decent measurement time. Q is defined as:

$$Q = \frac{4\pi \sin\frac{\theta}{2}}{\lambda}$$

Equation 3.1. Calculation of scattering vector Q

Where θ is the scattered angle and λ is the incident neutron wavelength. The incoherent scattering of water was measured as secondary calibration standard at 10 m sample-detector distance. All data were corrected for transmission, empty cell scattering and background scattering to receive absolute values for the differential cross section. Additional q values were measured with static light scattering. The solutions of nanoparticles were prepared by diluting the latexes by 1000 fold by direct dilution in D_2O. Scattering fits were calculated using a hard sphere model using open access software SASfit.

3.6.2.7 Static light scattering

Static light scattering measurements were performed as described in section 2.4.2.5.

3.6.2.8 Differential Refractometry.

Differential refractometry was performed as described in section 2.4.2.6.

3.6.2.9 Differential Scanning Calorimetry

Measurements were performed on dry samples of particle suspensions using a Mettler Toledo DSC1 using a scan rate of 10 K/min in a temperature range of -100 to 150°C. The glass transition temperature (T_g) was recorded as the first derivative (dH/dT) of the second heating run.

3.6.2.10 Transmission electron microscopy

Nanoparticles were diluted 1/1000 in pure water and a 10 μL drop of the diluted sample was immediately deposited onto a hydrophobic surface (plastic petri dish). The graphene oxide-coated surface of the TEM grid was then placed on the droplet for 1 minute, then left to dry before imaging. A JEOL 2100FX electron microscope at an acceleration voltage of 200 kV was used to carry out the imaging.

3.6.2.11 Cryogenic-transmission electron microscopy

Cryo-TEM images were obtained using conditions described in section 2.4.2.7.

3.6.2.12 Fluorescence excitation/emission spectroscopy

Fluorescence emission spectra were measured using an Agilent Cary Eclipse fluorescence spectrometer. Studies were performed by exciting at the absorption maxima of BODIPYA (528 nm) and measured from 530 nm to 750 nm. Excitation spectra were measured by setting the maximum emission to 542 nm, and recording from 300 to 530 nm. The photomultiplier voltage was set such that the maxima was below 1000 arbitrary units.

3.6.2.13 Atomic force microscopy and height profiles

Microscope slides were cleaned by sonication in Milli-Q water for 30 min, after which the glass slides were air-dried and left in a UV-ozone cleaner (Bioforce Nanoscience, USA) for 3 h to eliminate remnant organics. The UV-cleaned slides were rinsed with Milli-Q water and air-dried before being left in a desiccator. 2 mL (3-Aminopropyl)triethoxysilane (APTES) was added into a watch-glass and left in the same desiccator overnight for silanization. The success of silanization was confirmed by wetting angle measurement of the glass slides, increasing from 15 ± 2.3° (before silanization) to 50 ± 3.1° (after silanization).

A Bioscope II AFM (Bruker, USA) was used to carry out particle imaging using sharpened silicon nitride probes with a spring constant of 43.5 N/m (sensitivity: 38.5 nm/V) in tapping mode in dry state, scanning at 0.5 HZ (512 lines per image). Silanized microscope slides were cut (15 × 24.5 mm) and were dipped into particle dispersions (100H, 100M, 100S, 50H, 50M and 50S) with a concentration of ~ 0.05 mg mL^{-1} for 30 min to ensure particle adsorption on the silanized microscope slides, after which the microscope slides were rinsed with Milli-Q water to remove excess particles and left to air-dry before imaging.

3.6.3 Synthesis

3.6.3.1 BODIPY phenol synthesis

Hydroxybenzaldehyde (0.5 g, 4.07 mmol, 1 eq) was added to a stirred solution of kryptopyrrole (1 g, 8.11 mmol, 2 eq) in 200 mL anhydrous dichloromethane in an oven-dried 500 mL round bottomed flask. The mixture was purged with dinitrogen for 15 minutes. Four drops of trifluoroacetic acid (catalytic amounts) was added to the above mixture, turning it to a deep red colour, then sealed with a rubber septum and left to stir at room temperature overnight and progress checked using thin layer chromatography (100% DCM). In a separate flask, 2,3-dichloro-5,6-dicyano-1,4-benzoquinone (0.92 g, 4.07 mmol, 1 eq) was dissolved in 100 mL dichloromethane and added dropwise to the reaction mixture *via* syringe turning the solution a turbid black-red colour and left to stir at room temperature for 4 h. Diisopropylethylamine (3.67 g, 5 mL, 28.5 mmol, 7 eq) and subsequently boron trifluoride diethyl etherate (11.64 mL, 44.77 mmol, 11 eq) were added slowly *via* syringe and left to stir for 1 h at room temperature. The reaction mixture was then poured on to a 10-15 cm silica pad and washed using dichloromethane using Buchner filtration and the filtrate collected and subsequently evaporated under reduced pressure. The crude product was then dissolved in a small amount of dichloromethane and purified using automatic column chromatography using an eluent of 100% dichloromethane to yield BODIPY phenol as a bright red powder (488 mg, 30% yield). ^{1}H NMR (500 MHz, 298 K, $CDCl_3$) δ_H (ppm) 7.06 (d, J = 8.4 Hz, 2H, Ar-**H**), 6.87 (d, J = 8.4 Hz, 2H, Ar-**H**), 4.94 (s, 1H, Ar-O**H**), 2.46 (s, 6H, C**H**$_3$), 2.23 (q, J = 7.6 Hz, 4H, C**H**$_2$-CH$_3$), 1.28 (s, 6H, N=C-C**H**$_3$), 0.91 (t, J = 7.6 Hz, 6H, CH$_2$-C**H**$_3$). ^{13}C NMR (125 MHz, $CDCl_3$) δ_c (ppm) 156.07 (**C**-OH), 153.51 (**C**-CH$_3$), 140.10 (C=**C**-C), 138.43 (N=**C**-CH$_3$), 132.71 (**C**-CH$_2$-CH$_3$), 131.17 (C=**C**-Ar), 129.70 (OH-C-**C**H), 128.07 N-**C**), 116.02 (C-**C**H), 17.08 (C-**C**H$_2$-CH$_3$), 14.64 (C-CH$_2$-**C**H$_3$), 12.42 (C-**C**H$_3$), 11.85 (N=C-**C**H$_3$). ^{19}F NMR (282 MHz, $CDCl_3$) δ_F -145.57 (dd, J = 66.5, 32.1 Hz, B**F**$_2$). FTIR ν cm^{-1}: 3476 (s, O-H non-H bonded), 2961 (m, C-H aromatic), 2925 (m, C-H alkane), 2864 (m, C-H alkene), 1474 (s, aromatic C=C). ESI-MS: expected m/z = 419.21 $[M+Na]^+$, found m/z = 419.2 $[M+Na]^+$.

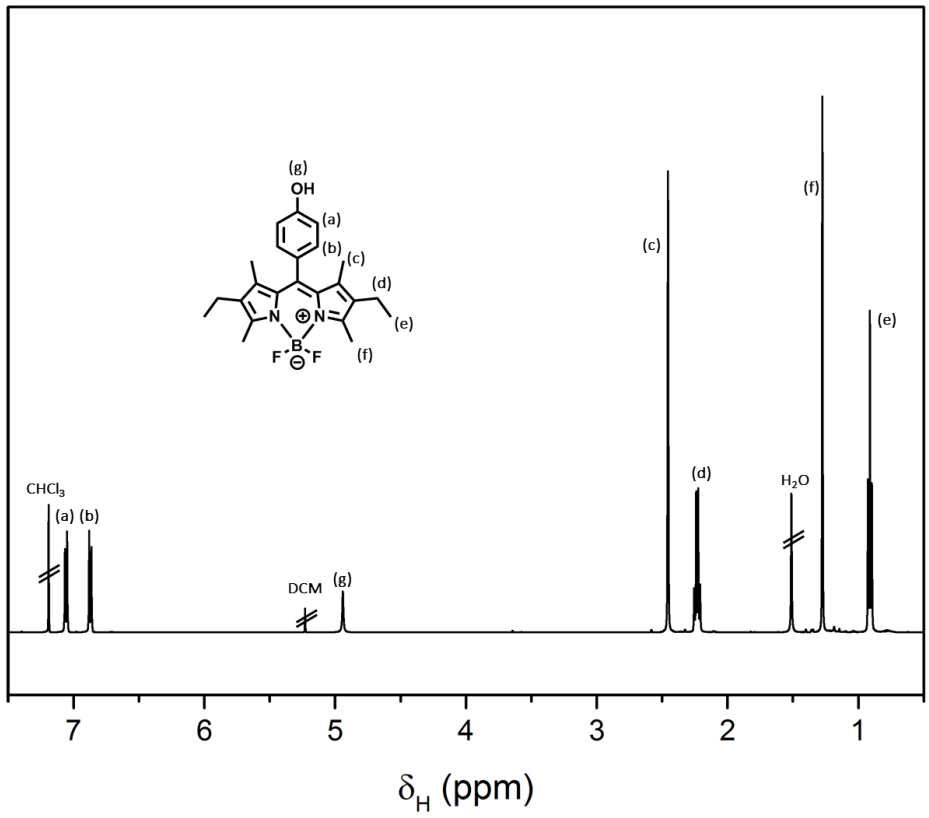

Figure 3.25. ^{1}H NMR spectrum of BODIPY phenol ($CDCl_3$, 500 MHz)

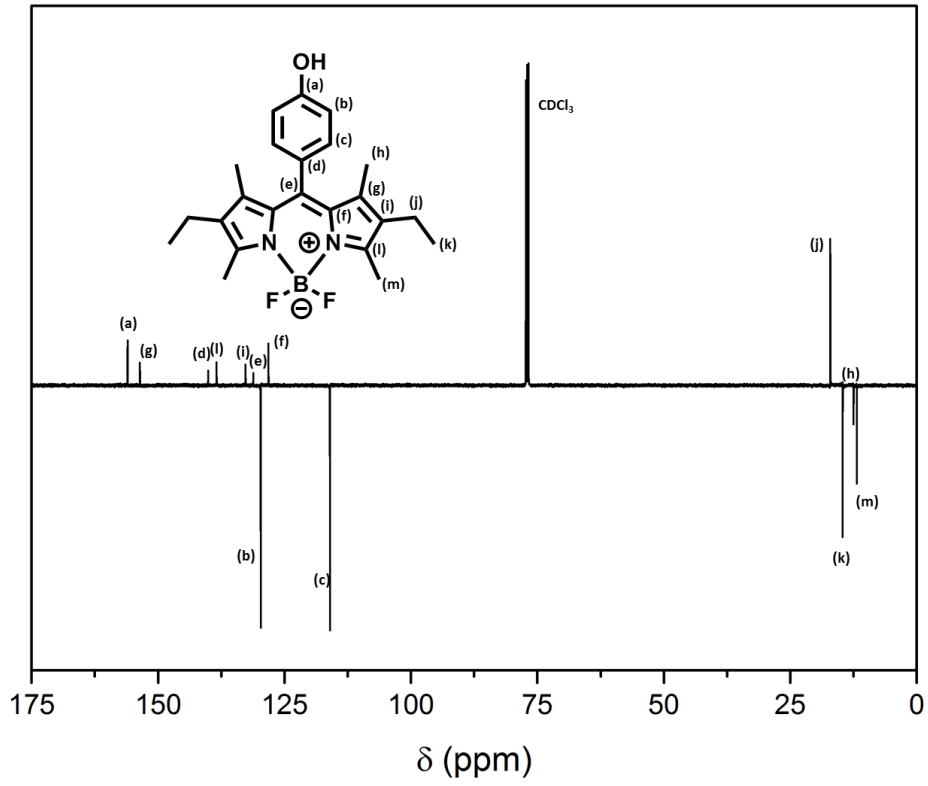

Figure 3.26. DEPT-135 ^{13}C NMR spectrum of BODIPY phenol ($CDCl_3$, 125 MHz)

3.6.3.2 BODIPY acrylate synthesis

1,8-Diazabicyclo[5.4.0]undec-7-ene (152 mg, 1 mmol, 2 eq) was added dropwise to a solution of BODIPY phenol (200 mg, 0.5 mmol, 1 eq), in a sealed 20 mL vial, turning it from bright red to dark brown. Acryloyl chloride (67.5 mg, 0.75 mmol, 1.5 eq) was added dropwise at which point the solution reverted to its original colour, and left to stir overnight at room temperature. Progress was monitored using thin layer chromatography. The reaction mixture was evaporated under reduced pressure and purified using automatic column chromatography using an eluent of 30% petroleum ether and 70% dichloromethane to yield BODIPY acrylate (160.1 mg, 70% yield). ^{1}H NMR (500 MHz, $CDCl_3$) δ_H (ppm) 7.22 (q, *J* = 8.6, 4H, Ar-**H**), 6.58 (d, *J* = 17.3, 0.7 Hz, 1H, CH=C**H**(H)), 6.29 (dd, *J* = 17.3, 10.4 Hz, 1H, COO-**C**H=CH_2), 5.99 (d, *J* = 10.5, 0.7 Hz, 1H, CH=C**H**(H)), 2.46 (s, 6H,N=C-C**H**$_3$), 2.24 (q, 4H, C-C**H**$_2$-CH_3), 1.26 (d, *J* = 7.6 Hz, 6H, C-C**H**$_3$), 0.91 (t, *J* = 7.6 Hz, 6H, C-CH_2-C**H**$_3$). ^{13}C NMR (126 MHz, $CDCl_3$) δ_C (ppm) 164.12 (**C**OO-CH=CH_2), 153.97 (COO-**C**), 151.02 (CH_3-**C**), 139.09 (C=C-**C**), 138.37 (CH_3-**C**=N), 133.39 (CH_3-CH_2-**C**), 132.94 (COO-CH=**C**H_2), 130.82 (N-C=**C**), 129.48 (O-**C**-CH), 127.83 (COO-**C**H-CH_2), 122.35 (O-C-CH-**C**H), 17.00 (C-**C**H_2-CH_3), 14.62 (C-CH_2-**C**H_3), 12.52 (N-C-C-**C**H_3), 11.85 (N=C-**C**H_3). ^{19}F NMR (282 MHz, $CDCl_3$) δ_F -145.57 (dd, *J* = 66.5, 32.1 Hz, B**F**$_2$). ESI-MS: 2963 (m, C-H aromatic), 2925 (m, C-H alkene), 2871 (m, C-H alkane), 1471 (s, aromatic C=C) expected *m/z* = 473.23 $[M+Na]^+$, found *m/z* = 473.2 $[M+Na]^+$.

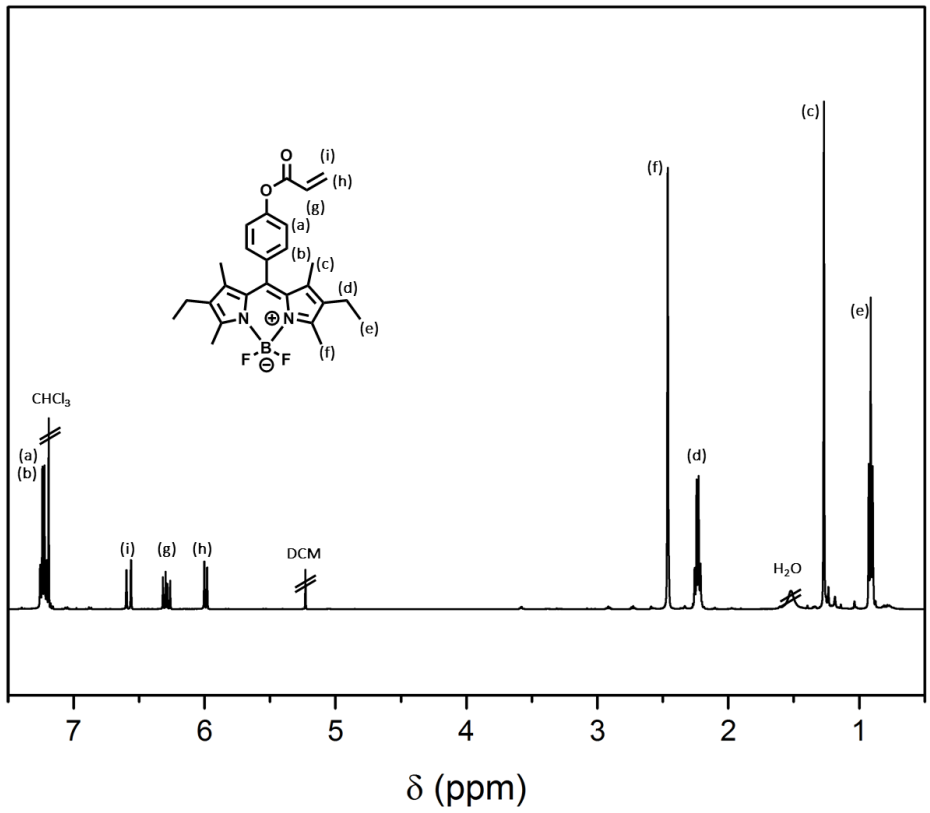

Figure 3.27. ^{1}H NMR spectrum of BODIPYA ($CDCl_3$, 500 MHz)

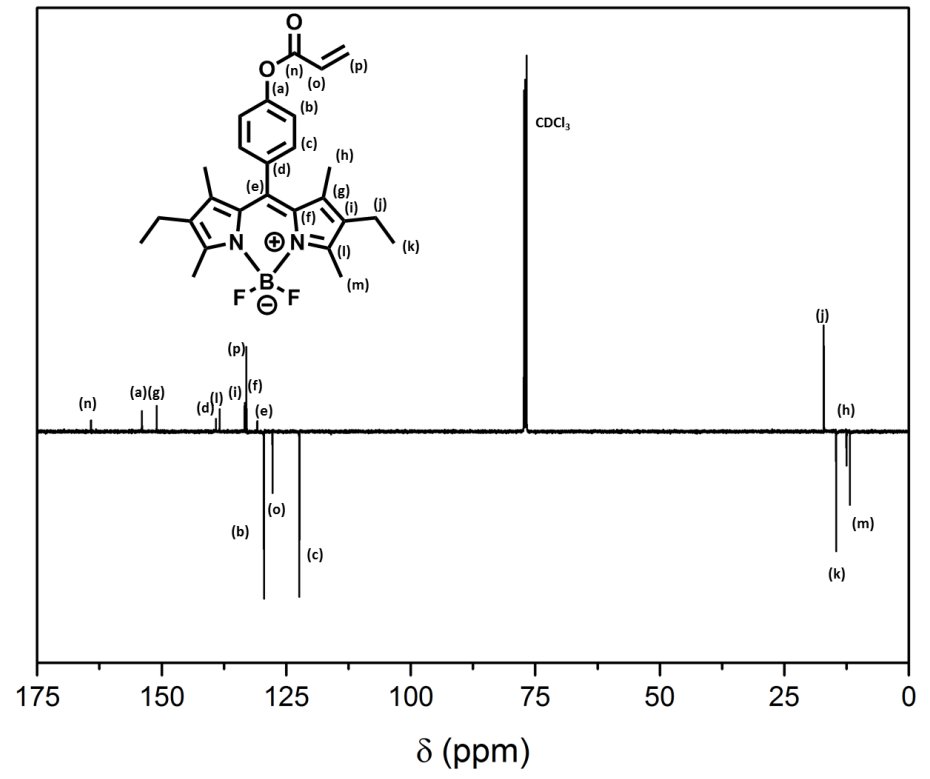

Figure 3.28. DEPT-135 ^{13}C NMR spectrum of BODIPY acrylate ($CDCl_3$, 125 MHz)

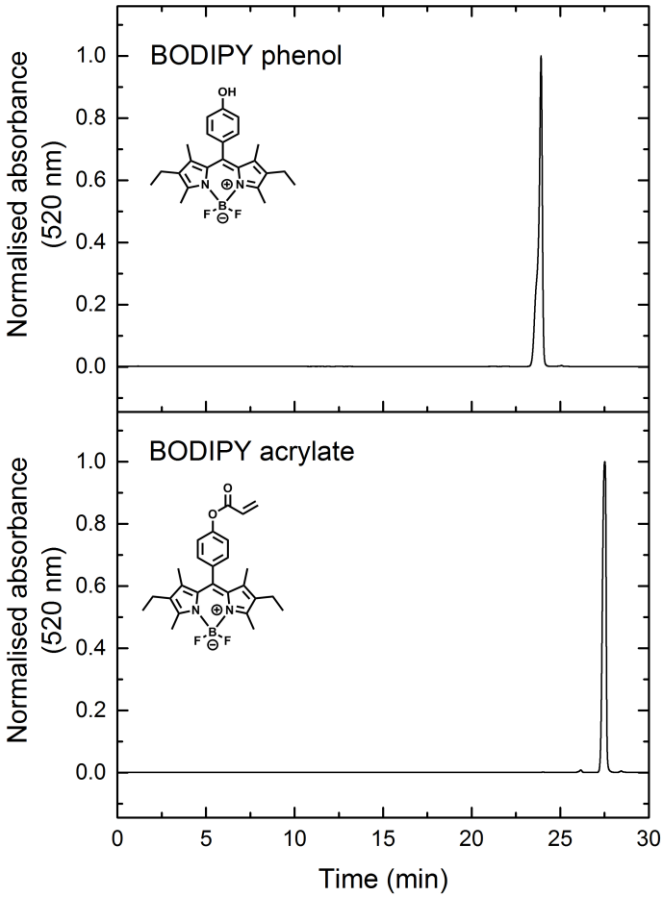

Figure 3.29. HPLC traces of BODIPY phenol and BODIPYA using UV detection at 520 nm, eluted on a gradient of 50% -100% methanol in water.

3.6.3.3 Synthesis of MRA-PS

MRA-PS was synthesised using adapted conditions from the literature,[26] and from section 2.4.3.2. Conditions are detailed in Table 3.6.

Table 3.6. Polymerisation conditions for the preparation of MRA-PS from MRA-PEGA. Solvent was 1,4-dioxane.

	Monomer	RAFT agent	Initiator	$[M]_0$/M	$[M]_0$/[macro-RAFT]$_0$	$[CTA]_0/[I]_0$	Time/h	Conversion (%)
MRA-PS	Styrene	**MRA-PEGA**	VA-086	5.5	8	20	18	94

3.6.3.4 Nanoparticle synthesis – RAFT emulsion polymerisation

RAFT emulsion polymerisations were performed as described in section 2.4.3.4. Polymerisation conditions are detailed in Table 3.7. Fluorescent derivatives were synthesised with the addition of 1 mol% BODIPYA relative to monomer.

Table 3.7. RAFT emulsion polymerisation conditions used to generate nanoparticles 100H, 100M, 100S, 50H, 50M and 50S (and non-fluorescent derivatives).

	Macro-RAFT agent	I	[Macro-RAFT] (mM)	$[M]_0$/ $[CTA]_0$	$[CTA]_0$/ $[I]_0$	T/° C	Reaction time (h)
100H	$P(PEGA)_8$-*b*-PS_8	ACVA	1.425	400	2.5	80	6
100M	$P(PEGA)_8$-*b*-P(*t*-$BA)_8$	ACVA	1.425	200	2.5	70	3
100S	$P(PEGA)_8$-*b*-P(*n*-$BA)_8$	ACVA	2.85	170	1.1	70	3
50H	$P(PEGA)_8$-*b*-PS_8	ACVA	2.85	120	1.1	80	6
50M	$P(PEGA)_8$-*b*-P(*t*-$BA)_8$	VA-057	2.85	170	1.1	57	3
50S	$P(PEGA)_8$-*b*-P(*n*-$BA)_8$	VA-057	2.85	130	1.1	57	3

All polymerisations were performed in aqueous conditions, with $[M]_0$ = 2.85 mM and reached full (>99%) monomer conversion.

3.6.3.5 Purification of fluorescent nanoparticles/ removal of free BODIPY monomer and unconsumed macro-RAFT agent

The nanoparticle suspension was transferred to a 100 kD MWCO Spectra/Por® Float-A-Lyzer dialysis device and dialysed against 4 x 1.5 L of 60% 1,4-dioxane 40% deionized water, changing the solvent periodically. After 4 days the solvent was changed to 100% deionized water and dialysed for 2 days (water changed 3 x) to remove any residual 1,4-dioxane. A small sample (100 μL) of latex was dried at 70°C, solids content was recorded and the polymers were analysed by SEC. Particles were re-analysed after purification using DLS to ensure dialysis did not perturb the colloidal stability.

3.6.3.6 Purification of non-fluorescent nanoparticles/ removal of unconsumed macro-RAFT agent

The nanoparticle suspension was transferred to a 100 kD MWCO Spectra/Por® Float-A-Lyzer dialysis device and dialysed against pure water for 4 days, with the dialysis water changed every day. A small sample (100 μL) of latex was dried at 70°C, solids content was recorded and the polymer were analysed by SEC. Particles were re-analysed after purification using DLS to ensure dialysis did not perturb the colloidal stability.

3.6.4 Cell culture, cytotoxicity and membrane activity

3.6.4.1 Cell culture

All cell lines in this study were purchased from ECACC (European Collection of Animal Cell Culture, Salisbury, UK) and cultured as single monolayers at 310 K in a humidified atmosphere containing 5% CO_2. Cells were sub-cultured at regular intervals, and passages made by trypsinising cells when at 80-90% confluence. Media used to culture cells are as follows: **A2780** – Roswell Park Memorial Institute medium (RPMI-1680) supplemented with 10% foetal calf serum, 1% glutamine and 1% pencillin/streptopmycin, **Caco-2** - 50:50 mixture of Dulbecco's Modified Eagle Medium (DMEM) and HAMS F12 supplemented with 10% of foetal calf serum, 1% of L-glutamine and 1% penicillin/streptomycin, **PC3** - Dulbecco's Modified Eagle Medium (DMEM) supplemented with 10% of foetal calf serum, 1% of L-glutamine and 1% penicillin/streptomycin, **3T3** - Dulbecco's Modified Eagle Medium (DMEM) supplemented with 10% of bovine calf serum, 1% of L-glutamine and 1% penicillin/streptomycin.

3.6.4.2 Sulforhodamine B cell viability assay

Cell viability experiments were performed as described in section 2.4.4.2 with A2780, Caco-2, PC3 and NIH 3T3 cell lines.

3.6.4.3 Haemolysis assay/ Membrane activity

Defibrinated sheep blood (2 mL) was split into two 1.5 mL Eppendorf tubes (1 mL each) and centrifuged at 4500 g / 8200 RPM in a mini-spin Eppendorf centrifuge for 60 seconds. The supernatant was removed and replaced with 750 µL PBS and mixed until the pellet had been fully resuspended. This process was repeated at least twice, until the supernatant became colourless. The red blood cell suspension was then diluted 1:150 in PBS. Particles were then diluted in PBS to make concentrations of 2 mg mL^{-1}, 1 mg mL^{-1} and 0.2 mg mL^{-1}. 20 µL of each particle suspension was then diluted with 380 µL of diluted red blood cells in 1.5 mL Eppendorf tubes such that the final concentration of particles was 0.1 mg mL^{-1}, 0.05 mg mL^{-1} and 0.01 mg mL^{-1}. Additionally, negative control mixtures of PBS and sterile water, and a 100% haemolysis positive control of 1% Triton-X in PBS were prepared. The mixtures were then incubated at 37°C in a pre-heated water bath for 1 h.

Samples were prepared in triplicate. Particle blood mixtures were then separated by centrifugation at 4500 g for 5 minutes and 200 μL of the supernatant from each tube was removed and transferred to a clear 96 well plate and the absorbance read at 404 nm using a Biotek Cytation 3 plate reader. The average Triton-X positive control value was set to 100% haemolysis. Errors were determined using the standard deviation of the three replicates.

3.6.5 Cellular uptake studies

Cellular uptake was quantified via measurement of intracellular fluorescence following incubation with BODIPY-labelled fluorescent nanoparticles. Experimental details for individual experiments can be found below. In all cases cells were seeded into a black 96 imaging well plate with a clear bottom at a density of 5000 cells per well and allowed to grow for 24 h. Cellular fluorescence was measured using a Cytation 3 Cell Imaging Multi-Mode Reader™ from Biotek®, with quantification from the Gen5™ software. Single cells were isolated using the blue channel (Hoechst 33258), and using a secondary mask, an area of (12 μm) and (15 μm) defined as the cell area for PC3 and Caco-2 respectively. Following background reduction using a roll ball model (25 μm), fluorescence associated with BODIPY (RFP filter, λ_{ex} = 531 nm, λ_{em} = 593 nm) was assigned as intracellular fluorescence. Data is represented as the arithmetic mean ± SD with experiments conducted in duplicate of triplicates.

3.6.5.1 Concentration dependent cellular uptake

For the concentration dependent cellular uptake experiments, after incubation for 24 h (from seeding), the cell culture medium was replaced with medium containing either 200, 100 or 50 μg mL^{-1} of each of the nanoparticle suspensions, and incubated for 2 h. Intracellular fluorescence was measured as described above.

3.6.5.2 Time dependent cellular uptake

For kinetic cellular uptake experiments, after incubation for 24 h (from seeding), the cell culture medium was replaced with medium containing 100 μg mL^{-1} nanoparticles, and incubated for 24 h, 4 h and 2 h. Then intracellular fluorescence was measured as described above.

3.6.5.3 Uptake at 4°C

For cellular uptake experiments at 4°C, after incubation for 24 h, the cells were cooled to 4°C for 1 h, then the culture medium was replaced with cold medium containing 100 μg mL^{-1} nanoparticles, and incubated at 4°C for 2 h. Then intracellular fluorescence was measured as described above.

3.6.5.4 Pathway inhibitors

For cellular uptake pathway inhibition experiments, after incubation for 24 h, the cells were pre-treated with inhibitors (chloropromazine (5 μg mL^{-1}), amiloride hydrochloride (2 mM) and genistein (50 μg mL^{-1})) for 3 h, then the culture medium was replaced with medium containing 100 μg mL^{-1} nanoparticles, and topped up with the respective inhibitor during the course of the experiment. Then intracellular fluorescence was measured as described above.

3.6.6 Confocal laser scanning microscopy/live cell imaging

3.6.6.1 Experiments performed at 37°C

Cells (PC3) were seeded at a density of 5,000 cells per well in a 10 well microscopy plate and incubated for 24 h prior to starting the experiment. The culture medium was replaced with media containing nanoparticles (100 μg mL^{-1}) and incubated with the cells for 24 h, 4 h and 2 h. 2 h and 30 min prior to imaging LysoTracker™ Deep Red and Hoechst 33258 respectively were added to the appropriate wells such that the final concentrations of organelle stain would be 50 nM and 5 μg mL^{-1} respectively. Cells were washed with PBS five times, and fresh phenol red free DMEM was added. Finally, an additional aliquot of LysoTracker™ Deep Red was added to the appropriate wells after washing. Confocal microscopy images were obtained with a Zeiss LSM 880 using a 40x oil objective. Excitation/Emission wavelengths for measurements were used as follows: nucleus/blue channel (405 / 410 – 500 nm), BODIPY/ green channel (488 / 520 – 600 nm) and LysoTracker™ Deep Red/ red channel (633 / 650 – 700 nm). Colocalisation values were determined using the Pearson's Colocalisation Coefficient (PCC) using ImageJ or Fiji software.

3.6.6.2 Experiments performed at 4°C

Experiments conducted at 4°C were performed as described in section 3.6.6.1 with the following adaptation. Prior to the addition of nanoparticle suspensions, the cells were cooled to 4°C for 1 h. Cells were then left to incubate for 2 h at 4°C, with all other experimental details identical to experiments conducted at 37°C.

References

1. C. He, Y. Hu, L. Yin, C. Tang and C. Yin, *Biomaterials*, 2010, **31**, 3657-3666.
2. N. Ma, C. Ma, C. Li, T. Wang, Y. Tang, H. Wang, X. Mou, Z. Chen and N. He, *J. Nanosci. Nanotechnol.*, 2013, **13**, 6485-6498.
3. X. Huang, X. Teng, D. Chen, F. Tang and J. He, *Biomaterials*, 2010, **31**, 438-448.
4. J. A. Champion, Y. K. Katare and S. Mitragotri, *J. Controlled Release,* 2007, **121**, 3-9.
5. E. Fröhlich, *Int. J. Nanomed.*, 2012, **7**, 5577-5591.
6. Z.-G. Yue, W. Wei, P.-P. Lv, H. Yue, L.-Y. Wang, Z.-G. Su and G.-H. Ma, *Biomacromolecules*, 2011, **12**, 2440-2446.
7. L. Ho, W.-Y. Yung, K. Sy, H. Li, C. K. Choi, K. Leung, T. W. Y. Lee and C. Choi, *ACS Nano*, 2017, **11**, 6085-6101.
8. S. A. Kulkarni and S.-S. Feng, *Pharm. Res.*, 2013, **30**, 2512-2522.
9. O. Chaudhuri, S. T. Koshy, C. Cunha, J.-W. Shin, C. S. Verbeke, K. H. Allison and D. J. Mooney, *Nat. Mater.*, 2014, **13**, 970-978.
10. T. Yeung, P. C. Georges, L. A. Flanagan, B. Marg, M. Ortiz, M. Funaki, N. Zahir, W. Ming, V. Weaver and P. A. Janmey, *Cell Motil. Cytoskeleton*, 2005, **60**, 24-34.
11. A. J. Engler, S. Sen, H. L. Sweeney and D. E. Discher, *Cell*, 2006, **126**, 677-689.
12. A. C. Anselmo, M. Zhang, S. Kumar, D. R. Vogus, S. Menegatti, M. E. Helgeson and S. Mitragotri, *ACS Nano*, 2015, **9**, 3169-3177.
13. H. Sun, E. H. H. H. H. Wong, Y. Yan, J. Cui, Q. Dai, J. Guo, G. G. Qiao and F. Caruso, *Chem. Sci.*, 2015, **6**, 3505-3514.
14. R. Hartmann, M. Weidenbach, M. Neubauer, A. Fery and W. J. Parak, *Angew. Chem., Int. Ed.*, 2015, **54**, 1365-1368.
15. W. Liu, X. Zhou, Z. Mao, D. Yu, B. Wang and C. Gao, *Soft Matter*, 2012, **8**, 9235-9245.
16. J. Sun, L. Zhang, J. Wang, Q. Feng, D. Liu, Q. Yin, D. Xu, Y. Wei, B. Ding, X. Shi and X. Jiang, *Adv. Mater.*, 2015, **27**, 1402-1407.
17. A. C. Anselmo and S. Mitragotri, *Adv. Drug Delivery Rev.*, 2016.
18. R. Singh and J. W. Lillard, *Exp. Mol. Pathol.*, 2009, **86**, 215-223.
19. R. K. Jain and T. Stylianopoulos, *Nat. Rev. Clin. Oncol.*, 2010, **7**, 653-664.
20. K. Raemdonck, J. Demeester and S. Smedt, *Soft Matter*, 2008, **5**, 707-715.
21. K. S. Anseth, C. N. Bowman and L. Brannon-Peppas, *Biomaterials*, 1996, **17**, 1647-1657.

22. A. Johnston, C. Cortez, A. S. Angelatos and F. Caruso, *Curr. Opin. Colloid Interface Sci.*, 2006, **11**, 203-209.

23. K. L. Ngai and D. J. Plazek, *Rubber Chem. Technol.*, 1995, **68**, 376-434.

24. S. Lorenz, C. P. Hauser, B. Autenrieth, C. K. Weiss, K. Landfester and V. Mailänder, *Macromol. Biosci.*, 2010, **10**, 1034-1042.

25. R. Hiorns, *Polym. Int.*, 2000, **49**, 807-807.

26. G. Moriceau, G. Gody, M. Hartlieb, J. Winn, H. Kim, A. Mastrangelo, T. Smith and S. Perrier, *Polym. Chem.*, 2017, **8**, 4152-4161.

27. P. B. Zetterlund, S. C. Thickett, S. Perrier, E. Bourgeat-Lami and M. Lansalot, *Chem. Rev.*, 2015, **115**, 9745-9800.

28. Y. Luo, J. Tsavalas and F. J. Schork, *Macromolecules*, 2001, **34**, 5501-5507.

29. C. Grazon, J. Rieger, R. Méallet-Renault, B. Charleux and G. Clavier, *Macromolecules*, 2013, **46**, 5167-5176.

30. X. Ma, R. Sun, J. Cheng, J. Liu, F. Gou, H. Xiang and X. Zhou, *J. Chem. Educ.*, 2016, **93**, 345-350.

31. J. M. Torres, C. M. Stafford and B. D. Vogt, *ACS Nano*, 2009, **3**, 2677-2685.

32. J. Key, A. L. Palange, F. Gentile, S. Aryal and C. Stigliano, *ACS Nano*, 2015, **9**, 11628-11641.

33. Y. A. N. Geng, P. Dalhaimer, S. Cai and R. Tsai, *Nat. Nanotechnol.*, 2007, **2**, 249-255.

34. C. Jiwei, D. R. Robert, B. J. P., J. A. P. R., A. Sheilajen, L. Kang, S. G. K., K. S. J. and C. Frank, *Adv. Mater.*, 2013, **25**, 3468-3472.

35. K. A. Beningo and W.-Y. of cell science, *J. Cell. Sci.*, 2002.

36. X. Banquy, F. Suarez, A. Argaw, J. M. Rabanel and G.-P. Matter, *Soft Matter*, 2009, **5**, 3984-3991.

37. X.-Y. Sun, Q.-Z. Gan and J.-M. Ouyang, *Sci. Rep.*, 2017, **7**, 41949.

38. H. Herd, N. Daum, A. T. Jones, H. Huwer, H. Ghandehari and C.-M. Lehr, *ACS Nano*, 2013, **7**, 1961-1973.

39. B. Yameen, W. Choi, C. Vilos, A. Swami, J. Shi and O. C. Farokhzad, *J. Controlled Release*, 2014, **190**, 485-499.

40. X. Zhang, F. He, K. Xiang, J. Zhang, M. Xu, P. Long, H. Su, Z. Gan and Q. Yu, *Biomacromolecules*, 2018, **19**, 883-895.

41. N. K. Y. Wong, R. A. Shenoi, S. Abbina, I. Chafeeva, J. N. Kizhakkedathu and M. K. Khan, *Biomacromolecules*, 2017, **18**, 2427-2438.

42. E. Spisni, M. C. Bianco, C. Griffoni, M. Toni, R. D'Angelo, S. Santi, M. Riccio and V. Tomasi, *J. Cell. Physiol.*, 2003, **197**, 198-204.

43. R. G. Parton and M. A. del Pozo, *Nat. Rev. Mol. Cell Biol.*, 2013, **14**, 98-112.

44. C. J. Ferguson, R. J. Hughes, D. Nguyen, B. T. Pham, R. G. Gilbert, A. K. Serelis, C. H. Such and B. S. Hawkett, *Macromolecules*, 2005, **38**, 2191-2204.

Chapter 4

Generating nanoparticles with functional alkyne coronas using RAFT emulsion polymerisation

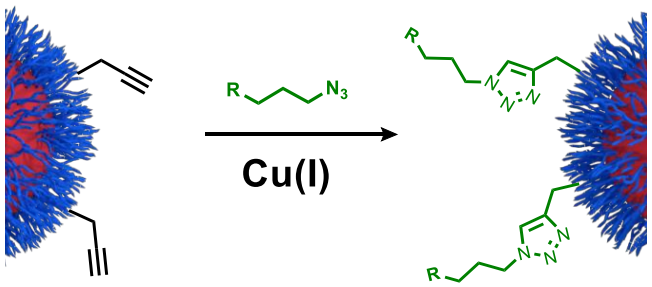

The multi-valent presentation of functional groups on nanoparticle surfaces has long been exploited to attach biologically active moieties. The conventional chemistries typically used (amide, ester, disulfide) however, are non-selective and inefficient. The Huisgen azide alkyne [1,4] cycloaddition (CuAAC) 'click' reaction has paved the way for atom economic, and orthogonal conjugation chemistries, and is now widely used in nanoparticle science. In this chapter, alkyne functionalised nanoparticles have been generated, without lengthy post-nanoparticle synthesis modification procedures, through RAFT emulsion polymerisations stabilised by functional macro-RAFT agents. Our results indicated that ester derived RAFT agents and addition of pendant charged groups are vital to retain colloidal stability and narrow molecular weight distributions. Finally, the nanoparticles and model polymers were functionalised with an azido functional polymer and fluorescent dye, showing the surfaces were accessible for post-functionalisation.

4.1 Introduction

One of the major advantages exhibited by nanomaterials, is their large total surface area (relative to macroscopic materials), which can be modified to present a high density of chemically functional groups. These can then be post-modified to introduce new functionality, useful for a variety of applications such as catalysis,[1] anti-fouling[2] and water treatment.[3] In the biomedical field this has been utilised to great effect, typically by attaching peptides,[4] antibodies[5] and carbohydrates[6] to improve nanoparticle cellular uptake and disease targeting. Furthermore, it has been shown that nanoparticles conjugated with fluorescent dyes,[7] radiolabels[8] and MRI contrast agents[9, 10] can be used to track nanoparticle *in vivo* distribution, and also act as highly sensitive diagnostic tools. Due to the advances in this area, many researchers have combined these approaches to generate theranostic nanoparticles, combining therapies and diagnostics on one nanoparticle, which is only achievable due to the high density of surface functionality available for modification.[11, 12] Nonetheless, most nanomaterials utilising these chemistries, typically rely on conventional functional groups such as amines,[13] carboxylic acids[14] and thiols,[15] which are not only highly prevalent in biological organisms, but can react promiscuously. Furthermore, commonly used reactions such as carbodiimide amide coupling in aqueous conditions are fraught with side-reactions and low conjugation efficiencies.[16]

Introduced in 2001, the 'click' chemistry concept represents an elegant solution to many of the problems found using conventional coupling techniques. Sharpless and co-workers laid out a set of criteria that a 'click' reaction must fulfil, including: being highly yielding, rapidly create physiologically stable products, have high atom economy and performed in any solvent, especially water.[17] There are now many reactions defined as a 'click', including (but not limited to) thiol-yne coupling,[18] Diels-Alder cycloaddition,[19] oxime coupling[20] and thiol-isocyanate coupling.[21] However, perhaps the most iconic and widely used, is the Huisgen azide alkyne [3+2] cycloaddition.[22] This reaction, between an azide and an alkyne, is now heavily used for bioconjugation, as both of the components can be used orthogonally with endogenously found functionalities.

This approach therefore represents a facile route to selectively functionalise the surface of nanomaterials, without the drawbacks of the traditional approaches described above. For instance, Bolley *et al*. reported improved functionalisation of superparamagnetic

nanoparticles with cyclic RGD integrin binding peptides, using both thiol-yne and Copper azide alkyne cycloaddition (CuAAC) click techniques, in comparison to classical carbodiimide amidation reactions.[23] Additionally, the CuAAC reaction has been used to convert otherwise bare gold nanoparticles into glycosylated systems with azido functional monosaccharides, capable of binding to cell surface lectins.[6] Due to the orthogonality of these moieties, Brennen *et al*. were able to conjugate acetylene-functionalised *Thermomyces lanuginosus* lipase to azide coated gold nanoparticles *via* the CuAAC reaction, which still retained its enzymatic activity post-conjugation.[24]

Although a vast array of substrates can be conjugated by introducing the complimentary functionality (either azide or alkyne) at the nanoparticle surface, in many cases this is non-trivial, and usually requires a multi-step synthesis approach. As mentioned in chapter 1 and 2, RAFT emulsion polymerisation combines the advantages of RDRP (narrow molecular weight distributions, controlled molar masses, block copolymers) and emulsion polymerisation (uniform nanoparticles, fast propagation rates and aqueous environments). Another major advantage of RDRP techniques is that there are now many examples of pre-functionalised RDRP initiators (RAFT agents, ATRP initiators etc) with either alkyne or azide groups which after polymerisation would be imparted at the chain ends ready for post-modification.[25] This could therefore be translated to RAFT emulsion polymerisation, through the use of functional macro-RAFT agents, making this an ideal method to generate nanoparticles with high surface functionality. An example of this, for nanoparticle functionalisation using RAFT emulsion polymerisation, was recently reported by Monteiro and co-workers.[26] They generated a series of multi-functional nanoworms/nanorods through aqueous RAFT emulsion polymerisation of styrene, using P(NIPAM) macro-RAFT agents containing pyridyl disulfide, alkyne, dopamine, thiolactone and biotin functional end-groups. However, as the emulsion polymerisation required stabilisation from an external surfactant, the functional groups were not imparted at the surface. After addition of toluene, and upon cooling, the spherical nanoparticles morphed into high aspect ratio nanoworms, to which a range of linear polymers and fluorescent dyes could be conjugated. While this shows it is possible to introduce a high density of functionality, this type of emulsion polymerisation requires the presence of cytotoxic surfactants and organic solvents to access the surface functionality. As of yet, this technique has not been used to produce any other morphology, such as spherical nanoparticles, which can be directly used for conjugation.

The aim in this chapter was therefore to introduce functional alkyne groups on the surface of our nanoparticles, by performing RAFT emulsion polymerisations with alkyne functional macro-RAFT agent ('R'). These groups would be imparted at the particle surface and therefore be available for reaction/conjugation. Herein, we report a synthesis of alkyne functional macro-RAFT agent stabilisers, with three different RAFT agents. Using some of these stabilisers, RAFT emulsion polymerisations with *n*-BA were performed to generate alkyne functional nanoparticles. Finally, CuAAC reactions were performed on both alkyne functional macro-RAFT agents and nanoparticles to assess their post-functionalisation properties.

4.2 Results and Discussion

4.2.1 Propagyl amide

4.2.1.1 Synthesis of amide based alkyne functional RAFT agent

As biomedical applications were the primary target for these nanoparticles, the chemistry used to introduce acetylene functionality should ideally not be susceptible to degradation *in vivo*. Amide bonds would be less vulnerable to hydrolytic or enzyme related degradation, making these more preferable than their ester counterparts. Therefore the alkyne functional RAFT agent, **Alkyne-PAmBTC** was synthesised with **PABTC** and propagyl amine using (benzotriazol-1-yl-oxytripyrrolidinophosphonium hexafluorophosphate) (PyBOP) as the coupling agent and N,N-Diisopropylethylamine (DIPEA) as a mild base, following previously described conditions (Scheme 4.1), at 68% yield.[27]

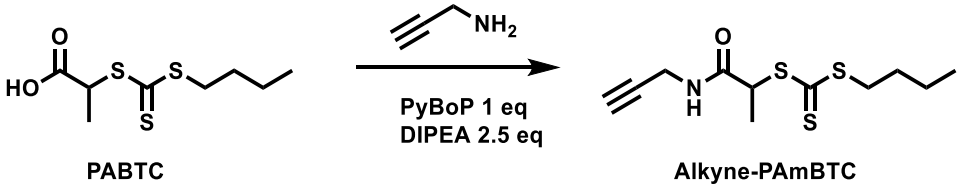

Scheme 4.1. Synthesis of **Alkyne-PAmBTC** *via* amide coupling of **PABTC** and propagyl amine.

4.2.1.2 PEGA polymerisation with Alkyne-PAmBTC

Prior to the synthesis of an alkyne functional macro-RAFT agent stabiliser, we verified **Alkyne-PAmBTC**s ability to act as a chain transfer agent, through a solution polymerisation of PEGA, targeting a DP of 20, using conditions described in section 2.2.2 (Figure 4.1a). Samples were taken periodically to assess the molecular weight distribution and monomer conversion over the course of the polymerisation.

$M_{n,SEC}$ showed a linear increase with monomer conversion, reaching 89% after 5 h (Figure 4.1c and Figure 4.1d). However, for a controlled polymerisation this linear increase should ideally begin at the molar mass of the RAFT agent (275 g mol^{-1}), but in our case we observed a $M_{n,SEC}$ at > 4000 g mol^{-1} after just 15-30 min. This suggests that during the initial stages of the polymerisation, the RAFT agent is unable to perform efficient chain

transfer and a small amount of free radical polymerisation takes place, producing much larger observed molar masses compared to theoretical values. Furthermore, in the first order plot, a deviation from the linear fit is observed after 3 h (80% monomer conversion), indicating an increase in termination reactions (Figure 4.1b). Both of these effects result in an asymmetric SEC chromatogram, caused by a shoulder at lower molar mass, even though the $Đ$ remained < 1.2 (Figure 4.1e). It is likely this was caused by two possible phenomena, firstly the presence of a terminal acetylene group, which can readily react with radical species (initiator derived, propagating chains etc), especially at high monomer conversion where propagation is reduced. Additionally, the amide 'acrylamide-like' reinitiating group of **Alkyne-PAmBTC**, is highly unstable, therefore pushing the pre-equilibrium step of the RAFT polymerisation towards the initiator derived chains (Scheme 4.2). This would result in slow consumption of the RAFT agent, and therefore imperfect control over the polymerisation. Overall, these results suggest that **Alkyne-PAmBTC** was not suitable to generate alkyne functional macro-RAFT agents.

Table 4.1. Data for the polymerisation kinetics of PEGA using **Alkyne-PAmBTC** as the CTA.

Time (h)	% conv[a]	$M_{n,th}$ (g mol^{-1})[b]	$M_{n,SEC}$ (g mol^{-1})[c]	$M_{w,SEC}$ (g mol^{-1})[c]	$Đ$[c]
0	0	275	-	-	-
0.25	12	1400	4750	5350	1.13
0.5	33	3400	6000	6900	1.15
1	52	5200	7500	8600	1.15
1.5	66	6600	8500	9700	1.15
2	73	7200	9000	10400	1.16
3	82	8100	9500	11100	1.17
4	87	8600	9700	11400	1.17
5	89	8800	9800	11550	1.18

[a]Determined by ^{1}H NMR spectroscopy. [b]Theoretical molar masses calculated with Equation 2.12. [c]Determined by THF-SEC and analysed against PMMA standards.

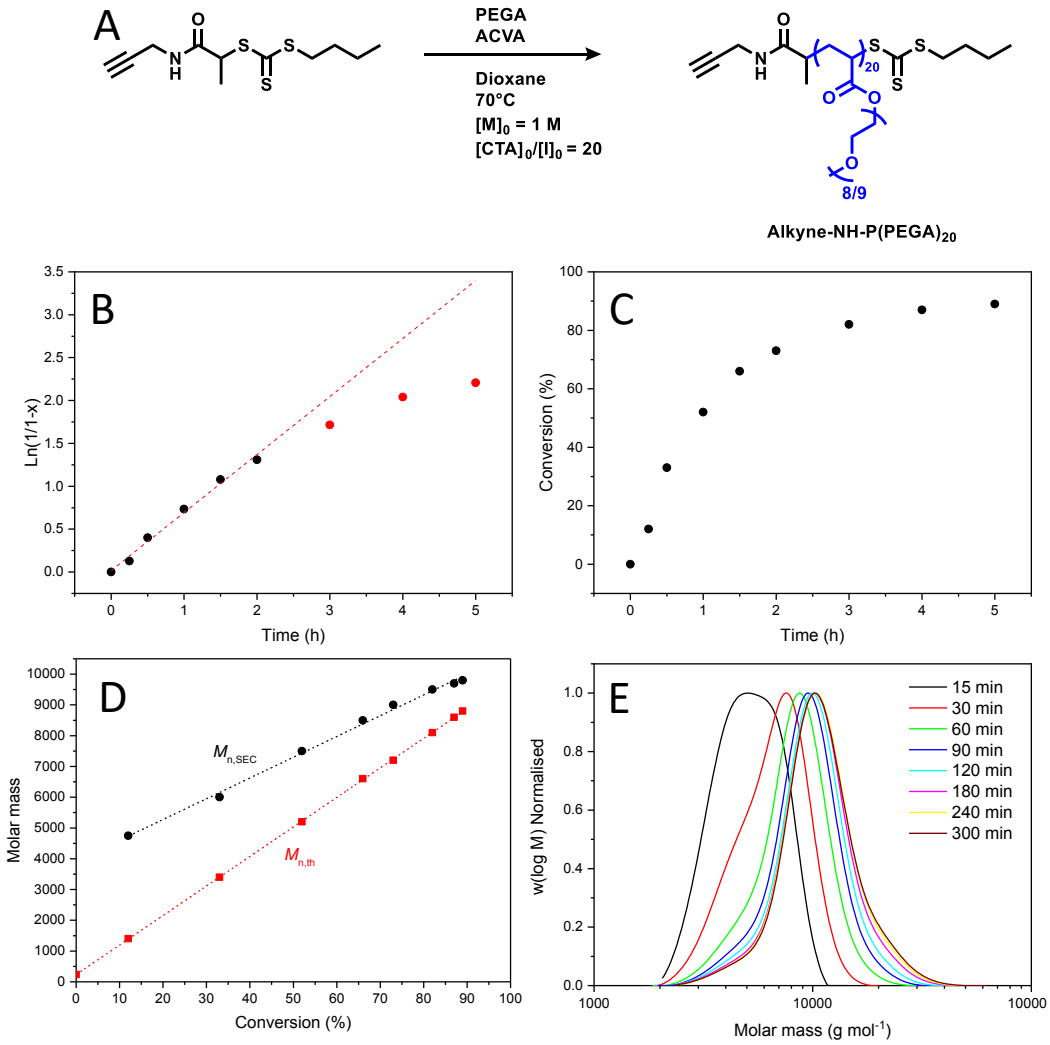

Figure 4.1. (A) Polymerisation of PEGA mediated by **Alkyne-PAmBTC**, (B) pseudo first order plot, red points indicate data masked from the linear fit (red dashed line), (C) time vs conversion, (D) conversion vs $M_{n,SEC}$ and linear fit (dashed black line), (E) evolution of SEC chromatograms over time.

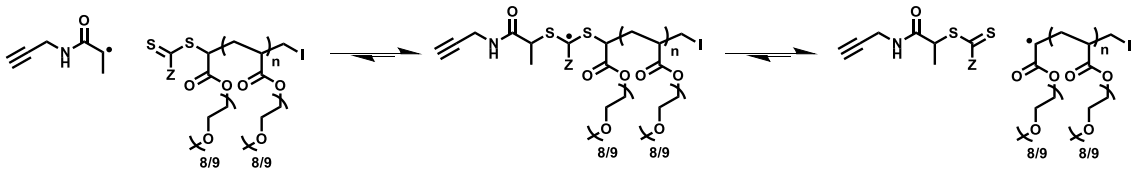

Scheme 4.2. Pre-equilibrium of a RAFT polymerisation of PEGA using **Alkyne-PAmbTC**.

4.2.2 Protected propagyl ester

4.2.2.1 Synthesis of TMS protected alkyne RAFT agent

To overcome both of these issues, an alternative RAFT agent was designed containing a trimethylsilyl group to protect the terminal alkyne, and an ester linkage to promote initiation of the RAFT agent during the pre-equilibrium. **TMS-Alkyne-PEsBTC** was synthesised *via* the esterification of **PABTC** with 3-(trimethylsilyl)propargyl alcohol using *N*,*N*'-Dicyclohexylcarbodiimide (DCC) and dimethylaminopyridine (DMAP) as coupling agent and catalyst respectively at 80% yield (Scheme 4.3).[28]

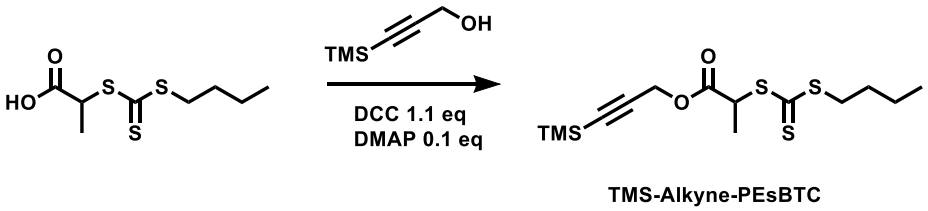

Scheme 4.3. Esterification of PABTC with 3-(trimethylsilyl)propargyl alcohol to yield **TMS-Alkyne-PEsBTC**.

4.2.2.2 Synthesis of TMS protected alkyne diblock macro-RAFT agent

A P(PEGA)-*b*-(*n*-BA) macroRAFT agent was then synthesised in two steps using **TMS-Alkyne-PEsBTC** as the CTA. As we were introducing a hydrophobic trimethylsilyl (TMS) and removing the negative carboxylate as compared to PABTC based macro-RAFT agents, we targeted a slightly larger macro-RAFT agent to improve steric stabilisation of the resulting nanoparticles. Firstly, PEGA was polymerised with DP_{target} of 15 mediated with **TMS-Alkyne-PEsBTC** at 70°C in 1,4-dioxane, using ACVA as the thermal initiator (Scheme 4.4). The polymerisation reached 82% monomer conversion in 5 h yielding **TMS-Alkyne-O-P(PEGA)$_{12}$**. THF-SEC analysis revealed a narrow molar mass distribution ($Đ$ = 1.11) and similar experimental molecular weights compared to theoretical values. Importantly, no high or low molar mass shoulders were evident, suggesting this RAFT agent was capable of controlling the polymerisation in comparison to **Alkyne-PAmBTC**. In chapter 3, we showed that the 'soft' P(*n*-BA) nanoparticles were preferentially taken up into cells in comparison to P(*t*-BA) and PS cores, and therefore we focussed on this variety of nanoparticles for the following study. Based on this, TMS-Alkyne-O-P(PEGA)$_{12}$ was then chain extended with 14 units of *n*-BA, reaching 90%

monomer conversion after 5 h, yielding **TMS-Alkyne-O-P[(PEGA)$_{12}$-*b*-(*n*-BA)$_{12}$]**, which again showed low dispersity values ($Đ$ = 1.14) and similar experimental molar masses to theoretical values (Table 4.2).

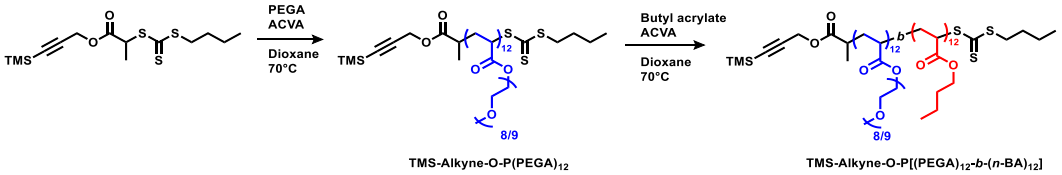

Scheme 4.4 Preparation of **TMS-Alkyne-O-P[(PEGA)$_{12}$-*b*-(*n*-BA)$_{12}$]** via a two-step polymerisation using TMS-Alkyne-PEsBTC as the RAFT agent.

Table 4.2. Characterisation data for **TMS-Alkyne-O-P(PEGA)$_{12}$** and **TMS-Alkyne-O-P[(PEGA)$_{12}$-*b*-(*n*-BA)$_{12}$]**

	% conv[a]	$M_{n,th}$ (g mol^{-1})[b]	$M_{n,SEC}$ (g mol^{-1})[c]	$M_{w,SEC}$ (g mol^{-1})[c]	$Đ$[c]
TMS-Alkyne-O-P(PEGA)$_{12}$	82%	6100	6500	7200	1.11
TMS-Alkyne-O-P[(PEGA)$_{12}$-*b*-(*n*-BA)$_{12}$]	90%	7600	8600	9900	1.14

[a]Determined by ^{1}H NMR spectroscopy. [b]Theoretical molar masses calculated with Equation 2.12. [c]Determined by THF-SEC and analysed against PMMA standards.

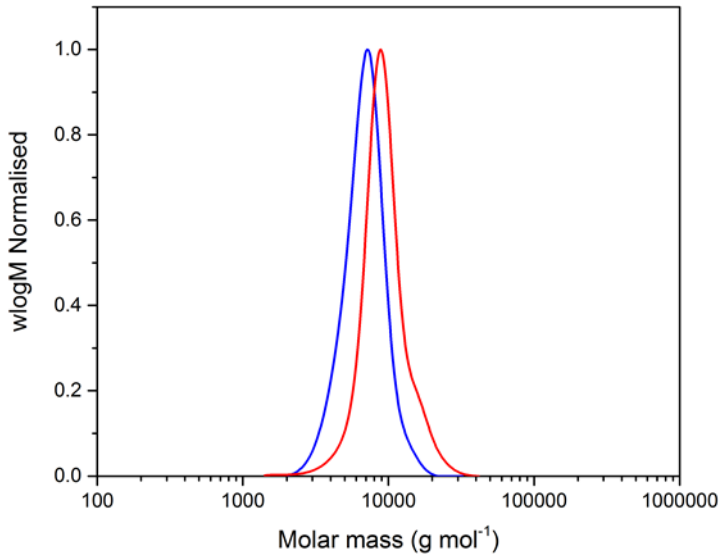

Figure 4.2. THF-SEC traces of **TMS-Alkyne-O-P(PEGA)$_{12}$** (blue line) and **TMS-Alkyne-O-P[(PEGA)$_{12}$-*b*-(*n*-BA)$_{12}$]** (red line).

4.2.2.3 RAFT emulsion polymerisation with TMS protected macro-RAFT agents

Initially, a RAFT emulsion polymerisation of *n*-BA was performed using **TMS-Alkyne-O-P[(PEGA)$_{12}$-*b*-(*n*-BA)$_{12}$]** as the macro-RAFT agent stabiliser, with conditions established in section 2.2.3, targeting a DP of 200. DLS analysis of the resulting latex revealed a highly polydisperse, multimodal particle size distribution (*PDi* = 0.235), with a large proportion of nanoparticles being > 1000 nm diameter (Figure 4.3a). Furthermore, a broad, multimodal molecular weight distribution was observed *via* SEC ($Đ$ = 6.51; Table 4.3, Figure 4.3b). It is likely this is due to the neutral hydrophobic surface imparted on the nanoparticles by the TMS protecting group, which during the early stages of the emulsion polymerisation would promote the migration of multiple propagating z-mers into each growing micelle, and therefore induce many termination events leading to broad molar mass distributions. Furthermore, the lack of electrostatic stabilisation and increased hydrophobicity, compared to PABTC based stabilisers, could result in weaker colloidal stability and potentially explain the broad particle size distribution observed by DLS.

To probe this further, a series of analogous RAFT emulsion polymerisations were performed with micelle blends of **TMS-Alkyne-O-P[(PEGA)$_{12}$-*b*-(*n*-BA)$_{12}$]** and **MRA-*n*BA** (P(PEGA)$_8$-*b*-P(*n*-BA)$_8$) (synthesised in chapter 2). Polymerisations were conducted with 0, 10, 25 and 50 mol% **TMS-Alkyne-O-P[(PEGA)$_{12}$-*b*-(*n*-BA)$_{12}$]** (relative to **MRA-*n*BA**) to introduce extra electrostatic stability from the carboxylated end group of **MRA-*n*BA,** potentially improving the latex stability. To ensure complete macro-RAFT agent micelle blends, a thin-film rehydration technique reported by O'Reilly and co-workers was conducted.[29] Briefly, both amphiphilic macro-RAFT agents were dissolved in THF, dried thoroughly at 70°C and were subsequently rehydrated by stirring in pure water for 16 h. The low T_g core of the micelles should induce efficient micelle blending due to the faster exchange of diblock copolymers.[29]

Analogous RAFT emulsion polymerisations were then performed using these blended micelle suspensions. Interestingly, with the exception of the polydisperse particle suspension of the 100% TMS macro-RAFT agent, a clear decreasing trend in particle diameter was observed with an increasing amount of carboxylated **MRA-*n*BA** macro-RAFT agent (143.6, 129.0, 108.6, 99.1 nm for 50, 25, 10 and 0% respectively; Figure 4.3b1, c1 and d1). Furthermore, these latexes displayed far narrower *PDi* values (< 0.1),

suggesting improved colloidal stability (Figure 4.3b-e). As expected, zeta-potentials of the nanoparticle became increasingly negative, with increasing amount of **MRA-*n*BA** present in the RAFT emulsion polymerisations (Table 4.3). Nonetheless, as with the 100% TMS macro-RAFT agent polymerisations, broad molar mass distributions were observed for reactions conducted with 50, 25 and 10% TMS macro-RAFT agent (Figure 4.3g-i; $Đ \sim 4.5$). However, as described in chapter 2, polymerisation with no TMS macro-RAFT agent (i.e. 100% carboxylated macro-RAFT agent **MRA-*n*BA**) yielded a narrower molar mass distribution ($Đ = 1.62$; Figure 4.3i). These observations support our previous hypothesis, suggesting the TMS protecting group is interfering with the colloidal stability and RAFT emulsion polymerisation, with full details found in Table 4.3. Although, stable latexes with narrow *PDi* values were obtained with 10, 25 and 50% TMS macro-RAFT agent, the poor molar mass distributions observed could indicate poor consumption of the macro-RAFT agent, and subsequently low level of alkyne functionality at the nanoparticle surface.

Table 4.3 Characterisation data for the *n*-BA RAFT emulsion polymerisations performed using the micelle blends of **MRA-*n*BA** and **TMS-Alkyne-O-P[(PEGA)$_{12}$-*b*-(*n*-BA)$_{12}$]** targeting a DP of 200.

% TMS macro-RAFT agent	D_h (nm)[a]	*PDi*[b]	ZP (mV)[c]	$M_{n,SEC}$ (g mol^{-1})[d]	$M_{w,SEC}$ (g mol^{-1})[d]	*Đ*[d]
100	100	0.235	-1.5	48100	313100	6.51
50	144	0.083	-11.7	32800	147300	4.49
25	129	0.091	-22.6	24400	99100	4.06
10	109	0.075	-29.4	24900	106600	4.28
0	99	0.059	-40.2	36300	58800	1.62

[a]Determined by DLS. [b]Calculated with Equation 2.13. [c]Determined with a zetasizer. [d]Measured with THF-SEC and analysed against PMMA standards. All polymerisations reached >99% conversion. $M_{n,th}$ for all polymerisations = 33200 g mol^{-1}.

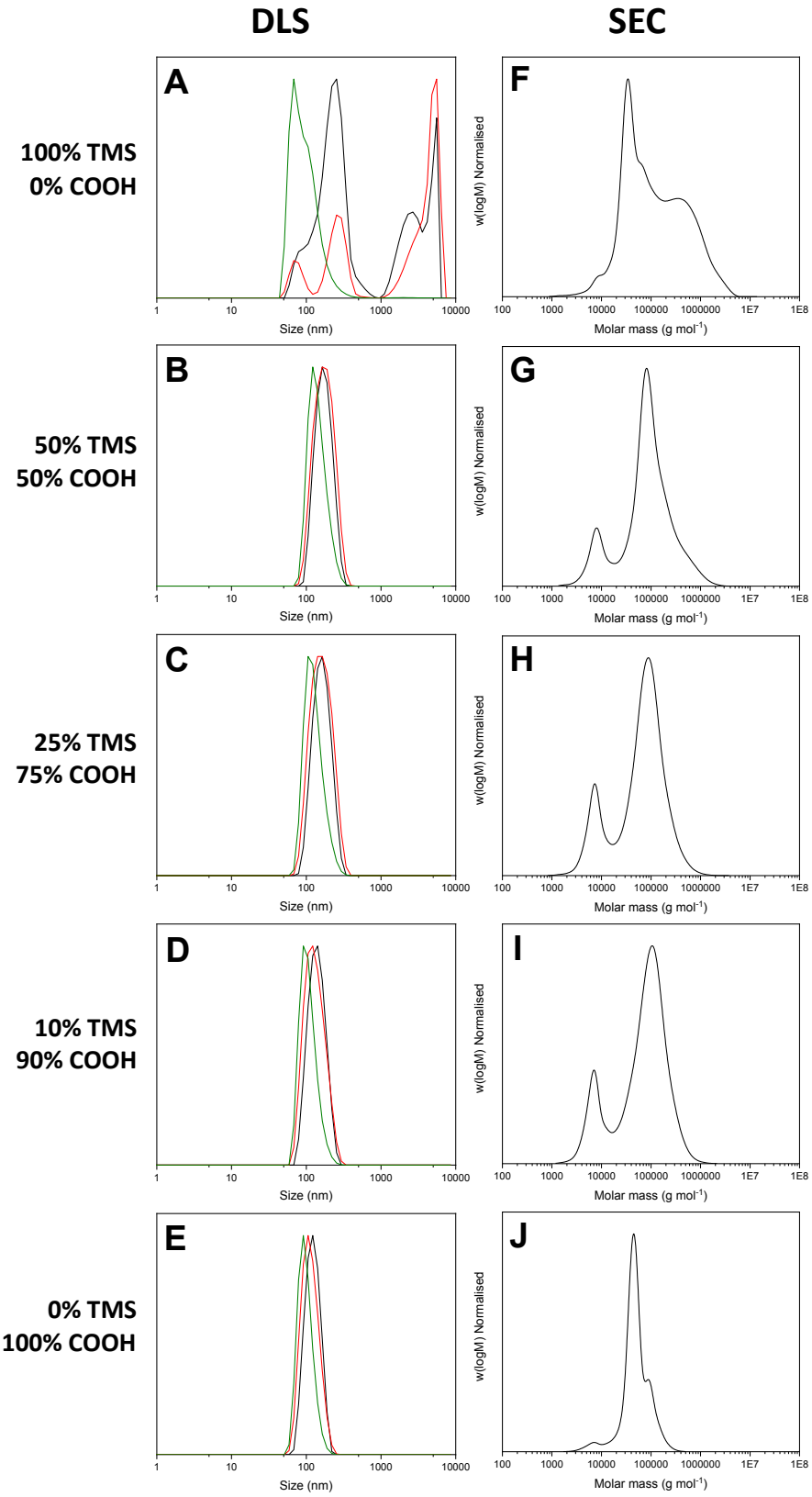

Figure 4.3 DLS (A-E) and THF-SEC (F-J) traces of *n*-BA RAFT emulsion polymerisations using micelle blends containing various ratios of **MRA-*n*BA** (COOH) and **TMS-Alkyne-O-P[(PEGA)$_{12}$-*b*-(*n*-BA)$_{12}$] (TMS).**

4.2.2.4 Addition of acrylic acid

We hypothesised that the poor consumption of macro-RAFT agent, and therefore broad molar mass distributions in the above RAFT emulsion polymerisations, arose from removing the carboxylated end-group and thus increasing the surface hydrophobicity and number of radical present (and therefore termination events) in each growing particle. A possible route to reintroduce the negatively charged surface, was to copolymerise a small amount of charged monomer with the hydrophilic PEGA block, restoring ionisation in the pendant side chains rather than the end group.

PEGA was therefore copolymerised with acrylic acid (AA) in an 80/20 molar ratio, targeting a total DP of 18 in 1,4-dioxane (Scheme 4.5). The polymerisation reached 84% total monomer conversion yielding **TMS-Alkyne-O-P[(PEGA)$_{12}$-*co*-(AA)$_3$]**. This was then chain extended with 15 units of *n*-BA which reached >99% monomer conversion yielding **TMS-Alkyne-O-P[(PEGA)$_{12}$-*co*-(AA)$_3$]-*b*-(*n*-BA)$_{15}$**. Both polymers had narrow molar mass distributions ($Đ$ < 1.2; Figure 4.4), with similar theoretical molar masses (determined by ^{1}H NMR spectroscopy) to experimentally determined values (*via* SEC; Table 4.4). Furthermore, a shift towards higher molar mass was evident, suggesting efficient chain extension.

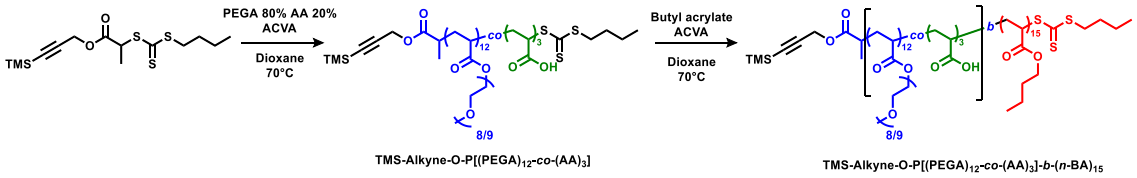

Scheme 4.5 Preparation of **TMS-Alkyne-O-P[(PEGA)$_{12}$-*co*-(AA)$_3$]-*b*-(*n*-BA)$_{15}$** via a two-step polymerisation using **TMS-Alkyne-PEsBTC** as the RAFT agent.

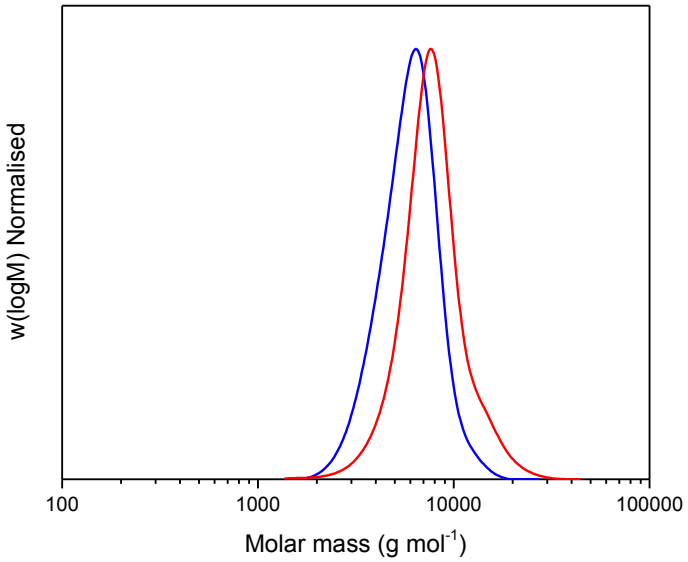

Figure 4.4 THF-SEC of **TMS-Alkyne-O-P[(PEGA)$_{12}$-*co*-(AA)$_3$]** (blue line) and **TMS-Alkyne-O-P[(PEGA)$_{12}$-*co*-(AA)$_3$]-*b*-(*n*-BA)$_{15}$** (red line).

Table 4.4 Characterisation data for **TMS-Alkyne-O-P[(PEGA)$_{12}$-*co*-(AA)$_3$]** and **TMS-Alkyne-O-P[(PEGA)$_{12}$-*co*-(AA)$_3$]-*b*-(*n*-BA)$_{15}$**

	% conv[a]	$M_{n,th}$ (g mol^{-1})[b]	$M_{n,SEC}$ (g mol^{-1})[c]	$M_{w,SEC}$ (g mol^{-1})[c]	$Đ$[c]
TMS-Alkyne-O-P(PEGA)$_{12}$	84	5900	5500	6200	1.12
TMS-Alkyne-O-P[(PEGA)$_{12}$-*b*-(*n*-BA)$_{12}$]	>99	7600	7200	8300	1.15

[a]Determined by ^{1}H NMR spectroscopy. [b]Theoretical molar masses calculated with Equation 2.12. [c]Determined by THF-SEC and analysed against PMMA standards.

4.2.2.5 RAFT emulsion polymerisation using TMS-Alkyne-O-P[(PEGA)$_{12}$-*co*-(AA)$_3$]-*b*-(*n*-BA)$_{15}$

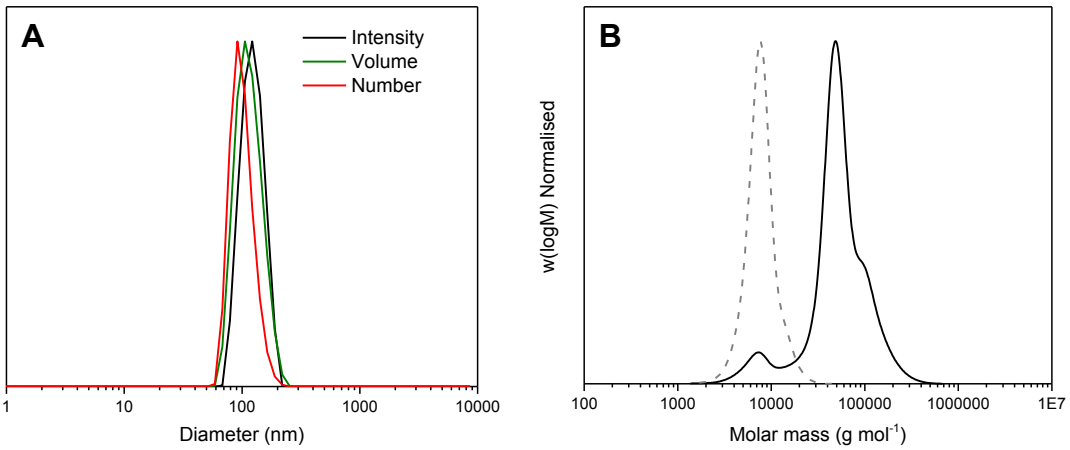

Figure 4.5. (A) DLS distributions (intensity (black), volume (green) and number (red)) of **TMS-Alkyne-O-P[(PEGA)$_{12}$-*co*-(AA)$_3$]-*b*-(*n*-BA)$_{12}$-*b*-(*n*-BA)$_{200}$]** nanoparticles (B) THF-SEC of **TMS-Alkyne-O-P[(PEGA)$_{12}$-*co*-(AA)$_3$]-*b*-(*n*-BA)$_{12}$- *b*-(*n*-BA)$_{200}$]** (black full line) and **TMS-Alkyne-O-P[(PEGA)$_{12}$-*b*-(*n*-BA)$_{12}$]** macro-RAFT agent (grey dashed line).

Table 4.5 Characterisation data for TMS protected alkyne functional nanoparticles, **TMS-Alkyne-O-P[(PEGA)$_{12}$-*co*-(AA)$_3$]-*b*-(*n*-BA)$_{12}$- *b*-(*n*-BA)$_{200}$]**.

	D_h (nm)[a]	*PDi*[b]	ZP (mV)[c]	$M_{n,SEC}$ (g mol^{-1})[d]	*Đ*[e]
TMS-Alkyne-O-P[(PEGA)$_{12}$-*co*-(AA)$_3$]-*b*-(*n*-BA)$_{12}$- *b*-(*n*-BA)$_{200}$]	101.4	0.055	-49.5	33000	1.92

[a]Determined by DLS. [b]Calculated with Equation 2.13. [c]Determined with a zetasizer. [d]Measured with THF-SEC and analysed against PMMA standards. All polymerisations reached >99% conversion. $M_{n,th}$ = 33200 g mol^{-1}.

A RAFT emulsion polymerisation of *n*-BA was then performed using only **TMS-Alkyne-O-P[(PEGA)$_{12}$-*co*-(AA)$_3$]-*b*-(*n*-BA)$_{15}$** (i.e. no micelle blending), again targeting a DP of 200. DLS revealed the formation of narrow 101 nm nanoparticles (*PDi* = 0.055; Table 4.5, Figure 4.5a). SEC of the dissolved nanoparticles displayed a clear shift towards higher molar mass indicating excellent chain extension. The resulting polymer (Figure 4.5b) had a relatively low dispersity (*Đ*=1.92) as compared to those where no acrylic acid was present in the macro-RAFT agent (Figure 4.3; Table 4.3). These findings support our hypothesis that the presence of a charged surface is imperative in maintaining colloidal stability, and the production of narrow dispersity polymers.

4.2.2.6 Test deprotection of TMS group on TMS macro-RAFT agent

Our previous results give a clear indication that **TMS-Alkyne-O-P[(PEGA)$_{12}$-*co*-(AA)$_3$]-*b*-(*n*-BA)$_{15}$**, is a suitable macro-RAFT agent to stabilise RAFT emulsion polymerisations. However, to utilise the imparted alkyne functionality, the TMS group must be removed. It is well known that these groups can be deprotected *via* the addition of fluoride ions, due to the strong Si-F bond created during the reaction. This is typically achieved using tetrabutyl ammonium fluoride (TBAF), as it is commercially available as a 1.0 M solution in THF, and can be used in organic solvents. When considering the deprotection of TMS groups on our nanoparticles, the presence of a large quantity of organic solvent could reduce the colloidal stability of the synthesised latexes as mentioned in section 3.2.2. Some reports however, describe the deprotection of TMS esters using potassium fluoride (KF), representing a promising route to remove the TMS group from our nanoparticles in aqueous conditions.[30]

The above TMS protected alkyne functional nanoparticles were subjected to 10 eq of KF for 16 h. The nanoparticles were subsequently dialysed to remove the resulting fluorotrimethylsilane by-product and then diluted in D_2O. ^1H NMR spectroscopy revealed the presence of a large singlet at ~0 ppm, suggesting the TMS deprotection was unsuccessful (Figure 4.6).

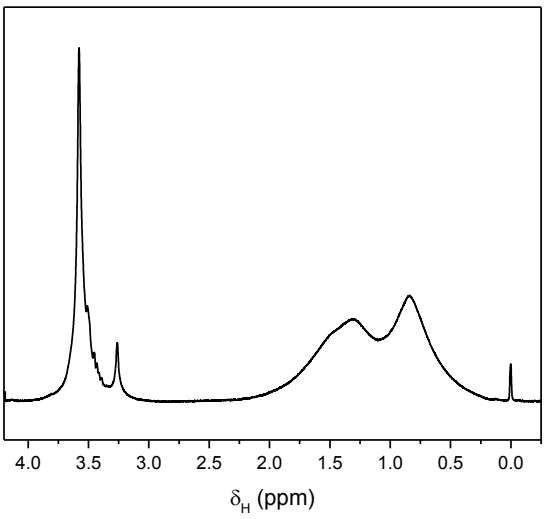

Figure 4.6 ^1H NMR spectrum of TMS protected nanoparticles after an attempted deprotection with 10 eq of KF in D_2O measureed with a 300 MHz spectrometer.

To investigate this further, the TMS protected macro-RAFT agent (**TMS-Alkyne-O-P[(PEGA)$_{12}$-*co*-(AA)$_3$**) was utilised as a model for a deprotection reaction with KF and TBAF. As before, the macro-RAFT agent was treated with 10 eq KF or TBAF (1.0 M in THF), dialysed and analysed with ^{1}H NMR spectroscopy. After treatment with TBAF, a large proportion of the salt had not been removed *via* dialysis likely due to poor water solubility (Figure 4.7). Nonetheless a clear reduction in the TMS peak at 0 ppm was observed, suggesting partial deprotection had indeed occurred. However, upon addition of KF, a less pronounced reduction in the TMS peak was evident, most probably due to the stronger ion pair formed between fluoride ions and potassium ions than with tetrabutylammonium ions (Figure 4.7). While these results indicate that deprotection is indeed possible in aqueous conditions, KF is not as efficient as TBAF, but is likely easier to removed after the reaction.

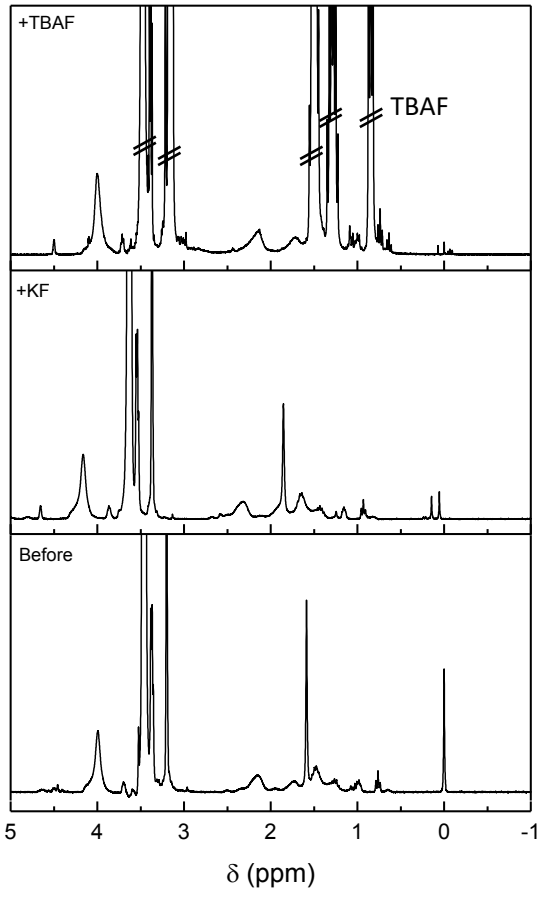

Figure 4.7 ^{1}H NMR spectra of **TMS-Alkyne-O-P[(PEGA)$_{12}$-*co*-(AA)$_3$]** before deprotection (bottom), after treatment with potassium fluoride (10 eq; middle), and after treatment with tetrabutyl ammonium fluoride (10 eq; top).

4.2.3 Unprotected propagyl ester

The results presented clearly show that an ester based RAFT agent is required to produce controlled molecular weight macro-RAFT agents. Furthermore, the addition of negative charge in the pendant chain of the nanoparticle shell is necessary to maintain colloidal stability. We envisaged that the inefficient polymerisation with **Alkyne-PAmbTC** could solely be due to the amide reinitiating group, and not the presence of a terminal alkyne. Therefore, with the unsuccessful deprotection of the TMS-alkyne coated nanoparticles with KF, a non-protected analogue of **TMS-Alkyne-PEsBTC** was synthesised, retaining the ester R group for more efficient initiation.

4.2.3.1 Synthesis of non-protected alkyne RAFT agent

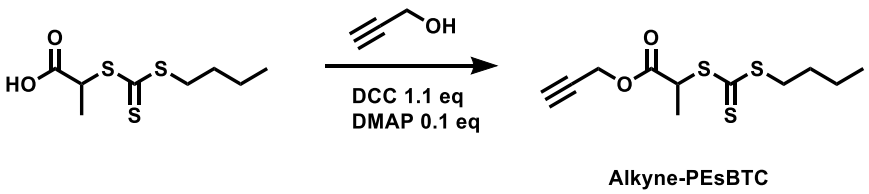

Scheme 4.6 Preparation of non-protected alkyne functional RAFT agent, **Alkyne-PEsBTC**.

Alkyne-PEsBTC was synthesised according to the conditions described in literature procedures (Scheme 4.6).[31] PABTC was esterified with propargyl alcohol, using *N,N'*-Dicyclohexylcarbodiimide (DCC) and dimethylaminopyridine (DMAP) as coupling agent and catalyst respectively at 70% yield.

4.2.3.2 Non-protected alkyne macro-RAFT agent synthesis

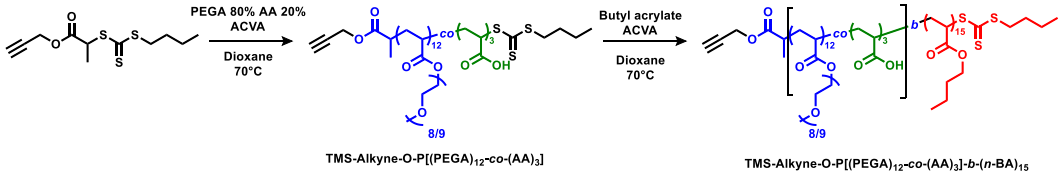

Scheme 4.7 Preparation of **TMS-Alkyne-O-P[(PEGA)$_{12}$-*co*-(AA)$_3$]-*b*-(*n*-BA)$_{15}$**

An analogous non-protected alkyne functional macro-RAFT agent to **TMS-Alkyne-*O*-P[(PEGA)$_{13}$-*co*-(AA)$_3$]-*b*-(*n*-BA)$_{15}$** was prepared *via* a two-step polymerisation. Copolymerisation of PEGA and AA (87% monomer conversion), and subsequent chain extension with *n*-BA (81% monomer conversion) mediated by **Alkyne-PEsBTC** yielded **Alkyne-O-P[(PEGA)$_{12}$-*co*-(AA)$_3$]-*b*-(*n*-BA)$_{15}$**. Both blocks had narrow molar mass

distributions ($Đ < 1.2$), with similar $M_{,th}$ and $M_{n,SEC}$ (Table 4.6). Additionally, a significant shift towards higher molar mass was evident, indicating successful chain extension (Figure 4.8). Although the terminal alkyne was not protected during the polymerisation, no low molecular weight shoulder or broadening was observed, suggesting the alkyne did not get consumed in the reaction. Furthermore, comparing the ^{1}H NMR spectrum of **Alkyne-PEsBTC** and **Alkyne-O-P[(PEGA)$_{12}$-*co*-(AA)$_3$]-*b*-(*n*-BA)$_{15}$,** the singlet at 4.6 ppm attributed to the CH_2 adjacent to the acetylene group, was retained, confirming this theory (Figure A 4.3). It is likely therefore that the poor molecular weight control, when using **Alkyne-PAmBTC,** could be mainly attributed to the amide reinitiating group as previously described, and not the unprotected alkyne.

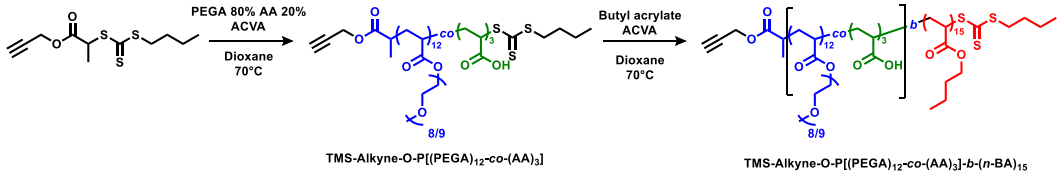

Scheme 4.8 Preparation of **Alkyne-O-P[(PEGA)$_{12}$-*co*-(AA)$_3$]-*b*-(*n*-BA)$_{15}$** via a two-step polymerisation using **Alkyne-PEsBTC** as the RAFT agent.

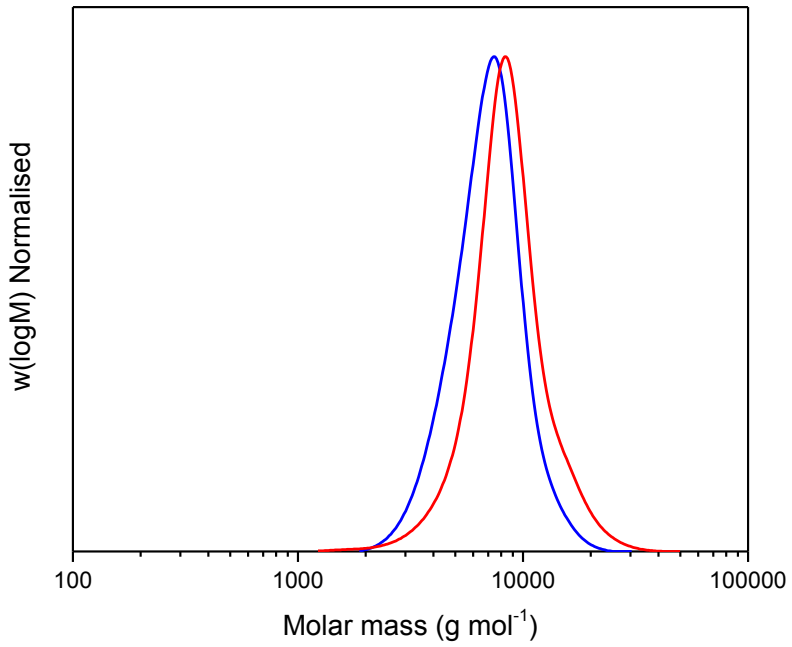

Figure 4.8 THF-SEC traces for **Alkyne-O-P[(PEGA)$_{12}$-*co*-(AA)$_3$]** (blue line) and **Alkyne-O-P[(PEGA)$_{12}$-*co*-(AA)$_3$]-*b*-(*n*-BA)$_{15}$** (red line).

Table 4.6 Characterisation data for **Alkyne-O-P[(PEGA)$_{12}$-*co*-(AA)$_3$]** and **Alkyne-O-P[(PEGA)$_{12}$-*co*-(AA)$_3$]-*b*-(*n*-BA)$_{15}$**.**

	% conv[a]	$M_{n,th}$ (g mol^{-1})[b]	$M_{n,SEC}$ (g mol^{-1})[c]	$M_{w,SEC}$ (g mol^{-1})[c]	$Đ$[c]
Alkyne-O-P[(PEGA)$_{12}$-*co*-(AA)$_3$]	87	5350	6500	7400	1.14
Alkyne-O-P[(PEGA)$_{12}$-*co*-(AA)$_3$]-*b*-(*n*-BA)$_{15}$	81	6900	7800	9100	1.16

[a]Determined by ^{1}H NMR spectroscopy, [b]Theoretical molar masses calculated with Equation 2.12, [c]Determined by THF-SEC and analysed against PMMA standards.

4.2.3.3 Test click reactions on model polymer

Although the above ^{1}H NMR spectra indicates the presence of an alkyne, the large steric bulk from the P(PEGA) chains may make this functionality inaccessible for further reactions. We envisaged that an azido functional fluorescent dye could be used as a model molecule in a CuAAC conjugation reaction, and the reaction monitored via UV detection SEC as in section 3.6.2.2 for the BODIPY labelled nanoparticles. Initially **Fluorescein-N$_3$** was synthesised *via* the amidation of the active ester derivative **Fluorescein-NHS** with azidopropanamine (Scheme 4.9). The reaction was shown to be quantitative, via the shift observed in HPLC, and the single molecular ion peak present in mass spectra, attributed to **Fluorescein-N$_3$**. Due to the low yield of the isolated compound (< 5 mg), unfortunately ^{1}H NMR and ^{13}C NMR spectra were not obtained.

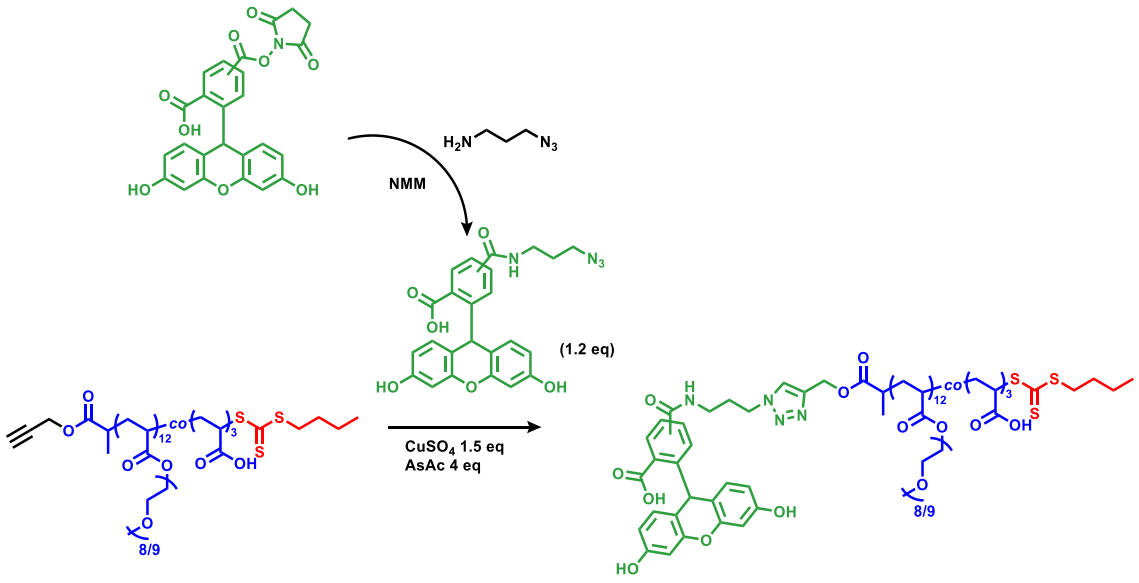

Scheme 4.9 Synthesis of **Fluorescein-N$_3$** and CuAAC conjugation of **Fluorescein-N$_3$** to **Alkyne-O-P[(PEGA)$_{12}$-*co*-(AA)$_3$]** yielding **Fluorescein-O-P[(PEGA)$_{12}$-*co*-(AA)$_3$]**.

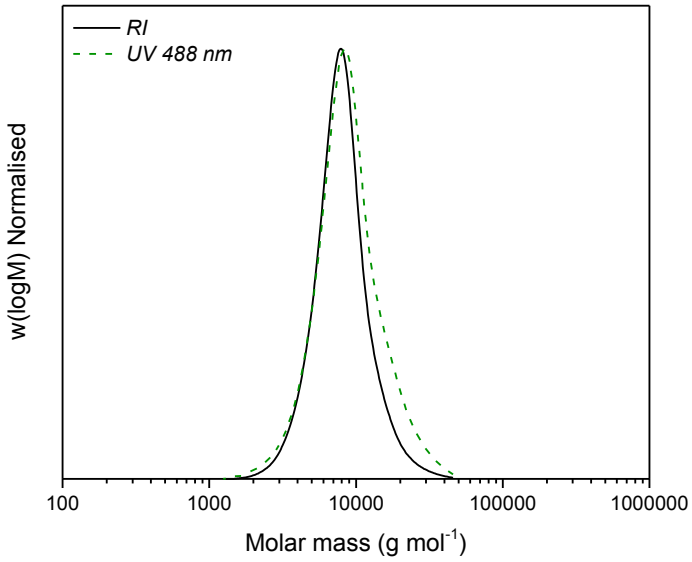

Table 4.7 THF-SEC of **Fluorescein-O-P[(PEGA)$_{12}$-*co*-(AA)$_3$]** using RI detection (black line) and UV detection at 488 nm (green dashed line).

Using previously described conditions, a CuAAC reaction was performed on **Alkyne-O-P[(PEGA)$_{12}$-*co*-(AA)$_3$]** with **Fluorescein-N$_3$** using copper sulfate as the Cu(II) source, and ascorbic acid as a reducing agent to generate Cu(I) *in situ* (Scheme 4.9).[32] After the reaction, a clear overlap between the RI and UV$_{488\ nm}$ (488 nm is the absorbance maxima of fluorescein; Table 4.7) traces could be observed, suggesting **Fluorescein-N$_3$** had been conjugated.

As some potential azide substrates may be larger than small molecules, the CuAAC reaction was further investigated using a 2 kDa azido function PEG (**PEG-2k-N$_3$**) and the same conditions as above (Scheme 4.10). The reaction was monitored using SEC, and after 2 h stirring at room temperature a clear shift towards higher molar mass (6500 g mol^{-1} for **Alkyne-O-P[(PEGA)$_{12}$-co-(AA)$_3$]** to 8000 g mol^{-1} for **PEG-2k-P[(PEGA)$_{12}$-*co*-(AA)$_3$]**) was observed, suggesting successful conjugation (Figure 4.9; Figure 4.8). A residual amount of **PEG-2k-N$_3$** was observed as a low molar mass shoulder, and is likely to be the extra 0.2 eq present at the end of the reaction. Overall, these results suggest that after producing the macro-RAFT agent with a non-protected alkyne end-group, it is still available for post polymerisation modification.

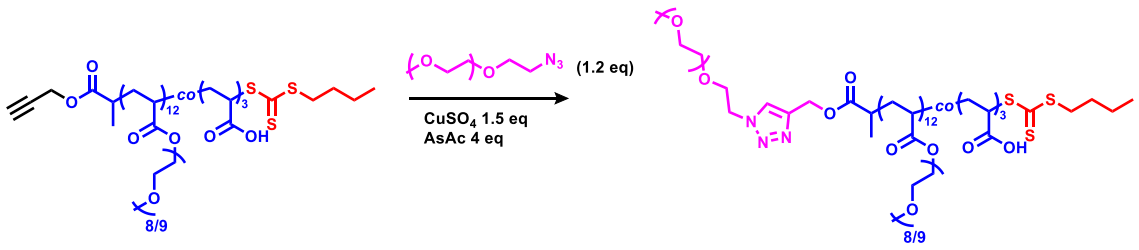

Scheme 4.10 CuAAC conjugation of **PEG-2k-N$_3$** to **Alkyne-O-P[(PEGA)$_{12}$-*co*-(AA)$_3$]** yielding PEG-2k-O-P[(PEGA)$_{12}$-*co*-(AA)$_3$].

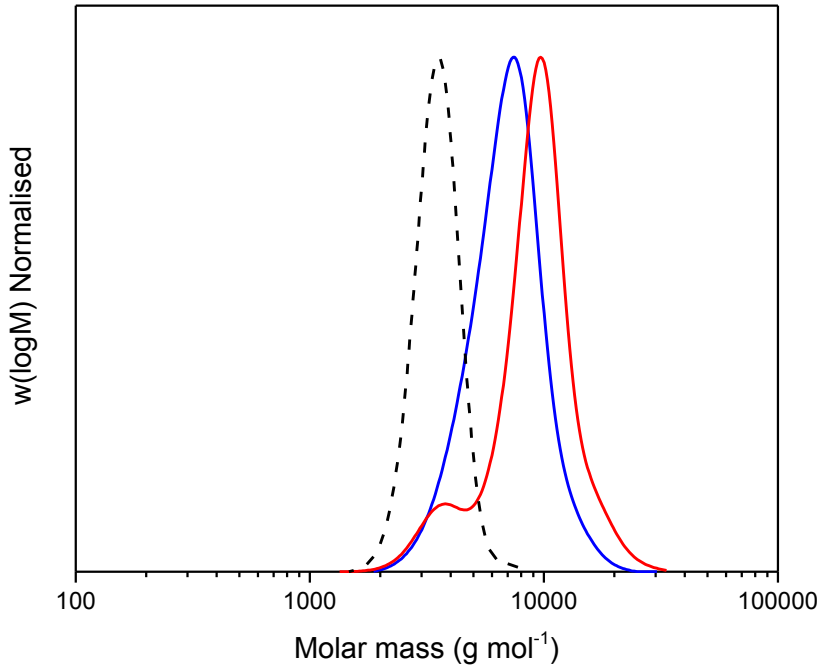

Figure 4.9 THF-SEC traces of **PEG-2k-N$_3$** (black dashed line), **Alkyne-O-P[(PEGA)$_{12}$-*co*-(AA)$_3$]** (blue line) and **PEG-2k-O-P[(PEGA)$_{12}$-*co*-(AA)$_3$]** (red line).

Table 4.8 Characterisation data for **PEG-2k-N$_3$**, **Alkyne-O-P[(PEGA)$_{12}$-*co*-(AA)$_3$]**, **PEG-2k-P[(PEGA)$_{12}$-*co*-(AA)$_3$]**.

	$M_{n,th}$ (g mol^{-1})^a	$M_{n,SEC}$ (g mol^{-1})^b	$M_{w,SEC}$ (g mol^{-1})^b	$Đ^c$
PEG-2k-N$_3$	2000	3400	3560	1.05
Alkyne-O-P[(PEGA)$_{12}$-*co*-(AA)$_3$]	5350	6500	7400	1.14
PEG-2k-P[(PEGA)$_{12}$-*co*-(AA)$_3$]	7900	8000	9600	1.20

[a]Determined using Equation 2.12. [c]Determined by THF-SEC, calibrated with PMMA standards.

4.2.3.4 RAFT emulsion polymerisation with non-protected alkyne macro-RAFT agent

Using the conditions described above, a RAFT emulsion polymerisation was performed using the non-protected alkyne macro-RAFT agent, **Alkyne-O-P[(PEGA)$_{12}$-*co*-(AA)$_3$]-*b*-(*n*-BA)$_{15}$**, targeting a DP of 200, to produce non-protected alkyne functional nanoparticles (Scheme 4.11).

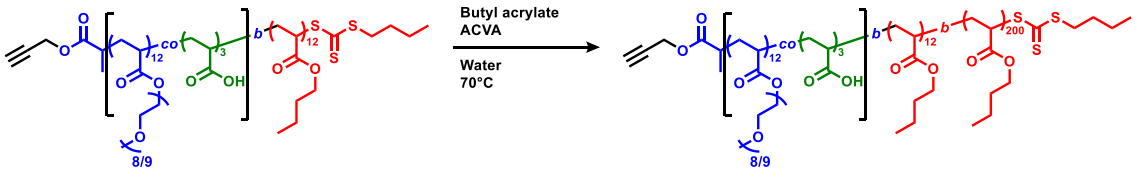

Scheme 4.11 RAFT emulsion polymerisation of *n*-BA using macro-RAFT agent **Alkyne-O-P[(PEGA)$_{12}$-*co*-(AA)$_3$]-(*n*-BA)$_{15}$** to generate **Alkyne-O-P[(PEGA)$_{12}$-*co*-(AA)$_3$]-(*n*-BA)$_{15}$-(*n*-BA)$_{200}$**.

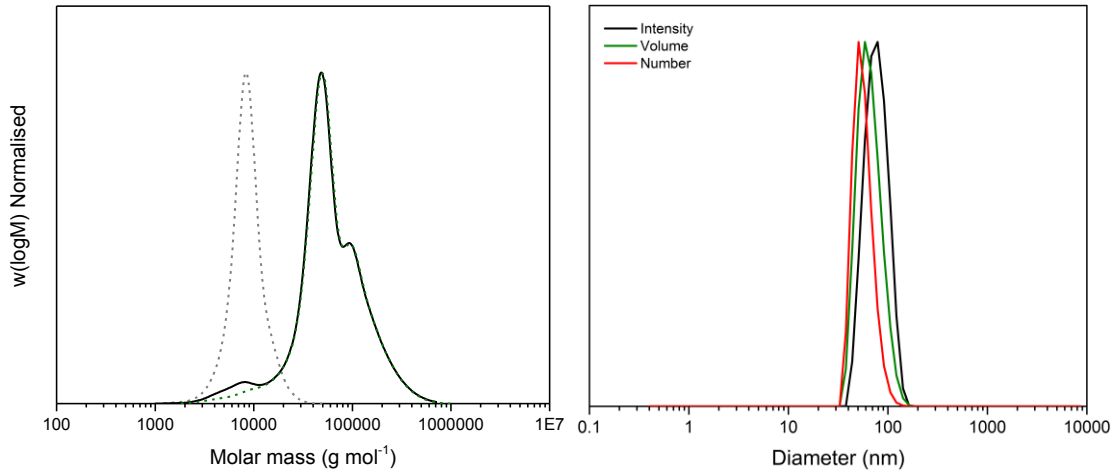

Figure 4.10. (A) SEC chromatograms of dissolved **Alkyne-O-P[(PEGA)$_{12}$-*co*-(AA)$_3$]-(*n*-BA)$_{15}$-(*n*-BA)$_{200}$** nanoparticles before dialysis (black line), after dialysis (green dashed line) and macro-RAFT agent **Alkyne-O-P[(PEGA)$_{12}$-*co*-(AA)$_3$]-(*n*-BA)$_{15}$** (grey dashed line).

Table 4.9 Characterisation data for non-protected alkyne functional nanoparticles, **Alkyne-O-P[(PEGA)$_{12}$-*co*-(AA)$_3$]-*b*-(*n*-BA)$_{12}$- *b*-(*n*-BA)$_{200}$]**.

	D_h (nm)[a]	*PDi*[b]	ZP (mV)[c]	$M_{n,SEC}$ (g mol^{-1})[e]	*Đ*[f]
TMS-Alkyne-O-P[(PEGA)$_{12}$-*co*-(AA)$_3$]-*b*-(*n*-BA)$_{12}$-*b*-(*n*-BA)$_{200}$]	101.4	0.055	-52.1	37000	2.12

[a]Determined by DLS. [b]Calculated with Equation 2.13. [c]Determined with a zetasizer. [d]Measured with THF-SEC and analysed against PMMA standards. All polymerisations reached >99% conversion. $M_{n,th}$ = 33100 g mol^{-1}.

Interestingly, the particles produced with this non-protected macro-RAFT agent had a far smaller diameter (54 nm; Figure 4.10b) than those extended from the TMS protected derivative (101 nm; Figure 4.5a). This is likely due to the increased surface hydrophilicity and electrostatic stability without the TMS protecting group and with the acrylic acid moieties respectively. As before, SEC analysis revealed a high chain extension efficiency and a relatively narrow dispersity compared to those obtained with the macro-RAFT agent without acrylic acid, and with the hydrophobic TMS group. Furthermore, similar $M_{n,th}$ and $M_{n,SEC}$ were observed (33100 and 37000 g mol^{-1} respectively) indicating good molecular weight control.

Prior to any CuAAC reactions directly on the nanoparticles, the latex was dialysed to remove any unconsumed macro-RAFT agent, resulting in a reduction of the lower molar mass region in the size exclusion chromatogram Figure 4.10a. This is of particular importance, as the residual macro-RAFT agent also had alkyne functionality and may compete against the acetylene groups at the nanoparticle surface during a CuAAC reaction.

4.2.3.5 Click reactions on nanoparticles

CuAAC reactions with both **PEG-2k-N$_3$** and **Fluorescein-N$_3$** were performed with the above alkyne functional nanoparticles, assuming that 100% of the macro-RAFT agent, and therefore alkyne moieties were available at the particle surface. After addition of the azido functional PEG, no shift in the SEC was observed, while some of the **PEG-2k-N$_3$** could still be seen at lower molar mass, likely due to incomplete conversion. However, any cycloaddition which did occur may not be detectable *via* SEC due to the small increase in molar mass in comparison to the original trace before reaction. Nonetheless, as in the CuAAC reactions with the model polymer, after addition of **Fluorescein-N$_3$** to the nanoparticles in the presence of $CuSO_4$ and ascorbic acid, a clear overlap could be observed between the RI and UV_{488} nm channel. These results indicate **Fluorescein-N$_3$** had been successfully clicked onto the nanoparticles. DLS analysis comparing before and after the reaction, showed negligible differences in particle size and *PDi* suggesting this process did not perturb colloidal stability. The above results could suggest that larger molecules cannot be conjugated to our nanoparticles, possibly due to the dense brush of P(PEGA) at the nanoparticle surface, while smaller molecules such as **Fluorescein-N$_3$** are able to diffuse close to the acetylene moieties at the surface and react successfully

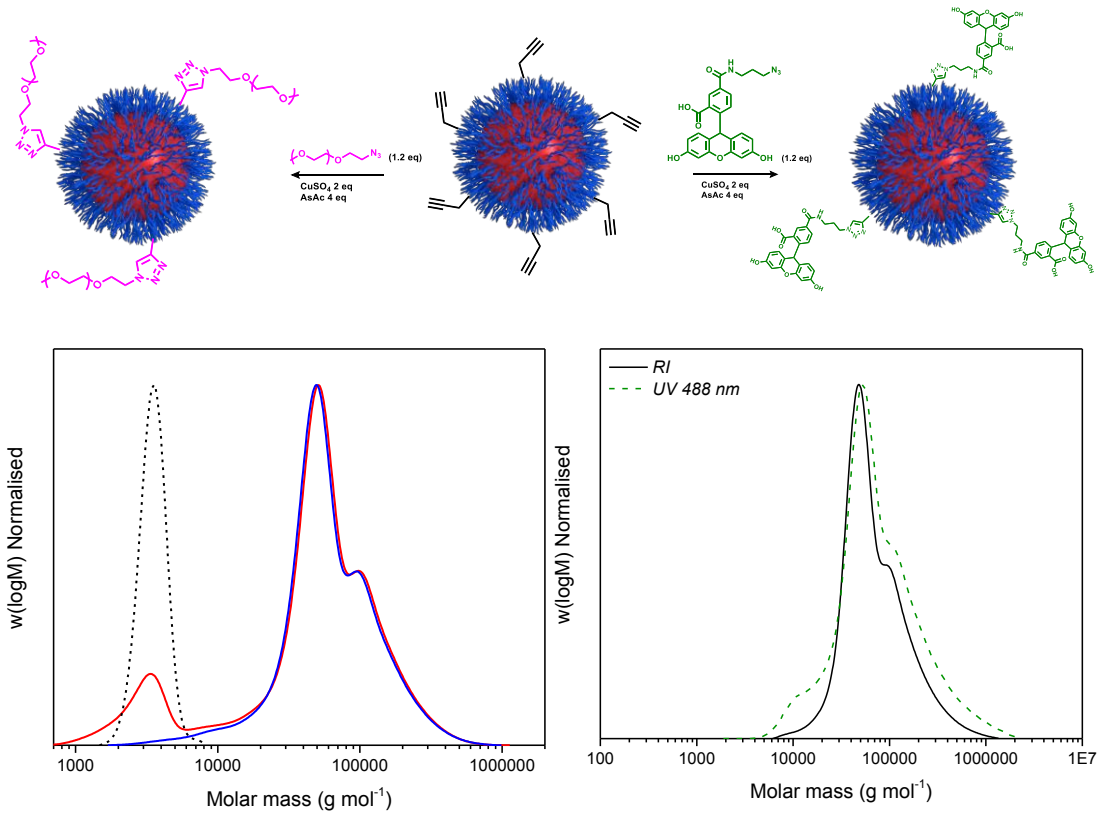

Figure 4.11 CuAAC reactions on the surface of the alkyne functional nanoparticles with (A) *left side* – **PEG-2k-N$_3$** and *right side* – **Fluorescein-N$_3$**. (B) THF-SEC for dissolved nanoparticles after (red line) CuAAC with **PEG-2k-N$_3$** (black dashed line), compared with chromatogram for before reaction (blue line). (C) THF-SEC RI and UV$_{488\ nm}$ detection after (green dashed line) CuAAC with **Fluorescein-N$_3$**, compared with before the reaction (black line).

4.2.3.6 Purification of Cu^{2+} and unreacted substrate on model nanoparticles

To use this approach for applications in biological systems, the Cu^{2+} source should ideally be removed from the latex to maintain biocompatibility.[33]

To test different purification techniques, the alkyne-functional nanoparticles were spiked with 10 mM Cu_2SO_4 and subjected to two purification techniques (a two-step dialysis against 10 mM EDTA, then against pure water, or a Sephadex SEC) and a control. After purification the particles were concentrated using Amicon centrifugation dialysis tubes such they were all at the same concentration, and treated with 100 mM EDTA and left to stir overnight. Any residual copper was monitored *via* the formation of the EDTA-Cu^{2+} which appears bright blue in aqueous solution. For the control treatment, as expected a bright blue colour was indeed observed. However, after both dialysis and Sephadex

column purification no colour change was seen, suggesting most, if not all, of the copper had been successfully removed. Having two possible purification approaches could be highly useful, as the dialysis approach can take up to 72 h, whereas the Sephadex column requires only 30 min to perform, which is perhaps beneficial for sensitive samples (proteins, radiolabels etc.)

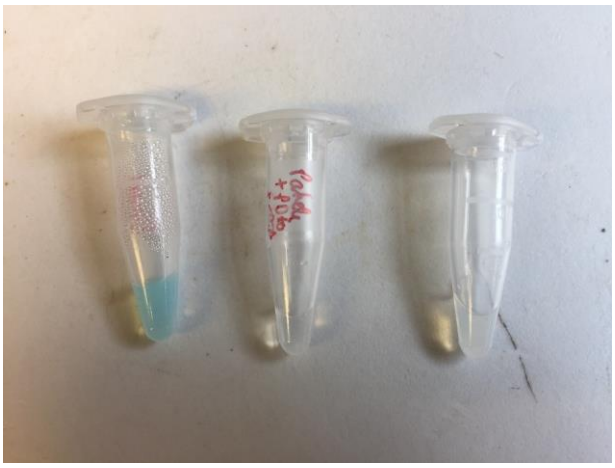

Figure 4.12 Digital photograph of **Alkyne-O-P[(PEGA)$_{12}$-*co*-(AA)$_3$]-(*n*-BA)$_{15}$-*b*-(*n*-BA)$_{200}$** nanoparticles spiked with 10 mM $CuSO_4$ and then purified *via* dialysis (right) or sephadex size exclusion chromatography (middle) or non-purified (left) post-addition of 100 mM EDTA.

Finally, to investigate the efficiency of removing a model substrate, the azide functional nanoparticles were instead spiked with **Fluorescein-N$_3$** and purification attempted with Sephadex SEC. 1 mL fractions were collected (11 fractions total), then the fluorescence intensity (λ_{ex} = 488 nm, λ_{em} = 512 nm; **Fluorescein-N$_3$**) and the scattering intensity (nanoparticles) was measured for each fraction.

It was found that the nanoparticles eluted quickly from the column, between fractions 2 and 5, while the spiked **Fluorescein-N$_3$** eluted slower between fractions 5 and 11. This shows that small compounds can be separated effectively from the larger nanoparticles, with only 1 overlapping fraction (F4).

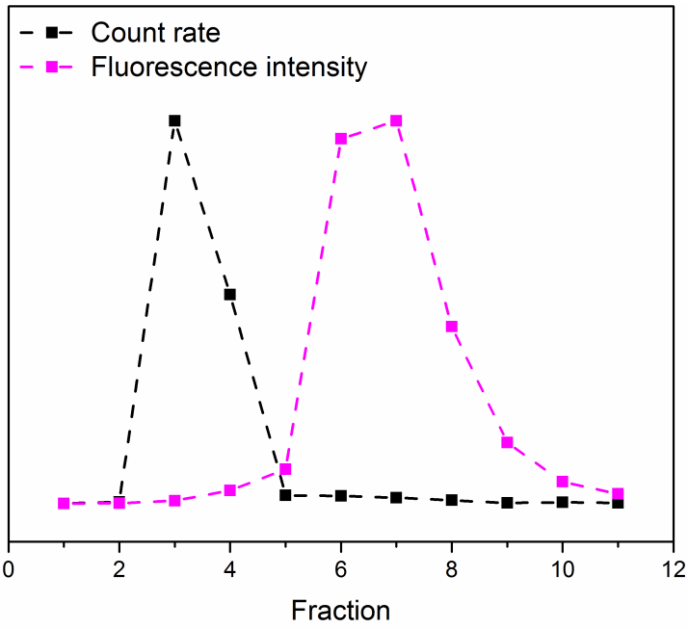

Figure 4.13 Scattering intensity (black squares; measured with DLS), and fluorescence intensity (λ_{ex} = 488 nm, λ_{em} = 512 nm) of **Fluorescein-N$_3$** spiked alkyne functional **Alkyne-O-P[(PEGA)$_{12}$-*co*-(AA)$_3$]-(*n*-BA)$_{15}$-*b*-(*n*-BA)$_{200}$** nanoparticles, for each fraction post-separation with a PD-10 sephadex column.

4.3 Conclusion

In conclusion, through a systematic polymerisation study using three different alkyne functional RAFT agents (amide coupled, ester coupled and TMS protected ester coupled), we have investigated the requirements for generating alkyne functional nanoparticles *via* RAFT emulsion polymerisation. Our results indicate that the presence of an amide bond at the reinitiating group severely reduces molecular weight control. Furthermore, protection of terminal alkynes throughout the synthesis is required to generate low dispersity macro-RAFT agent stabilisers. However, replacement of the carboxylate end-group dramatically impacts the colloidal stability of the nanoparticles. This was overcome by reintroducing this functionality into the side chain by copolymerisation of acrylic acid into the hydrophilic block of the stabilising macro-RAFT agent. Finally, we showed that the resultant alkyne functional nanoparticles could be post-modified with either an azido-functional linear PEG or fluorescein azide. This methodology, as a way to introduce functionality at the nanoparticle surface, paves the way for the generation of complex biomaterials.

4.4 Experimental

4.4.1 Materials

Propagyl amine, propagyl alcohol, 3-(Trimethylsilyl)propargyl alcohol, DCC, DMAP, PyBOP, DIPEA, polyethylene glycol methyl ether acrylate, *n*-butyl acrylate, acrylic acid, $CuSO_4$ and ascorbic acid were purchased from Sigma Aldrich. All monomers were passed through basic aluminium oxide to remove inhibitors before polymerisation. Deuterium oxide, chloroform-d_3 were obtained from Sigma Aldrich and used for NMR spectroscopy. Thermal initiator 4,4′-azobis(4-cyanovaleric acid) (ACVA, >98%, Aldrich) was used as received. RAFT agent PABTC was synthesised as previously described.[34] Macro-RAFT agent **MRA-*n*BA** (P[(PEGA)$_8$-*b*-(*n*-BA)$_8$]) was synthesised as described in chapter 2. Solvents were acquired from commercial sources. PD-10 acquired from GE healthcare.

4.4.2 Instrumentation and Analysis

4.4.2.1 NMR spectroscopy

^{1}H NMR and ^{13}C NMR spectra were recorded as described in section 2.4.2.1

4.4.2.2 Size exclusion chromatography

THF-SEC was performed using conditions described in section 2.4.2.2

4.4.2.3 Theoretical molar mass calculation

Theoretical molar masses were calculated as described in section 2.4.2.3

4.4.2.4 Dynamic light scattering and ζ-potential

DLS and ζ-potential measurements were carried out as described in 2.4.2.4.

4.4.3 Synthesis

4.4.3.1 Synthesis of Alkyne-PAmBTC[27]

A stirred solution of PyBOP (1.64 g, 3.15 mmol, 1 eq) and DIPEA (0.97 g, 6.74 mmol, 2.4 eq) in DCM (5 mL) was added to a separate solution of PABTC (0.75 g, 3.15 mmol, 1 eq; dissolved in 5 mL DCM) in a 25 mL round bottomed flask fitted with a magnetic stirrer, turning the solution deep red. Propagyl amine (173 mg, 3.15 mmol, 1 eq) was added subsequently dropwise to the PABTC solution. After all of the amine had been added, the solution returned to its original yellow colour and was left to stir at room temperature overnight. The reaction was monitored with TLC using a 50/50 hexane/ethyl acetate eluent. The reaction mixture was then concentrated under reduced pressure, and purified *via* automatic column chromatography using a gradient eluent (10% -50% ethyl acetate in hexane, over 30 min) yielding **Alkyne-PAmBTC** (589.6 mg, 68% yield) as a pale yellow solid. ^{1}H NMR (500 MHz, $CDCl_3$) δ 6.57 (br, J = 45.1 Hz, 1H, N**H**), 4.77 (q, J = 7.4 Hz, 1H, CH_3-C**H**), 4.05 (qdd, J = 17.6, 5.3, 2.5 Hz, 2H, NH-C**H**$_2$), 3.41 (t, 2H, S-C**H**$_2$), 2.25 (t, J = 2.4 Hz, 1H, C≡C**H**), 1.72 (p, 2H, S-CH_2-C**H**$_2$), 1.61 (d, J = 7.3 Hz, 3H, CH-C**H**$_3$), 1.46 (h, 2H, C**H**$_2$-CH_3), 0.97 (t, J = 7.4 Hz, 3H, CH_2-C**H**$_3$). ^{13}C NMR (126 MHz, $CDCl_3$) δ 224.04 (**C**=S), 170.16 (**C**=O), 79.05 (**C**≡CH), 71.82 (C≡**C**H), 47.48 (S-**C**H), 37.35 (S-**C**H_2), 29.86 (NH-**C**H_2), 29.55 (S-CH_2-**C**H_2), 22.06 (CH_3-**C**H_2), 16.06 (CH-**C**H_3), 13.59 (CH_2-**C**H_3). FTIR ν cm^{-1}: 3281(s, C-H alkyne), 2957 + 2927 (m, N-H amide), 2868 (m, C-H alkane), 1656 (s, C=O amide). ESI-MS m/z: 276.0 $[M+H]^+$.

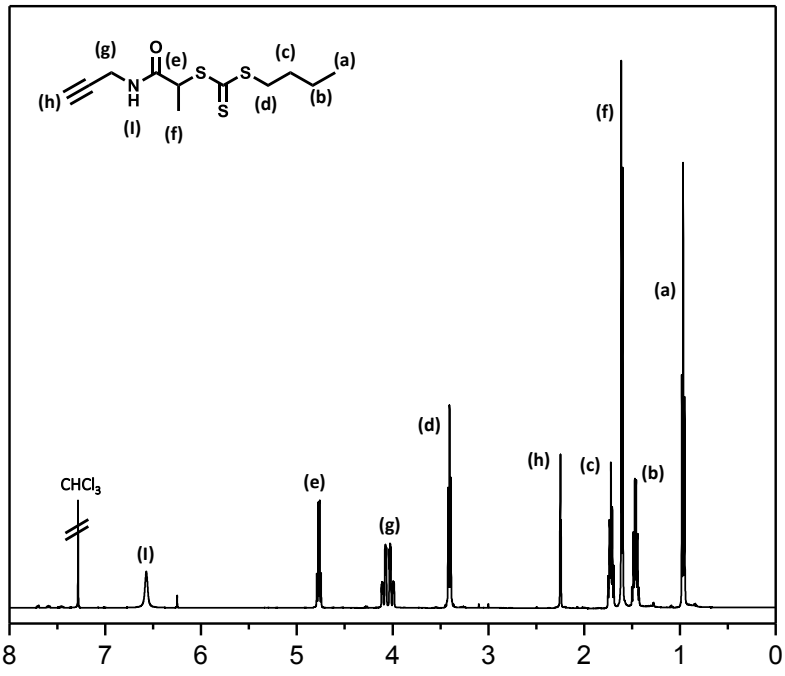

Figure 4.14 ^{1}H NMR spectrum of **Alkyne-PAmBTC** measured at 500 MHz in $CDCl_3$.

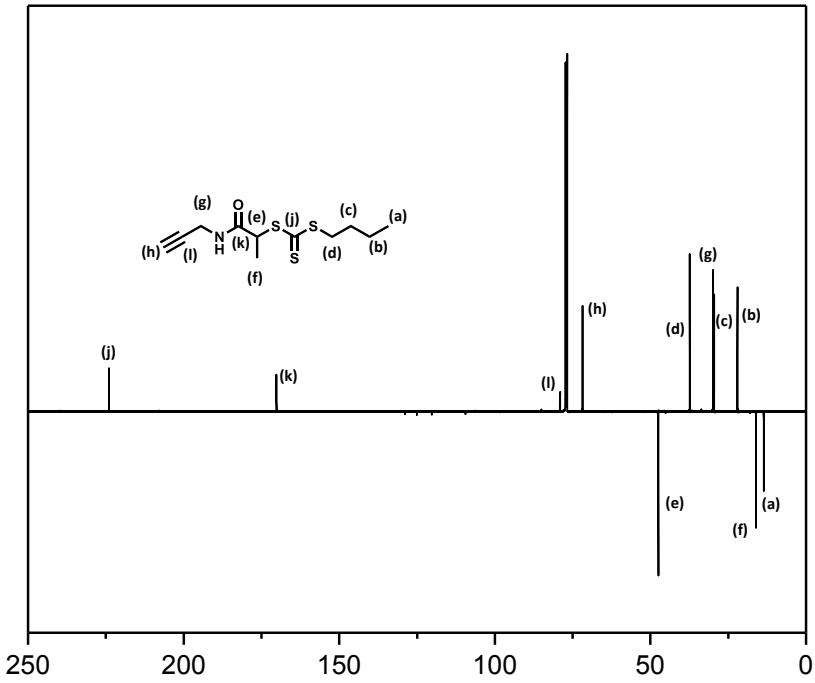

Figure 4.15 DEPT-135 ^{13}C NMR spectrum of **Alkyne-PAmBTC** measured at 126 MHz in $CDCl_3$.

4.4.3.2 Synthesis of TMS-Alkyne-PEsBTC[28]

DCC (0.714 g, 3.46 mmol, 1.1 eq) and DMAP (38 mg, 0.315 mmol, 0.1 eq) was added to a stirred solution of PABTC (0.750 g, 3.15 mmol, 1 eq) in DCM (20 mL), in a 50 mL round bottomed flask turning the solution deep red. 3-(Trimethylsilyl)propargyl alcohol (0.444 g, 3.46 mmol, 1.1 eq) was added to the activated PABTC solution and stirred overnight at room temperature. The mixture was washed with 50 mL water (3x) and 1 M HCl (3 x), the organic phase dried over sodium sulfate, and purified *via* flash column chromatography using a gradient eluent (0% - 20% ethyl acetate in hexane over 30 min), yielding **TMS-Alkyne-PEsBTC** as a bright yellow oil (0.53 g, 48% yield). ^{1}H NMR (500 MHz, $CDCl_3$) δ 4.84 (q, *J* = 7.4 Hz, 1H, S-C**H**), 4.73 (d, *J* = 3.1 Hz, 2H, O-C**H**$_2$), 3.36 (t, *J* = 7.4 Hz, 2H, S-C**H**$_2$), 1.68 (quint, 2H, S-CH_2-C**H**$_2$), 1.62 (d, *J* = 7.4 Hz, 3H, CH-C**H**$_3$), 1.43 (sext, 2H, CH_3-C**H**$_2$) 0.93 (t, *J* = 7.4 Hz, 3H, CH_2-C**H**$_3$), 0.18 (s, 9H, Si-C**H**$_3$). ^{13}C NMR (126 MHz, $CDCl_3$) δ 222.07 (**C**=S), 170.81 (**C**=O), 98.64 (**C**≡C-Si), 93.10 (C≡**C**-Si), 54.29 (O-**C**H_2), 48.10 (S-**C**H), 37.30 (S-**C**H_2), 30.24 (S-**C**H_2-**C**H_2), 22.39 (CH_3-**C**H_2), 17.04 (CH-**C**H_3), 13.91 (CH_2-**C**H_3), -0.01 (Si-**C**H_3). FTIR ν cm^{-1}: 2958 + 2931 (m, N-H amide), 2872 (m, C-H alkane), 2186 (w, C≡C alkyne), 1741 (s, C=O ester). ESI-MS m/z: 349.6 $[M+H]^+$.

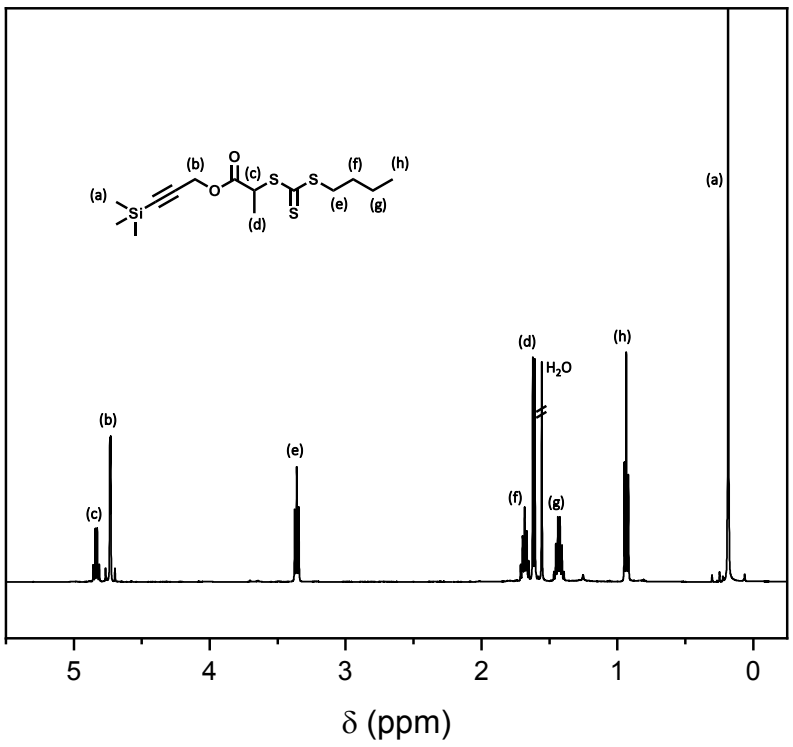

Figure 4.16 ^{1}H NMR spectrum of **TMS-Alkyne-PEsBTC** measured at 500 MHz in $CDCl_3$.

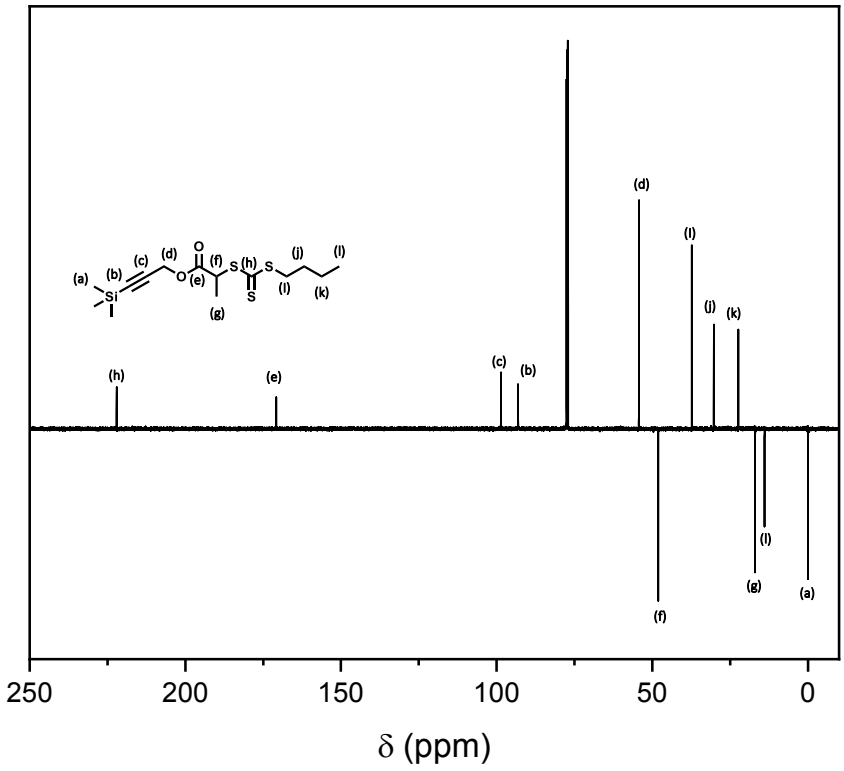

Figure 4.17 DEPT-135 ^{13}C NMR spectrum of **Alkyne-PEsBTC** measured at 126 MHz in $CDCl_3$.

4.4.3.3 Synthesis of Alkyne-PEsBTC[31]

EDC (3.86 g, 20.1 mmol, 1.2 eq) and DMAP (0.240 g, 2.1 mmol, 0.12 eq) was added to a stirred solution of PABTC (4 g, 16.7 mmol, 1 eq) in DCM (20 mL), in a 50 mL round bottomed flask turning the solution deep red. Propargyl alcohol (1.13 g, 20.1 mmol, 1.2 eq) was added to the activated PABTC solution and stirred overnight at room temperature. The mixture was washed with 50 mL water (3x) and 1 M HCl (3 x), the organic phase dried over sodium sulfate, and purified *via* flash column chromatography using a gradient eluent (0% - 50% ethyl acetate in hexane over 30 min), yielding **Alkyne-PEsBTC** (4.20 g, 91% yield) as an orange oil. ^1H NMR (500 MHz, $CDCl_3$) δ 4.85 (q, J = 7.4 Hz, 1H, S-C**H**), 4.73 (t, J = 2.8 Hz, 2H, O-C**H**$_2$), 3.36 (t, J = 7.4 Hz, 2H, S-C**H**$_2$), 2.50 (t, J = 2.4 Hz, 1H, C≡C-**H**), 1.72 – 1.65 (m, 2H, S-CH$_2$-C**H**$_2$), 1.62 (d, J = 7.4 Hz, 3H, S-CH-C**H**$_3$), 1.47 – 1.38 (m, 2H, CH$_3$-C**H**$_2$), 0.93 (t, J = 7.4 Hz, 3H, CH$_2$-C**H**$_3$). ^{13}C NMR (126 MHz, $CDCl_3$) δ 221.75 (**C**=S), 170.51 (**C**=O), 75.43 (**C**≡CH), 53.18 (O-**C**H$_2$), 47.62 (S-**C**H), 37.03 (S-**C**H$_2$), 29.91 (S-CH$_2$-**C**H$_2$), 22.07 (CH$_3$-**C**H$_2$), 16.70 (CH-**C**H$_3$), 13.60 (CH$_2$-**C**H$_3$). FTIR ν cm^{-1}: 3290(s, C-H alkyne) 2957 + 2930 (m, N-H amide), 2871 (m, C-H alkane), 2131 (w, C≡C alkyne), 1738 (s, C=O ester). ESI-MS m/z: 277.0 $[M+H]^+$.

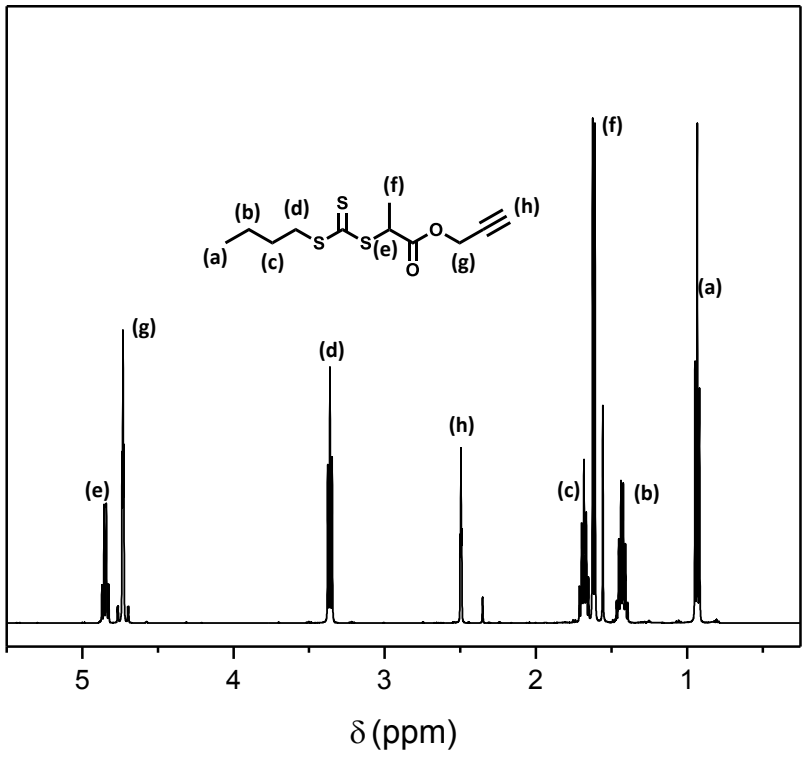

Figure 4.18 ^{1}H NMR spectrum of **Alkyne-PEsBTC** measured at 500 MHz in $CDCl_3$.

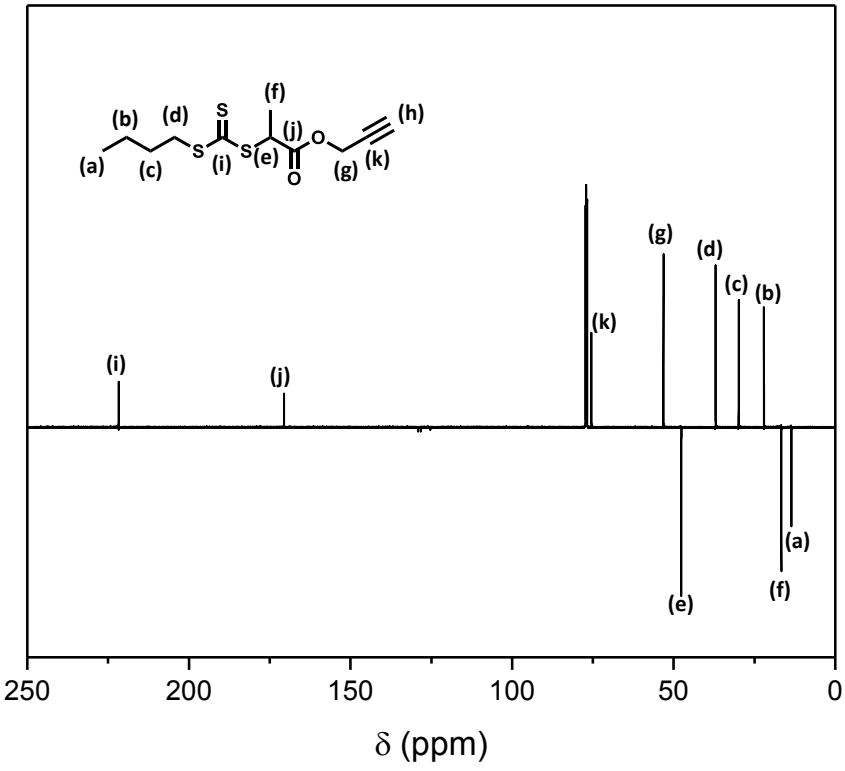

Figure 4.19 DEPT-135 ^{13}C NMR spectrum of **Alkyne-PEsBTC** measured at 126 MHz in $CDCl_3$.

4.4.3.4 Preparation of macro-RAFT agents

Macro-RAFT agents **TMS-Alkyne-O-P[(PEGA)$_{12}$-*b*-(*n*-BA)$_{12}$]**, **TMS-Alkyne-O-P[(PEGA)$_{12}$-*co*-(AA)$_3$]-(*n*-BA)$_{15}$** and **Alkyne-O-P[(PEGA)$_{12}$-*co*-(AA)$_3$]-(*n*-BA)$_{15}$** were prepared using the conventional RAFT polymerisation procedure described in section 2.4.3.3. Full details for polymerisation conditions can be found in Table A4.3.

4.4.3.5 Preparation of micelle blends[29]

Micelle blends of **TMS-Alkyne-O-P[(PEGA)$_{12}$-*b*-(*n*-BA)$_{12}$]** and **MRA-*n*BA**, were prepared by dissolving both di-block macro-RAFT agents in THF (10 mg mL^{-1}), which were mixed in separate test tubes in 5 molar ratios (see Table 4.3). The mixtures were then dried thoroughly at 70°C, were rehydrated in 1 mL of water, and were left to stir overnight. RAFT emulsion polymerisations were then performed using these micelle blends using conditions described in section 2.4.3.4.

4.4.3.6 RAFT emulsion polymerisation

RAFT emulsion polymerisations (without micelle blending) were performed using conditions described in section 2.4.3.4. Monomer conversion was determined using gravimetric techniques.

4.4.3.7 Deprotection of TMS protected nanoparticles

The TMS protected alkyne functional nanoparticles (1 eq alkyne), were treated with KF (10 eq) and stirred overnight. The nanoparticle suspension was then dialysed three times in D_2O (30 mL) using a 30,000 Da MWCO centrifugation dialysis tube. The nanoparticle suspension was then analysed directly with ^{1}H NMR spectroscopy.

4.4.3.8 Deprotection of TMS protecting group using TBAF or KF

TMS-Alkyne-O-P[(PEGA)$_{12}$-*co*-(AA)$_3$] (20 mg, 3.38 μmol, 1 eq) was dissolved in water (1 mL) and treated with either TBAF (1M in THF; 33.8 μmol, 10 eq) or KF (33.8 μmol, 10 eq). The mixtures were stirred overnight, then dialysed (3500 Da MWCO) against pure water for 24 h. Both solutions were then freeze-dried and the product extracted with $CDCl_3$, then analysed with ^{1}H NMR spectroscopy directly.

4.4.3.9 Synthesis of Fluorescein-N_3

N-methyl morpholine (NMM; 19 mg, 0.19 mmol, 3 eq) was added to solution of **Fluorescein-N_3** (30 mg, 63.4 µmol, 1 eq) dissolved in 1 mL DMSO and stirred for 5 min. Azidopropanamine (6.3 mg, 63.4 µmol, 1.0 eq) was added directly and stirred overnight. The reaction mixture was analysed *via* HPLC showing complete conversion into **Fluorescein-N_3**. This was then precipitated into methyltertbutyl ether (5 mL), collected *via* centrifugation, and dried under reduced pressure yielding **Fluorescein-N_3** (5 mg, 10.5 mmol, 16%) as an orange powder. ESI-MS m/z: 457.1 $[M-H]^-$.

4.4.3.10 CuAAC reactions on P(PEGA)$_{12}$-*co*-(AA)$_3$

Alkyne-O-P[(PEGA)$_{12}$-*co*-(AA)$_3$] (25 mg, 4.67 µmol, 1 eq), $CuSO_4$ (1.75 mg, 7.00 µmol, 1.5 eq) and either **Fluorescein-N_3** (2.13 mg, 4.7 µmol, 1. eq) or **PEG-2k-N_3** (11.2 mg, 5.6 µmol, 1.2 eq) were dissolved in 1 mL water, and purged with dinitrogen for 5 min. A 0.5 mL solution of ascorbic acid (3.29 mg, 18.7 µmol, 4 eq) was then transferred *via* syringe and stirred overnight. The reaction mixture was then lyophilised, the organic components extracted in $CHCl_3$ and analysed with THF-SEC and ^{1}H NMR spectroscopy.

4.4.3.11 CuAAC reactions on alkyne functional nanoparticles

The alkyne functional nanoparticles (100 µL, 0.285 µmol alkyne, 1 eq), $CuSO_4$ (0.128 mg, 0.513 µmol, 1.8 eq) and **PEG-2k-N_3** (0.855 mg, 0.427 µmol, 1.5 eq) were dissolved in 1 mL water, and purged with dinitrogen for 5 min. A 0.5 mL solution of ascorbic acid (0.2 mg, 1.14 µmol, 4 eq) was then transferred *via* syringe and stirred overnight. CuAAC reactions were performed on the alkyne functional nanoparticles with **Fluorescein-N_3** with identical conditions.

4.4.3.12 Removal of $CuSO_4$ from latex nanoparticles *via* dialysis

The alkyne functional nanoparticles (200 µL) were spiked with 10 mM $CuSO_4$ and dialysed against 1 L 10 mM EDTA for 48 h (changing the media 3 x), then against 1L pure water for 48 h (changing the media 3 x). The nanoparticle suspension was then concentrated to 100 µL using dialysis centrifuge tubes (30000 Da MWCO). The presence of Cu^{2+} was monitored via the addition of 100 mM EDTA.

4.4.3.13 Removal of $CuSO_4$ from nanoparticles *via* SEC

As above, the alkyne functional nanoparticles (200 μL) were spiked with 10 mM $CuSO_4$, diluted to 2 mL and passed through a prepacked PD10 G25 sephadex column. 1 mL fractions were collected until all of the nanoparticles had eluted, which were then combined and concentrated with dialysis centrifugation (30000 Da MWCO). The presence of Cu^{2+} was monitored via the addition of 100 mM EDTA.

4.4.3.14 Removal of Fluorescein-N_3 from latex nanoparticles *via* SEC

The alkyne functional nanoparticles (200 μL) were spiked with 2 mg **Fluorescein-N_3**, diluted to 2 mL, and passed through a prepacked PD10 G25 sephadex column. 11 1 mL fractions were collected, and the fluorescence intensity (λ_{ex} = 488 nm, λ_{em} = 512 nm) and scattering intensity monitored with *via* dynamic light scattering with a fixed attenuation, for each fraction.

References

1. L. Pasquato, P. Pengo and P. Scrimin, *Supramol. Chem.*, 2005, **17**, 163-171.
2. K. C. Anyaogu, A. V. Fedorov and D. C. Neckers, *Langmuir*, 2008, **24**, 4340-4346.
3. H. Qian, L. A. Pretzer, J. C. Velazquez, Z. Zhao and M. S. Wong, *J. Chem. Technol. Biotechnol.*, 2013, **88**, 735-741.
4. J. Zong, S. L. Cobb and N. R. Cameron, *Biomater. Sci.*, 2017, **5**, 872-886.
5. L. Feng, L. Liu, F. Lv, G. C. Bazan and S. Wang, *Adv. Mater.*, 2014, **26**, 3926-3930.
6. V. Poonthiyil, T. K. Lindhorst, V. B. Golovko and A. J. Fairbanks, *Beilstein J. Org. Chem.*, 2018, **14**, 11-24.
7. R. Serrano García, S. Stafford and Y. Gun'ko, *Appl. Sci.*, 2018, **8**, 172.
8. K. Stockhofe, J. M. Postema, H. Schieferstein and T. L. Ross, *Pharmaceuticals*, 2014, **7**, 392-418.
9. L. c. Moriggi, C. Cannizzo, E. Dumas, C. d. R. Mayer, A. Ulianov and L. Helm, *J. Am. Chem. Soc.*, 2009, **131**, 10828-10829.
10. L. Esser, N. P. Truong, B. Karagoz, B. A. Moffat, C. Boyer, J. F. Quinn, M. R. Whittaker and T. P. Davis, *Polym. Chem.*, 2016, **7**, 7325-7337.
11. S. M. Janib, A. S. Moses and A. J. MacKay, *Adv. Drug Delivery Rev.*, 2010, **62**, 1052-1063.
12. N. Ahmed, H. Fessi and A. Elaissari, *Drug Discov. Today*, 2012, **17**, 928-934.
13. H. Wang, J. Zhuang and S. Thayumanavan, *ACS Macro Lett.*, 2013, **2**, 948-951.
14. S. Chen and K. Kimura, *Langmuir*, 1999, **15**, 1075-1082.
15. E. D. H. Mansfield, K. Sillence, P. Hole, A. C. Williams and V. V. Khutoryanskiy, *Nanoscale*, 2015, **7**, 13671-13679.
16. N. Nakajima and Y. Ikada, *Bioconjugate Chem.*, 1995, **6**, 123-130.
17. H. C. Kolb, M. G. Finn and B. K. Sharpless, *Angew. Chem., Int. Ed.*, 2001, **40**, 2004-2021.
18. A. B. Lowe, C. E. Hoyle and C. N. Bowman, *J. Mat. Chem.*, 2010, **20**, 4745-4750.
19. M. Tasdelen, *Polym. Chem.*, 2011, **2**, 2133-2145.
20. S. Ulrich, D. Boturyn, A. Marra, O. Renaudet and P. Dumy, *Chem. Eur. J.*, 2014, **20**, 34-41.
21. H. Li, B. Yu, H. Matsushima, C. E. Hoyle and A. B. Lowe, *Macromolecules*, 2009, **42**, 6537-6542.
22. R. Huisgen, *Angew. Chem., Int. Ed.*, 1963, **2**, 565-598.

23. J. Bolley, E. Guenin, N. Lievre, M. Lecouvey, M. Soussan, Y. Lalatonne and L. Motte, *Langmuir*, 2013, **29**, 14639-14647.

24. J. L. Brennan, N. S. Hatzakis, R. T. Tshikhudo, V. Razumas, S. Patkar, J. Vind, A. Svendsen, R. J. M. Nolte, A. E. Rowan and M. Brust, *Bioconjugate Chem.*, 2006, **17**, 1373-1375.

25. U. Mansfeld, C. Pietsch, R. Hoogenboom, R. C. Becer and U. S. Schubert, *Polym. Chem.*, 2010, **1**, 1560-1598.

26. Z. Jia, V. A. Bobrin, N. P. Truong, M. Gillard and M. J. Monteiro, *J. Am. Chem. Soc.*, 2014, **136**, 5824-5827.

27. D. Gräfe, P. Frank, T. Erdmann, A. Richter, D. Appelhans and B. Voit, *ACS Appl. Mater. Interfaces*, 2017, **9**, 7565-7576.

28. H. Kakwere, C. K. Y. Chun, K. A. Jolliffe, R. J. Payne and S. Perrier, *Chem. Commun.*, 2010, **46**, 2188-2190.

29. D. B. Wright, J. P. Patterson, N. C. Gianneschi, C. Chassenieux, O. Colombani and R. K. O'Reilly, *Polym. Chem.*, 2016, **7**, 1577-1583.

30. J. N. Kremsky and N. D. Sinha, *Bioorg. Med. Chem. Lett.*, 1994, **4**, 2171-2174.

31. D. Konkolewicz, A. Gray-Weale and S. Perrier, *J. Am. Chem. Soc.*, 2009, **131**, 18075-18077.

32. S. I. Presolski, V. P. Hong and M. G. Finn, *Curr. Protoc. Chem. Biol.*, 2011, **3**, 153-162.

33. H. K. Chuttani, P. S. Gupta, S. Gulati and D. N. Gupta, *Am. J. Med.*, 1965, **39**, 849-854.

34. C. J. Ferguson, R. J. Hughes, D. Nguyen, B. T. Pham, R. G. Gilbert, A. K. Serelis, C. H. Such and B. S. Hawkett, *Macromolecules*, 2005, **38**, 2191-2204.

Chapter 5

Heparin mimicking sulfonated nanoparticles *via* RAFT emulsion polymerisation-induced self-assembly

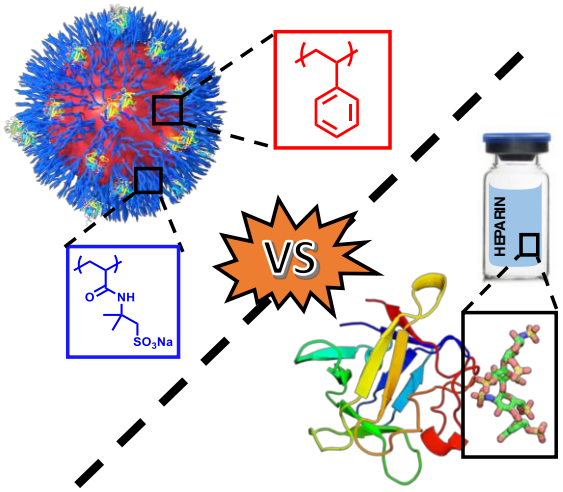

Heparin plays a significant role in wound-healing and tissue regeneration applications, through stabilisation of fibroblast growth factors (FGF). Risks associated with batch-to-batch variability and contamination from its biological sources have led to the development of synthetic highly sulfonated polymers as promising heparin mimics. In this work, a systematic study of an aqueous polymerisation-induced self-assembly (PISA) of styrene from poly(2-acrylamido-2-methylpropane sodium sulfonate) (P(AMPS)) macro-RAFT agents produced a variety of spherical heparin mimicking nanoparticles, which were further characterised with light scattering and electron microscopy techniques. None of the nanoparticles tested showed toxicity against mammalian cells, however significant haemolytic activity was observed. Nonetheless, the heparin mimicking nanoparticles outperformed both heparin and linear P(AMPS) in cellular proliferation assays, suggesting increased bFGF stabilisation efficiencies possibly due to the high density of sulfonated moieties at the particle surface.

5.1 Introduction

Heparin is an endogenous highly sulphated polysaccharide imperative to many biological processes such as anticoagulation, protein binding and the anti-inflammatory response.[1-3] Its biological activity is typically associated with its high charge density, which allows for strong electrostatic interactions with over 400 different proteins.[4] In particular, heparins ability to bind to and stabilise the basic fibroblast growth factor (bFGF), and its role in aiding complexation with the receptor, has attracted significant interest due to its essential function in cell proliferation, tissue regeneration and wound healing. Despite its heavy clinical use, this versatile polysaccharide can only be sourced from animal tissues (typically bovine and porcine), raising major biological safety concerns (virus contamination and large batch-batch variation/variable patient response). To overcome these challenges, researchers have studied the bFGF stabilisation efficiency of a variety of linear polysulfated/sulfonated heparin mimics, including sulfated glycopolymers, polyaromatics and polystyrenes and polyacrylamides.[5-9] For example, Maynard and co-workers recently showed 200% proliferative activity (similar to heparin + bFGF) of human dermal fibroblast cells after addition of bFGF stabilised with polystyrenesulfonate copolymers.[9]

Nanoparticles (NPs) are now well established in biomedicine for enhanced drug delivery,[10] bio-imaging[11] and diagnostics applications.[12] Their large size promotes extended circulation times and in the case of cancer treatment, they demonstrate passive tumour accumulation *via* the enhanced permeability and retention (EPR) effect.[13, 14] Furthermore, their high surface area can be functionalised with a broad range of moieties, making them ideal candidates for protein binding.[15] Although the synthesis of sulfonated/sulfated polymeric NPs has already been explored,[16-18] only one report exists on synthetic heparin mimicking NPs as growth factor stabilisers.[19] Koide *et al*. recently reported a library of polymeric NPs based on glycosylated sulfated/sulfonated polyacrylamides able to stabilise a vascular endothelial growth factor ($VEGF_{165}$) which outperformed heparin in protein binding and anti-angiogenic experiments.[19] This pioneering study revealed huge potential for NP heparin mimics, but as of yet has not been explored in the stabilisation of bFGF.

NP's designed with advanced controlled radical polymerisation techniques, such as reversible addition fragmentation chain transfer mediated (RAFT) polymerisation

induced self-assembly (PISA) can be exploited to overcome these challenges.[20, 21] PISA is typically performed through chain extension of a solvophilic macro-RAFT agent with either: a solvophilic monomer which when polymerised becomes solvophobic (RAFT dispersion polymerisation); or a solvophobic monomer (RAFT emulsion polymerisation).[22-24] This results in the formation of sterically stabilised, diblock copolymer core-shell NPs, where the particle surface is decorated with the solvophilic block of the stabilising macro-RAFT agent. Using this approach many parameters such as particle size, and stabiliser chain length can be modified, hence most PISA studies focus on nano-object synthesis and morphology control.[25-28] However, this synthetic approach has also been used for a wide range of applications. For instance, Whittaker and co-workers reported polyethylene glycol (PEG) coated NPs, copolymerised with a ^{19}F containing monomer synthesised *via* PISA for an *in vitro* cellular uptake study using magnetic nuclear resonance (MRI).[29] Furthermore, Ladmiral *et al*. reported PISA using a galactose functional monomer to enhance delivery of a model drug *via* cell surface lectin binding.[30] We have recently reported synthesis of polyacrylamide coated NPs *via* RAFT emulsion polymerisation, and their use as micro-RNA vectors and their *in vivo* biodistribution.[23, 31] Outside of biological applications, Armes and co-workers recently reported the synthesis of sulfated NPs *via* PISA both in dispersion and emulsion to further understand NP occlusion in calcite and zinc oxide crystals.[32, 33] Due to the highly sulfated nature of the above NPs, we envisaged that similar systems may be able to act as heparin mimics. However, to the best of our knowledge, there are no reports of synthetic heparin mimicking NPs specifically applied to bFGF stabilisation, or indeed any other growth factor than $VEGF_{165}$.[19]

Herein we report the synthesis of a series of heparin mimicking core-shell NPs *via* RAFT mediated PISA of styrene from poly(2-acrylamido-2-methyl propane sulfonic acid) (P(AMPS)) macro-RAFT agents. The NPs were characterised *via* dynamic light scattering and electron microscopy. Their toxicity and membrane (haemolytic) activity was evaluated *in vitro* on murine embryonic fibroblast cells (NIH-3T3) and erythrocytes, respectively. Finally, the bFGF stabilisation efficiency was determined through an *in vitro* proliferation assay using IL-3 dependent murine pro B cells (BaF3), which are engineered to over-express FGF receptors and do not produce heparin themselves.

5.2 Results and Discussion

5.2.1 Synthesis of linear polymers

Firstly, a series of three P(AMPS) homopolymers (DP20, DP50 and DP100) were prepared *via* aqueous RAFT polymerisation at 90°C using BDMAT as chain transfer agent, and VA-086 as thermal initiator (Figure 5.1a) (Prepared by Caroline P. Bray).[34] All three polymers had narrow molar mass distributions ($Đ < 1.2$; Figure 5.1) with similar experimental and theoretical molecular weights determined *via* ^{1}H NMR spectroscopy and aqueous SEC respectively (Figure 5.1). Molecular weights determined by aqueous SEC deviated slightly from the theoretical values, likely due to the differences in hydrodynamic volume of the P(AMPS) homopolymers with the poly(ethyleneglycol) calibration.

Table 5.1 Polymerisation conditions for P(AMPS) macro-RAFT agents

	Monomer	[M] (M)	$[M]_0$/ $[RAFT]_0$	$[CTA]_0$/ $[I]_0$	Conv (%)[a]	$M_{n,th}$ (g mol^{-1})[b]	$M_{n,NMR}$ (g mol^{-1})	$M_{n,SEC}$ (g mol^{-1})[c]	$Đ$[c]
P(AMPS)$_{20}$	AMPS®	1.5	20	30	>99	4,800	5,200	8,100	1.10
P(AMPS)$_{50}$	AMPS®	1.5	50	12	>99	11,600	11,400	13,000	1.11
P(AMPS)$_{100}$	AMPS®	1.5	100	6	>99	23,000	21,900	17,600	1.16

[a]Determined with ^{1}H NMR spectroscopy. [b]Calculated with Equation 2.12. [c]Determined with aqueous SEC against PEG/PEO standards. Data obtained by Caroline P. Bray.

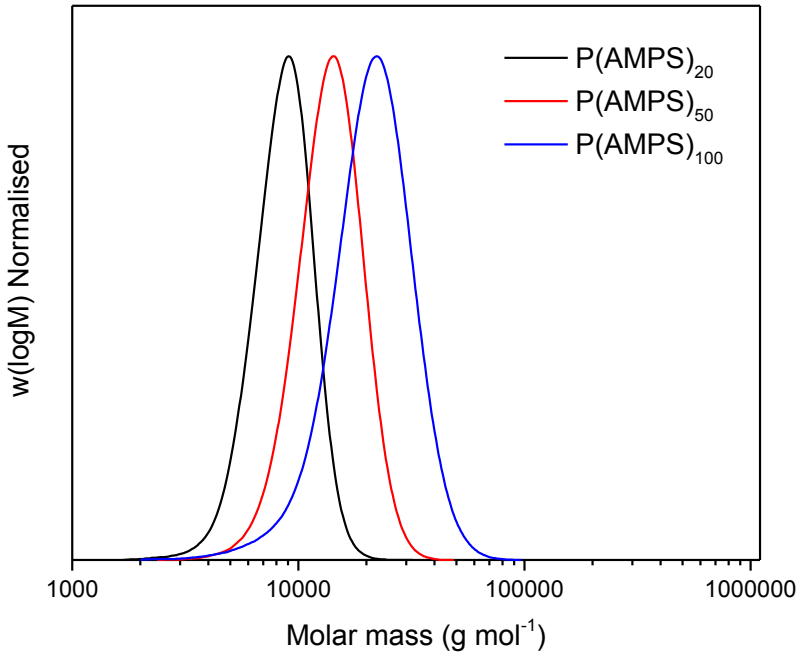

Figure 5.1 Aqueous size exclusion molecular weight distributions of P(AMPS)$_{20}$, P(AMPS)$_{50}$ and P(AMPS)$_{100}$ macro-RAFT agents. Data obtained by Caroline P. Bray.

5.2.2 Preliminary synthesis

In the previous chapters, diblock macro-RAFT agents were synthesised as the stabilisers for RAFT emulsion polymerisations. However, the vast differences in solubility between P(AMPS) and hydrophobic monomers would make the synthesis of analogous diblock macro-RAFT agents non-trivial. Therefore, as our P(AMPS) macro-RAFT agent synthesis reached full monomer conversion, and were performed in water, emulsion polymerisations could be performed directly without macro-RAFT agent purification. In a preliminary NP synthesis, $P(AMPS)_{50}$ was diluted in distilled water and directly chain extended with styrene (5 wt% monomer; 450 units) at 80°C, using ACVA as a thermal initiator, 1 mM $P(AMPS)_{50}$ and 400 RPM stirring (Table A5.1; Figure 5.1a). The reaction was sampled periodically for 8 h to measure conversion, molar mass and particle size evolution over time. Between 0 - 1 h, negligible monomer conversion was observed (determined *via* gravimetry, Figure 5.1e), likely due to the low aqueous styrene concentration prior to micellisation. However, after 1 h, both monomer conversion and particle size (measured with DLS; Figure 5.1c) rapidly increased, suggesting the formation of nano-objects and transport of styrene monomer into the growing particles. Both particle size and monomer conversion plateaued after 6 h at 78.5 nm and 96% respectively, indicating completion of the reaction. It should be noted that the latter time points exhibited artificial conversion values greater than 100%, which we anticipate was due to small weighing errors associated with the scale and volume of both the polymerisation and the samples taken. TEM analysis of the final latex (t = 8 h) revealed spherical NPs (Figure 5.1f) with relatively high polydispersity not revealed by DLS (*PDi* = 0.052; Table A5.1– *Latex 1*), possibly due to skewed sensitivity for larger species in light scattering. The polydispersity may be attributed to the ionic macro-RAFT agents reducing chain extension efficiency, affecting the uniformity of particle growth by electrostatic repulsion of similarly charged species in the aqueous phase.[35] This finding may also be attributed to the swollen corona in DLS measurements, which may artificially decrease the resulting *PDi* in comparison to TEM, in which the corona is fully collapsed. The highly amphiphilic block copolymer NPs were insoluble in traditional SEC eluents for polystyrene characterisation (THF, $CHCl_3$), therefore analyses were performed in DMF eluent with 0.1 wt% LiBr with polar columns. Since PS is known to swell in DMF and is not ideal for molecular weight determination, SEC chromatograms were only used to qualitatively assess molecular weight evolution and macro-RAFT agent consumption.

Using these, a clear increasing trend in molar mass over time was observed (Figure 5.1d), suggesting chain extension from $P(AMPS)_{50}$ had indeed occurred, however, some macro-RAFT agent remained unconsumed. Nonetheless, the highly negative zetapotentials of the NPs (-56.4 mV) suggests a dense sulfonated polymeric shell at the NP surface.

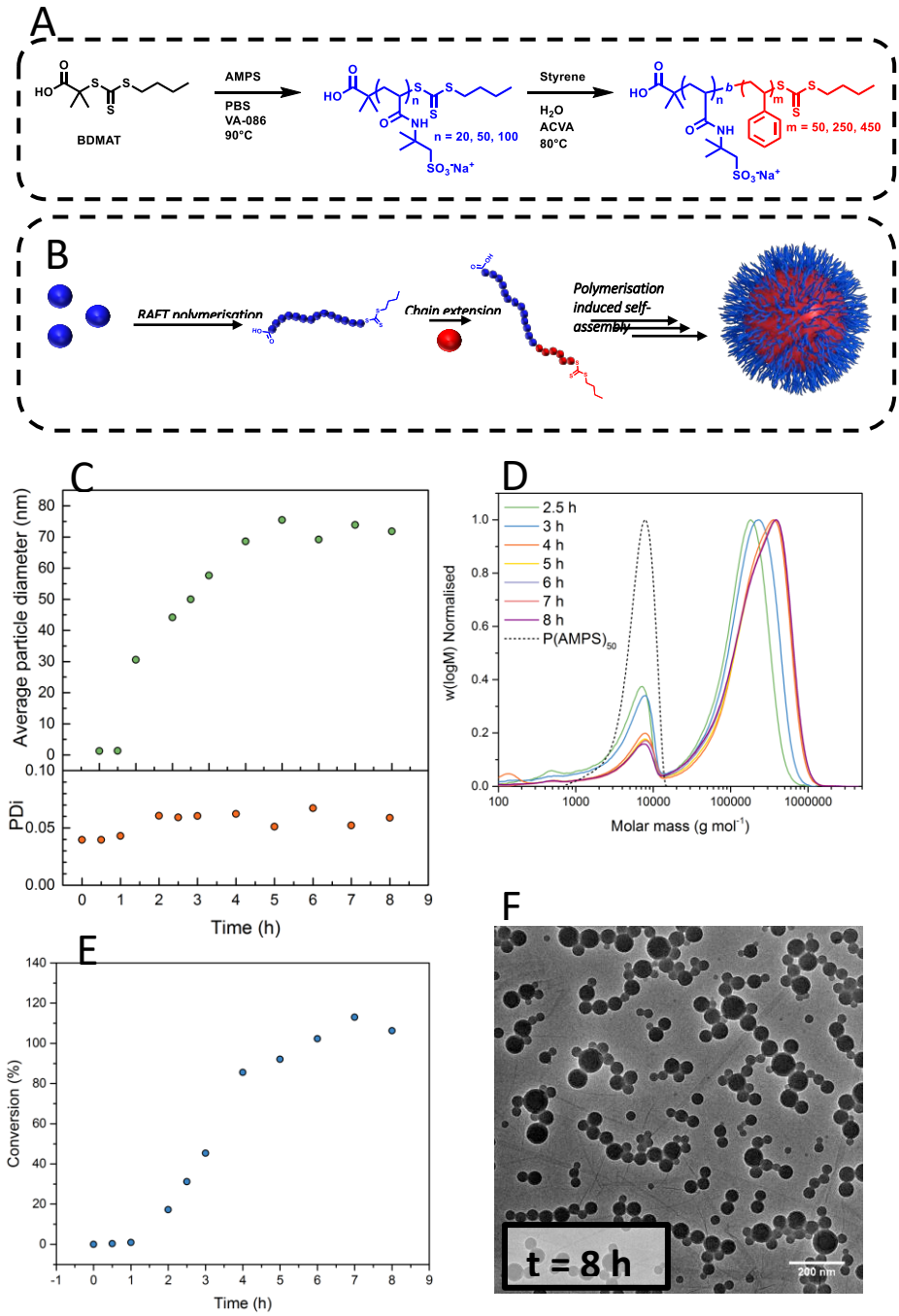

Figure 5.1 General synthesis scheme (A) and schematic representation (B) for the preparation of P(AMPS) macro-RAFT agents, and subsequent PISA *via* chain extension of styrene to generate heparin mimicking nanoparticles. Kinetic data for *Latex 1* (A) particle diameter (green circles) and polydispersity index (red circles) measured with DLS, (B) molar mass evolution of the dissolved nanoparticle unimers *via* DMF SEC (C) conversion measured with gravimetric techniques and (D) representative TEM image at the 8 h time point.

5.2.3 Systematic study

A systematic study on initiator type, temperature, initiator concentration, stirring speed, polystyrene DP, P(AMPS) DP and hydrophobic monomer type was then performed to improve nanoparticle polydispersity and control particle size. It should be noted that many of the latexes described below were completely insoluble in the DMF + 0.1 wt% LiBr SEC eluent, therefore for clarity only the particle size via DLS and TEM is discussed. Full characterisation and reaction conditions can be found in the appendix (Table A5.1).

5.2.3.1 Effect of initiator

The above-mentioned polymerisation was repeated using similar conditions but replacing ACVA (*Latex 1*) with VA-086 (*Latex 2*) and VA-057 (*Latex 3*). To account for the different 10 h half-life temperatures, the concentration of each initiator was adjusted such that the same number of radicals was generated within 6 h (Equation S2 and S3). Interestingly, the NPs synthesised with VA-086 were larger (94.2 nm) than with ACVA (78.5 nm), while those with VA-057 were smaller (59.6 nm). It is likely that, as a neutral initiator, VA-086 imparted less electrostatic stabilisation to the growing particles, resulting in fewer larger particles comprised of a higher number of polymer chains. A charged initiator, ACVA, was therefore used for all future polymerisations as no clear differences other than particle size were observed. [36, 37]

5.2.3.2 Effect of temperature

Similarly, the preliminary polymerisation at 80°C (*Latex 1)* was repeated at both 70°C (*Latex 4*) and 90°C (*Latex 5),* again with adjusted amounts of initiator as detailed above. At 70°C, only 71% conversion was attained, while at higher temperatures (80 and 90°C) monomer conversions higher than 90% were achieved likely due to higher propagation rates. Both temperatures yielded larger nanoparticles (91.4 nm at 70°C and 100.4 nm at 90°C). The difference at 70°C, could be explained by a decreased solubility of styrene during the early phase of the emulsion polymerisation, resulting in fewer macro-RAFT agents being chain extended, cumulating in less colloidal stability.[38] At 90°C the increase in size could also be attributed to particle-particle coalescence at high temperatures.[39]

5.2.3.3 Effect of initiator concentration

By increasing the concentration of initiator (ACVA) (*Latex 1*; $[CTA]_0/[I]_0$ = 4.65) to double (*Latex 6*; $[CTA]_0/[I]_0$ = 2.33) and quadruple (*Latex 7*; $[CTA]_0/[I]_0$ = 0.93) the original amount, only a small increase in particle size was observed (78.5 nm (*Latex 1*) to approximately 95 nm for both concentrations). In both cases, it is likely that an increased number of radicals may result in more termination in the aqueous phase, thus leaving the effective radical concentration unaffected by $[I]_0$ in the growing particles.

5.2.3.4 Effect of stirring speed

Increasing the stirring speed from 400 RPM (*Latex 1*) to 800 RPM (*Latex 8*) and 1200 RPM (*Latex 9*) resulted in larger NP diameters, (128.5 nm (800 RPM) and 157.7 nm (1200 RPM)). The faster, and possibly asymmetrical agitation (1200 RPM), may promote inter-particle coalescence and therefore larger diameters.[40] However, transmission electron micrographs of these NPs revealed uniform suspensions at 800 rpm, which most likely had uniform stirring. This stirring speed was therefore used for all future experiments.

5.2.3.5 Effect of polystyrene chain length

It has been widely reported that the balance of hydrophilic and hydrophobic chain length can heavily influence particle size and morphology in PISA formulations.[21] It was possible to modify the hydrophobic length (core forming block) by either increasing $[P(AMPS)_{50}]_0$ or reducing $[Styrene]_0$ in the emulsion polymerisations. This was attempted by targeting a polystyrene core with a DP of 250 (*Latex 10* and *Latex 12*) and 50 (*Latex 11* and *Latex 13*), compared to the *Latex 8* (DP_{target} = 450), by reducing $[Styrene]_0$ or increasing $[macro\text{-}RAFT]_0$. Targeting a DP of 250 both gave smaller NPs, 120.7 nm and 92.4 nm for $[Styrene]_0$ equal to 250 and 50 mM respectively, of which both phenomena have been previously reported for similar systems.[24, 35] Further decreasing the DP_{target} to 50 however, resulted in the absence of nano-object formation, suggesting that this was below the critical hydrophobic chain length for self-assembly using this type of anionic macro-RAFT agent. If compared to non-ionic stabilisers, many reports indicate that very short hydrophobic chain lengths are able to induce micellisation, e.g. below DP 20.[25]

5.2.3.6 Effect of P(AMPS) chain length

Using the synthesised homopolymers $P(AMPS)_{20}$ (*Latex 15*) and $P(AMPS)_{100}$ (*Latex 16*), RAFT emulsion polymerisations analogous to *Latex 8* ($P(AMPS)_{50}$) were then performed. For the shorter macro-RAFT agent (DP = 20), a large increase in particle size was observed (248.8 nm) compared to DP 50 (120.7 nm), probably due to the reduced electrostatic stability of the growing particles, leading to coalescence. Unexpectedly, larger diameters (161.6 nm) were also observed with increased chain length (*Latex 16,* $P(AMPS)_{100}$ macro-RAFT agent). It is possible that this higher overall charge may promote chain-chain repulsion and therefore a reduced number at the surface of the growing particles, with the total effect of less colloidal stability and larger particles. This could also improve the rate of radical entry and therefore account for the increase in NP uniformity with $P(AMPS)_{20}$ and $P(AMPS)_{100}$ stabilisers. It is also possible that the larger (DP 100 vs DP 50) swollen anionic corona is partially responsible for this increase in size observed in DLS.[41]

5.2.3.7 Effect of hydrophobic monomer

Finally, polymerisations were conducted by replacing styrene (*Latex 8*) with *n*-butyl acrylate, another well-established monomer for emulsion polymerisations (*Latex 14*). This resulted in larger NPs (200.5 nm), which can be attributed to the poorer reinitiation of an acrylamide macro-RAFT agent with an acrylate monomer, thus reducing the number of sulfonated chains at the particle surface. It should be noted that due the low T_g of P(*n*-BA), *Latex 14* was imaged with cryo-transmission electron microscopy, instead of in the dry state.

In general, altering the conditions of polymerisation of these sulfonated systems did not dramatically affect the resulting NP size. However, stirring speed and P(AMPS) chain length had the greatest effect on particle size and polydispersity. The average diameter of all NPs synthesised was found to be comparable between DLS and TEM measurements, while all zeta-potentials remained similar (~ -55 to -65 mV) regardless of polymerisation conditions. All of the final latexes had pH values between 6.5 and 6.6 which was most probably caused by the P(AMPS) macro-RAFT agent/surface functionality. Furthermore, unlike other monomer combinations, our emulsion system only yielded

spherical NPs, which was also observed by Armes and co-workers when using sulfated polymethacrylate macro-RAFT agent stabilisers.[32, 33]

Table 5.1 Characterisation data for the nanoparticles used in biological studies (cytotoxicity, haemolysis and cellular proliferation).

				Water			PBS	
	Target structure	**Monomer**	**Conv (%)[a]**	**D_h (nm)[b]**	***PDi*[c]**	**ZP (mV)[d]**	**D_h (nm)[b]**	***PDi*[c]**
Latex 8	$P(AMPS)_{50}$-b-PS_{450}	Styrene	90	128.5	0.052	-60.3	122.0	0.072
Latex 14	$P(AMPS)_{50}$-$P(n\text{-BA})_{450}$	*n*-BA	93	200.5	0.051	-62.9	206.4	0.044
Latex 16	$P(AMPS)_{100}$-PS_{450}	Styrene	89	161.6	0.050	-61.6	165.7	0.047

[a]Determined using gravimetric techniques. [b]Determined using DLS (intensity distribution). [c]Calculated using equation S4. [d]Determined using a zetasizer.

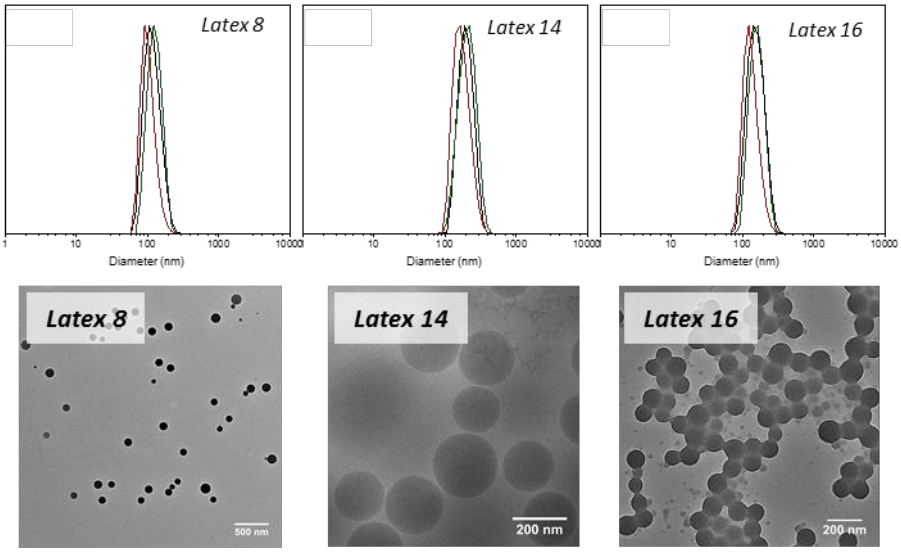

Figure 5.2 DLS particle size distributions (top row) (intensity = green, volume = black, number = red) measured in water at 25˚C and TEM images (bottom row) of *Latex 8*, *Latex 14* (cryogenic TEM) and *Latex 16*.

5.2.4 Biological studies

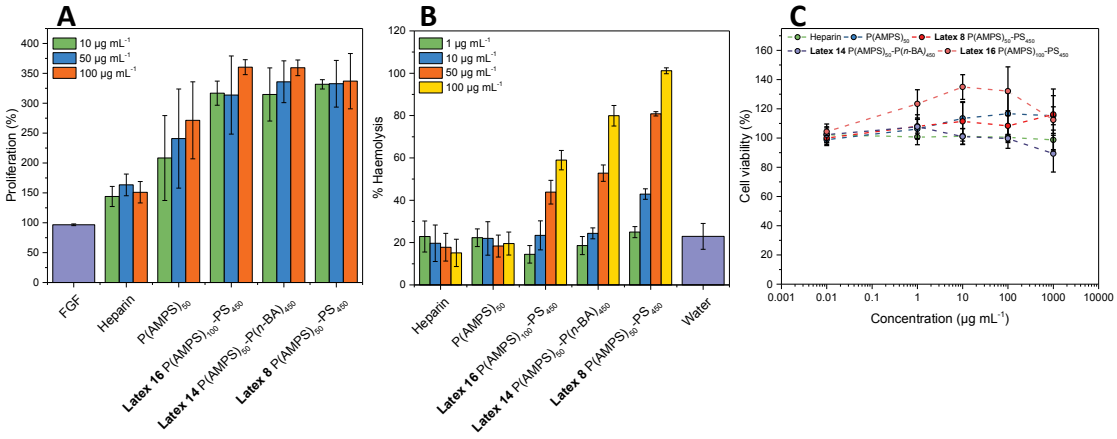

Figure 5.3 (A) bFGF stabilisation / BaF3 proliferation (controls of untreated cells and bFGF only) (B) haemolytic activity (controls of PBS and water) and (C) cytotoxicity against NIH-3T3 fibroblasts of heparin (controls of untreated cells), $P(AMPS)_{50}$, *Latex 16* $P(AMPS)_{100}$-PS_{450}, *Latex 14* $P(AMPS)_{50}$-$P(n\text{-}BA)_{450}$ and *Latex 8* $P(AMPS)_{50}$-PS_{450}. Data shown represent mean ± standard deviation across triplicates from two independent experiments (N=6).

Latex 8 ($P(AMPS)_{50}$-b-PS_{450}), *Latex 14* ($P(AMPS)_{50}$-$P(n\text{-}BA)_{450}$) and *Latex 16* ($P(AMPS)_{100}$-PS_{450}) were chosen to study their heparin mimicking behaviour in order to isolate differences between the influence of core monomer (*n*-BA and styrene) and AMPS chain length (DP 50 and DP 100) on bFGF stabilisation. Additionally, these samples appeared as the most uniform from TEM images (Figure 5.2). Prior to these experiments, the NPs were dialysed for 48 h against a 100 kDa MWCO membrane to remove any styrene monomer, and unconsumed macro-RAFT agent which may compete against the NPs in biological studies. Importantly, the hydrodynamic diameter of the chosen latexes was comparable in PBS and in water, suggesting the NPs would be colloidally stable in biological experiments (Table 5.1). $P(AMPS)_{50}$ and heparin itself were also included in these experiments for comparison.

The haemolytic activity of all compounds was assessed by incubating red blood cells (1 h at 37°C) with the chosen NPs and polymers at four concentrations (100 µg mL^{-1} to 1 µg mL^{-1} in PBS) and monitoring the release of haemoglobin *via* UV spectroscopy at 414 nm. Positive (Triton-X) and negative (PBS) membrane disruption controls were also performed in parallel, with water (5% in PBS) also used as a vehicle control. Low haemolytic activity (~20%), comparable to H_2O, was observed for heparin and $P(AMPS)_{50}$, however much higher activity (> 50% haemolysis) was seen for all of the NPs following the trend *Latex 8* ($P(AMPS)_{50}$-PS_{450} particles) > *Latex 14* ($P(AMPS)_{50}$-

P(*n*-BA)$_{450}$ particles) > *Latex 15* (P(AMPS)$_{100}$-PS$_{450}$ particles) (Figure 5.3a). In contrast, none of the compounds (polymers or NPs) showed acute toxicity towards murine embryonic fibroblast cells for concentrations up to 1 mg mL^{-1} (Figure 5.3b). This major difference between haemolysis and cytotoxicity could be due to the highly amphiphilic 'surfactant-like' nature of the particle surface-core interface, which is known to have significant membrane disruption activity.[41] The observed trends appear to support this hypothesis, as the large P(AMPS)$_{100}$ chains present on the surface of *Latex 15* will better shield erythrocytes from the PS interface compared to the shorter P(AMPS)$_{50}$. Furthermore, P(*n*-BA) is less hydrophobic than PS, and therefore NPs with these cores may be less amphiphilic, accounting for the reduction in haemolytic activity of *Latex 14*.

Finally, stabilisation of bFGF was tested using a typical proliferation assay using BaF3 cells, an IL-3 dependent murine pro B cell line which was modified to lack cell-surface heparin sulfate, and express the bFGF receptor (FGFr1c). Using this assay, heparin or a heparin mimic must be present to stabilise bFGF and promote its binding to FGFr1c receptor, thus inducing enhanced cellular proliferation. To assess this, the NPs, P(AMPS)$_{50}$ and heparin (100, 10 and 1 μg mL^{-1}) were incubated with BaF3 cells and bFGF (5 ng mL^{-1}) for 48 h, and the cellular proliferation evaluated with a cell viability assay (CellTiter-Blue®). Results were normalised to untreated cells (100%) (Figure 5.3c). Addition of heparin induced a small amount of proliferation (150%) which appeared independent of concentration for the range studied.[8] The linear polymer, P(AMPS)$_{50}$, resulted in approximately 250% proliferation. In contrast, all of the NPs displayed greater than 400% cellular proliferation, with no obvious differences between core composition, P(AMPS) shell length, or concentration. The full mechanism of the bFGF-heparin-bFGFR proliferation pathway is not yet fully understood, however the key requirements are now known.[42] Heparin must induce dimerization of bFGF and simultaneously bind to bFGFR to achieve the active bFGF-heparin-bFGFR triplex required for effective proliferation.[42] A recent study by Zbinden *et al*. revealed that polymer conjugates with increased display of bFGF drastically enhanced proliferation of endothelial cells.[43] They also noted that higher densities of bFGF resulted in larger conjugate hydrodynamic volumes, which may also contribute to this effect.[43] It is probable that our large NPs with numerous surface-active P(AMPS) chains may be able to bind multiple bFGF on the same species, thus improving its multivalent display. However, the smaller size of linear P(AMPS)$_{50}$ and heparin could mean that only one, or a few of the polymers could interact

with a single bFGF molecule, potentially explaining the greater cellular proliferation with the NPs. Furthermore, Garcia-Fernandez *et al*. showed that greater hydrophobicity of sulfonated linear polymers had a profound increase on bFGF stability, therefore exposed styrene from the hydrophobic NP cores may also have a similar effect.[44] It should be noted that our study evaluates cellular proliferation heparin as a function of treatment weight (e.g. 1 g of NP's vs 1 g of polymer). However, due to the higher weight proportion of PS compared to P(AMPS) in our NPs, the molar concentration of sulfonated residues is exceptionally low compared to the counterpart polymers. This highlights how the use of NP architecture could have an even greater efficacy if the number of P(AMPS) chains per particle could be elucidated, and sulfonated moieties directly compared.

5.3 Conclusions

In conclusion, we have shown a parameter screening study to generate uniform, heparin mimicking polystyrene NPs *via* aqueous RAFT emulsion polymerisation/PISA from P(AMPS) hydrophilic macro-RAFT agents. The optimised NPs showed no cytotoxic effect against NIH-3T3 fibroblasts. However, compared to linear P(AMPS) and heparin, the NPs displayed major disruption of erythrocytes rationalised by the highly amphiphilic nature of the P(AMPS)-PS interface. Finally, all of the tested NPs exhibited much greater cellular proliferation, in comparison to heparin and linear P(AMPS) control polymers, likely due to the multivalent presentation of sulfonated chains at the NP surface. However, no apparent trends were observed between nanoparticle varieties (core properties and surface chain length) on cell proliferation. Overall, the polymerisation-induced self-assembly approach allows the facile generation of highly sulfonated NPs, and represent a promising platform for heparin mimicry in the future.

5.4 Experimental

5.4.1 Materials

Sodium 2-acrylamido-2-methylpropane sulfonate (AMPS®2405, 50 wt% in water) was donated by Lubrizol. Thermal initiators 4,4′-azobis(4-cyanovaleric acid) (ACVA, 98%), 2,2′-azobis[2-methyl-N-((2-hydroxyethyl)propionamide] (VA-086, 98%) and 2,2'-Azobis[*N*-(2-carboxyethyl)-2-methylpropionamidine]tetrahydrate (VA-057, 98%) were obtained from Wako Chem. Bovine calf serum (BCS, Sterile-Filtered), IL-3 mouse recombinant expressed in E. coli (> 98%, Sterile), Heparin sodium salt from porcine intestinal mucosa (180 USP units/mg); 2,3-Bis(2-methoxy-4-nitro-5-sulfophenyl)-2H-tetrazolium-5-carboxanilide inner salt (XTT sodium salt, > 90%), Phenazine methosulfate (PMS, > 90%), Triton X-100 and Styrene (>99%) were purchased from Sigma Aldrich. RPMI1640 medium with GlutaMAX supplement (Invitrogen, Sterile), Geneticin selective antibiotic (G418 Sulfate, Invitrogen, 50 mg mL^{-1} in water, Sterile), Basic Fibroblast Growth Factor human recombinant (bFGF, Corning, Sterile-Filtered-Lyophilised, > 95%) and Defibrinated sheep blood (Thermo Scientific Oxoid) were purchased from Fischer Scientific. CellTiter-Blue Cell Viability Assay was purchased from Promega. Dulbecco's Modified Eagle Medium (DMEM), Foetal bovine serum (FBS), Phosphate-buffered saline (PBS), L-glutamine and sterile water were prepared under sterile condition by the media preparation service at the School of Life Science at the University of Warwick. Methanol-d_4 (MeOD, 99.8% D atom) was purchased from Sigma Aldrich and used for ^{1}H NMR spectroscopy. TEM grids were purchased from EM Resolutions (Sheffield, UK). 2-(((butylthio)-carbonothioyl)thio)-2-methylpropanoic acid (BDMAT) was synthesised using previous literature conditions.[1]

5.4.2 Instrumentation and Analysis

5.4.2.1 ^{1}H NMR spectroscopy

^{1}H NMR were recorded as described in section 2.4.2.1

5.4.2.2 Calculation of initiator consumption over time

Initiator consumptions were calculated using Equation 2.1 and Equation 2.2

5.4.2.3 Size exclusion chromatography

Aqueous SEC

Agilent PL50 instrument equipped with differential refractive index (DRI) detector. The system was equipped with 2 x PL Aquagel OH Mixed M columns (30 cm x 7.5 mm ID) with 8 μm pore size and an Aquagel 8 μm guard column. The mobile phase used was 80:20 0.1 M $NaNO_3$(aq):methanol. Samples were run at 1 mL min^{-1} at 35°C regulated with a column oven. Poly(ethylene oxide) standards (Agilent EasyVials) were used for calibration between 1,368,000 – 106 g/mol. Analyte samples were prepared at a final concentration of 1 mg mL^{-1} and filtered through a membrane with 0.22 μm pore size before injection. Respectively, experimental molar mass ($M_{n,SEC}$) and dispersity ($Đ$) values of synthesised polymers were determined by conventional calibration using Agilent GPC/SEC software.

DMF + 0.1 wt% LiBr SEC

Agilent PL50 instrument equipped with differential refractive index (DRI) and ultra-violet (UV) detectors. The system was equipped with 2 x PolarGel M columns (30 cm x 7.5 mm ID) and a PolarGel 5 μm guard column. The mobile phase used was DMF with 0.1% (w/v) LiBr additive. Samples were run at 1 mL/min at 50°C regulated with a column oven. Poly(methyl methacrylate) standards (Agilent EasyVials) were used for calibration between 955,000 – 550 g/mol. Analyte samples were prepared at a final concentration of 1 mg mL^{-1} and filtered through a nylon membrane with 0.22 μm pore size before injection Respectively, experimental molar mass ($M_{n,SEC}$) and dispersity ($Đ$) values of synthesised polymers were determined by conventional calibration using Agilent GPC/SEC software.

5.4.2.4 Dynamic light scattering, size and zeta-potential measurements

DLS and zetapotential measurements were performed as described in 2.4.2.4. *PDi* values were calculated as described in Equation 2.13.

5.4.2.5 Transmission electron microscopy

Transmission electron micrographs were obtained as described in section 3.6.2.10

5.4.2.6 Cryogenic transmission electron microscopy

Cryogenic transmission electron micrographs were obtained as described in section 2.4.2.7

5.4.3 Synthetic Procedures

5.4.3.1 P(AMPS) macro-RAFT agent synthesis via RAFT polymerisation

P(AMPS) macro-RAFT agents were synthesised using previously reported conditions.[1] A general procedure for DP 50 is described below. BDMAT (26 mg, 0.1 mmol), AMPS® (2.00 g, 5.1 mmol), phosphate buffer (1.5 mL), sodium hydroxide (5.1 x 10^{-2} mmol, 2 mg) and VA-086 (8.4 x 10^{-3} mmol, 2.4 mg) (from stock solution at 20.0 mg mL^{-1}) were introduced into a flask equipped with a magnetic stirrer bar and sealed with a rubber septum. The solution was purged with dinitrogen for 10 minutes, and the vial immersed in an oil bath a set to 90°C for 2 h. At the end of the reaction, the mixture was allowed to cool down to room temperature and exposed to air. The final mixture was characterised using ^{1}H NMR spectroscopy and SEC, and used further without purification.

5.4.3.2 Nanoparticle synthesis via PISA RAFT emulsion polymerisation

A general procedure for *Latex 1* is detailed below. $P(AMPS)_{50}$ solution (338 µL (343 mg mL^{-1} solution), 116 mg, 10 µmol), ACVA (predissolved in water with 2 eq NaOH at 5 mg mL; 140 µL, 0.7 mg, 2.5 µmol) and water (8.95 mL) were added to a 30 mL microwave vial equipped with a magnetic stirrer, and sealed with a disposable septum cap purged with dinitrogen for 10 minutes. Deoxygenated styrene (570 µL, 520 mg, 5 mmol) was added *via* syringe. The mixture was then immersed in an oil bath set to 80°C, and stirred at 400 RPM for 8 h. The polymerisation turned a milky white after

nanoparticle formation. Before biological assays, the suspensions were dialysed against water with a 100 kDa dialysis membrane for 48 h.

5.4.4 Biological Studies

5.4.4.1 Cell culture

NIH-3T3 cells were purchased from Sigma Aldrich and cultured as monolayers at 37°C in a humidified atmosphere containing 5% CO_2. Cells were cultured in Dulbecco's Modified Eagle Medium (DMEM) supplemented with 10% foetal calf serum, 1% L-Glutamine and 1% penicillin/streptomycin. Cells were sub-cultured at regular intervals and passages made by trypsinising cells when at 80-90% confluence. BaF3-FR1C cells were kindly provided by Prof. Jerry Turnbull (Liverpool University, UK) and were cultivated at 37°C in suspension in a humidified atmosphere containing 5% CO_2. Cells were cultured in RPMI1640 GlutaMAX media supplemented with 10% foetal bovine serum (FBS), 2 ng/mL of recombinant mouse IL-3, 600 µg/mL of G418. Cells were sub-cultured at regular intervals and passages made by centrifuging them at 1000 rpm for 5 min and diluted to keep a density between 500,000 to 1,000,000 cells/mL and were used for up to one month.

5.4.4.2 Cell viability assay

NIH-3T3 cells were seeded at a density of 10,000 cells per well in a flat bottomed clear 96 well plate and incubated for 24 h. The medium was replaced with 100 µL of fresh medium containing the tested compounds (heparin, $P(AMPS)_{50}$, *Latex 16*, *Latex 14* and *Latex* 8) at 0.01 µg mL^{-1}, 1 µg mL^{-1}, 10 µg mL^{-1}, 100 µg mL^{-1} and 1 mg mL^{-1}. The cells were incubated with the compounds for 48 h, and cell viability established with the XTT assay. The media in each well was removed and replaced with fresh culture medium containing 25 µL of XTT (1 mg mL^{-1}) and PMS (25 µmol/L) and was further incubated for 12 hours. Absorbance of each well was measured using a Synergy HTX plate reader at 475 nm and 650 nm (background) with $A = A_{475nm} - A_{475nm(blank)} - A_{650nm}$. The cell viability was normalised to untreated cells. All experiments were carried out as duplicates of triplicates in two independent experiments (N=6).

5.4.4.3 Haemolysis assay

Haemolytic activity of the nanoparticles was determined using procedures described in section 3.6.4.3.

5.4.4.4 Cell proliferation assay

BaF3-FR1C cells were seeded at a density of 20,000 cells/well (in 50 μL media) in the internal wells of a 96-well plate with medium absent of IL-3 and G418. A further 50 μL of medium containing polymers or nanoparticles (heparin, $P(AMPS)_{50}$, *Latex 16*, *Latex 14* and *Latex* 8) and bFGF were added such that the final concentrations were 100 μg mL^{-1}, 50 μg mL^{-1}, 10 μg mL^{-1} and 5 ng mL^{-1} respectively. Controls of untreated cells and cells in the presence of 5 ng mL^{-1} of bFGF were used as reference. External wells were filled with 100 μL of PBS and a gas permeable moisture barrier seal (4titude) was used to decrease the evaporation from the plate. After incubation for 48 hours, 20 μL of the CellTiter-Blue® assay was added into each well and further incubated for 6 hours. Fluorescence of each well was measured using a Synergy HTX plate reader with the excitation wavelength set to 560 nm and emission at 590 nm. Cell proliferation was calculated by normalising treated cells to untreated cells (100%). Each sample had four replicates and the experiment was repeated four times independently

References

1. P. Olczyk, L. Mencner and K. Komosinska-Vassev, *BioMed Research International*, 2015, **2015**, 549417.
2. D. Wardrop and D. Keeling, *Br. J. Haematol.*, 2008, **141**, 757-763.
3. M. Wang, Z. Lyu, G. Chen, H. Wang, Y. Yuan, K. Ding, Q. Yu, L. Yuan and H. Chen, *Chem. Commun.*, 2015, **51**, 15434-15437.
4. F. Peysselon and S. Ricard-Blum, *Matrix Biol.*, 2014, **35**, 73-81.
5. S. J. Paluck and H. D. Maynard, *Polym. Chem.*, 2017, **8**, 4548-4556.
6. S. J. Paluck, T. H. Nguyen and H. D. Maynard, *Biomacromolecules*, 2016, **17**, 3417-3440.
7. S. J. Paluck, T. H. Nguyen, J. P. Lee and H. D. Maynard, *Biomacromolecules*, 2016, **17**, 3386-3395.
8. T. H. Nguyen, S. J. Paluck, A. J. McGahran and H. D. Maynard, *Biomacromolecules*, 2015, **16**, 2684-2692.
9. T. H. Nguyen, S. H. Kim, C. G. Decker, D. Y. Wong, J. A. Loo and H. D. Maynard, *Nat. Chem.*, 2013, **5**, 221-227.
10. T. Sun, Y. S. Zhang, B. Pang, D. C. Hyun, M. Yang and Y. Xia, *Angew. Chem., Int. Ed.*, 2014, **53**, 12320-12364.
11. P. Sharma, S. Brown, G. Walter, S. Santra and B. Moudgil, *Adv. Colloid Interface Sci.*, 2006, **123**, 471-485.
12. I. Brigger, C. Dubernet and P. Couvreur, *Adv. Drug Delivery Rev.*, 2012, **64**, 24-36.
13. J. Fang, H. Nakamura and H. Maeda, *Adv. Drug Delivery Rev.*, 2011, **63**, 136-151.
14. H. Maeda, J. Wu, T. Sawa, Y. Matsumura and K. Hori, *J. Controlled Release*, 2000, **65**, 271-284.
15. P. Ke, S. Lin, W. J. Parak, T. P. Davis and F. Caruso, *ACS Nano*, 2017, **11**, 11773-11776.
16. S. B. Brijmohan, S. Swier, R. A. Weiss and M. T. Shaw, *Ind. Eng. Chem. Res.*, 2005, **44**, 8039-8045.
17. N. Yeole, D. Hundiwale and T. Jana, *J. Colloid Interface Sci.*, 2011, **354**, 506-510.
18. N. Isahak, J. Sanchez, S. Perrier, M. J. Stone and R. J. Payne, *Org. Biomol. Chem.*, 2016, **14**, 5652-5658.
19. H. Koide, K. Yoshimatsu, Y. Hoshino, S.-H. Lee, A. Okajima, S. Ariizumi, Y. Narita, Y. Yonamine, A. C. Weisman, Y. Nishimura, N. Oku, Y. Miura and K. J. Shea, *Nat. Chem.*, 2017, **9**, 715.

20. P. B. Zetterlund, S. C. Thickett, S. Perrier, E. Bourgeat-Lami and M. Lansalot, *Chem. Rev.*, 2015, **115**, 9745-9800.

21. S. L. Canning, G. N. Smith and S. P. Armes, *Macromolecules*, 2016, **49**, 1985-2001.

22. P. Gurnani, A. M. Lunn and S. Perrier, *Polymer*, 2016, **106**, 229-237.

23. C. K. Poon, O. Tang, X.-M. Chen, B. T. T. Pham, G. Gody, C. A. Pollock, B. S. Hawkett and S. Perrier, *Biomacromolecules*, 2016, **17**, 965-973.

24. C. J. Ferguson, R. J. Hughes, D. Nguyen, B. T. Pham, R. G. Gilbert, A. K. Serelis, C. H. Such and B. S. Hawkett, *Macromolecules*, 2005, **38**, 2191-2204.

25. J. L. d. l. Haye, X. Zhang, I. Chaduc, F. Brunel, M. Lansalot and F. D'Agosto, *Angew. Chem., Int. Ed.*, 2016, **55**, 3739-3743.

26. S. Dong, W. Zhao, F. P. Lucien, S. Perrier and P. B. Zetterlund, *Polym. Chem.*, 2015, **6**, 2249-2254.

27. W. Zhang, F. D'Agosto, O. Boyron, J. Rieger and B. Charleux, *Macromolecules*, 2012, **45**, 4075-4084.

28. L. A. Fielding, M. J. Derry, V. Ladmiral, J. Rosselgong, A. M. Rodrigues, L. P. D. Ratcliffe, S. Sugihara and S. P. Armes, *Chem. Sci.*, 2013, **4**, 2081.

29. W. Zhao, H. T. Ta, C. Zhang and A. K. Whittaker, *Biomacromolecules*, 2017, **18**, 1145-1156.

30. V. Ladmiral, M. Semsarilar, I. Canton and S. P. Armes, *J. Am. Chem. Soc.*, 2013, **135**, 13574-13581.

31. C. K. Poon, O. Tang, X. M. Chen, B. Kim, M. Hartlieb, C. A. Pollock, B. S. Hawkett and S. Perrier, *Macromol. Biosci.*, 2017, **17**, 1600366.

32. Y. Ning, L. A. Fielding, L. P. D. Ratcliffe, Y.-W. Wang, F. C. Meldrum and S. P. Armes, *J. Am. Chem. Soc.*, 2016, **138**, 11734-11742.

33. Y. Ning, L. A. Fielding, T. S. Andrews, D. J. Growney and S. P. Armes, *Nanoscale*, 2015, **7**, 6691-6702.

34. C. Bray, R. Peltier, H. Kim, A. Mastrangelo and S. Perrier, *Polym. Chem.*, 2017, **8**, 5513-5524.

35. I. Chaduc, A. Crepet, O. Boyron, B. Charleux, F. D'Agosto and M. Lansalot, *Macromolecules*, 2013, **46**, 6013-6023.

36. K. Y. van Berkel, G. T. Russell and R. G. Gilbert, *Macromolecules*, 2003, **36**, 3921-3931.

37. C. S. Chern, S. Y. Lin, S. C. Chang, J. Y. Lin and Y. F. Lin, *Polymer*, 1998, **39**, 2281-2289.

38. I. Capek, S. Y. Lin, T. J. Hsu and C. S. Chern, *J. Polym. Sci., Part A: Polym. Chem.*, 2000, **38**, 1477-1486.

39. E. Gonzalez, C. Tollan, A. Chuvilin, M. J. Barandiaran and M. Paulis, *ACS Appl. Mater. Interfaces*, 2012, **4**, 4276-4282.

40. M. Nomura, M. Harada, W. Eguchi and S. Nagata, *J. Appl. Polym. Sci.*, 1972, **16**, 835-847.

41. B. Isomaa, A. Engblom and H. Hägerstrand, *Toxicology*, 1988, **48**, 285-291.

42. S. Sarabipour and K. Hristova, *Nat. Commun.*, 2016, **7**, 10262.

43. A. Zbinden, S. Browne, E. I. Altiok, F. L. Svedlund, W. M. Jackson and K. E. Healy, *Biomater. Sci.*, 2018, **6**, 1076-1083.

44. L. García-Fernández, M. R. Aguilar, M. M. Fernández, R. M. Lozano, G. Giménez and J. S. Román, *Biomacromolecules*, 2010, **11**, 626-634.

Chapter 6

Conclusions and outlook

The initial chapter detailed the current state of these synthetic strategies to produce nanoparticles useful for biological applications. The overall conclusion of this thorough study revealed that the limited monomer families, surfactant use, scalability concerns and non-aqueous polymerisation environments meant that dispersion, miniemulsion and suspension polymerisations may be incompatible. In contrast, RAFT emulsion polymerisation is a highly modular synthetic approach and allows the modification of individual nanoparticle components (core size, core composition, corona functionality and shell composition), however, it remains underused for biological applications. The aim of this thesis was therefore to exploit RAFT emulsion polymerisation, to overcome current limitations in nanoparticle synthesis and design.

In chapter 2, using PEGylated macro-RAFT agents, the RAFT emulsion polymerisation of *n*-BA and *t*-BA was optimised (initiator and pH) to yield low dispersity nanoparticle suspensions with narrow molecular weight distributions. A library of nanoparticles of different sizes for each core type was synthesised, with all polymerisations achieving full monomer conversion and fully characterised with static light scattering and electron microscopy. This work is the first to study the toxicity of nanoparticles synthesised with RAFT emulsion polymerisation *in vivo*, with our results showing excellent tolerability, similar to *in vitro* experiments. The biodistribution of fluorescently labelled 50 nm derivatives was then evaluated using an *in vivo* fluorescence imager, with particles displaying > 76 h retention and accumulation in the liver post-administration. Considering the excellent biocompatibility, and 'green' polymerisation conditions, this synthetic approach may have some potential for industrial scale up, assuming limitations on macro-RAFT agent scalability could be overcome.

The main aim in chapter 3 was to evaluate if rigidity played a significant role in nanoparticle cellular uptake, and in particular, if there were any secondary effects with particle size. By utilising RAFT emulsion polymerisation, a series of nanoparticles with

different core T_g were generated simply by modifying the monomer composition (styrene, t-BA and n-BA for hard medium and soft respectively). Clear differences in uptake were observed, with softer nanoparticles taken up faster and in greater quantities than harder analogues in two malignant mammalian cell lines. Perhaps most interestingly, these observations were only seen in 100 nm derivatives, with 50 nm nanoparticles showing negligible differences in uptake, which have been attributed to less correlation between T_g and core rigidities at this reduced size scale. While all of the nanoparticle displayed strong colocalisation in lysosome compartments, their cellular entry mechanisms were indeed largely different. Most prominently, the increasing trend in cavolae- mediated endocytosis of hard > medium > soft potentially revealed the drastic differences the mechanosensing behaviour that caveolae may have on nanoparticle cellular uptake. Overall, these results highlight that rigidity does indeed have a major effect on cellular uptake, with size being important when considering this parameter. Moreover, this study clearly represents the precise control over maintained individual nanoparticle properties when using RAFT emulsion polymerisation, allowing for complex fundamental biological studies.

Chapter 4 details a synthetic study, outlining the requirements to generate alkyne surface functional nanoparticles *via* RAFT emulsion polymerisation. Initial attempts to simply repeat procedures detailed in chapters 2 and 3 with alkyne functional macro-RAFT agents revealed significant colloidal instability and poor molecular weight control. A systematic study revealed that ester functional RAFT agents, and carboxylated macro-RAFT agents were essential to overcome the limitations above. Test CuAAC reactions with azido functional PEG and fluorescein showed efficient ligation with model polymer. However, only the smaller substrate (fluorescein azide) was efficiently conjugated when repeated on the alkyne functional nanoparticles, attributed to steric hindrance from the PEG brush polymeric shell. Overall, this study reveals that introducing surface functionality using RAFT emulsion polymerisation is indeed possible, however careful attention must be paid to the macro-RAFT agent design.

Finally, in chapter 5, moving away from the PEGA based macro-RAFT agents, polysulfonated nanoparticles were prepared using a one-pot RAFT emulsion stabilised by linear poly(2-acrylamido-2-methylpropane sodium sulfonate) macro-RAFT agents, as potential heparin mimics for bFGF stabilisation. A systematic study of various reaction

conditions revealed that macro-RAFT agent length and stirring speed had the greatest effect on particle size and polydispersity, evaluated with DLS and TEM. A selection of the nanoparticles were taken forward for biological studies and revealed minimal cytotoxicity against NIH-3T3 cells. Finally, all of the nanoparticles displayed enhanced bFGF stabilisation compared to heparin and linear P(AMPS) through greater proliferation of BaF3 cells. This was attributed to the potentially greater display of bFGF on the nanoparticle surface, which was able to stabilise a multitude of growth factors on each nanoparticle species. In general, this study highlights that nanoparticles represent a promising candidate as heparin mimics.

In summary, the presented thesis demonstrates that the RAFT emulsion polymerisation process is highly beneficial for generating nanoparticles for biomedical applications. The ability to modify individual components, has allowed the study of a variety of biological research questions, including *in vivo* toxicology, fundamental *in vitro* cellular uptake and growth factor stabilisation. There are however some limitations to this study.

For instance, only a brief *in vivo* study was performed looking at body weight and preliminary biodistribution with one injection route. Ideally, a more detailed toxicology identifying any stress markers could have been performed along with multiple injection routes and studying the long term (> 1 week) accumulation of the nanoparticles *in vivo*. Furthermore, in our cellular uptake study described in chapter 3, instead of relative intracellular fluorescence measurements, a fully quantitative measure (i.e. exact number of particles per cell) would allow us to look more deeply at the differences between 50 and 100 nm particles, as here they cannot directly compared. When preparing alkyne functional diblock copolymers and nanoparticles, ester and amide reinitiating groups with and without pendant acrylic acid moieties were tested for their stabilisation of RAFT emulsion polymerisation. There is however a gap in this study, as in the final instance we assumed that the acid groups were completely essential, as seen for the TMS protected derivative. It would be interesting to see if using the non-protected analogue without pendant acrylic acids causes the same destabilisation observed for the TMS versions. Finally, although we are potentially the first to show heparin mimicking nanoparticles for bFGF stabilisation, we did not quantify exactly how many sulfonates are at the surface of each nanoparticle and as such cannot be directly compared to the linear equivalent. However, as stated at the end of the chapter, by weight, the linear derivatives contain a

higher proportion of sulfonate moieties which would only accentuate the difference if compared by molar amount of sulfonate groups.

Although synthesis and design of biomedical nanoparticles is an active field of work, there are still very few formulations which are in clinical trials, and even fewer which are clinically used. As the long-term effects of nanoparticles are still unknown, it is expected that new designs aimed at the clinic should be degradable such that they do not accumulate indefinitely. This is potentially the major drawback of all RDRP techniques, including the systems described in this thesis, as the inert C-C backbone of common poly(acrylates/methacrylates/acrylamides etc.) cannot be physiologically destroyed. Due to this, the systems presented would not at their current stage, be targeted towards clinical use.

Given this, the major challenge going forward would be to introduce degradable units within the polymer backbone, without much modification of the RAFT emulsion procedures described. This could be achieved through the addition of cyclic ketene acetal monomers, which impart ester groups within the polymeric backbone. If this was achieved, coupled with the findings in this work that these nanoparticles accumulate in the liver, and softer particles are internalised better by cells, one can imagine that future systems could be used to target liver diseases, without the current limitations of bioaccumulation. Without degradability, the precision in which the nanoparticles described can be tuned means that they would be more useful to study fundamental aspects (i.e. particle size, surface charge/functionality etc.), which would lead the design of future clinical therapies.

Appendix 2

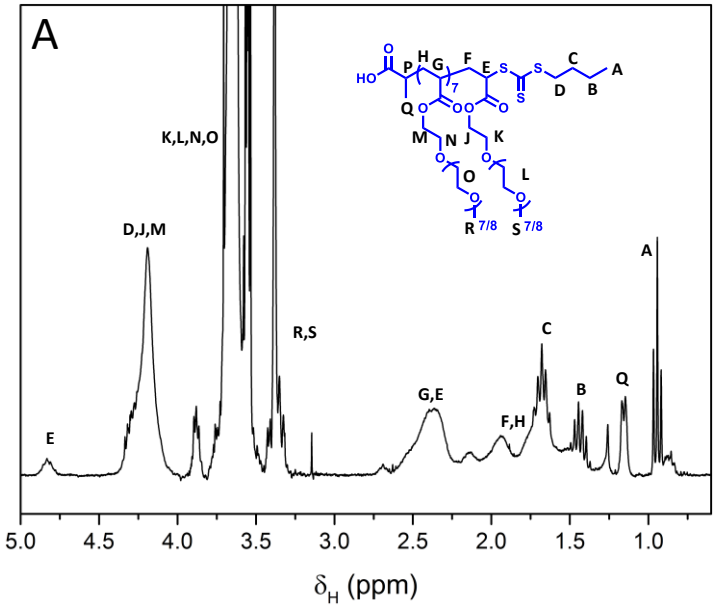

Figure A2.1 ^{1}H NMR spectrum of **MRA-PEGA** in $CDCl_3$.

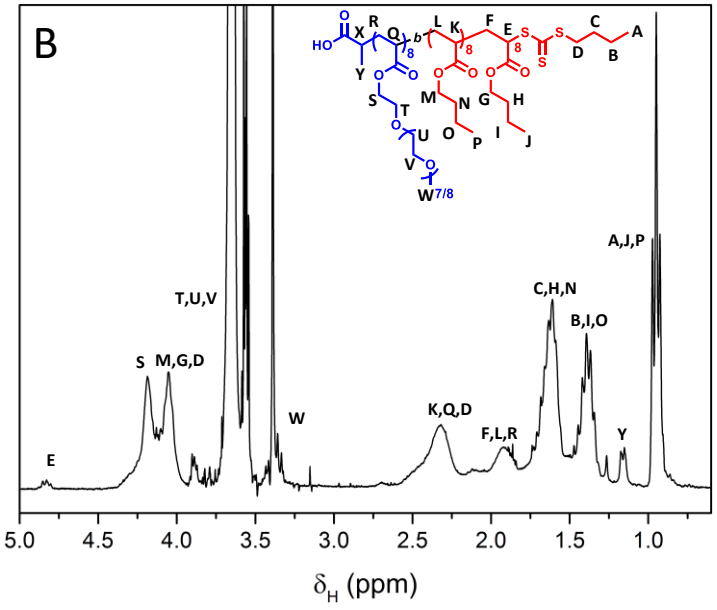

Figure A2.2 ^{1}H NMR spectrum of **MRA-*n*BA** in $CDCl_3$.

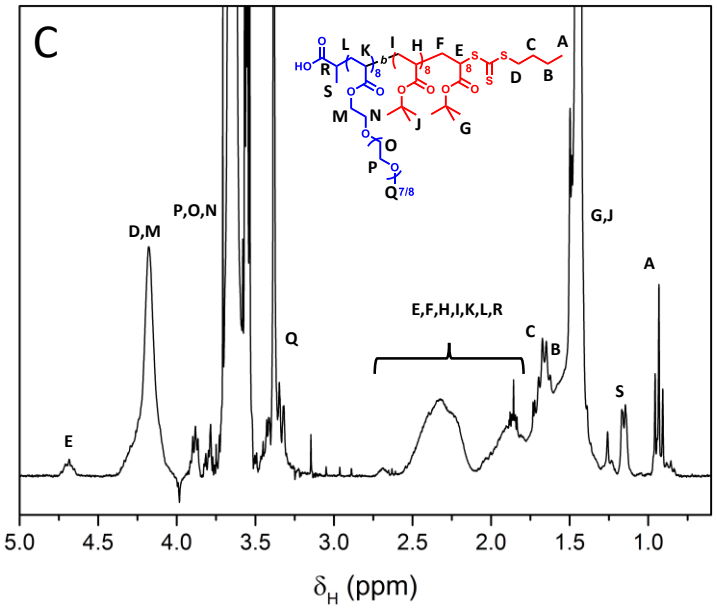

Figure A2.3 ^{1}H NMR spectrum of **MRA-*t*BA** in $CDCl_3$.

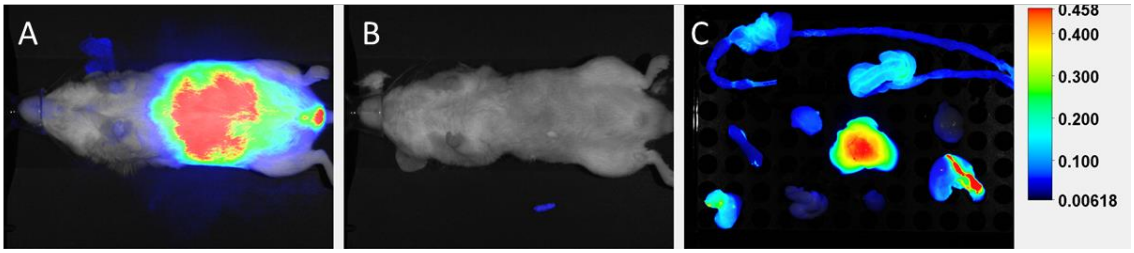

Figure A2.4 Fluorescence images (800 nm channel) of (A) mouse treated with Cy7.5 loaded 50 nm P(*n*-BA) nanoparticles after 76 h post injection. (B) Untreated mouse with a faecal pellet (C) *Ex vivo* organs taken 76 h post injection. All images have the same brightness and contrast settings, indicating a small degree of 800 nm fluorescence emitted by the faecal pellet.

Appendix 3

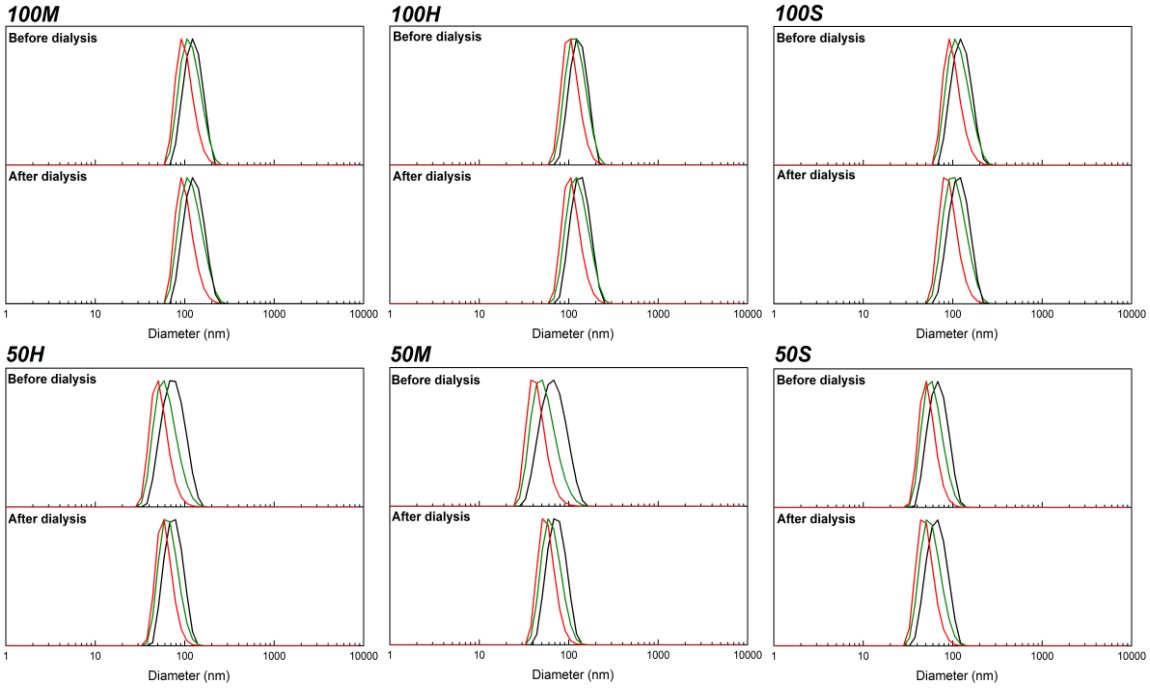

Figure A3.1 Intensity (black), volume (green) and number (red) DLS size distributions of 100H, 100M, 100S, 50H, 50M and 50S fluorescently labelled nanoparticles within this study before and after dialysis in 60% 1,4-dioxane, 40% water to remove unconsumed BODIPY acrylate and unconsumed macro-RAFT agent.

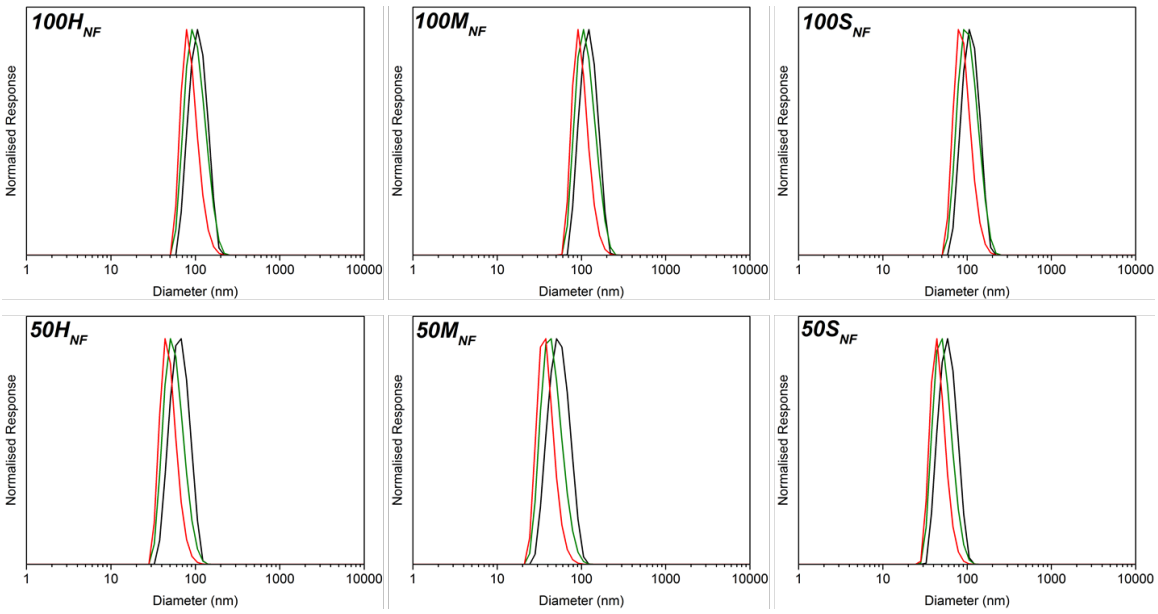

Figure A3.2 Intensity (black), volume (green) and number (red) DLS size distributions of $100H_{NF}$, $100M_{NF}$, $100S_{NF}$, $50H_{NF}$, $50M_{NF}$ and $50S_{NF}$ non-fluorescent nanoparticles.

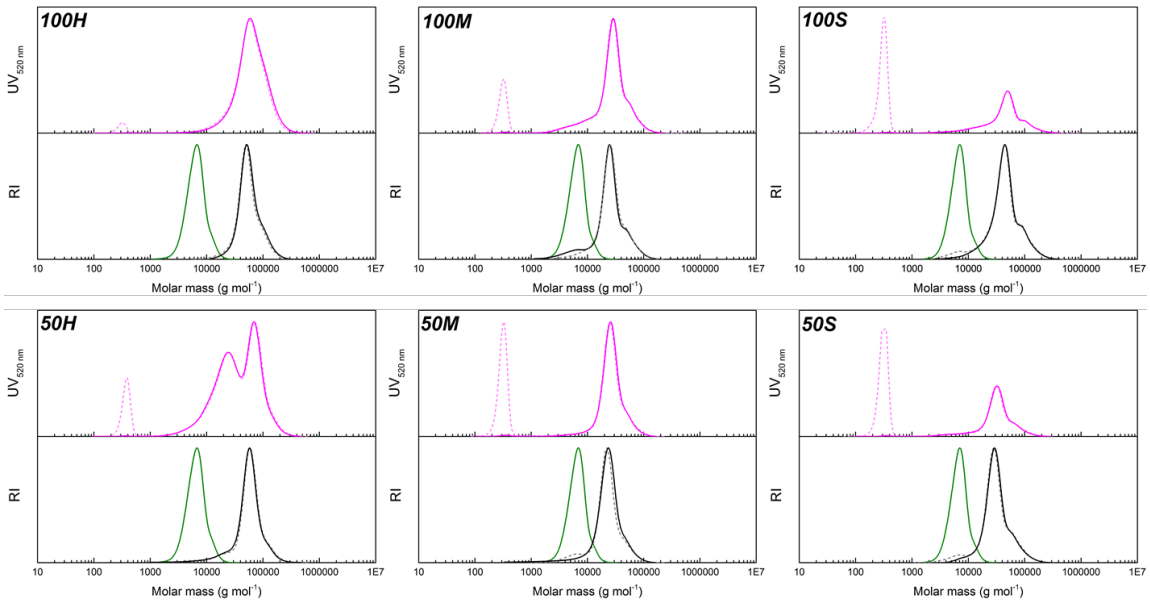

Figure A3.3 THF-SEC chromatograms of dried and dissolved fluorescent nanoparticles 100H, 100M, 100S, 50H, 50M and 50S using UV detection at 520 nm (top chart) and RI detection (bottom chart) both before (dashed light pink line for UV and dashed grey line for RI) and after (full pink line for UV and full black line) dialysis against a 60/40 1,4-dioxane/water (v/v) solvent mixture. Chromatograms for the respective macro-RAFT agents are also shown (full green line).

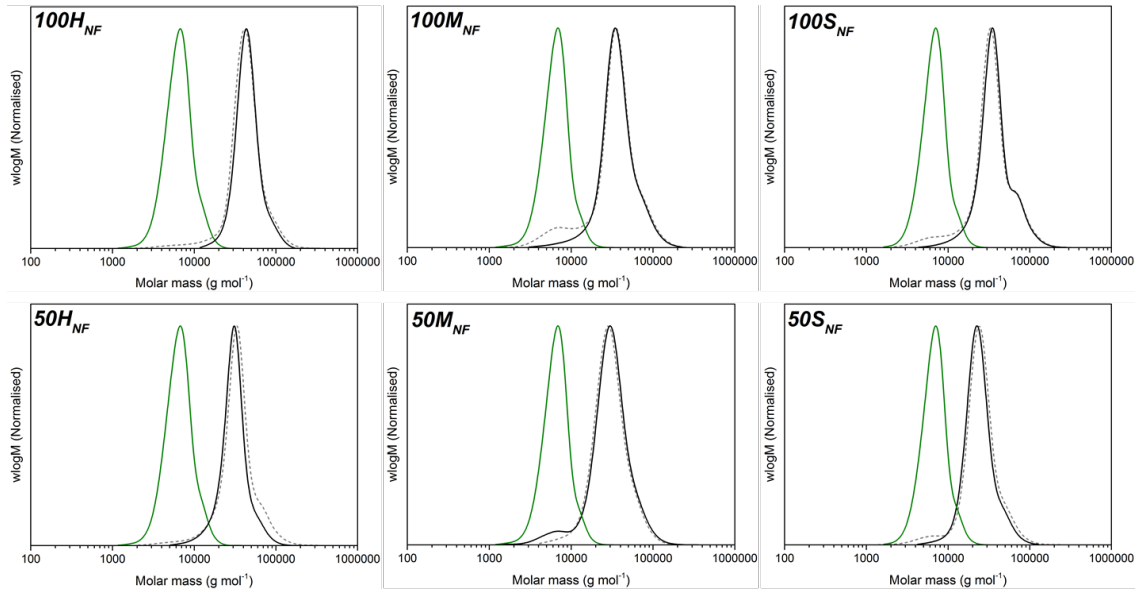

Figure A3.4 THF-SEC of dried and dissolved non-fluorescent nanoparticles $100H_{NF}$, $100M_{NF}$, $100S_{NF}$, $50H_{NF}$, $50M_{NF}$, $50S_{NF}$ using (RI detection) both before (dashed grey line) and after (full black line) dialysis against pure water. Chromatograms for the respective macro-RAFT agents are also shown (full green line).

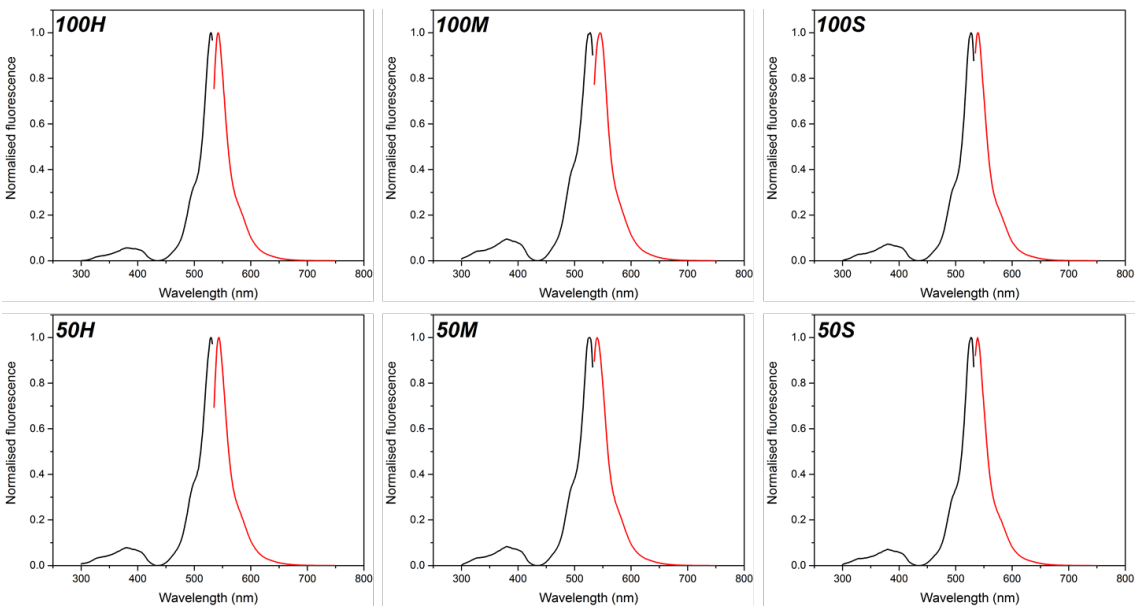

Figure A3.5 Fluorescence emission (red line; λ_{ex} = 528 nm) and excitation spectra (black line: λ_{ex} = 542 nm) for fluorescent nanoparticles 100H, 100M, 100S, 50H, 50M and 50S.

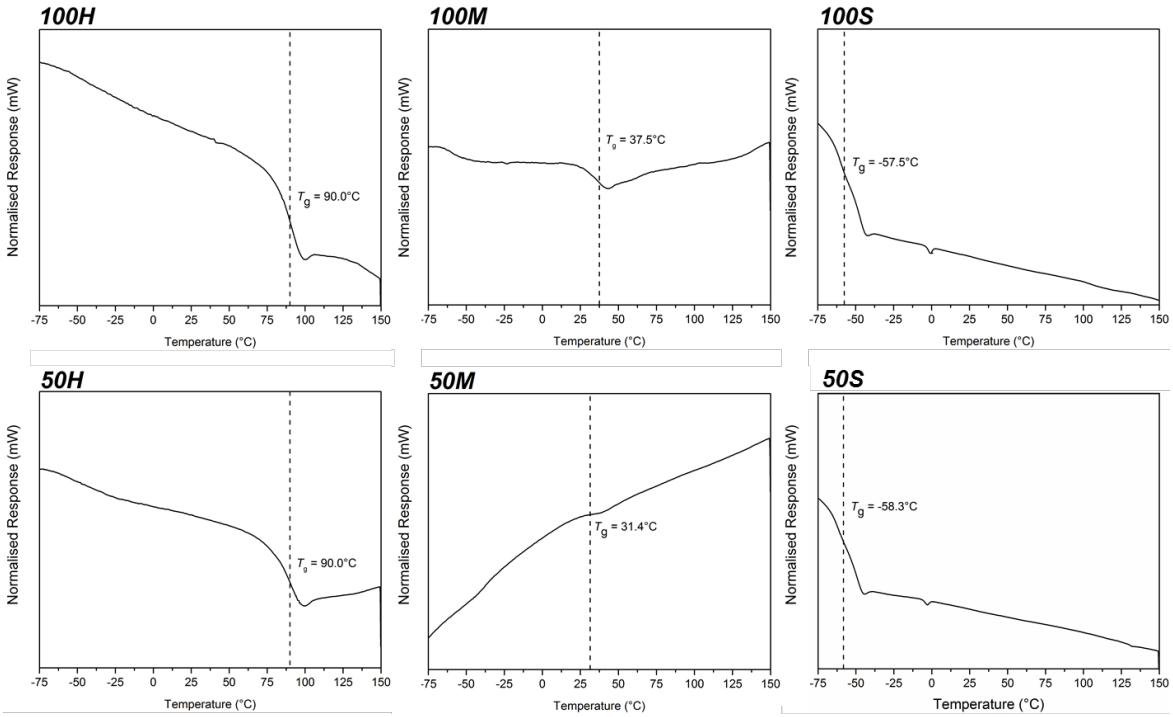

Figure A3.6 Normalised DSC thermograms of dried fluorescent nanoparticles 100H, 100M, 100S, 50H, 50M, 50S.

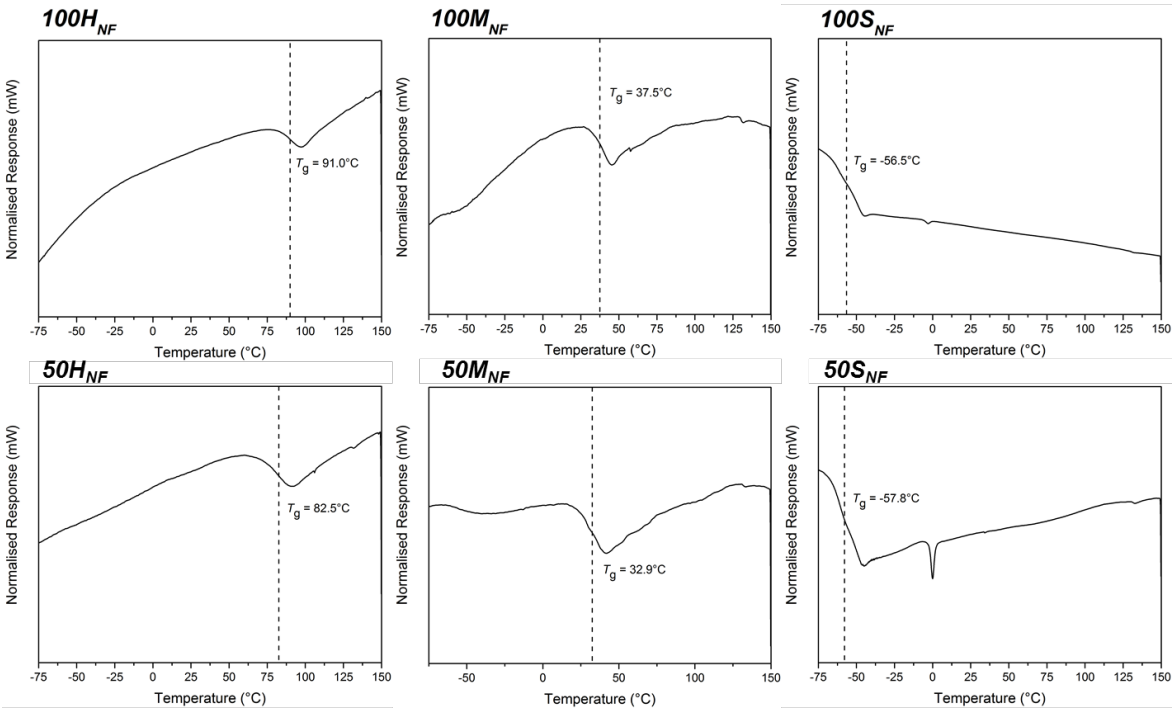

Figure A3.7 Normalised DSC thermograms of dried non-fluorescent nanoparticles $100H_{NF}$, $100M_{NF}$, $100S_{NF}$, $50H_{NF}$, $50M_{NF}$, $50S_{NF}$.

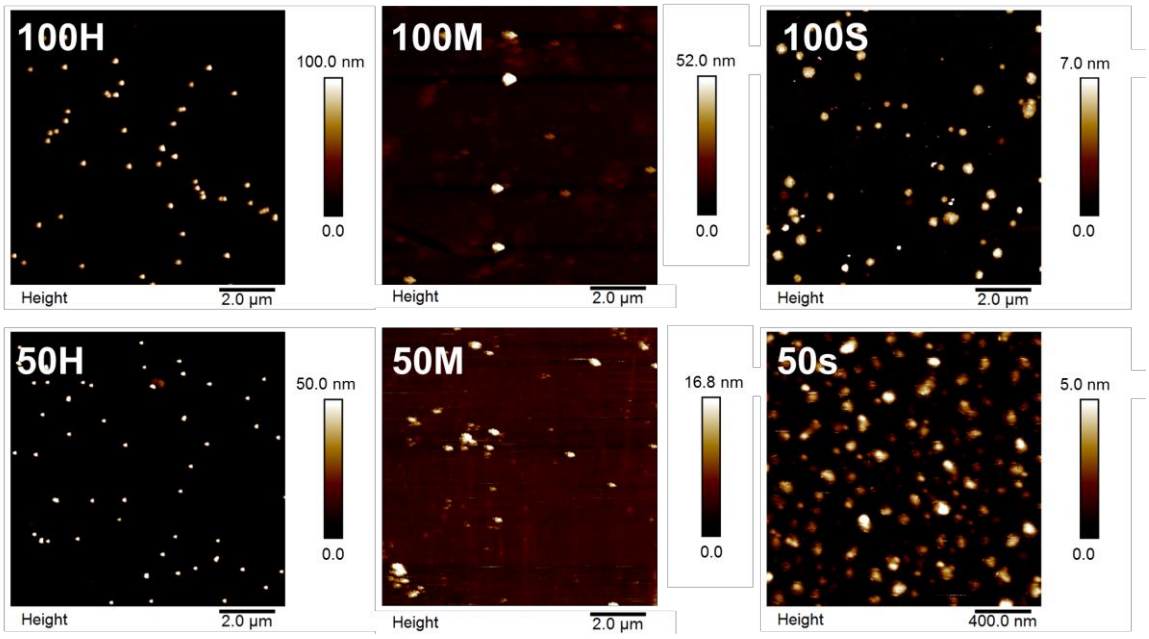

Figure A3.8 AFM images of 100H, 100M, 100S, 50H, 50M and 50S deposited on silanised glass at 0.05 mg mL^{-1}. Data obtained by Dr Kai Yu and Dr Christopher Hodges at the University of Leeds.

Note: ANOVA tests were performed in SPSS 14 software, with the nanoparticles 100H, 100M, 100S, 50H, 50M and 50S labelled as 1, 2, 3, 4, 5, 6 respectively.

PC3 time dependent cellular uptake – 2 h, 4 h and 24 h 100 nm particles

ANOVA

2 h

	Sum of Squares	df	Mean Square	F	Sig.
Between Groups	1.021	2	.510	126.148	.000
Within Groups	.061	15	.004		
Total	1.082	17			

Table A3.1 Analysis of variance (ANOVA) results table comparing intracellular fluorescence (PC3 cells) of the 100 nm nanoparticles after 2 h incubation.

Multiple Comparisons

Dependent Variable: 2 h
Tukey HSD

(I) Particles	(J) Particles	Mean Difference (I-J)	Std. Error	Sig.	95% Confidence Interval	
					Lower Bound	Upper Bound
1	2	-.175958596*	.0367256405	.0006556865	-.271352355	-.080564837
	3	-.569639319*	.0367256405	.0000000061	-.665033077	-.474245560
2	1	.175958596*	.0367256405	.0006556865	.0805648374	.2713523549
	3	-.393680722*	.0367256405	.0000000627	-.489074481	-.298286964
3	1	.569639319*	.0367256405	.0000000061	.4742455599	.6650330774
	2	.393680722*	.0367256405	.0000000627	.2982869637	.4890744813

*. The mean difference is significant at the 0.05 level.

Table A3.2 Post-hoc Tukey-Kramer test results comparing intracellular fluorescence (PC3 cells) of the 100 nm nanoparticles after 2 h incubation.

ANOVA

4 h

	Sum of Squares	df	Mean Square	F	Sig.
Between Groups	1.318	2	.659	110.732	.000
Within Groups	.089	15	.006		
Total	1.408	17			

Table A3.3 Analysis of variance (ANOVA) results table comparing intracellular fluorescence (PC3 cells) of the 100 nm nanoparticles after 4 h incubation.

Multiple Comparisons

Dependent Variable: 4 h
Tukey HSD

(I) Particles	(J) Particles	Mean Difference (I-J)	Std. Error	Sig.	95% Confidence Interval	
					Lower Bound	Upper Bound
1	2	-.174908873*	.0445471023	.0036221986	-.290618646	-.059199100
	3	-.641231083*	.0445471023	.0000000068	-.756940856	-.525521310
2	1	.174908873*	.0445471023	.0036221986	.0591991003	.2906186462
	3	-.466322210*	.0445471023	.0000000839	-.582031983	-.350612437
3	1	.641231083*	.0445471023	.0000000068	.5255213103	.7569408562
	2	.466322210*	.0445471023	.0000000839	.3506124370	.5820319830

*. The mean difference is significant at the 0.05 level.

Table A3.4 Post-hoc Tukey-Kramer test results comparing intracellular fluorescence (PC3 cells) of the 100 nm nanoparticles after 4 h incubation.

ANOVA

24 h

	Sum of Squares	df	Mean Square	F	Sig.
Between Groups	1.384	2	.692	169.232	.000
Within Groups	.057	14	.004		
Total	1.441	16			

Table A3.5 Analysis of variance (ANOVA) results table comparing intracellular fluorescence (PC3 cells) of the 100 nm nanoparticles after 24 h incubation.

Multiple Comparisons

Dependent Variable: 24 h

Tukey HSD

(I) Particles	(J) Particles	Mean Difference (I-J)	Std. Error	Sig.	95% Confidence Interval	
					Lower Bound	Upper Bound
1	2	-.336202523*	.0369203615	.0000008403	-.432833465	-.239571580
	3	-.712236098*	.0387224019	.0000000063	-.813583486	-.610888710
2	1	.336202523*	.0369203615	.0000008403	.2395715799	.4328334654
	3	-.376033575*	.0387224019	.0000003872	-.477380963	-.274686187
3	1	.712236098*	.0387224019	.0000000063	.6108887102	.8135834857
	2	.376033575*	.0387224019	.0000003872	.2746861875	.4773809630

*. The mean difference is significant at the 0.05 level.

Table A3.6 Post-hoc Tukey-Kramer test results comparing intracellular fluorescence (PC3 cells) of the 100 nm nanoparticles after 24 h incubation.

PC3 time dependent cellular uptake – 2 h, 4 h and 24 h 50 nm particles

Table A3.7 Analysis of variance (ANOVA) results table comparing intracellular fluorescence (PC3 cells) of the 50 nm nanoparticles after 2 h incubation.

ANOVA

2 h

	Sum of Squares	df	Mean Square	F	Sig.
Between Groups	.330	2	.165	128.274	.000
Within Groups	.019	15	.001		
Total	.349	17			

Table A3.8 Post-hoc Tukey-Kramer test results comparing intracellular fluorescence (PC3 cells) of the 50 nm nanoparticles after 2 h incubation.

Multiple Comparisons

Dependent Variable: 2 h

Tukey HSD

(I) Particles	(J) Particles	Mean Difference (I-J)	Std. Error	Sig.	95% Confidence Interval	
					Lower Bound	Upper Bound
4	5	.0119159583	.0207081228	.835	-.041872775	.0657046912
	6	-.281103465*	.0207081228	.000	-.334892198	-.227314732
5	4	-.011915958	.0207081228	.835	-.065704691	.0418727746
	6	-.293019423*	.0207081228	.000	-.346808156	-.239230691
6	4	.281103465*	.0207081228	.000	.2273147322	.3348921980
	5	.293019423*	.0207081228	.000	.2392306905	.3468081563

*. The mean difference is significant at the 0.05 level.

Table A3.9 Analysis of variance (ANOVA) results table comparing intracellular fluorescence (PC3 cells) of the 50 nm nanoparticles after 4 h incubation.

ANOVA

4 h

	Sum of Squares	df	Mean Square	F	Sig.
Between Groups	.265	2	.132	95.929	.000
Within Groups	.021	15	.001		
Total	.285	17			

Table A3.10 Post-hoc Tukey-Kramer test results comparing intracellular fluorescence (PC3 cells) of the 50 nm nanoparticles after 4 h incubation.

Multiple Comparisons

Dependent Variable: 4 h

Tukey HSD

(I) Particles	(J) Particles	Mean Difference (I-J)	Std. Error	Sig.	95% Confidence Interval	
					Lower Bound	Upper Bound
4	5	.0203196807	.0214433123	.620	-.035378685	.0760180466
	6	-.246462410*	.0214433123	.000	-.302160776	-.190764044
5	4	-.020319681	.0214433123	.620	-.076018047	.0353786853
	6	-.266782090*	.0214433123	.000	-.322480456	-.211083725
6	4	.246462410*	.0214433123	.000	.1907640438	.3021607758
	5	.266782090*	.0214433123	.000	.2110837245	.3224804564

*. The mean difference is significant at the 0.05 level.

Table A3.11 Analysis of variance (ANOVA) results table comparing intracellular fluorescence (PC3 cells) of the 50 nm nanoparticles after 24 h incubation.

ANOVA

24 h

	Sum of Squares	df	Mean Square	F	Sig.
Between Groups	.086	2	.043	9.778	.002
Within Groups	.066	15	.004		
Total	.152	17			

Table A3.12 Post-hoc Tukey-Kramer test results comparing intracellular fluorescence (PC3 cells) of the 50 nm nanoparticles after 24 h incubation.

Multiple Comparisons

Dependent Variable: 24 h

Tukey HSD

(I) Particles	(J) Particles	Mean Difference (I-J)	Std. Error	Sig.	95% Confidence Interval	
					Lower Bound	Upper Bound
4	5	.0809916719	.0383326770	.121	-.018576316	.1805596600
	6	-.088472859	.0383326770	.085	-.188040847	.0110951288
5	4	-.080991672	.0383326770	.121	-.180559660	.0185763162
	6	-.169464531*	.0383326770	.001	-.269032519	-.069896543
6	4	.0884728594	.0383326770	.085	-.011095129	.1880408475
	5	.169464531*	.0383326770	.001	.0698965431	.2690325194

*. The mean difference is significant at the 0.05 level.

Comparison between time points

Table A3.13 Analysis of variance (ANOVA) results table comparing intracellular fluorescence (PC3 cells) between time points for all nanoparticles.

ANOVA

		Sum of Squares	df	Mean Square	F	Sig.
100H	Between Groups	.219	2	.109	190.582	.000
	Within Groups	.009	15	.001		
	Total	.227	17			
100M	Between Groups	.621	2	.310	157.767	.000
	Within Groups	.030	15	.002		
	Total	.650	17			
100S	Between Groups	.436	2	.218	18.058	.000
	Within Groups	.169	14	.012		
	Total	.605	16			
50H	Between Groups	1.515	2	.758	169.347	.000
	Within Groups	.067	15	.004		
	Total	1.583	17			
50M	Between Groups	1.211	2	.606	815.771	.000
	Within Groups	.011	15	.001		
	Total	1.222	17			
50S	Between Groups	.768	2	.384	206.759	.000
	Within Groups	.028	15	.002		
	Total	.796	17			

Table A3.14 Post-hoc Tukey-Kramer test results comparing intracellular fluorescence (PC3 cells) between time points for all nanoparticles.

Multiple Comparisons

Tukey HSD

Dependent Variable	(I) time	(J) time	Mean Difference (I-J)	Statistics		95% Confidence Interval	
				Std. Error	Sig.	Lower Bound	Upper Bound
100H	2	4	-.028306170	.0138280751	.1351996192	-.064224183	.0076118442
		24	-.246666213*	.0138280751	.0000000058	-.282584227	-.210748200
	4	2	.0283061696	.0138280751	.1351996192	-.007611844	.0642241833
		24	-.218360044*	.0138280751	.0000000060	-.254278058	-.182442030
	24	2	.246666213*	.0138280751	.0000000058	.2107481997	.2825842272
		4	.218360044*	.0138280751	.0000000060	.1824420302	.2542780576
100M	2	4	-.027256447	.0256112958	.5497030078	-.093781026	.0392681324
		24	-.406910140*	.0256112958	.0000000060	-.473434719	-.340385561
	4	2	.0272564467	.0256112958	.5497030078	-.039268132	.0937810258
		24	-.379653693*	.0256112958	.0000000064	-.446178272	-.313129114
	24	2	.406910140*	.0256112958	.0000000060	.3403855609	.4734347191
		4	.379653693*	.0256112958	.0000000064	.3131291142	.4461782724
100S	2	4	-.099897934	.0634566929	.2886241577	-.265981900	.0661860313
		24	-.389262993*	.0665539409	.0001175805	-.563453325	-.215072660
	4	2	.0998979342	.0634566929	.2886241577	-.066186031	.2659818998
		24	-.289365059*	.0665539409	.0018099693	-.463555391	-.115174726
	24	2	.389262993*	.0665539409	.0001175805	.2150726601	.5634533254
		4	.289365059*	.0665539409	.0018099693	.1151747259	.4635553911
50H	2	4	-.074252332	.0386198445	.1665911142	-.174566229	.0260615652
		24	-.649282123*	.0386198445	.0000000059	-.749596021	-.548968226
	4	2	.0742523321	.0386198445	.1665911142	-.026061565	.1745662294
		24	-.575029791*	.0386198445	.0000000064	-.675343688	-.474715894
	24	2	.649282123*	.0386198445	.0000000059	.5489682260	.7495960206
		4	.575029791*	.0386198445	.0000000064	.4747158939	.6753436885
50M	2	4	-.065848610*	.0157299202	.0021562411	-.106706610	-.024990610
		24	-.580206410*	.0157299202	.0000000058	-.621064410	-.539348410
	4	2	.065848610*	.0157299202	.0021562411	.0249906098	.1067066097
		24	-.514357800*	.0157299202	.0000000058	-.555215800	-.473499800
	24	2	.580206410*	.0157299202	.0000000058	.5393484098	.6210644096
		4	.514357800*	.0157299202	.0000000058	.4734998000	.5552157999
50S	2	4	-.039611277	.0248819882	.2792980209	-.104241501	.0250189473
		24	-.456651518*	.0248819882	.0000000058	-.521281742	-.392021293
	4	2	.0396112768	.0248819882	.2792980209	-.025018947	.1042415009
		24	-.417040241*	.0248819882	.0000000059	-.481670465	-.352410017
	24	2	.456651518*	.0248819882	.0000000058	.3920212935	.5212817416
		4	.417040241*	.0248819882	.0000000059	.3524100167	.4816704648

*. The mean difference is significant at the 0.05 level.

Inhibitors

Table A3.15 Analysis of variance (ANOVA) results table comparing intracellular fluorescence (PC3 cells) between 100 nm particles after treatment with endocytosis inhibitors.

ANOVA

		Sum of Squares	df	Mean Square	F	Sig.
Clathrin	Between Groups	.749	2	.375	28.972	.000
	Within Groups	.181	14	.013		
	Total	.931	16			
Macropinocytosis	Between Groups	.631	2	.315	106.197	.000
	Within Groups	.018	6	.003		
	Total	.649	8			
Caveolae	Between Groups	.370	2	.185	59.152	.000
	Within Groups	.047	15	.003		
	Total	.417	17			

Table A3.16 Post-hoc Tukey-Kramer test results comparing intracellular fluorescence (PC3 cells) between 100 nm particles after treatment with endocytosis inhibitors.

Multiple Comparisons

Tukey HSD

Dependent Variable	(I) V1	(J) V1	Mean Difference (I-J)	Std. Error	Sig.	95% Confidence Interval	
						Lower Bound	Upper Bound
Clathrin	1	2	-.397691597*	.0688666526	.000	-.577934945	-.217448249
		3	-.467028445*	.0656617769	.000	-.638883734	-.295173155
	2	1	.397691597*	.0688666526	.000	.2174482492	.5779349448
		3	-.069336848	.0688666526	.585	-.249580195	.1109065002
	3	1	.467028445*	.0656617769	.000	.2951731555	.6388837337
		2	.0693368476	.0688666526	.585	-.110906500	.2495801954
Macropinocytosis	1	2	-.503174588*	.0444979963	.000	-.639706661	-.366642516
		3	-.605886494*	.0444979963	.000	-.742418566	-.469354422
	2	1	.503174588*	.0444979963	.000	.3666425161	.6397066605
		3	-.102711906	.0444979963	.130	-.239243978	.0338201664
	3	1	.605886494*	.0444979963	.000	.4693544219	.7424185662
		2	.1027119057	.0444979963	.130	-.033820166	.2392439779
Caveolae	1	2	-.188512610*	.0322808098	.000	-.272361054	-.104664167
		3	-.350785249*	.0322808098	.000	-.434633692	-.266936805
	2	1	.188512610*	.0322808098	.000	.1046641672	.2723610538
		3	-.162272638*	.0322808098	.000	-.246121081	-.078424195
	3	1	.350785249*	.0322808098	.000	.2669368053	.4346336919
		2	.162272638*	.0322808098	.000	.0784241948	.2461210814

*. The mean difference is significant at the 0.05 level.

Table A3.17 Analysis of variance (ANOVA) results table comparing intracellular fluorescence (PC3 cells) between 100 nm particles after treatment with endocytosis inhibitors.

ANOVA

		Sum of Squares	df	Mean Square	F	Sig.
Clathrin	Between Groups	.200	2	.100	13.127	.001
	Within Groups	.114	15	.008		
	Total	.314	17			
Macropinocytosis	Between Groups	2.259	2	1.130	40.713	.000
	Within Groups	.333	12	.028		
	Total	2.592	14			
Caveolae	Between Groups	.060	2	.030	6.506	.009
	Within Groups	.069	15	.005		
	Total	.129	17			

Table A3.18 Post-hoc Tukey-Kramer test results comparing intracellular fluorescence (PC3 cells) between 50 nm particles after treatment with endocytosis inhibitors.

Multiple Comparisons

Tukey HSD

Dependent Variable	(I) V1	(J) V1	Mean Difference (I-J)	Std. Error	Sig.	95% Confidence Interval	
						Lower Bound	Upper Bound
Clathrin	4	5	-.245044152*	.0503737099	.001	-.375888365	-.114199939
		6	-.192726445*	.0503737099	.004	-.323570658	-.061882232
	5	4	.245044152*	.0503737099	.001	.1141999388	.3758883649
		6	.0523177067	.0503737099	.565	-.078526506	.1831619197
	6	4	.192726445*	.0503737099	.004	.0618822321	.3235706582
		5	-.052317707	.0503737099	.565	-.183161920	.0785265064
Macropinocytosis	4	5	-.961325283*	.1177843525	.000	-1.27555788	-.647092689
		6	-.978766141*	.1177843525	.000	-1.29299873	-.664533547
	5	4	.961325283*	.1177843525	.000	.6470926893	1.275557876
		6	-.017440858	.0961705211	.982	-.274010696	.2391289802
	6	4	.978766141*	.1177843525	.000	.6645335473	1.292998734
		5	.0174408580	.0961705211	.982	-.239128980	.2740106962
Caveolae	4	5	-.118674303*	.0392258602	.022	-.220562308	-.016786298
		6	-.126066686*	.0392258602	.015	-.227954691	-.024178681
	5	4	.118674303*	.0392258602	.022	.0167862979	.2205623078
		6	-.007392384	.0392258602	.981	-.109280388	.0944956215
	6	4	.126066686*	.0392258602	.015	.0241786814	.2279546913
		5	.0073923835	.0392258602	.981	-.094495621	.1092803885

*. The mean difference is significant at the 0.05 level.

Caco-2 timecourse

Table A3.19 Analysis of variance (ANOVA) results table comparing intracellular fluorescence (Caco-2 cells) of the 100 nm nanoparticles after 2h, 4 h and 24 h incubation.

ANOVA

		Sum of Squares	df	Mean Square	F	Sig.
2 h	Between Groups	.523	2	.262	92.850	.000
	Within Groups	.042	15	.003		
	Total	.566	17			
4 h	Between Groups	.690	2	.345	93.512	.000
	Within Groups	.055	15	.004		
	Total	.745	17			
24 h	Between Groups	.757	2	.378	4.229	.035
	Within Groups	1.342	15	.089		
	Total	2.099	17			

Table A3.20 Post-hoc Tukey-Kramer test results comparing intracellular fluorescence (Caco-2 cells) between 100 nm particles after 2h, 4 h and 24 h incubation.

Multiple Comparisons

Tukey HSD

Dependent Variable	(I) Particle	(J) Particle	Mean Difference (I-J)	Std. Error	Sig.	95% Confidence Interval	
						Lower Bound	Upper Bound
2 h	1	2	-.08484759*	.0306528959	.037	-.164104745	-.004864774
		3	-.396515378*	.0306528959	.000	-.476135363	-.316895393
	2	1	.08484759*	.0306528959	.037	.0048647741	.1641047446
		3	-.312030619*	.0306528959	.000	-.391650604	-.232410634
	3	1	.396515378*	.0306528959	.000	.3168953929	.4761353634
		2	.312030619*	.0306528959	.000	.2324106336	.3916506041
4 h	1	2	-.088962825	.0350677045	.056	-.180050144	.0021244944
		3	-.452597240*	.0350677045	.000	-.543684560	-.361509921
	2	1	.0889628248	.0350677045	.056	-.002124494	.1800501439
		3	-.363634416*	.0350677045	.000	-.454721735	-.272547096
	3	1	.452597240*	.0350677045	.000	.3615099212	.5436845596
		2	.363634416*	.0350677045	.000	.2725470965	.4547217348
24 h	1	2	-.246103909	.1727078797	.354	-.694707489	.2024996710
		3	-.502270942*	.1727078797	.028	-.950874522	-.053667362
	2	1	.2461039091	.1727078797	.354	-.202499671	.6947074891
		3	-.256167033	.1727078797	.326	-.704770613	.1924365467
	3	1	.502270942*	.1727078797	.028	.0536673624	.9508745224
		2	.2561670333	.1727078797	.326	-.192436547	.7047706134

*. The mean difference is significant at the 0.05 level.

Table A3.21 Analysis of variance (ANOVA) results table comparing intracellular fluorescence (Caco-2 cells) of the 50 nm nanoparticles after 2h, 4 h and 24 h incubation.

ANOVA

		Sum of Squares	df	Mean Square	F	Sig.
2 h	Between Groups	.656	2	.328	118.166	.000
	Within Groups	.036	13	.003		
	Total	.692	15			
4 h	Between Groups	.550	2	.275	25.341	.000
	Within Groups	.163	15	.011		
	Total	.712	17			
24 h	Between Groups	.852	2	.426	9.416	.002
	Within Groups	.678	15	.045		
	Total	1.530	17			

Table A3.22 Post-hoc Tukey-Kramer test results comparing intracellular fluorescence (Caco-2 cells) between 50 nm particles after 2h, 4 h and 24 h incubation.

Multiple Comparisons

Tukey HSD

Dependent Variable	(I) Particle	(J) Particle	Mean Difference (I-J)	Std. Error	Sig.	95% Confidence Interval	
						Lower Bound	Upper Bound
2 h	4	5	-.065842680	.0340008924	.168	-.155619899	.0239345385
		6	-.441165627*	.0304113227	.000	-.521464813	-.360866441
	5	4	.0658426802	.0340008924	.168	-.023934539	.1556198989
		6	-.375322947*	.0340008924	.000	-.465100166	-.285545728
	6	4	.441165627*	.0304113227	.000	.3608664415	.5214648126
		5	.375322947*	.0340008924	.000	.2855457281	.4651001656
4 h	4	5	-.032073133	.0601238100	.856	-.188242941	.1240966748
		6	-.385680861*	.0601238100	.000	-.541850669	-.229511053
	5	4	.0320731333	.0601238100	.856	-.124096675	.1882429414
		6	-.353607728*	.0601238100	.000	-.509777536	-.197437920
	6	4	.385680861*	.0601238100	.000	.2295110530	.5418506692
		5	.353607728*	.0601238100	.000	.1974379197	.5097775359
24 h	4	5	.526060632*	.1227743082	.002	.2071580187	.8449632457
		6	.336109762*	.1227743082	.038	.0172071483	.6550123754
	5	4	-.526060632*	.1227743082	.002	-.844963246	-.207158019
		6	-.189950870	.1227743082	.298	-.508853484	.1289517432
	6	4	-.336109762*	.1227743082	.038	-.655012375	-.017207148
		5	.1899508703	.1227743082	.298	-.128951743	.5088534838

*. The mean difference is significant at the 0.05 level.

Table A3.23 Post-hoc Tukey-Kramer test results comparing intracellular fluorescence (Caco-2 cells) between time points for all nanoparticles.

Multiple Comparisons

Tukey HSD

Dependent Variable			Mean Difference (I-J)	Std. Error	Sig.	95% Confidence Interval	
						Lower Bound	Upper Bound
100H	2	4	-0.0424122913	0.1196061385	0.9333400300	-0.3530856782	0.2682610956
		24	-.399139643000000*	0.1196061385	0.0117889795	-0.7098130302	-0.0884662563
	4	2	0.0424122913	0.1196061385	0.9333400300	-0.2682610956	0.3530856782
		24	-.356727352000000*	0.1196061385	0.0237924745	-0.6674007389	-0.0460539650
	24	2	.399139643000000*	0.1196061385	0.0117889795	0.0884662563	0.7098130302
		4	.356727352000000*	0.1196061385	0.0237924745	0.0460539650	0.6674007389
100M	2	4	-0.0468903567	0.1123114387	0.9089620520	-0.3386159778	0.2448352643
		24	-.560758793000000*	0.1123114387	0.0004441717	-0.8524844140	-0.2690331719
	4	2	0.0468903567	0.1123114387	0.9089620520	-0.2448352643	0.3386159778
		24	-.513868436000000*	0.1123114387	0.0009990254	-0.8055940573	-0.2221428152
	24	2	.560758793000000*	0.1123114387	0.0004441717	0.2690331719	0.8524844140
		4	.513868436000000*	0.1123114387	0.0009990254	0.2221428152	0.8055940573
100S	2	4	-0.0984941535	0.0712591608	0.3745641934	-0.2835877040	0.0865993970
		24	-.504895207000000*	0.0712591608	0.0000105220	-0.6899887580	-0.3198016570
	4	2	0.0984941535	0.0712591608	0.3745641934	-0.0865993970	0.2835877040
		24	-.406401054000000*	0.0712591608	0.0001170070	-0.5914946045	-0.2213075034
	24	2	.504895207000000*	0.0712591608	0.0000105220	0.3198016570	0.6899887580
		4	.406401054000000*	0.0712591608	0.0001170070	0.2213075034	0.5914946045
50H	2	4	-0.1145611069	0.0940173956	0.4608836751	-0.3587684954	0.1296462816
		24	-1.061716452000000*	0.0940173956	0.0000000340	-1.3059238408	-0.8175090639
	4	2	0.1145611069	0.0940173956	0.4608836751	-0.1296462816	0.3587684954
		24	-.947155345000000*	0.0940173956	0.0000001355	-1.1913627339	-0.7029479570
	24	2	1.061716452000000*	0.0940173956	0.0000000340	0.8175090639	1.3059238408
		4	.947155345000000*	0.0940173956	0.0000001355	0.7029479570	1.1913627339
50M	2	4	-0.0807915600	0.0821691599	0.5997680422	-0.2977540608	0.1361709407
		24	-.469813140000000*	0.0821691599	0.0001949908	-0.6867756408	-0.2528506392
	4	2	0.0807915600	0.0821691599	0.5997680422	-0.1361709407	0.2977540608
		24	-.389021580000000*	0.0734943309	0.0003984322	-0.5830787401	-0.1949644198
	24	2	.469813140000000*	0.0821691599	0.0001949908	0.2528506392	0.6867756408
		4	.389021580000000*	0.0734943309	0.0003984322	0.1949644198	0.5830787401
50S	2	4	-0.0590763410	0.0772621527	0.7296523598	-0.2597624843	0.1416098023
		24	-.284441063000000*	0.0772621527	0.0059168754	-0.4851272067	-0.0837549202
	4	2	0.0590763410	0.0772621527	0.7296523598	-0.1416098023	0.2597624843
		24	-.225364722000000*	0.0772621527	0.0270524949	-0.4260508658	-0.0246785792
	24	2	.284441063000000*	0.0772621527	0.0059168754	0.0837549202	0.4851272067
		4	.225364722000000*	0.0772621527	0.0270524949	0.0246785792	0.4260508658

Caco-2 inhibitors

Table A3.24 Analysis of variance (ANOVA) results table comparing intracellular fluorescence (Caco-2 cells) between 100 nm particles after treatment with endocytosis inhibitors.

ANOVA

		Sum of Squares	df	Mean Square	F	Sig.
Clathrin	Between Groups	1.033	2	.517	23.954	.001
	Within Groups	.151	7	.022		
	Total	1.184	9			
Macropinocytosis	Between Groups	.134	2	.067	4.703	.045
	Within Groups	.114	8	.014		
	Total	.249	10			
Caveolae	Between Groups	.230	2	.115	9.690	.003
	Within Groups	.142	12	.012		
	Total	.372	14			

Table A3.25 Post-hoc Tukey-Kramer test results comparing intracellular fluorescence (Caco-2) between 100 nm particles after treatment with endocytosis inhibitors.

Multiple Comparisons

Tukey HSD

Dependent Variable	(I) V1	(J) V1	Mean Difference (I-J)	Std. Error	Sig.	95% Confidence Interval	
						Lower Bound	Upper Bound
Clathrin	1	2	-.688621674*	.1121616859	.001	-1.01894439	-.358298959
		3	-.717384871*	.1199058859	.001	-1.07051471	-.364255036
	2	1	.688621674*	.1121616859	.001	.3582989592	1.018944388
		3	-.028763198	.1121616859	.965	-.359085912	.3015595167
	3	1	.717384871*	.1199058859	.001	.3642550359	1.070514707
		2	.0287631978	.1121616859	.965	-.301559517	.3590859122
Macropinocytosis	1	2	-.197779643	.0845200744	.107	-.439291049	.0437317629
		3	-.259328978	.0912921144	.051	-.520191111	.0015331547
	2	1	.1977796429	.0845200744	.107	-.043731763	.4392910487
		3	-.061549335	.0912921144	.784	-.322411468	.1993127977
	3	1	.2593289780	.0912921144	.051	-.001533155	.5201911108
		2	.0615493351	.0912921144	.784	-.199312798	.3224114679
Caveolae	1	2	-.242010440*	.0769757436	.021	-.447371229	-.036649651
		3	-.338135463*	.0769757436	.002	-.543496252	-.132774674
	2	1	.242010440*	.0769757436	.021	.0366496507	.4473712285
		3	-.096125023	.0628504315	.312	-.263801405	.0715513587
	3	1	.338135463*	.0769757436	.002	.1327746740	.5434962519
		2	.0961250234	.0628504315	.312	-.071551359	.2638014054

*. The mean difference is significant at the 0.05 level.

Table A3.26 Analysis of variance (ANOVA) results table comparing intracellular fluorescence (Caco-2 cells) between 50 nm particles after treatment with endocytosis inhibitors.

ANOVA

		Sum of Squares	df	Mean Square	F	Sig.
Clathrin	Between Groups	.312	2	.156	14.306	.003
	Within Groups	.076	7	.011		
	Total	.389	9			
Macropinocytosis	Between Groups	.240	2	.120	6.622	.017
	Within Groups	.163	9	.018		
	Total	.404	11			
Caveolae	Between Groups	.006	2	.003	.239	.792
	Within Groups	.119	10	.012		
	Total	.125	12			

Table A3.27 Post-hoc Tukey-Kramer test results comparing intracellular fluorescence (Caco-2 cells) between 50 nm particles after treatment with endocytosis inhibitors.

Multiple Comparisons

Tukey HSD

Dependent Variable	(I) V1	(J) V1	Mean Difference (I-J)	Std. Error	Sig.	95% Confidence Interval	
						Lower Bound	Upper Bound
Clathrin	4	5	-.424634460*	.0852861978	.004	-.675807293	-.173461627
		6	-.344122218*	.0797779330	.009	-.579072889	-.109171547
	5	4	.424634460*	.0852861978	.004	.1734616274	.6758072927
		6	.0805122421	.0797779330	.595	-.154438429	.3154629132
	6	4	.344122218*	.0797779330	.009	.1091715468	.5790728891
		5	-.080512242	.0797779330	.595	-.315462913	.1544384290
Macropinocytosis	4	5	-.317594301*	.0952372251	.022	-.583497169	-.051691433
		6	-.279001461*	.0952372251	.040	-.544904329	-.013098593
	5	4	.317594301*	.0952372251	.022	.0516914333	.5834971691
		6	.0385928404	.0952372251	.914	-.227310027	.3044957083
	6	4	.279001461*	.0952372251	.040	.0130985929	.5449043287
		5	-.038592840	.0952372251	.914	-.304495708	.2273100275
Caveolae	4	5	-.049406001	.0733297192	.784	-.250424404	.1516124010
		6	-.037772806	.0772963110	.878	-.249664807	.1741191953
	5	4	.0494060015	.0733297192	.784	-.151612401	.2504244040
		6	.0116331956	.0733297192	.986	-.189385207	.2126515981
	6	4	.0377728059	.0772963110	.878	-.174119195	.2496648071
		5	-.011633196	.0733297192	.986	-.212651598	.1893852069

*. The mean difference is significant at the 0.05 level.

Appendix 4

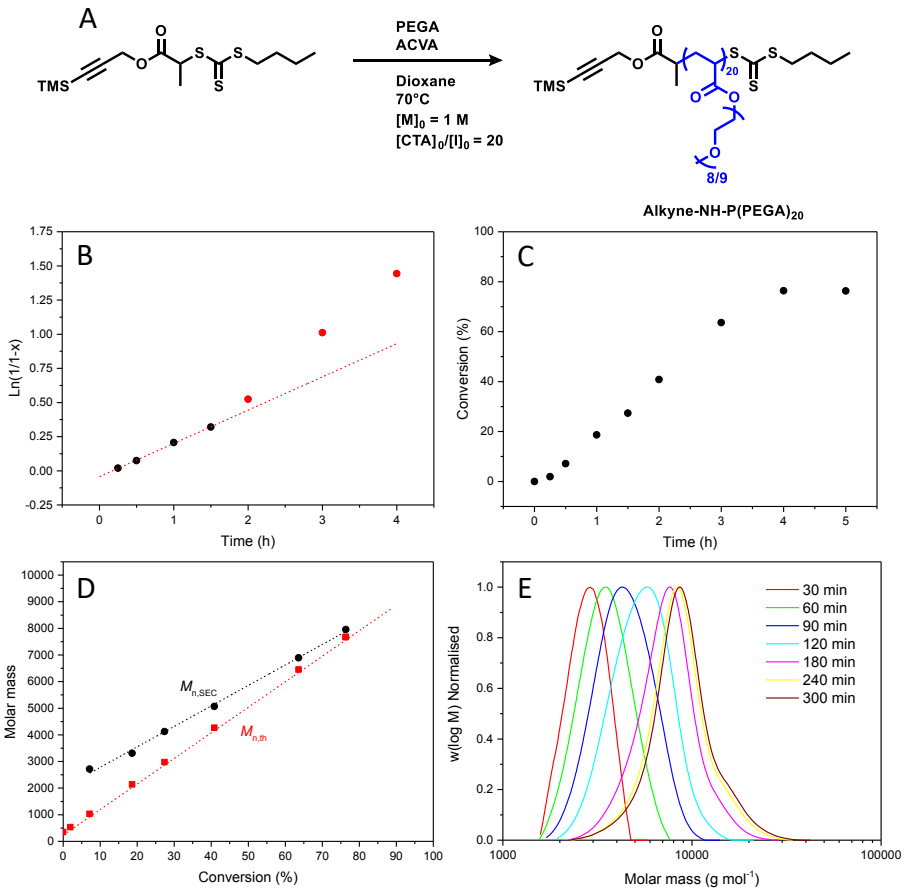

Figure A4.1. (A) Polymerisation of PEGA mediated with **TMS-Alkyne-PEsBTC**, (B) pseudo first order plot, red points indicate data masked from the linear fit (red dashed line), (C) time vs conversion, (D) conversion vs $M_{n,SEC}$ and linear fit (dashed black line), (E) evolution of SEC chromatograms over time.

Table A4.1 Data for the polymerisation kinetics of PEGA using with **TMS-Alkyne-PEsBTC** as the CTA.

Time (h)	% conv[a]	$M_{n,th}$ (g mol^{-1})[b]	$M_{n,SEC}$ (g mol^{-1})[c]	$M_{w,SEC}$ (g mol^{-1})[c]	$Đ$[c]
0	0	348	-	-	
0.25	2	500	-	-	
0.5	7	1000	2700	2900	1.05
1	18	2100	3300	3600	1.1
1.5	27	3000	4100	4600	1.12
2	41	4300	5100	5700	1.13
3	64	6500	6900	7900	1.14
4	76	7700	8000	9100	1.14
5	76	7700	8300	9500	1.15

[a]Determined by ^{1}H NMR spectroscopy, [b]Theoretical molar masses calculated with Equation 2.12, [c]Determined by THF-SEC and analysed against PMMA standards.

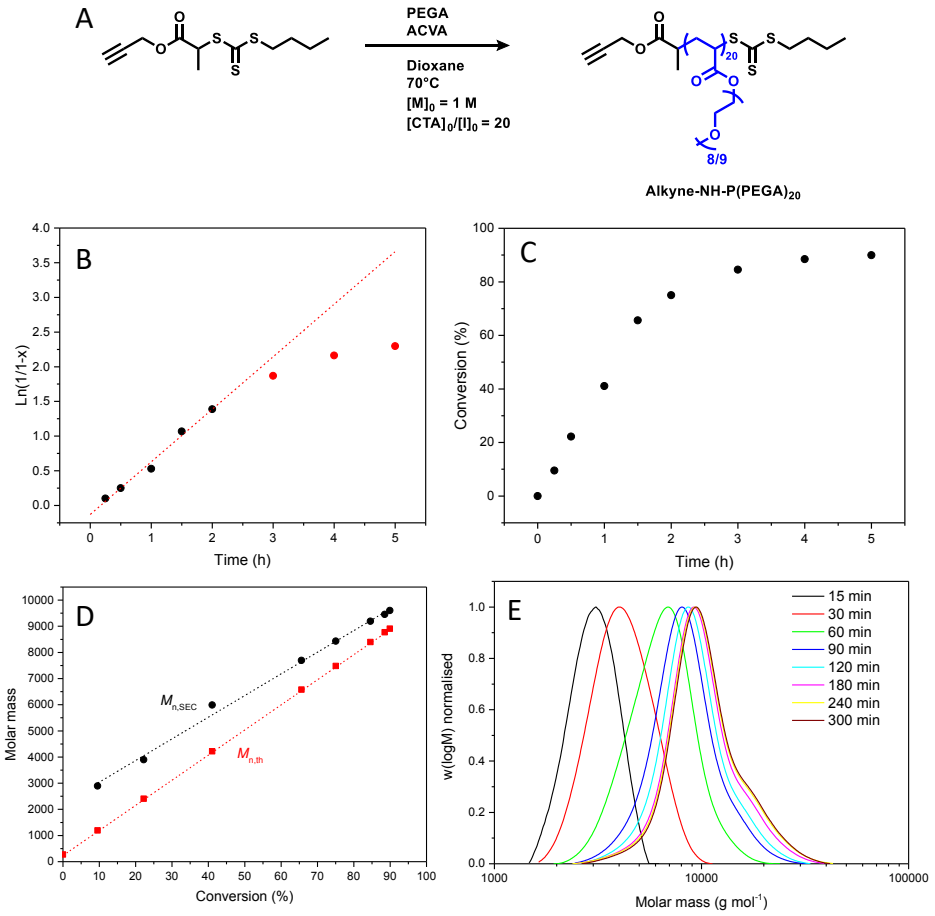

Figure A4.2. (A) Polymerisation of PEGA mediated with **Alkyne-PEsBTC**, (B) pseudo first order plot, red points indicate data masked from the linear fit (red dashed line), (C) time vs conversion, (D) conversion vs $M_{n,SEC}$ and linear fit (dashed black line), (E) evolution of SEC chromatograms over time.

Table A4.2 Data for the polymerisation kinetics of PEGA using with **Alkyne-PEsBTC** as the CTA.

Time (h)	% conv[a]	$M_{n,th}$ (g mol^{-1})[b]	$M_{n,SEC}$ (g mol^{-1})[c]	$M_{w,SEC}$ (g mol^{-1})[c]	$Đ$[c]
0	0	276	-	-	
0.25	10	1200	2900	3100	1.13
0.5	22	2400	3900	4300	1.15
1	41	4200	6000	6800	1.15
1.5	66	6600	7700	8800	1.15
2	75	7500	8400	9700	1.16
3	85	8400	9200	10700	1.17
4	88	8800	9500	11100	1.17
5	89	8900	9600	11200	1.18

[a]Determined by ^{1}H NMR spectroscopy, [b]Theoretical molar masses calculated with Equation 2.12, [c]Determined by THF-SEC and analysed against PMMA standards.

Table A4.3 Polymerisation conditions for macro-RAFT agents synthesised in chapter 4.

	Monomer	RAFT agent	$[M]_0/[RAFT]_0$	Polymerisation Time (h)	$[CTA]_0/[I]_0$	Conversion (%)
TMS-Alkyne-O-P[(PEGA)$_{12}$	PEGA	**TMS-Alkyne-PEsBTC**	15	5	20	82
TMS-Alkyne-O-P[(PEGA)$_{12}$-*b*-(*n*-BA)$_{12}$]	*n*-BA	**TMS-Alkyne-O-P[(PEGA)$_{12}$**	14	5	20	90
TMS-Alkyne-O-P[(PEGA)$_{12}$-*co*-(AA)$_3$]	PEGA + AA	**TMS-Alkyne-PEsBTC**	15+3	5	20	84
TMS-Alkyne-O-P[(PEGA)$_{12}$-*co*-(AA)$_3$]-(*n*-BA)$_{15}$	*n*-BA	**TMS-Alkyne-O-P[(PEGA)$_{12}$-*co*-(AA)$_3$]**	15	5	10	99
Alkyne-O-P[(PEGA)$_{12}$-*co*-(AA)$_3$]	PEGA + AA	**Alkyne-PEsBTC**	15+3	5	20	87
Alkyne-O-P[(PEGA)$_{12}$-*co*-(AA)$_3$]-(*n*-BA)$_{15}$	*n*-BA	**Alkyne-O-P[(PEGA)$_{12}$-*co*-(AA)$_3$]**	15	5	20	81

All reactions were performed at [M] = 1M, at 70°C using ACVA as thermal initiator and 1,4-dioxane as the solvent.

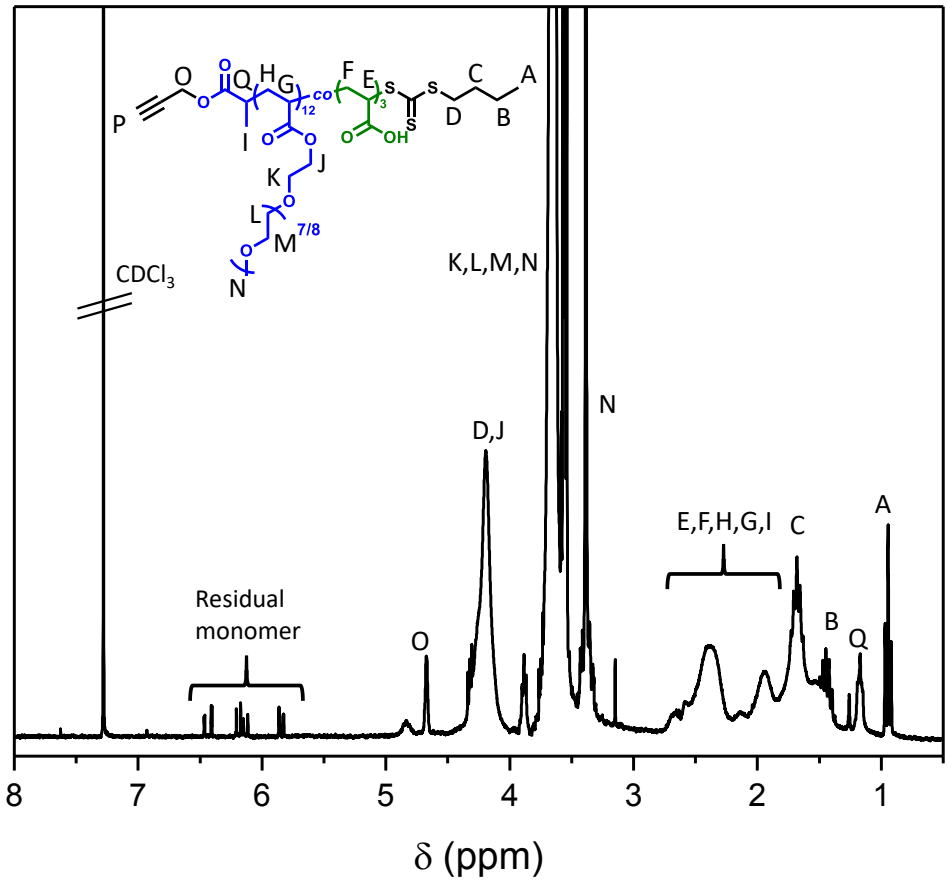

Figure A 4.3 ^{1}H NMR spectrum **of Alkyne-O-P[(PEGA)$_{12}$-co-(AA)$_{3}$]** in $CDCl_3$.

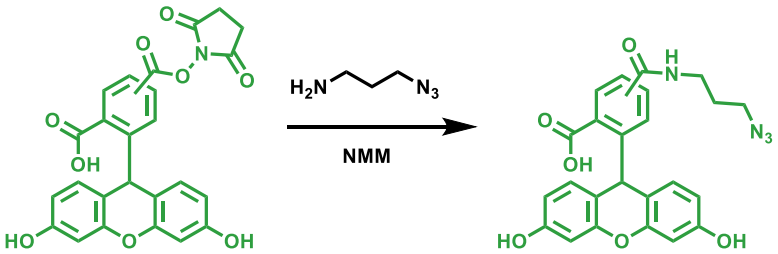

Scheme A4.1 Preparation of **Fluorescein-N$_3$** from **Fluorescein-NHS** and azidopropanamine

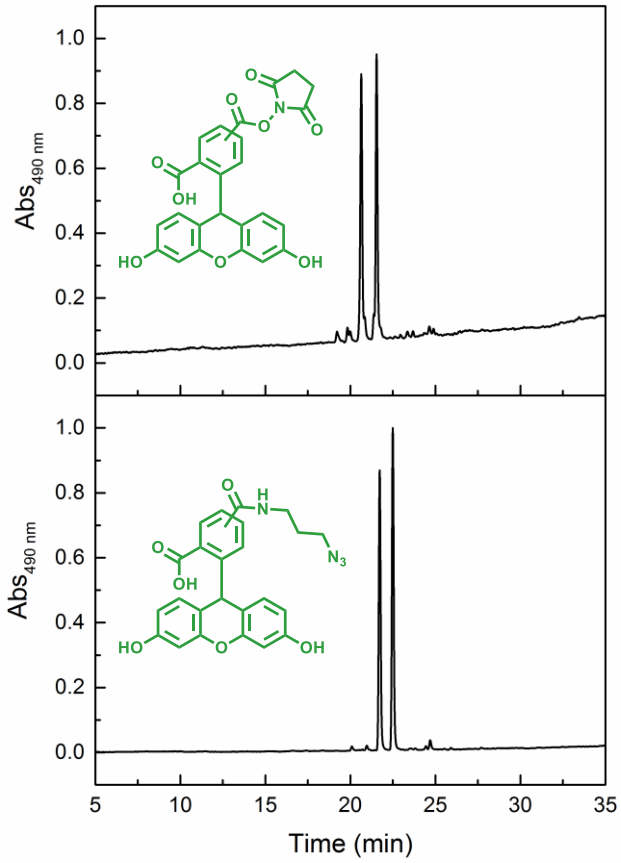

Figure A4.4 HPLC traces of **Fluorescein-NHS** and **Fluorescein-N_3** using absorbance detection at 490 nm over a 5-95% gradient (MeOH/water).

Appendix 5

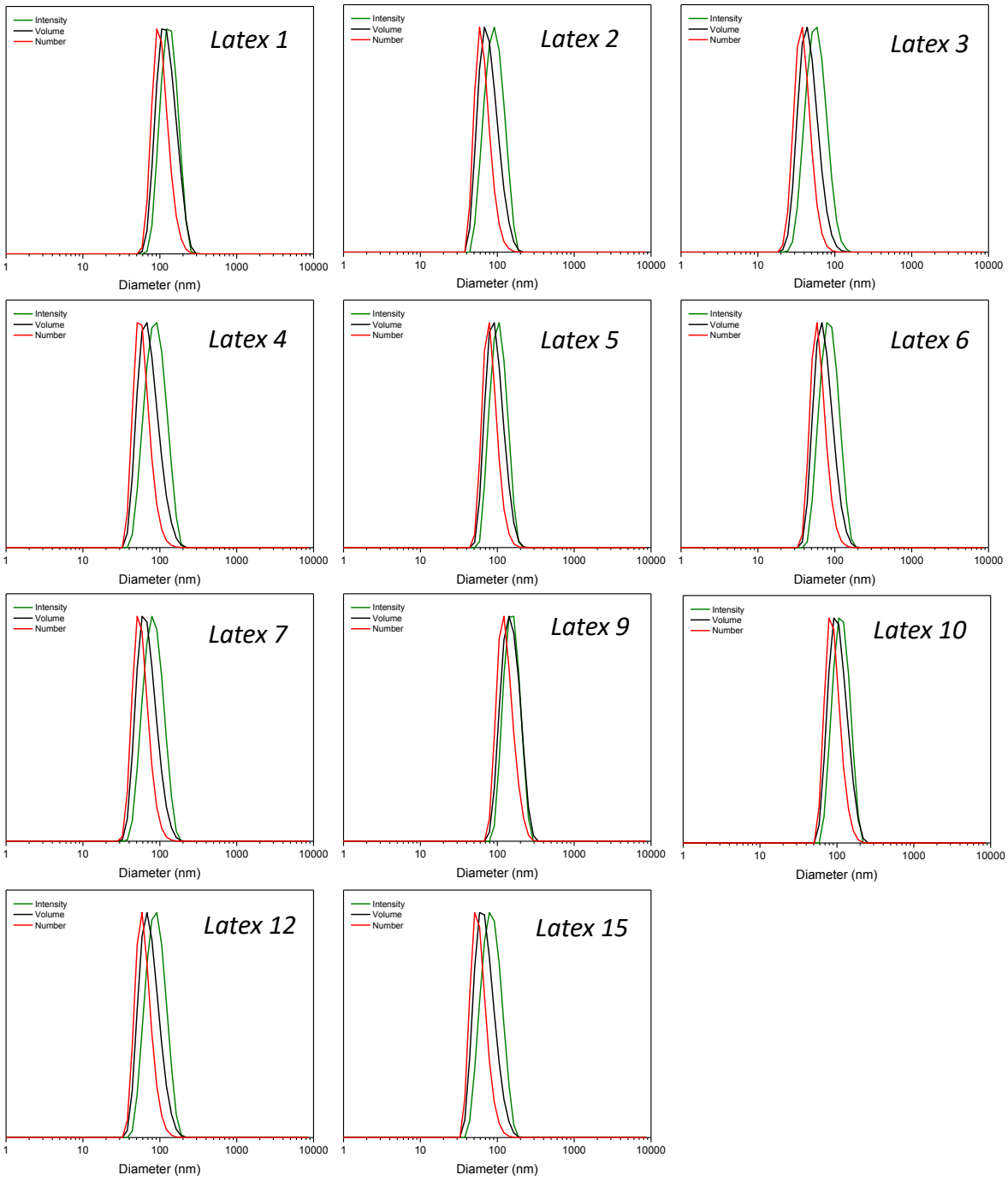

Figure A5.1 DLS particle size distributions (intensity = green, volume = black, number = red) measured in water at 25˚C for *Latex 1-7*, *Latex 9-10, Latex 12* and *Latex 15*.

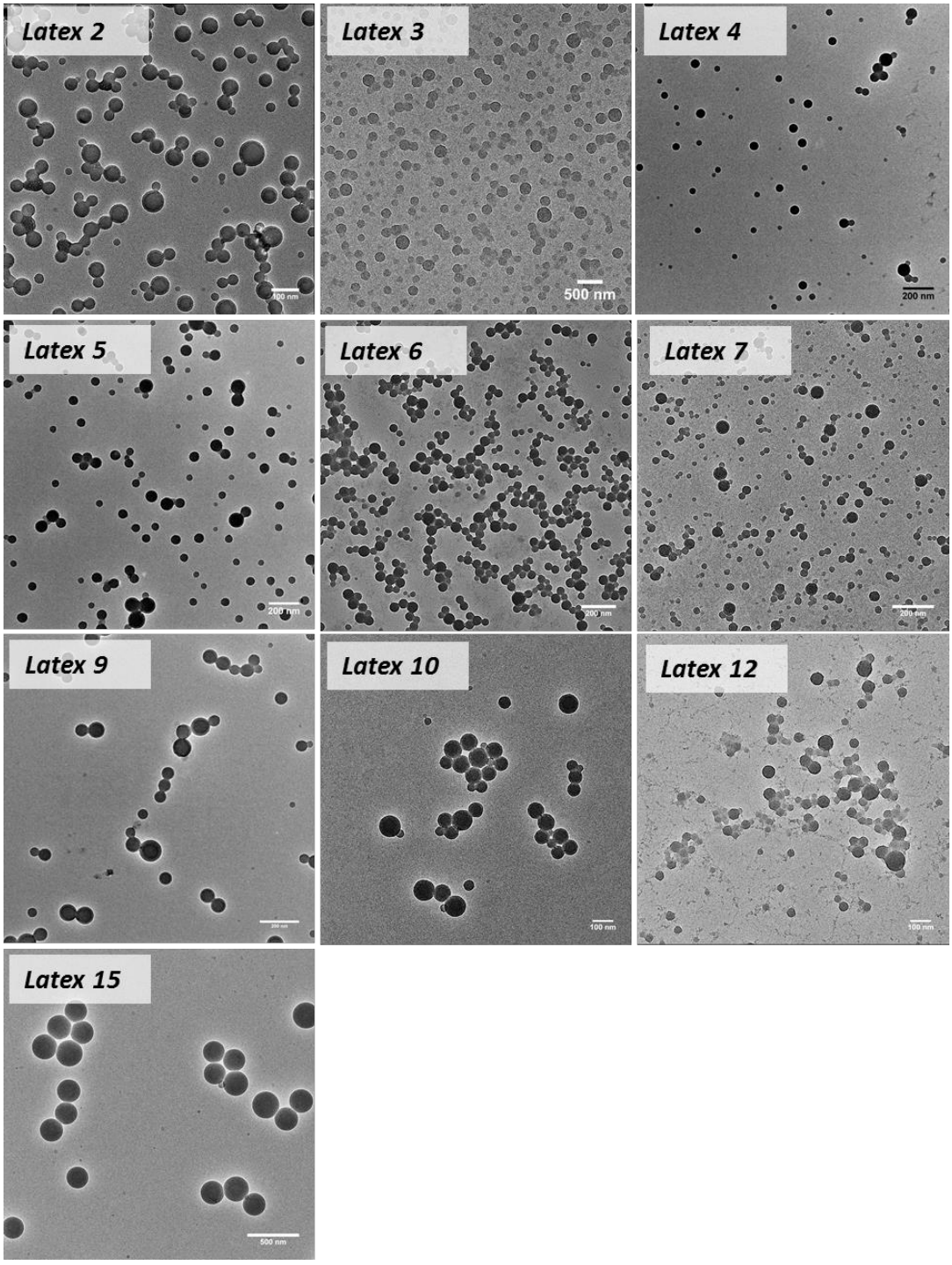

Figure A5.2 TEM images for *Latex 2-7*, *Latex 9-10, Latex 12* and *Latex 15*.

Table A5.1 Polymerisation conditions for the systematic nanoparticle synthesis study. Orange cells represent changes from *Latex* 1 for *Latex 2-9* and *Latex 8* for *Latex 10-16*.

		Macro-RAFT agent	Monomer	Initiator	[M]/[CTA]	[M] (mM)	[CTA] (mM)	[CTA]/[I]	T/°C	Time (h)	Stirring speed (RPM)	Conv (%)[a]	Particle diameter (nm)[b]	PDi[c]	ZP (mV)[d]
	Latex 1	$P(AMPS)_{50}$	Styrene	ACVA	450	450	1	4.65	80	6	400	96	78.5	0.052	-56.4
Effect of initiator	*Latex 2*	$P(AMPS)_{50}$	Styrene	**VA-086**	450	450	1	0.85	80	6	400	86	94.2	0.076	-50.8
	Latex 3	$P(AMPS)_{50}$	Styrene	**VA-057**	450	450	1	4.65	80	6	400	87	59.6	0.096	-51.5
Effect of temperature	*Latex 4*	$P(AMPS)_{50}$	Styrene	ACVA	450	450	1	1.8	**70**	6	400	71	91.4	0.091	-56.3
	Latex 5	$P(AMPS)_{50}$	Styrene	ACVA	450	450	1	4.65	**90**	6	400	95	100.4	0.056	-60.7
Effect of initiator concentration	*Latex 6*	$P(AMPS)_{50}$	Styrene	ACVA	450	450	1	**2.325**	80	6	400	88	97.2	0.073	-59.1
	Latex 7	$P(AMPS)_{50}$	Styrene	ACVA	450	450	1	**0.93**	80	6	400	85	95.5	0.083	-54.7
Effect of stirring speed	*Latex 8*	$P(AMPS)_{50}$	Styrene	ACVA	450	450	1	4.65	80	6	**800**	90	128.5	0.052	-60.3
	Latex 9	$P(AMPS)_{50}$	Styrene	ACVA	450	450	1	4.65	80	6	**1200**	85	157.7	0.052	-54.9
Effect of DP (differing [M])	*Latex 10*	$P(AMPS)_{50}$	Styrene	ACVA	**250**	**250**	1	4.65	80	6	800	96	120.7	0.049	-67.2
	Latex 11	$P(AMPS)_{50}$	Styrene	ACVA	**50**	**50**	1	4.65	80	6	800	85	-	-	-
Effect of DP (differing [CTA])	*Latex 12*	$P(AMPS)_{50}$	Styrene	ACVA	**250**	450	**1.75**	8.12	80	6	800	96	92.4	0.071	-57.7
	Latex 13	$P(AMPS)_{50}$	Styrene	ACVA	**50**	450	**8.75**	40.6	80	6	800	85	-	-	-
Effect of monomer	*Latex 14*	$P(AMPS)_{50}$	***n*-BA**	ACVA	450	450	1	4.65	80	6	800	93	200.5	0.051	-62.9
Effect of macro-CTA length	*Latex 15*	$P(AMPS)_{20}$	Styrene	ACVA	450	450	1	4.65	80	6	800	89	248.8	0.049	-58.3
	Latex 16	$P(AMPS)_{100}$	Styrene	ACVA	450	450	1	4.65	80	6	800	95	161.6	0.050	-61.6

[a]Measured using gravimetry. [b]Determined with DLS. [c]Calculated using equation S4. [c]Measured with a zetasizer.